

**DEVELOPMENT AND APPLICATION OF A  
MORPHOLOGICAL MODEL FOR TRABECULAR BONE**

**ABHISHEK VISHWANATH RAMMOHAN SUBRAMANIAN**

**NATIONAL UNIVERSITY OF SINGAPORE**

**2014**

**DEVELOPMENT AND APPLICATION OF A  
MORPHOLOGICAL MODEL FOR TRABECULAR BONE**

**ABHISHEK VISHWANATH RAMMOHAN SUBRAMANIAN  
(B.ENG (Hons.))**

**A THESIS SUBMITTED  
FOR THE DEGREE OF DOCTOR OF PHILOSOPHY  
DEPARTMENT OF MECHANICAL ENGINEERING  
NATIONAL UNIVERSITY OF SINGAPORE**


**2014**

## **Declaration**

I hereby declare that this thesis is my original work and it has been written by me in its entirety.

I have duly acknowledged all the sources of information which have been used in the thesis.

This thesis has also not been submitted for any degree in any university previously.



**ABHISHEK VISHWANATH RAMMOHAN SUBRAMANIAN**

04/08/2014

## **Acknowledgement**

Most professors are very knowledgeable in their fields. Many are patient and helpful. Some possess genuine concern for their students. What makes my own supervisor, A/P Vincent Beng Chye Tan, exceptional, is his magnanimity (in the etymologically strict sense of *magnus*, ‘great’, + *animus*, ‘mind’, ~largeheartedness). It is for having had the privilege to be a witness to this spirit of his that I am especially grateful.

I thank my co-supervisor, Dr Lee Taeyong, for his contribution during the course of this project, and the panel of examiners for their comments. Credit is due to Ms. Lim Yong Xian (FYP student, AY 2011/2012) for the work reported in Chapter 4 Section 4.2. All published figures are reproduced with permission from the publisher.

I learned how to do research from Michel Foucault; it is Ananda K. Coomaraswamy who teaches me how to think.

There are always those to whom one’s sense of gratitude is of the ineffable kind – is it not fitting that they are passed over in silence? – for, after all, they know themselves.

Acknowledgement	I
Summary	VII
List Of Symbols	X
List Of Figures	1
List Of Tables	1
<b>CHAPTER 1. INTRODUCTION AND LITERATURE REVIEW</b>	<b>1</b>
<b>1.1 Multi-scale analysis of bone</b>	<b>1</b>
1.1.1 Hierarchical nature of bone	1
1.1.2 Conventional density-modulus mapping techniques	7
1.1.3 Micromechanically-informed macro-scale analysis of bone	12
1.1.4 Some recently published studies on multi-scale analysis of bone	15
<b>1.2 Morphological modelling of bone</b>	<b>19</b>
1.2.1 Extant microstructural models of bone	19
1.2.2 Some applications of morphological models of bone	30
<b>1.3 Mechanisms of bone degeneration and failure</b>	<b>35</b>
1.3.1 Ageing	35
1.3.2 Osteoporosis and osteopenia	36
1.3.3 Mechanics of micro-scale (trabecular-level) failure	37
1.3.4 Mechanics of macro-scale (femur-level) failure	41
<b>1.4 Aims and Objectives of Our Study</b>	<b>43</b>
<b>CHAPTER 2. THE GYROID-BASED UNIT CELL AS A MODEL FOR FEMORAL BONE</b>	<b>45</b>
<b>2.1 Generation of gyroid-based unit cell</b>	<b>48</b>

<b>2.2</b>	<b>Morphometric analysis of gyroid-based unit cell</b>	<b>50</b>
<b>2.3</b>	<b>Addition of geometric irregularities</b>	<b>51</b>
<b>2.4</b>	<b>Determination of mechanical properties using FEA</b>	<b>53</b>
2.4.1	Material properties	53
2.4.2	Boundary conditions	54
2.4.3	Finite element analysis	54
2.4.4	Homogenization	55
<b>2.5</b>	<b>Results</b>	<b>56</b>
<b>2.6</b>	<b>Adaptations of the gyroid-based unit cell:</b>	<b>59</b>
2.6.1	For regions of very low $V_f$	59
2.6.2	For modelling vertebral trabecular bone resembling cubic lattice-like structures	61
<b>2.7</b>	<b>Discussion</b>	<b>64</b>
 <b>CHAPTER 3. INVESTIGATION OF OTHER EXISTING MODELS OF</b>		
<b>TRABECULAR BONE</b>		<b>68</b>
<b>3.1</b>	<b>The Gibson-Ashby model</b>	<b>68</b>
3.1.1	Construction of the model	68
3.1.2	Mechanical properties of the model	69
3.1.3	Morphological properties of the model	74
<b>3.2</b>	<b>The Kelvin cell (rod-type) model</b>	<b>76</b>
3.2.1	Construction of the model	76
3.2.2	Mechanical properties of the model	77
3.2.3	Morphological properties of the model	78
<b>3.3</b>	<b>The Kelvin cell (plate-type model)</b>	<b>81</b>
3.3.1	Construction of the model	81

3.3.2	Mechanical properties of the model	82
3.3.3	Morphological properties of the model	84
<b>3.4</b>	<b>Discussion and Conclusion</b>	<b>86</b>
 <b>CHAPTER 4. ASSESSMENT OF TWO NOVEL METHODS FOR MODELLING BONE</b>		 <b>91</b>
<b>4.1</b>	<b>Voronoi tessellation for modelling the femoral neck</b>	<b>91</b>
4.1.1	Introduction	91
4.1.2	Modeling algorithm	92
4.1.3	Discussion and Conclusions	97
<b>4.2</b>	<b>The ellipsoid-cuboid unit cell as a model for trabecular bone</b>	<b>98</b>
4.2.1	Introduction	98
4.2.2	Generation of the ellipsoid-cuboid unit cell	99
4.2.3	Finite element analysis of the unit cells	103
4.2.4	Results	105
4.2.5	Summary of results and comparison with published experimental data	109
4.2.6	Conclusions	111
 <b>CHAPTER 5. INVESTIGATION OF THE EFFECT OF TRABECULAR MICROSTRUCTURE ON THE FEMUR SCALE</b>		 <b>112</b>
<b>5.1</b>	<b>Non-concurrent dual-scale FE simulations of the femur</b>	<b>114</b>
5.1.1	Source of femur model	114
5.1.2	Assignment of material properties	115
5.1.3	Boundary conditions	118
5.1.4	Finite element analysis and post-processing procedure	120
5.1.5	Mesh density dependence	121

<b>5.2 Results</b>	<b>122</b>
5.2.1 Mechanical behaviour of femur bone at macro-scale	122
5.2.2 Mesh density dependence	129
<b>5.3 Discussion</b>	<b>129</b>
5.3.1 On the importance of dual-scale simulations for bone analysis	129
5.3.2 On the effect of incorporating micro-level (gyroid-based) mechanical properties on macro-level behaviour	130
5.3.3 Limitations	132
<b>5.4 Conclusions</b>	<b>133</b>
<b>CHAPTER 6. DEFORMATION MECHANISMS IN THE FEMORAL NECK REGION</b>	<b>134</b>
<b>6.1 Generation of femoral neck (FN) structure</b>	<b>134</b>
6.1.1 Extraction of FN slice from computed tomographic dataset	134
6.1.2 Processing of CT slice to obtain geometric and densitometric properties	136
6.1.3 Generation of gyroid-based FN structure using geometric and densitometric properties obtained from CT slice	137
<b>6.2 Finite element (FE) simulation on FN structure</b>	<b>140</b>
6.2.1 Mechanical properties of bone tissue material	140
6.2.2 Loading and boundary conditions	140
6.2.3 Results	141
<b>6.3 Continuum-based simulations – A comparison</b>	<b>147</b>
6.3.1 Using classical density-modulus mapping algorithms	147
6.3.2 Using classical density-modulus mapping with phenomenological plasticity	150
6.3.3 Using material properties derived by homogenized gyroid-based unit cells	151
<b>6.4 Yield surface of FN structure</b>	<b>154</b>



## Table of Contents

6.4.1	Boundary conditions and FE analysis	154
6.4.2	Plotting and fitting of yield points	159
6.4.3	Translation between organ (i.e., femur) scale and FN scale	162
6.4.4	Discussion	164
<b>6.5</b>	<b>Deformation mechanisms active at the trabecular scale</b>	<b>168</b>
6.5.1	Theoretical considerations	168
6.5.2	FE simulations on a simple cylindrical geometry	170
6.5.3	Discussion	174
<b>6.6</b>	<b>Discussion of the relationships between trabecular-scale and macro-scale failure</b>	<b>177</b>
6.6.1	Case 1:	178
6.6.2	Case 2:	181
6.6.3	Case 3:	183
<b>6.7</b>	<b>Conclusion:</b>	<b>187</b>
<b>CHAPTER 7.</b>	<b>CONCLUSIONS AND SCOPE FOR FUTURE WORK</b>	<b>188</b>
<b>REFERENCES</b>		<b>192</b>

## Summary

Human bone is well-known to be a very complex structure with a diverse range of geometries, densities, and mechanical properties at different length scales. It is also generally recognized that variations in bone shape and attenuations in bone density, especially during ageing or with the onset of morbid conditions like osteoporosis, may play no small part in undermining the strength and mechanical integrity of the skeletal system. However, only very recently are we realizing that the problem at hand, if it is to be genuinely understood and resolved, requires a more *multi-scale* approach: it is imperative to know how the mechanical behaviour and, more particularly, the deformation mechanisms at any one scale of the bone may have an effect on adjacent scales, potentially leading to eventual catastrophic failure of the entire bone.

In our work, we investigated the capability of the triply-periodic minimal surface solid called the gyroid to act as a morphological model of trabecular bone. Our results showed that, based on both its mechanical behaviour and morphometric properties, the gyroid-based unit cell can act as a reasonably good representative of real trabecular bone. We compared the gyroid model with some of the models previously proposed in the literature and discovered that it possesses several merits germane to our purposes.

We next obtained the mechanical properties of gyroid-based unit cells for a range of apparent densities and used these to construct a database of input parameters for subsequent macro-scale numerical simulations of the entire proximal femur. By performing analyses on the same structure after enforcing

severe attenuation of trabecular bone density, we were able to understand the effect of ageing or osteoporosis (both of which cause substantial bone loss) on the femur-level strength and stiffness. We discovered that femora that have suffered severe loss of trabecular bone exhibit a remarkable reduction in their structural stiffness and a peculiar plateau-like behaviour in their load-displacement curves, indicating that their capacity to withstand any further increase in external loads has been compromised.

Lastly, with the aim of shedding more light on the relationship between failure mechanisms at two adjacent length scales, i.e., the individual trabecular strut level and the femoral neck region at large, we used the gyroid model, together with a CT-image obtained from a real femoral neck cross-section, to generate a structure that resembled the femoral neck in geometry as well as in bone density distribution. Performing numerical simulations on this structure using various boundary conditions (both stance and fall) furnished us with a macro-scale yield envelope that could enable one to diagnose whether a given set of loading conditions is likely, or not, to result in structural yield of the femoral neck. At the trabecular level, we explored the phenomenon of strut buckling by using simplified cylindrical geometries and discovered that, based on typical statistical data for the slenderness ratios of femoral trabecular spicules in the middle-aged and elderly, inelastic buckling is a very real possibility in trabecular bone. Further inspection of our computational model of the femoral neck structure after macro-scale yield revealed that trabecular struts in low volume fraction areas of the superior-most region of the femoral neck did indeed manifest inelastic buckling in fall mode, and not in stance mode. We

concluded that our findings could be of significance in improving our understanding of the aetiology and hierarchical nature of fall-related fractures.

**List of Symbols**

$V_f$	volume fraction
$\rho_{app}$	apparent density
SMI	structure model index
Tb.Th	trabecular thickness
Tb.Sp	trabecular spacing/separation
Tb.N	trabecular number
BV	bone volume
TV	total volume
BS	bone surface area
FEA	finite element analysis
FE	finite element

## List of Figures

Figure 1.1 Human proximal femur showing cortical and trabecular bones (adapted from [2]) .2	2
Figure 1.2 Scanning electron micrographs showing the heterogeneous nature of human trabecular bone: (a) The rod-rod cellular structure from the femoral head (b) The plate-rod cellular structure from the femoral head (c) The plate-rod cellular structure from the femoral condyle (from [3]) .....	3
Figure 1.3 (a) Original femur bone obtained by stacking CT slices (b) 3D reconstruction of solid geometry (c) Body-fitting mesh generated from the femur bone using tetrahedral elements.....	6
Figure 1.4 (a) Micro-CT scan of a trabecular bone sample (b) A typical volume mesh of a trabecular bone specimen rendered using MIMICS and 3-matic software suite .....	7
Figure 1.5 Graph of effective stiffness vs. apparent density for femoral bone (from [5]).....	9
Figure 1.6 (a) Schematic illustration of dual-scale analysis of cortical bone [26], (b) RVE of cortical bone showing hydroxyapatite mineral, collagen matrix, and the interphase region [26] .....	16
Figure 1.7 (a) Geometry of mineralized collagen fibril, (b) RVE showing periodic distribution of hydroxyapatite crystals in organic collagen matrix, (c) Zoomed-in view of the nano-scale RVE [27] .....	17
Figure 1.8: RVE of trabecular bone showing cubic grid-like lattice, containing both solid and fluid phases (excerpted from [29]) .....	18
Figure 1.9 Open-celled variant of the Gibson-Ashby model [45] .....	20
Figure 1.10 Deformation mechanisms in the Gibson-Ashby cell (a) linear elastic strut bending (b) cell collapse by elastic buckling (c) plastic yielding, and (d) brittle crushing [47].....	21
Figure 1.11 The regular tetrakaidecahedron, showing the six square faces and the eight hexagonal faces .....	23
Figure 1.12 The generalized tetrakaidecahedral cell as used by Zysset et al. [51] showing the three independent edge lengths and the three independent edge angles .....	23
Figure 1.13 The open (rod-like) and partially-closed (plate-like) finite element models employing 3-node beam elements and 6-node shell elements respectively [51]. Note the lack of shell element at the square faces in the latter .....	24
Figure 1.14 (a) Original Voronoi diagram with black dots depicting Voronoi generators; (b) Voronoi diagram subsequent to perturbations of Voronoi sites .....	25
Figure 1.15 Generation of a two-dimensional model of a bone cross-section using Voronoi tessellation followed by application of a remodelling rule, showing density-dependent distribution of Voronoi sites [58] .....	27
Figure 1.16 Micro-CT image of aged vertebral trabecular bone (left); Trabecular bone model lattice (right) with 0.3 lattice perturbation factor [60] .....	27
Figure 1.17 Hexagonal column structure model of vertebral trabecular bone [61] .....	29
Figure 1.18 A central portion of the trabecular specimen showing regions of yielded tissue at the apparent level yield points in tension (left) and compression (right). The percentage of tissue yielding in tension and compression are also shown [49] .....	32
Figure 1.19 The open-celled rod-based honeycomb structure used by [49] to understand the uniformity of yield strains in tension but not in compression. On the right is a free body diagram of a single oblique strut, modelled as a circular cylinder .....	32
Figure 1.20 Graph showing regions where tissue-level yielding occurs first, be it in tension or compression, although the apparent level loading is compressive. The shaded region represents tissue-level yielding in tension. $\eta$ is the slenderness ratio, and $\theta$ is the angle made between the oblique strut and the axis of compressive loading [49] .....	33

Figure 1.21 Regression of trabecular thickness on age in the femur [70] .....	36
Figure 1.22 Reflected light photomicrograph of bovine trabecular bone tested in uniaxial strain to 15% compression, showing buckling of one trabecula and shear failure of another (from [85]).....	39
Figure 2.1 Gyroid-based unit cell, (a) showing the threshold surface corresponding to $t = -1$ ; (b) after binarization, corresponding to $t = -0.87$ .....	49
Figure 2.2 Schematic showing the addition of random geometric perturbations to the original gyroid .....	51
Figure 2.3 (a) $V_f = 17\%$ ( $t = -0.87$ ); (b) $V_f \sim 25\%$ ( $t = -0.62$ ); (c) $V_f \sim 35\%$ ( $t = -0.31$ ); (d) $V_f \sim 45\%$ ( $t = 0$ ). Note: (a) is rendered before addition of geometric irregularities, while (b) – (d) are rendered after addition of geometric irregularities. ‘Pits’ and ‘mounds’ can be seen on the surface of the unit cells in (b) to (d).....	52
Figure 2.4 Typical finite element mesh of gyroid-based unit cell .....	55
Figure 2.5 Stress contours showing von Mises’ stress on the gyroid of $V_f = 25\%$ .....	57
Figure 2.6 Homogenized stress-strain graph for the gyroid-based unit cell of $V_f = 25\%$ , showing the linear elastic modulus, $E$ , calculated at small strains .....	57
Figure 2.7 Homogenized stress-strain graphs depicting the compressive behavior of the gyroid under small and large deformations. A graph from [20] is re-plotted and superposed for comparison .....	58
Figure 2.8 Graph showing small-strain elastic moduli of gyroid structure against apparent density. Graphs depicting published data [115-118] on the human femur are re-plotted and superposed for comparison.....	58
Figure 2.9 Gyroid-based unit cells for decreasing values of $t$ , showing the disconnected struts at very low $V_f$ .....	60
Figure 2.10 Unit cells based on the skeleton of the gyroid equation, showing struts still connected at $V_f$ as low as 0.9% .....	61
Figure 2.11 (a) Human vertebral trabecular bone, showing cubic grid-like structure [39] (free for non-commercial use), and (b) unit cell used by [40] to model vertebral trabecular bone...	62
Figure 2.12 Unit cells based on the skeletal primitive minimal surface which can be used to model vertebral trabecular bone .....	63
Figure 3.1 (a) Schematic of the Gibson-Ashby unit cell (from [47]), (b) CAD model of the Gibson-Ashby unit cell, for $t/l = 0.1$ , and $V_f = 2.1\%$ .....	69
Figure 3.2 CAD model showing assembly of 3 by 3 by 3 Gibson-Ashby unit cells of constant volume fraction.....	69
Figure 3.3 (a) Schematic showing cell struts bending, (b) Our FE simulation showing cell struts bending, occurring at $\epsilon_y = 7.6\%$ , (c) Schematic showing cell struts buckling, (d) Our FE simulations showing cell struts buckling, occurring at $\epsilon_y = 29\%$ . The contour plots in (b) and (d) represent von Mises’ stresses in MPa. Images (a) and (c) are from [127]. .....	71
Figure 3.4 (a) Schematic of stress vs. strain showing the primary deformation regimes for an elastoplastic foam in compression [47, 127], and (b) Our FE simulation results for the Gibson-Ashby cell of $V_f = 2.1\%$ , showing a similar deformation path .....	72
Figure 3.5 (a) CAD model showing Gibson-Ashby unit cell of $V_f = 14.9\%$ , (b) Stress contour plots showing lack of strut buckling, (c) Graph of engineering stress vs. engineering strain for the same cell.....	73
Figure 3.6 Graph of effective stiffness values vs. $V_f$ for the Gibson-Ashby model, fitted using a power-law equation .....	73
Figure 3.7 Schematic showing a single strut of the Gibson-Ashby cell .....	74

Figure 3.8 (a) Schematic of the rod-type Kelvin cell showing the eight hexagons and six quadrilaterals that constitute the tetrakaidecahedral structure (b) The rod-type Kelvin cell corresponding to $t/l = 0.1$ after meshing the cell struts with beam elements .....	76
Figure 3.9 Graph of engineering stress vs. engineering strain for the Kelvin (rod-type) cell corresponding to $t/l = 0.1$ .....	78
Figure 3.10 Graph of effective Young's modulus vs. thickness-to-length ratio for the Kelvin (rod-type) cell with a power-law fit.....	78
Figure 3.11 Schematic showing a single strut of the Kelvin (rod-type) cell .....	79
Figure 3.12 (a) Schematic of the plate-type Kelvin cell showing the eight hexagons and six quadrilaterals that constitute the tetrakaidecahedral structure. Note the absence of cell walls on the quadrilateral faces. (b) The plate-type Kelvin cell corresponding to $t/l = 0.1$ after replacing the cell walls with quadratic shell elements of thickness $t$ .....	82
Figure 3.13 Graph of engineering stress vs. engineering strain for the Kelvin (plate-type) cell corresponding to $t/l = 0.1$ .....	83
Figure 3.14 Graph of effective Young's modulus vs. thickness-to-length ratio for the Kelvin (plate-type) cell with a power law fit.....	83
Figure 3.15 Schematic showing a single face of the Kelvin (plate-type) cell.....	84
Figure 3.16 Graph showing effective initial stiffness vs. the apparent density for the three unit cells and the gyroid-based structure, superposed on published empirical data from the human femur [5].....	87
Figure 3.17 Summary of changes in SMI with changing volume fraction for each of the models .....	89
Figure 4.1 Segmentation of the femoral neck CT image into cortical and trabecular bone using VA-BATTS meshing tool.....	94
Figure 4.2 (a) Butterfly mesh of trabecular core (b) Voronoi generators distributed based on the trabecular core apparent density (c) Trabecular core after Voronoi tessellation .....	96
Figure 4.3 Typical femoral neck cross-sections of three subjects (Top row: original CT image. Bottom row: computational model rendered using proposed method). A: Anterior; I: Inferior; S: Superior; P: Posterior .....	97
Figure 4.4 Schematic showing the difference between the FEM mesh and the FSM mesh .....	98
Figure 4.5 (a) Illustration of the design of the ellipsoid-cuboid unit cell (the cuboid is outlined in black while the nine ellipsoids are in grey), (b) The ellipsoid-cuboid unit cell, (c) An assembly created by stacking 3x3x3 unit cells .....	99
Figure 4.6 (a) Minimum, and (b) maximum volume fraction of unit cell possible for given cube, (c) minimum, and (d) maximum strut thickness (shown between black arrows) for model with averaged volume fraction for the same cube .....	100
Figure 4.7 Geometric parameters used to define the ellipsoid and the cuboid .....	101
Figure 4.8 Maximum (left) and minimum (right) volume fractions at which the trabecular-like model is still distinguishable .....	102
Figure 4.9 The unit cell should include an opening in each of the walls to better resemble highly porous trabecular bone .....	102
Figure 4.10 Tie constraints applied between the shaded regions on the (a) left and the right, and (b) front and back, walls of the unit cell, (c) uniaxial compression applied on the top surface of the model while the bottom surface is held fixed .....	104
Figure 4.11 Absence of openings in the side surfaces .....	106
Figure 4.12 Graphs of simulation results superposed onto those obtained by experimental studies on the proximal tibia (from [5]).....	110
Figure 5.1 Flowchart showing overall methodology adopted in assigning material properties to finite element mesh of femur.....	119



Figure 5.2 (a) Material assignment in a coronal longitudinal section of the original femur mesh, after meshing with linear brick elements. (b) Legend describing corresponding  $V_f$  (%) for each element in the mesh for Cases A – D ..... 119

Figure 5.3 Graphs showing reaction force vs. nodal displacement for stance mode for Cases A - D..... 122

Figure 5.4 Graphs showing reaction force vs. nodal displacement for sideways-fall mode for Cases A – D (legend identical to Figure 5.3 above) ..... 123

Figure 5.5 Plot of maximum principal strains in stance mode for (a) Case A, (b) Case B, (c) Case C and (d) Case D. By convention, positive and negative strains denote tension and compression, respectively. White filled circle in (a) schematically shows the location of the node chosen for calculation of nodal displacements. All plots were obtained at identical nodal displacement of approximately 4 mm..... 125

Figure 5.6 Plot of maximum principal strains in sideways-fall mode for (a) Case A, (b) Case B, (c) Case C and (d) Case D. By convention, positive and negative strains denote tension and compression, respectively. White filled circle in (a) schematically shows the location of the node chosen for calculation of nodal displacements. All plots were obtained at identical nodal displacement of approximately 3mm. .... 128

Figure 6.1 Original CT dataset after importing into MIMICS. The white rectangle shows the process of reslicing perpendicular to the FN axis..... 135

Figure 6.2 CT image of the femoral neck after reslicing perpendicular to the FN axis. A: Anterior, I: Inferior, P: Posterior, S: Superior. Also shown is the Ward’s triangle, a region of very low bone density that occurs due to the nature of the trabecular pattern in the femoral neck ..... 136

Figure 6.3 . Schematic showing procedure for assembling gyroid-based unit cells into macroscale structure, based on the density distribution of a CT image obtained perpendicular to the longitudinal axis of the femoral neck ..... 139

Figure 6.4 (a) Three-dimensional macroscale structure generated using the assembly procedure, showing the heterogeneous density distribution across the femoral neck, (b) Side view of the macroscale structure, (c) Zoom-in on the low volume fraction region labelled A in (a) showing relatively thin trabecular struts, and (d) Zoom-in on the high volume fraction location labelled B in (a) showing relatively thick trabecular struts..... 139

Figure 6.5 Schematic showing the boundary conditions applied on the gyroid-based femoral neck structure under pure compression ..... 141

Figure 6.6 Schematic showing the procedure for obtaining the force vs. displacement graph for the gyroid-based femoral neck structure..... 141

Figure 6.7 Graphs of reaction force vs. displacement for the gyroid-based femoral neck structure with different tissue materials..... 142

Figure 6.8 (a) undeformed structure showing the relatively thinner trabecular struts at a region of low volume fraction; (b) deformed structure at the same location as in (a), showing large deformation bending behaviour occurring in the thinner trabecular struts; (c) undeformed structure showing the relatively thicker trabecular struts at a region of high volume fraction; (d) deformed structure at the same location as in (c) showing lack of any large deformation bending behaviour in the thick trabecular struts ..... 143

Figure 6.9 Femoral neck structure showing the locations of the three node sets chosen for further investigation of trabecular buckling phenomena ..... 143

Figure 6.10 Zoom-in on Node Set 3, showing the nodes (circled) on the top surface of a particular trabecular strut at a region of low volume fraction ..... 144

Figure 6.11 Force vs. displacement graph for node set 1 ..... 144

Figure 6.12 Force vs. displacement graph for node set 2 ..... 144

Figure 6.13 Force vs. displacement graph for node set 3 ..... 145

Figure 6.14 Schematic showing procedure followed to assign material properties to original CT slice ..... 149

Figure 6.15 Graphs of force vs. displacement for the femoral neck structure with materials defined by classical density-modulus mapping compared with gyroid-generated microstructure (bilinear elasto-plastic material properties) ..... 149

Figure 6.16 Graphs of force vs. displacement for the femoral neck structure with materials defined by classical density-modulus mapping with phenomenological plasticity included superimposed onto Figure 6.15 ..... 151

Figure 6.17 Material assignment in the femoral neck structure..... 153

Figure 6.18 Graphs of force vs. displacement for the femoral neck structure with materials defined by various methods ..... 153

Figure 6.19 (a) Original CT image of the narrow-neck region. Axes in grey indicate the default ImageJ coordainte system (b) Location of the area centroid C (256.7 pixels, 240.6 pixels) and angle  $\theta$  (19 degrees) subtended by one of the principal axes of the moment of inertia to the positive x-axis..... 155

Figure 6.20 (a) Macroscopic view of the proximal femur, showing the narrow neck region (in black dashed lines), and the right-hand coordinate system; (b) FN structure based on Section A-A, showing the location of the reference point (RP) and the orientation of the right-hand coordinate system as used in ABAQUS ..... 156

Figure 6.21 Schematic showing the boundary conditions applied on the FN structure. Arrows in black denote the longitudinal compressive displacement and the angular displacement about the z-axis being applied at the RP node..... 157

Figure 6.22 Graph of reaction force (-RF1) vs. displacement (-U1) ..... 158

Figure 6.23 Graph of reaction moment (RM3) vs. angular displacement (UR3) ..... 158

Figure 6.24 Procedure showing the determination of the point of first yield at the macroscale ..... 159

Figure 6.25 Yield surface of femoral neck structure ..... 161

Figure 6.26 (a) Macroscopic view of the proximal femur, showing the forces acting on the proximal femur (R: hip joint reaction force; G: ground reaction force present during fall; D: force exerted by distal femur) (b) FN structure based on Section A-A. .... 162

Figure 6.27 Polar plot of R vs. theta showing the yield surface of the femoral neck structure ..... 163

Figure 6.28 Graph showing sample calculations to assess possibility of macro-scale yield for two cases ..... 165

Figure 6.29 (a) CT image showing cross-section of human femoral neck (b) Analytical model used by [1, 155] (Used with permission from Elsevier) ..... 166

Figure 6.30 Cylindrical column representative of a single trabecular strut (based on [87])... 171

Figure 6.31 Typical graph of force vs. displacement for a trabecular strut showing the critical load that causes buckling in each of the two cases (linear elastic material, and elasto-plastic material) ..... 173

Figure 6.32 Graph of critical stress vs. slenderness ratio showing the effect of inelastic buckling in decreasing the critical stress in columns of intermediate slenderness ratio (i.e., intermediate columns) ..... 173

Figure 6.33 Graph of force vs. displacement for a column of intermediate slenderness ratio, showing the Mises stress contours at the critical load. Note the formation of plastic 'hinges' at the mid-span of the column at the point of buckling, followed by substantial lateral deflection thereafter..... 176

Figure 6.34 Yield surface of femoral neck structure illustrating the three cases to be investigated..... 178

## List of Figures

Figure 6.35 Active yield regions (in red) corresponding to Case 1 .....	180
Figure 6.36 Mises stress contours showing formation of plastic hinges in the superior-most region.....	180
Figure 6.37 Contours showing significant lateral displacements in the same locations as in Figure 6.36 .....	180
Figure 6.38 Active yield regions (in red) corresponding to Case 2 .....	182
Figure 6.39 Active yield regions (in red) corresponding to Case 3 .....	185
Figure 6.40 Mises stress contours showing formation of plastic hinges in low volume fraction areas of both the superior and inferior regions .....	185
Figure 6.41 Contours showing significant lateral displacements in one of the locations as in .....	186

## List of Tables

Table 2.1 Morphometric parameters for the gyroid structure ( $V_f$ : volume fraction; Tb.Th: trabecular thickness; Tb.Sp: trabecular separation; SMI: Structure Model Index).....	50
Table 2.2 Results of mesh convergence study on the gyroid-based unit cell .....	59
Table 3.1 <b>Tb.Th</b> values for Gibson-Ashby model of different volume fractions .....	75
Table 3.2 <b>Tb.Sp</b> values for Gibson-Ashby model of different volume fractions .....	76
Table 3.3 <b>Tb.Th</b> values for Kelvin (rod-type) model of different volume fractions .....	80
Table 3.4 <b>Tb.Sp</b> values for Kelvin (rod-type) model of different volume fractions .....	81
Table 3.5 <b>Tb.Th</b> values for Kelvin (plate-type) model of different volume fractions.....	85
Table 3.6 <b>Tb.Sp</b> values for Kelvin (plate-type) model of different volume fractions .....	86
Table 7 Simulations results for Model 1A.....	105
Table 8 Simulation results for Model 1B .....	106
Table 6.1 Table showing the tangent stiffness values along the force vs. displacement graph .....	160
Table 6.2 Classification of cylindrical columns and their predominant failure mechanisms under axial compression.....	174
Table 6.3 Summary of micro-scale mechanisms for the three cases (fall, stance, and pure compression) .....	187

**Chapter 1. Introduction and Literature Review**

*“Everything has been said before, but since nobody listens we have to say them again.”  
(André Gide, Le Traité de Narcisse)*

This chapter is divided into four subsections. The first three subsections are intended as a thematically-organized introduction and review of the literature pertaining to our work. In Section 1.1, we describe the hierarchical nature of bone and provide a survey of the multi-scale techniques currently being used to study bone at different length scales. Section 1.2 focuses on some of the morphological models that have previously been proposed to study trabecular bone, for example, the Gibson-Ashby unit cell and the tetrakaidecahedral model, amongst others. We expound on several aspects of bone degeneration and mechanisms of failure in Section 1.3. Lastly, Section 1.4 is an outline of our own aims and objectives in undertaking this work.

**1.1 Multi-scale analysis of bone****1.1.1 Hierarchical nature of bone**

Human bone is known to be a hierarchical composite comprising four scales [1]:

- i. mineralized collagen fibrils (approximately 0.1 micron),
- ii. lamellar and woven bone (approximately 10 microns), the former containing unidirectional fibrils in alternating angles between layers, and the latter containing randomly oriented fibrils,

- iii. primary lamellar, Haversian (a type of cortical bone), and laminar bones (approximately 500 microns),
- iv. trabecular or cortical bones (greater than 1000 microns).

At the highest hierarchical level ( $> 1\text{mm}$ ) we may therefore distinguish between two types of bone: cortical (or compact) bone, which is the densest bone in the human skeleton, and trabecular (also called spongy or cancellous) bone, whose density is much less than that of cortical bone. Cortical bone is usually found in the diaphyseal regions of long bones such as the femur and the tibia, while trabecular bone is present at the epiphyseal regions of long bones, between the more dense outer layers of cortical bone (Figure 1.1).

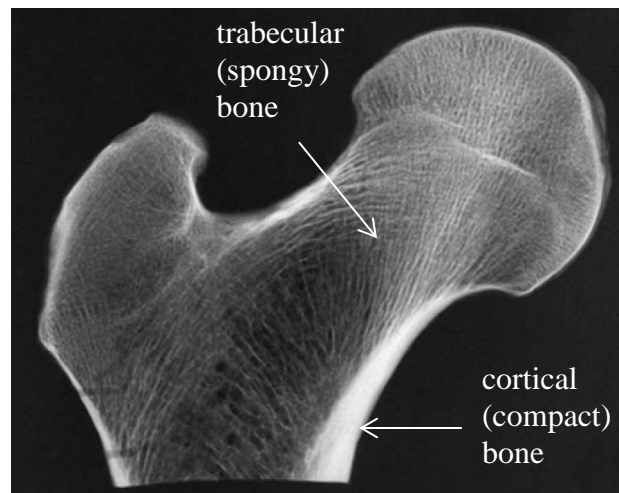


**Figure 1.1 Human proximal femur showing cortical and trabecular bones (adapted from [2])**

Human trabecular bone is remarkable for its vast structural heterogeneity across anatomic locations, subjects, and age. Trabecular spicules in young subjects (whose bones are very dense) are observed to be more plate-like and highly connected, while those in elderly or osteoporotic subjects (whose bones have suffered substantial decrease in density) tend to become more slender, rod-like, and poorly connected. In normal bones, the trabecular bone usually

has a combination of rod- and plate-like features, with the former predominating in highly porous regions and the latter in less porous ones (Figure 1.2).

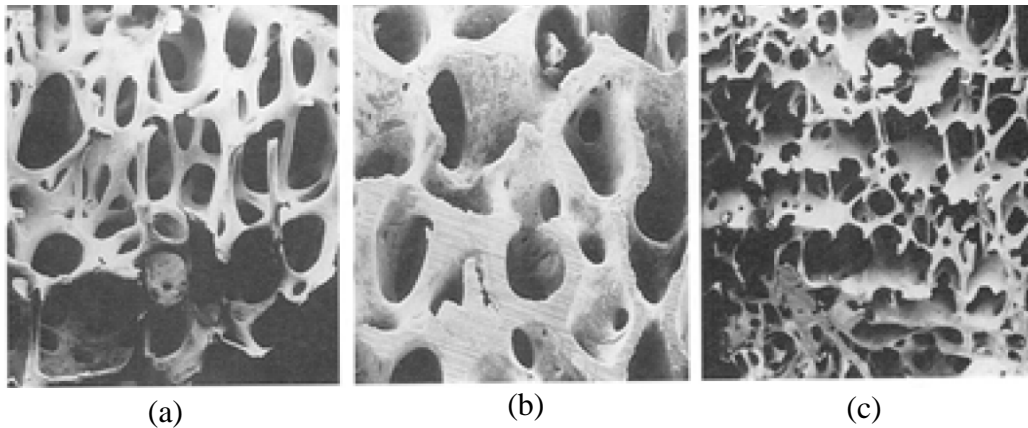


**Figure 1.2 Scanning electron micrographs showing the heterogeneous nature of human trabecular bone: (a) The rod-rod cellular structure from the femoral head (b) The plate-rod cellular structure from the femoral head (c) The plate-rod cellular structure from the femoral condyle (from [3])**

Though there often exists no clearly defined demarcation between cortical and trabecular bone, the porosity of cortical bone is rarely above 30% (i.e., its volume fraction is above 70%), while the porosity of trabecular bone is usually above 40% (i.e., its volume fraction is below 60%). Hence, the distinction between cortical and trabecular bone is fairly obvious in a clinical computed tomography (CT) image.

From a morphological point of view, there exists a fundamental difference between cortical and trabecular bones, one that has considerable implications for their overall mechanical behaviour and physiological function in the skeleton. This difference lies in the scale of their porosities: while cortical bone contains voids (in the form of Haversian and Volkmann's canals, lacunae, etc) that are always smaller than 200 microns, trabecular bone is a network of interconnected rods and plates (called trabeculae) of typical

thickness 100 to 300 microns, and inter-trabecular spacing of 500 to 1500 microns [1]. In other words, the volume fraction of trabecular bone (which usually lies between 5% and 50% in human bone) is dominated by the spaces between individual trabeculae, and not the voids within the bone tissue itself as is the case in cortical bone.

Furthermore, we shall distinguish henceforth between tissue density and apparent density as follows: tissue density,  $\rho_{tissue}$ , is the ratio of bone mass to volume of the actual bone tissue, without consideration of any porosity, whereas apparent density,  $\rho_{app}$ , is the ratio of the mass of bone tissue to the total bulk volume (i.e., the volume of the bounding box enclosing the specimen) inclusive of the volume of the porosities. The volume fraction,  $V_f$ , of the specimen is the ratio of the apparent density to the tissue density:

$$V_f = \frac{\rho_{app}}{\rho_{tissue}} \quad .1)$$

Though there does exist some difference in the degree of mineralization between cortical and trabecular bone, especially between anatomic locations, it is frequently assumed that the tissue density of both cortical and trabecular bones is constant and identical, with a value lying typically between  $1.8 \text{ g/cm}^3$  and  $2 \text{ g/cm}^3$  [4]. For the purpose of this study we assumed a standard value of  $1.8 \text{ g/cm}^3$  for the tissue density [5].

We shall further distinguish between the organ-scale (femur-level, or macro-scale) and the microstructural (trabeculae-level, or micro-scale) properties. The femur-level properties pertain to those that can be seen when measurements are taken at the level of the femur, with no regard for trabecular microarchitecture. In other words, at the macro-level, the mechanical



properties arising from the presence of individual trabecular spicules are averaged ('smeared' out) to obtain homogenized values, that are then employed in studying the femur-scale behaviour. Examples of femur-scale properties include the structural stiffness of the entire proximal femur, yield behaviour of the femoral neck region, etc. In contradistinction, the trabeculae-level properties take into account the behaviour of individual trabecular spicules under loading. Examples of trabeculae-level properties include the structural stiffness of a single trabecular strut, buckling behaviour of a slender trabecular rod under axial loads, etc.

The difference in the length scales between the whole femur and the constituent trabecular spicules has implications for engineering analyses (e.g., finite element analysis) based on computed tomographic (CT) images. Computed tomography (CT) is a medical imaging technique whereby digital geometry processing is used to generate a three-dimensional image of the inside of an object from a large series of two-dimensional X-ray images obtained from a single axis of rotation [6]. The pixels in a CT image display the relative radio-density of the bone at that location. This corresponds to the mean attenuation of the tissue, on a scale from +3071 (most attenuating) to -1024 (least attenuating) on the Hounsfield scale. For example, water has an attenuation of 0 Hounsfield units (HU), air is -1000 HU, cancellous bone is about +400 HU, and cortical bone may exceed +1500 HU. The smallest feature visible in the CT image is limited by the resolution settings of the scanner. Micro-scale parameters like trabecular geometry are not captured by commercially available clinical CT.

CT images can be directly converted into finite element (FE) models using a combination of MIMICS and 3-matic software. Subsequently, material properties can be mapped from the CT images directly onto the corresponding elements in the mesh (more details in Section 1.1.2 below). The mesh thus generated closely follows the geometry of the scanned bone, and also contains appropriate material properties derived from the corresponding bone locations (Figure 1.3).

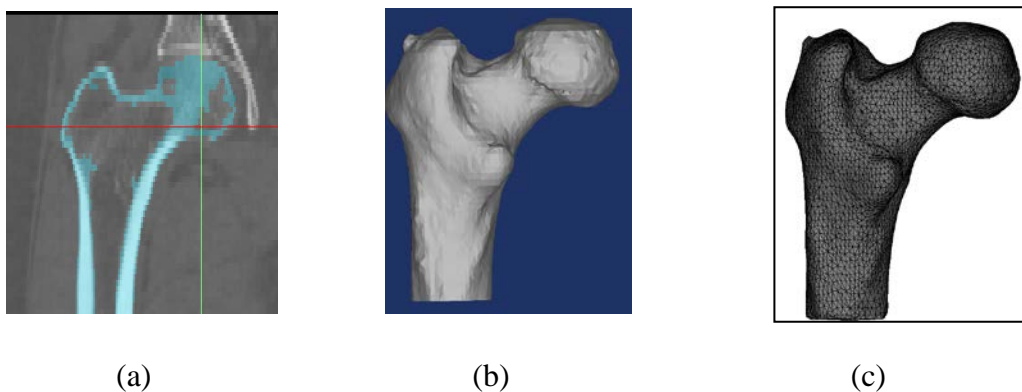


**Figure 1.3 (a) Original femur bone obtained by stacking CT slices (b) 3D reconstruction of solid geometry (c) Body-fitting mesh generated from the femur bone using tetrahedral elements**

Micro-computed tomography ( $\mu$ CT) differs from CT in that the pixel dimensions in  $\mu$ CT are in the order of micrometers. It is used primarily when there is a need for microstructural detail in the materials being scanned. Typical uses include studying small animals, foodstuffs, polymers and plastics, geological materials like rock samples, etc. Owing to the design of the  $\mu$ CT scanner, the technology is currently only used to scan peripheral sites on the human body, for example, the ankle and wrist joints [7]. Furthermore, the high radiation dose involved in  $\mu$ CT scans prevents its application in studying core regions of the body, like the hip joint. Hence, there is, at the moment, no  $\mu$ CT scan of the femoral neck region obtained *in vivo*.

A  $\mu$ CT scan of a trabecular bone sample obtained from a cadaveric specimen is shown below (Figure 1.4(a)). Well-documented meshing procedures in MIMICS and 3-matic software produce the high-resolution tetrahedral mesh shown (Figure 1.4(b)).

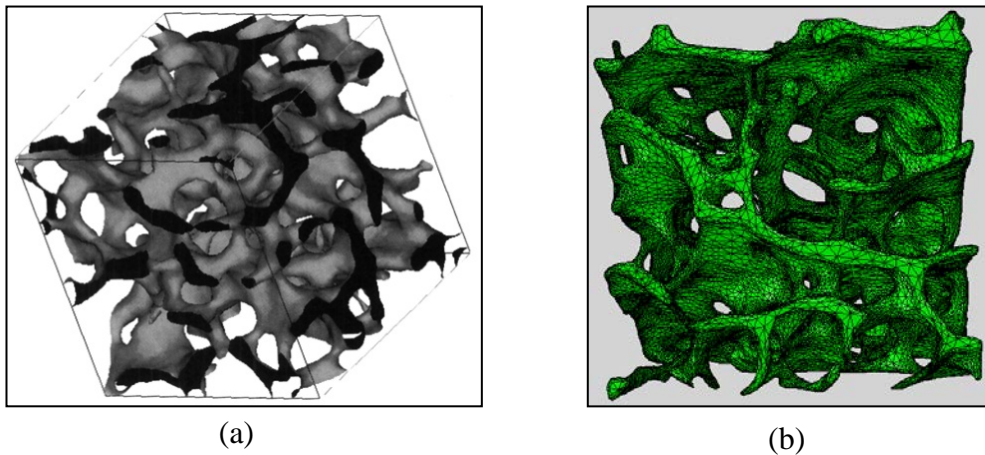


**Figure 1.4 (a) Micro-CT scan of a trabecular bone sample (b) A typical volume mesh of a trabecular bone specimen rendered using MIMICS and 3-matic software suite**

## **1.1.2 Conventional density-modulus mapping techniques**

### **1.1.2.1 History and current methods**

Once an FE mesh of appropriate mesh density has been rendered from a CT image, material properties (e.g., Young's modulus and Poisson's ratio) need to be assigned to each element in the mesh. Traditionally, this process has been carried out by some form of mapping technique that relates the apparent density of the bone as depicted by the CT image to the continuum-level (i.e., apparent-level) Young's modulus. Various mapping algorithms, most of them empirically derived, have been proposed in the literature. Helgason et al. [5] have undertaken a rather exhaustive review of these density-modulus relationships dating back to the pioneering works of CarterHayes [4], together with an analysis and explanation of their relative merits and demerits.

Typically, a trabecular specimen of dimension appropriate to the testing equipment is excised from a larger bone and mounted in a mechanical testing machine. Loads are applied at a pre-determined strain rate (usually quasi-statically) and the corresponding displacements recorded. The stiffness can then be calculated by processing the graph of stress versus strain at the apparent (i.e., homogenized) level. Other testing set-ups have also been employed, including ultrasound techniques [8, 9].

Linde et al. [10] have called attention to the fact that there exists an almost ten-fold difference between various empirical studies in the values of Young's modulus for a given apparent density (Figure 1.5). This discrepancy can be partially accounted for by considering the fact that these empirical studies were performed on bone specimens of different sizes, excised from different donors and anatomic locations, and employed significantly different measurement techniques and boundary conditions in evaluating their specimens.

The debate on which, if any, of the above-described techniques is most appropriate for assigning material properties in FE analyses, is still going on – indeed, very recently [11], there has been a call for *subject-specific* density-modulus relationships, whereby the most accurate relationship is not one that has been generated from a pooled set of data obtained from donors in the past, but one that is true for the particular specimen whose bone is being studied. Needless to say, in FE analyses of CT images derived from living subjects, it is not possible to obtain *subject-specific* data and one still has to rely on classically established mapping algorithms.

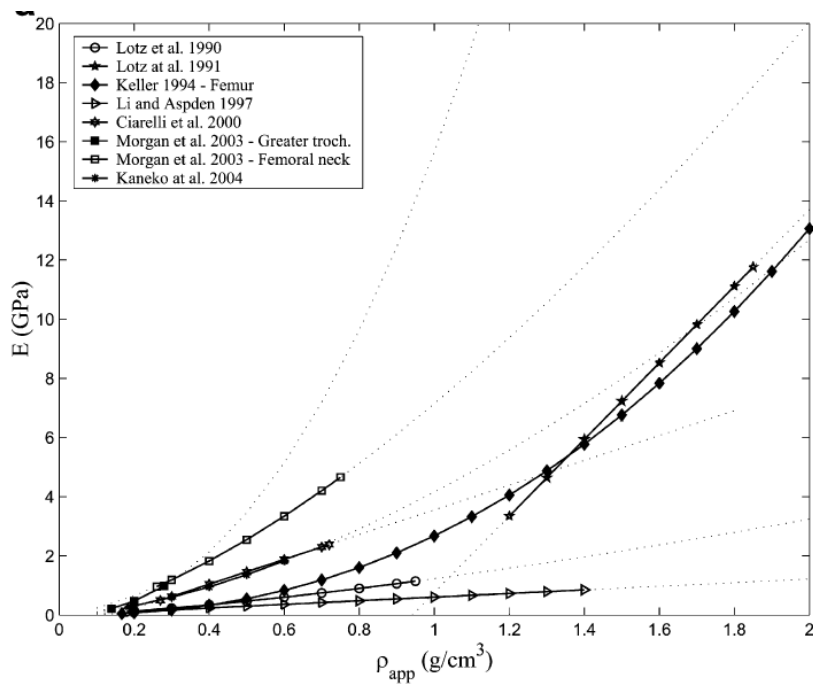


**Figure 1.5** Graph of effective stiffness vs. apparent density for femoral bone (from [5])

Various software (e.g., MIMICS, BoneMat) are capable of automatically assigning material properties to an FE mesh based on an underlying CT image, provided the user has furnished the most suitable density-modulus relationship, usually in the form of a power law:

$$E = a + b(\rho_{app})^c \quad .2)$$

where  $E$  is the Young's modulus, and  $a$ ,  $b$ , and  $c$  are coefficients obtained by fitting the experimental data. In principle, this process would result in a finite element mesh with as many material cards as there are elements; however, most software have a limit on the number of materials they can handle, implying that the user may have to discretize the number of materials by lumping elements into ranges of material properties.

There has been much debate regarding the importance of incorporating material anisotropy in FE simulations. Though it is relatively well-established that real trabecular bone is oriented preferentially in accordance with Wolff's

law and that it possesses orthotropic symmetry or in some cases transverse isotropy [12], a large number of FE studies continue to assume isotropy in assigning material properties [13-15]. This is primarily because these FE studies derive their information on bone geometry and material properties from CT scans, which do not contain any explicit information on bone anisotropy [13]. The assumption of isotropy, although frequently criticized for its simplicity [16], was shown to give results similar to those obtained using orthotropic bone material properties [17, 18].

It is to be noted that for FE analyses on trabecular-level specimens (i.e., where the trabecular rods and plates constitute the finite elements), homogeneous material properties are often assumed for the trabecular tissue, based on the fact that there is little variation in the material composition between sites [19].

The primary advantage of using these empirically-obtained density-modulus maps when assigning material properties to continuum elements is that they facilitate the generation and analysis of very large and computationally-intensive FE models, e.g., the entire femur or vertebral column. Since the individual trabecular spicules are not explicitly captured in the geometry of the FE mesh, but are instead ‘smeared’ out to obtain continuum material properties, the number of degrees of freedom present in an analysis of an entire bone is drastically decreased. Researchers have thus been able to obtain great insight into the mechanics and failure behaviour of entire bones under various very complex forms of loading, including dynamic (gait) conditions. Furthermore, density-modulus maps have improved our understanding of the relationships obtaining between bone volume fraction and corresponding structural stiffness, which could be of importance when testing the efficacy of

anti-osteoporosis drugs (that work by increasing volume fraction) on the overall quality and structural integrity of the whole bone.

### 1.1.2.2 Limitations

Notwithstanding the advantages inherent in creating macro-level FE meshes containing continuum elements with mechanical properties based on the above-described density-modulus maps, there exist some crucial limitations to the method. When the individual trabecular spicules are ‘smeared’ out to obtain continuum-level mechanical properties to be used as input parameters in the macro-scale FE analysis, an implicit assumption is being made that may not be tenable in real bone, namely, that the continuum-level properties capture *all* relevant modes of deformation possible at the trabecular level. However, it is to be recalled that the density-modulus maps are calculated based on experiments conducted at small apparent-level strains, and that, furthermore, they usually generate linear elastic materials. Hence, the possibility of large-deformation bending (or buckling) of individual trabecular struts is not accounted for in the macro-level analysis.

Some workers have called attention to the importance of trabecular buckling in determining macro-level failure behaviour. Cellular solids theory [3] predicts that while high-density trabecular bone is most likely to fail by tissue-level yield, low-density trabecular bone would suffer large-deformation bending or buckling during failure. Bevill et al. [20] studied the influence of bone volume fraction and micro-architecture on large-deformation failure mechanisms of trabecular bone and discovered that the reduction in overall bone strength in compression was substantial for specimens of volume fraction below

approximately 20%. StolkenKinney [21] discovered that for slender trabecular rods, it is important to activate the option of geometrically nonlinear analysis in FE software, in order to capture large-deformation bending (buckling) of the rods. In a review article, Christen et al. [22] emphasized the need for organ-level nonlinear FE models that accurately resolve trabecular micro-architecture. In contradistinction, Verhulp et al. [7] (see also [23]) compared micro- and continuum-level FE models of the proximal femur under fall mode and concluded that, unless the continuum mesh is very coarse, both models produced similar stress and strain distributions. However, their work used only stress and strain distribution plots to ascertain the importance of microstructure in macro-level analyses, and did not study the failure mechanisms prevalent at each scale and their mutual interactions.

Given the findings outlined above, it is probable that there indeed exists a very close link between the macro-scale properties and failure of the whole bone and the micro-scale failure of individual trabecular spicules through buckling. If this hypothesis is true, then it is imperative to include the possibility of micro-scale trabecular failure (through buckling) in performing a large-scale FE analysis of a full bone – an enterprise to be undertaken through so-called multi-scale analyses (or, more strictly, *dual*-scale analyses, since only two scales are here involved).

### **1.1.3 Micromechanically-informed macro-scale analysis of bone**

In the recent past, workers have introduced several techniques for performing multi-scale simulations and demonstrated them on various materials including bone. The biggest challenge in such multi-scale simulations lies arguably in



the transfer of information between scales: how to transmit the macro-scale loads (e.g., those experienced by the proximal femur during stance) to the micro-scale structure (i.e., the trabecular rods and plates), and subsequently, how to pass the information on micro-scale mechanical behaviour (e.g., the structural stiffness, and failure modes like yield and buckling at the trabecular level) back to the macro-scale simulation for further analysis and processing. This challenge becomes especially acute when either or both scales are at the point of failure, for example, when the buckling of trabecular struts inside the proximal femur has progressed to such an extent that the overall strength and integrity of the entire proximal femur is itself compromised and catastrophic failure becomes imminent. Complex numerical algorithms are being developed to handle such cases [24, 25]. Here, we briefly describe two methods commonly used to transmit information between scales in numerical simulations.

### **1.1.3.1 Sequential coupling**

Here, the micro-scale specimens are homogenized to obtain ‘effective’ properties that are then used as input parameters for the macro-scale simulations. This technique is also known as non-concurrent coupling since there is no flow of information from the macro-scale to the micro-scale. Since the morphology of trabecular bone varies across anatomic sites, it is not possible to employ a *representative* volume element; instead *unit cells* corresponding to a range of apparent density need to be generated *a priori* and their homogenized material properties calculated. Then, for each of the finite elements located in the macro-scale FE domain, the material properties obtained from the corresponding micro-scale unit cell are assigned.

Algorithms that depend on sequential coupling between scales are simpler to implement numerically but their accuracy is decreased owing to the fact that there is no explicit transfer of information from the macro-scale back to the micro-scale.

In our work (Chapter 5), we develop a simple dual-scale analysis of the proximal femur using sequential coupling, employing a database of material properties homogenized from the micro-scale unit cells as input parameters in a macro-scale study of the large-deformation mechanical behaviour of the proximal femur.

### **1.1.3.2 Concurrent coupling**

In concurrent coupling algorithms, there is a two-way transfer of information between the scales: while the macro-scale boundary conditions *drive* the micro-scale simulation, the results obtained by homogenizing the latter in turn *constitute* the material properties of the macro-scale problem. This results in more accurate studies that capture all possible interactions between the phenomena occurring at the disparate scales; however, they are computationally challenging to formulate and implement.

A variant of this method is the use of a model which simultaneously contains two or more scales in itself. In other words, a macro-scale model of the bone can be generated with the entire microstructure (i.e., all trabecular rods and plates) explicitly present in the structure. This usually leads to immense computational difficulties owing to the very large number of degrees of freedom necessary to capture geometric features at both scales with acceptable accuracy. However, for somewhat smaller macro-scale domains, for instance

the femoral neck region in isolation, it may be possible to undertake a concurrent study of both scales simultaneously, in order to arrive at an improved understanding of how failure phenomena occurring at one scale drive or are driven by those occurring at the other scale. We describe an application of this type of dual-scale analysis in Chapter 6.

#### **1.1.4 Some recently published studies on multi-scale analysis of bone**

Specifically within the context of cortical bone, Ghanbari and Naghdabadi [26] developed a hierarchical (concurrent) multi-scale modelling scheme based on a representative volume element (RVE) containing hydroxyapatite mineral, collagen matrix and an interphase material. The macroscale domain was discretized by a finite element mesh and a macroscopic deformation gradient calculated for every material point. This macroscopic deformation gradient was then used to formulate the boundary conditions for the micro-scale domain, which was subsequently homogenized by volume-averaging to obtain the macroscopic stress tensor that was in turn transferred back to the macro-scale. Figure 1.6 below shows a schematic of their approach and the RVE they used to model the nanostructure of cortical bone.

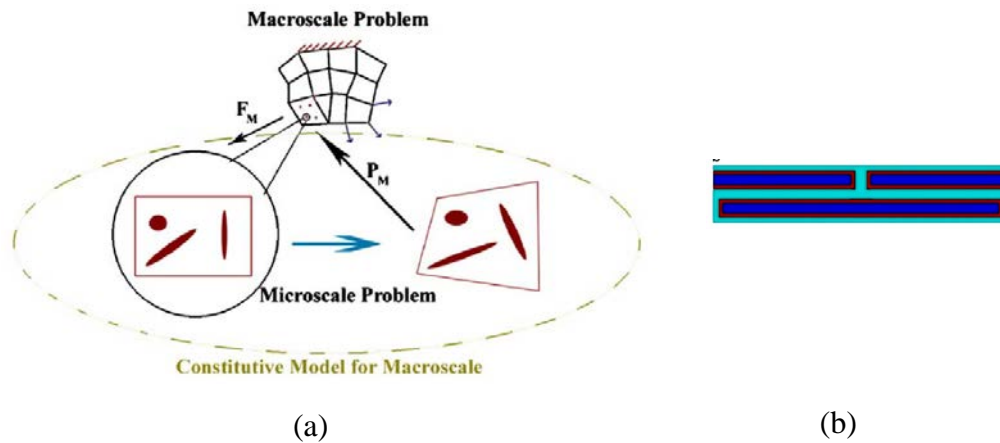


**Figure 1.6** (a) Schematic illustration of dual-scale analysis of cortical bone [26], (b) RVE of cortical bone showing hydroxyapatite mineral, collagen matrix, and the interphase region [26]

They intend to extend their work to trabecular bone as well, where they would have to account for the heterogeneous macroscopic porosity as well – it would be of interest to follow their progress and see how they solve this problem.

Very recently, Vaughan et al., [27] published a three-scale investigation into the effects of tissue mineralisation and lamellar organisation in both cortical and trabecular bone. At the nanostructural level, they employed an RVE comprising hydroxyapatite mineral crystals periodically distributed within organic collagen fibrils, as shown in Figure 1.7.

At the microstructural scale, they modelled osteons using eight concentrically arranged lamellae with and without a central vascular channel for cortical bone and trabecular bones, respectively. After applying appropriate boundary conditions (including periodicity) on the RVE, they homogenized the nano-scale stress and strain values to obtain the micro-scale effective properties corresponding to cortical and trabecular bones. Their results showed that the predicted stiffness values of the lamellae corresponded well with those obtained experimentally through nanoindentation. They also suggested that

variations in mineral volume fraction, crystal size, and orientation of the lamellae could be responsible for the discrepancies in tissue-level properties that have previously been noted [9, 28]. Again, similar to the article cited above [26], it would be interesting to see how these workers propose to model the variations in the apparent density of trabecular bone at the macro-scale (i.e., at the organ level).

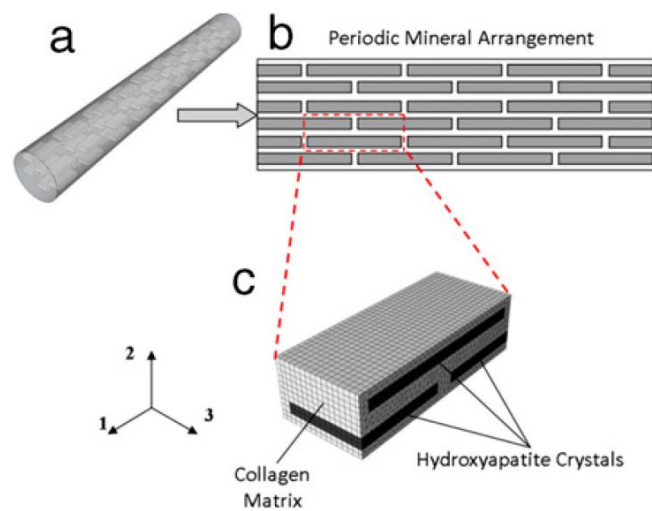


**Figure 1.7 (a) Geometry of mineralized collagen fibril, (b) RVE showing periodic distribution of hydroxyapatite crystals in organic collagen matrix, (c) Zoomed-in view of the nano-scale RVE [27]**

A simple cubic grid-like structure was proposed by Ilic et al. [29], who used numerical solutions to study the effect of porosity on the effective properties of trabecular bone. Their model included the fluid that is known to permeate the solid bony structure and possibly to contribute to its effective properties (Figure 1.8). They simulated ultrasonic tests and obtained results that corroborated experimental findings.

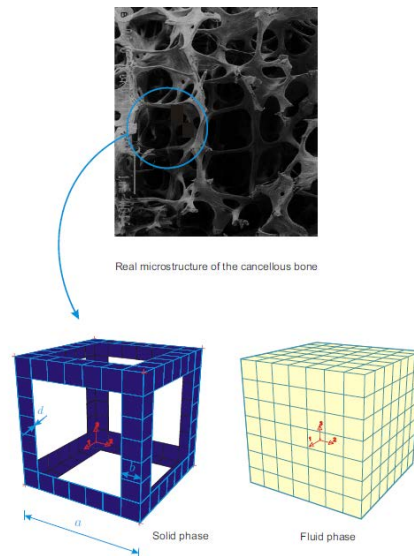


**Figure 1.8: RVE of trabecular bone showing cubic grid-like lattice, containing both solid and fluid phases (excerpted from [29])**

Other multi-scale frameworks in various stages of development include [30], where a self-consistent mean-field method is used to predict mechanical properties based on the molecular structure of the constituents, [31] who used a nano-scale RVE similar to the one in Figure 1.6 above, along with analytical solutions like the Mori-Tanaka and the tension-shear models to predict tissue-level properties of cortical bone, [32] where cortical bone was studied at five successive scales, [33] which is particularly noteworthy for its consideration of the presence of fluid inside the cavities of undrained cortical bone, and [34, 35] where a novel RVE is proposed for fluid-filled cortical bone based on the so-called SiNuPrOs structure. Our sampling of the literature in this subsection shows that, to date, attention from the multi-scale modelling community has been focused for the most part on cortical bone, and particularly on the effect of its nanoscale constituents on its overall tissue properties. The organ-level variation in apparent density, in cortical and especially in trabecular bone, has not yet received sufficient emphasis (noteworthy exceptions include [36] where the aspect of bone remodelling/adaptation is studied using RVEs, the

work by Hellmich and co-workers [37, 38] which detail a quest for ‘universal’ microstructural patterns in bone, and that by Podshivalov and colleagues [39, 40] where a multidomain-based approach is attempted).

As a side note, there exists a community of researchers applying so-called *generalized continuum* theories (based on Eringen’s pioneering work on micro-continuum fields [41] and nonlocal theories [42]) to investigate the hierarchical structure of bone (see, e.g., [43, 44]). Perhaps partly because of their complexity, these theories have not yet gained full acceptance even within the mechanics community, let alone the bone biomechanics group, and are therefore outside the scope of our work.

## **1.2 Morphological modelling of bone**

### **1.2.1 Extant microstructural models of bone**

#### **1.2.1.1 Gibson-Ashby model**

The Gibson-Ashby model was one of the earliest unit cells to be applied in the context of bone modelling (Figure 1.9). Proposed in 1982 by Gibson and Ashby, it was initially used to understand the relative importance of different deformation mechanisms (like cell wall bending and buckling, plastic hinge formation, and plastic collapse) in polymeric foams [45].

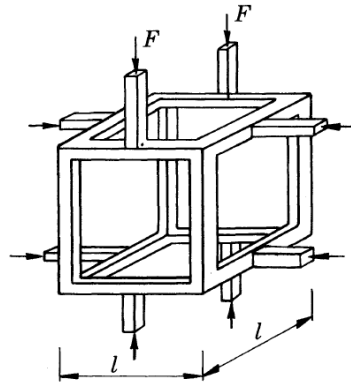


**Figure 1.9 Open-celled variant of the Gibson-Ashby model [45]**

The authors also derived semi-empirical power relationships between the apparent density, the effective stiffness, and the strength of the structure – these relationships were later to prove instrumental in validating and comparing other morphological models of bone and their respective deformation mechanisms. For example, at low densities, Gibson and Ashby discovered that the Young's modulus  $E$  of cellular solids can be correlated with their density  $\rho$  through the following equation:

$$\frac{E}{E_s} = C \left( \frac{\rho}{\rho_s} \right)^n \quad .3)$$

where  $E_s$  and  $\rho_s$  are the Young's modulus and density of the cell wall material, and the constants  $C$  and  $n$  depend on the microstructure in a complex fashion. RobertsGarboczi [46], while investigating this relationship, asserted that the constants  $C$  and  $n$  depend on the cell character (i.e., open-celled or close-celled), the geometrical arrangement of the cell elements (e.g., angle of intersection between struts), shape of the cell struts or walls (e.g., cross-sectional shape, presence of geometric irregularities, initial curvature, etc).



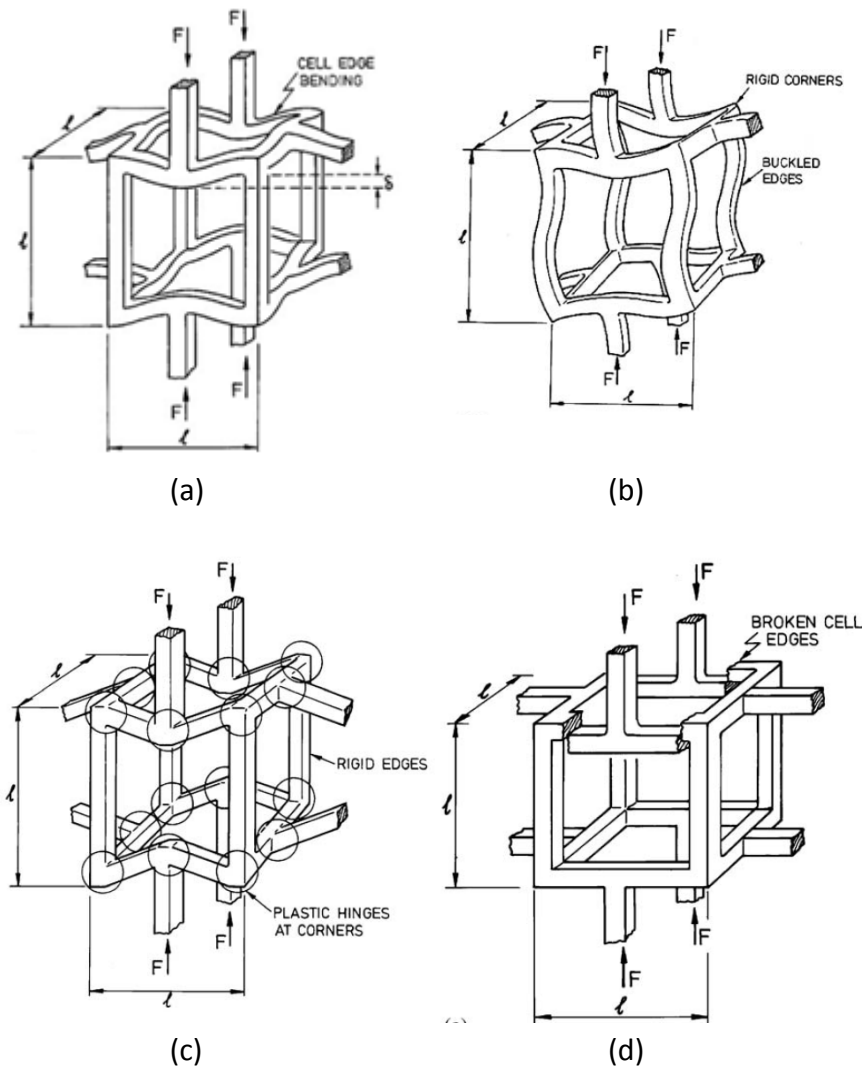


**Figure 1.10** Deformation mechanisms in the Gibson-Ashby cell (a) linear elastic strut bending (b) cell collapse by elastic buckling (c) plastic yielding, and (d) brittle crushing [47]

In [48], explicit and detailed connections are made between the idealized unit cell models and various biological materials, e.g., wood, cork, iris leaves, plant stems, porcupine quills (see also [47]). Biomaterials with a cellular structure, e.g., titanium foam and collagen-glycosaminoglycan are also described as being susceptible of deformation and collapse through mechanisms similar to those observed in the idealized unit cell (Figure 1.10). It was also asserted that linear elastic deformation in low-density trabecular bone is dominated by bending of the cell struts, and that the compressive strength of trabecular bone

is associated with the buckling of those struts aligned parallel to the compression axis.

Recently, the Gibson-Ashby unit cell has been put to good use in somewhat different contexts. For example, BayraktarKeaveny [49] incorporated some of the findings of Gibson's cellular solids theory to account for the remarkable uniformity of trabecular yield strains measured at specific anatomic sites (see Section 1.2.2.2), and YooJasiuk [44] adapted the Gibson-Ashby unit cell to study the couple-stress moduli of trabecular bone with bone marrow intact. We undertake a more rigorous and in-depth study of the Gibson-Ashby unit cell, with emphasis on its mechanical behaviour and its morphometric properties, in Chapter 3.

#### **1.2.1.2 Kelvin cell (tetrakaidecahedron) model**

The tetrakaidecahedron, sometimes known as the tetradecehedron, is a polyhedron with fourteen sides (Figure 1.11). There exist several classes of tetrakaidecahedra, based on the number of edges possessed by each of these sides and their orientation. The particular class of tetrakaidecahedron that has been applied to bone in the past is the truncated octahedron, an Archimedean solid. In 1887, Lord Kelvin considered the question of how space could be partitioned into cells of equal volume with the least surface area between them (i.e., Plateau's soap-bubble problem), and discovered that the truncated octahedron would be the most suitable model [50]. In his honour, the tetrakaidecahedron is also known as the Kelvin cell. It may of interest to note that, more recently, Weiare and his group employed computer-based

simulations to suggest a superior solution to the Kelvin problem – the so-called Weaire-Phelan structure [50].

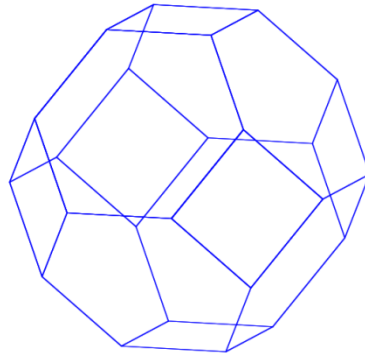


**Figure 1.11** The regular tetrakaidecahedron, showing the six square faces and the eight hexagonal faces

Application of the tetrakaidecahedron to bone modelling dates back to the mid-1990s, specifically to the works of Zysset and co-workers [51], in which an anisotropic variant of the structure was proposed and compared against experimental data (Figure 1.12).

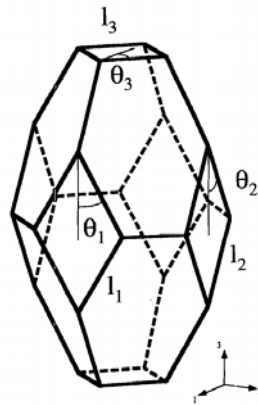


**Figure 1.12** The generalized tetrakaidecahedral cell as used by Zysset et al. [51] showing the three independent edge lengths and the three independent edge angles

They investigated both the closed-cell and the open-cell versions of the tetrakaidecahedron, and discovered that the structures closely correspond to the mechanical behaviour of real trabecular bone for a wide range of volume fractions and anisotropy (Figure 1.13). They also studied the relationships

between the fabric tensor of the tetrakaidecahedron and its effective stiffnesses and yield behaviour, thereby developing bounds for the effective properties of the unit cell.

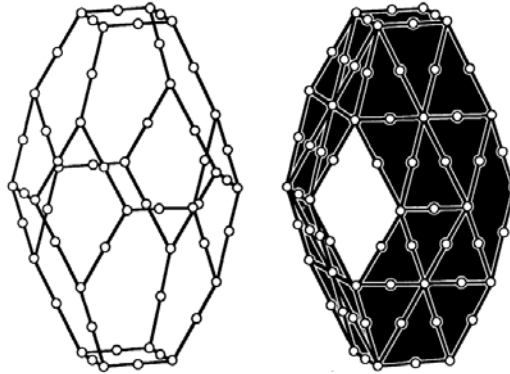


**Figure 1.13** The open (rod-like) and partially-closed (plate-like) finite element models employing 3-node beam elements and 6-node shell elements respectively [51]. Note the lack of shell element at the square faces in the latter

The mathematical relationships between the cell geometry and its mechanical properties will be studied in greater depth in Chapter 3.

More recently, there has been a revival in researchers' interest in the tetrakaidecahedron as a model for bone, with specific emphasis on investigating the effects of bone loss and trabecular strut thinning on overall bone strength [52].

### 1.2.1.3 Voronoi tessellation – based model

The concept of partitioning space based on a predefined algorithm has been in use for a long time [53]. One such algorithm, known as Voronoi tessellation (after Georgy Voronoi), or Dirichlet tessellation (after Peter Gustav Lejeune Dirichlet), has been applied by several workers in the past in modelling bone [54] as well as various other materials (e.g.,[46]). The theory underlying the model is as follows: given a set  $S$  of points  $s$  (called the Voronoi generators or

Voronoi sites) on a plane, a Voronoi cell  $V(s)$  for point  $s$  comprises the set of all points closer to generator  $s$  than to any other generator. The edges of each Voronoi cell  $V(s)$  are therefore a set of points that are equidistant to the two nearest generators. A Voronoi node is a point that is equidistant to three or more generators.

In the two-dimensional version used by [55, 56], an array of 20 x 20 Voronoi sites spaced 1x1 mm apart was generated and their coordinates then perturbed by -0.3 to +0.3 mm in each direction (Figure 1.14). Voronoi tessellation was then performed using a FORTRAN script. The Voronoi mesh was converted to a finite element mesh using beam elements to represent the Voronoi edges.

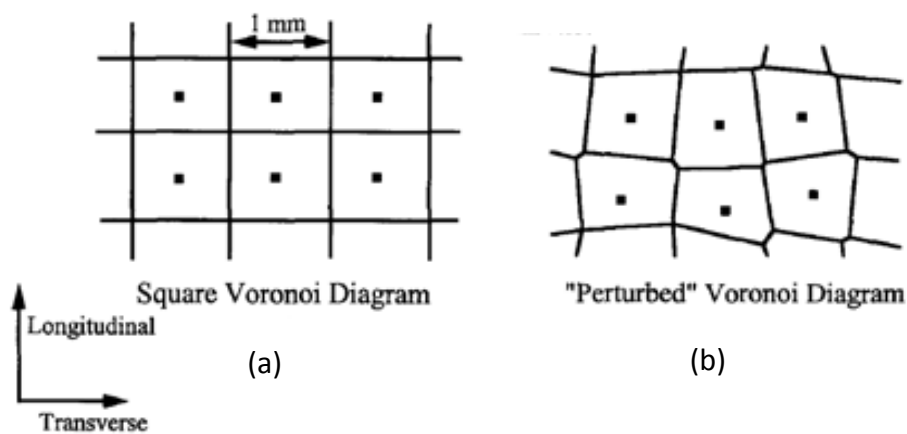


**Figure 1.14 (a) Original Voronoi diagram with black dots depicting Voronoi generators; (b) Voronoi diagram subsequent to perturbations of Voronoi sites**

The advantage of Voronoi-based models for bone is the ease with which they can be digitally rendered. Commercially available mathematical packages, e.g., MATLAB and Maple, have in-built functions for performing Voronoi tessellations and are capable of handling very large three-dimensional arrays. Subsequent conversion of the Voronoi mesh into the required format for finite element analysis is also trivial. Researchers have successfully employed

Voronoi meshes to study the mechanical effects of various parameters, e.g., strut tenuity, bone volume fraction, orientation and distribution of struts, etc, as described in Section 1.2.2.1 below.

The disadvantages of Voronoi-based models have to do with the fact that the Voronoi cell edges are typically replaced during finite element analysis with beam elements of constant cross-section. This results in spurious stress concentrations occurring at the vertices between two connected struts, which may compromise the veracity of the data and conclusions drawn therefrom. Furthermore, the rod-like nature of all trabecular struts generated using Voronoi tessellation implies that the model is suitable only for anatomic locations where the natural trabecular bone is known to be rod-like, e.g., in the vertebral column, and not for locations where the struts may be more plate-like, e.g, in the high-density regions of the femur [57].

More recently, Kim and colleagues [58, 59] have attempted to generate Voronoi-based models for entire bone cross-sections using an algorithm that distributes Voronoi sites in proportion to the density of the bone at that location and then deletes particular struts based on a remodelling rule (Figure 1.15). This method has resulted in two-dimensional models that bear remarkable fidelity to the original bone cross-section, and may be of importance in understanding the relationship between bone density attenuation and strength.

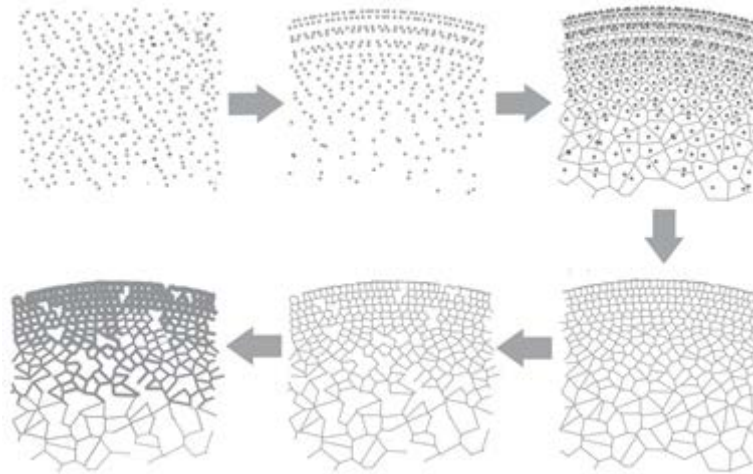


**Figure 1.15** Generation of a two-dimensional model of a bone cross-section using Voronoi tessellation followed by application of a remodelling rule, showing density-dependent distribution of Voronoi sites [58]

#### 1.2.1.4 Perturbed rectangular lattice model

McDonald et al. [60] chose a simple lattice based on a rectangular grid as a model for osteoporotic trabecular bone, specifically in the vertebrae (Figure 1.16). They asserted that the rod-like nature of vertebral osteoporotic bone could be best mimicked by a three-dimensional network of longitudinal and transverse struts.

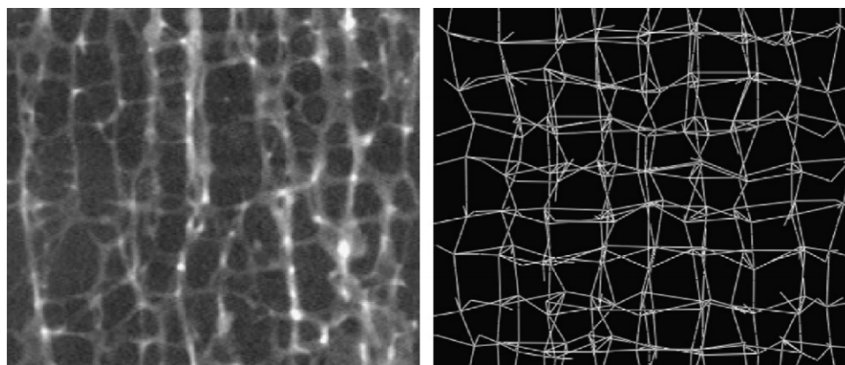


**Figure 1.16** Micro-CT image of aged vertebral trabecular bone (left); Trabecular bone model lattice (right) with 0.3 lattice perturbation factor [60]

To develop their macro-scale model, they first simulated the compression of a single longitudinal strut to validate its buckling mechanism, and then used it as

the building block for assembling larger structures. The addition of an external cortical shell surrounding the trabecular core furnished them with a complete L3 lumbar vertebral bone, which was then tested computationally and validated against experimental results.

Part of the novelty of this work lies in its use of geometric perturbations to capture the inherent irregularity of real bone. Subsequent to the creation of the regular lattice structure, the position of each vertex node was perturbed by a fixed ‘perturbation factor’  $x\%$  such that its displacement from its original position was up to  $\pm x\%$  of the trabecular spacing value. The actual distance moved by each node was randomly assigned based on a Gaussian distribution. It has previously been suggested that the geometric irregularity of natural trabecular bone may play a pernicious role during ageing by mitigating bone strength [56]; hence, it may be important to incorporate this irregularity in modelling trabecular bone.

The limitations of the model are two-fold. Firstly, the rectangular grid-based distribution of longitudinal and transverse struts implies that the model is suited only to vertebral trabecular bone, and that it cannot be applied directly to other anatomic locations where the trabecular network is known to be differently oriented. Secondly, the constant cross-sectional areas of the individual trabecular struts lead to spuriously high stress concentrations at the intersections of two struts. Real bone is known to remodel itself in order to minimize the manifestation of such stress singularities at strut intersections [1].



### 1.2.1.5 The doubly-tapered strut model of KimAl-Hassani [61]

Typical vertebral trabecular bone is known to comprise predominantly vertically oriented columns with intermittently horizontal struts that reinforce the structure [62]. KimAl-Hassani [61] observe that naturally occurring cellular microstructures, including vertebral trabecular bone, have a network of doubly-tapered struts that thicken near the strut joints, and point out that previous analytical models have failed to take into account the mechanical repercussions of the strut taper. They proposed a regular hexagonal cellular structure comprising doubly tapered struts as shown in Figure 1.17, and investigated the effect of the tapers on the effective mechanical properties as well as on the plastic collapse strength. Their results revealed a significant increase in the effective Young's moduli and uniaxial plastic collapse stress in the tapered strut model over that with struts of uniform cross-section.

Despite the advantages of the anisotropic doubly-tapered strut model, the fact that it consists of primarily vertical struts with few horizontal struts limits its applicability to vertebral bone, whose morphology it closes matches. Trabecular bone in other locations of the human anatomy, e.g., the femur, may possess different morphology, being isotropic and significantly denser.

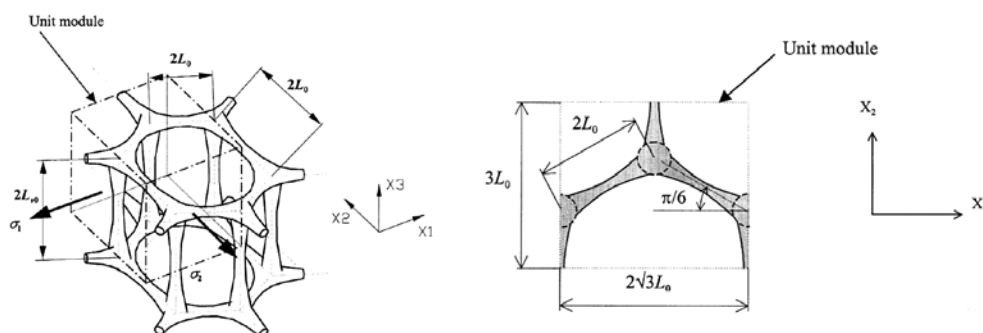


Figure 1.17 Hexagonal column structure model of vertebral trabecular bone [61]

## **1.2.2 Some applications of morphological models of bone**

### **1.2.2.1 Understanding the influence of bone loss on stiffness and strength**

Vajjhala et al. [54] used Voronoi tessellation to generate a three-dimensional truss structure, which they then analysed using the finite element method. Their motivation was primarily to understand the biomechanical significance of bone loss through strut thinning and resorption, a phenomenon associated with osteoporosis. They aimed to quantify the relative importance of density reduction through uniform thinning of struts and that through complete removal of struts (analogous to resorption).

After performing finite element analysis on the resulting structure, the effective stiffness and the yield strength of the structure were quantified. Beam elements were randomly deleted from the structure to simulate bone loss and finite element analyses performed on the resultant structures. The authors noted that with decreasing bone density, the effective Young's modulus decreases faster in the case of strut removal than in that of uniform strut thinning.

By extrapolating their findings from three-dimensional cellular structures to trabecular bone, the authors concluded that changes in bone density due to resorption of trabecular struts would have a more dramatic effect on attenuating bone strength and stiffness than those arising due to uniform strut thinning alone. The implication of their findings for clinical practice is that therapy for osteoporosis should commence at an early stage, when bone is being lost primarily due to strut thinning and complete resorption of struts has not yet set in.

### 1.2.2.2 Understanding the uniformity of yield strains of trabecular bone

Here, we outline a recent application of the cellular solids theory (originally proposed in [47]) in understanding the uniformity of yield strains for trabecular bone [49]. The yield strains of trabecular bone, both at the tissue level as well as at the apparent level, have been of interest to researchers as they may provide an additional indicator of bone strength (especially given that they represent the ratio of yield stress to elastic modulus). It is remarkable that, while the strength and moduli of trabecular bone vary across anatomic sites by up to an order of magnitude [63], the corresponding variations in yield strain are very small (approximately 10% coefficient of variation).

Bayraktar and Keaveny [49] discovered that the tissue yield strains were equivalent to the apparent level yield strains only for tensile loading, not for compressive loading (Figure 1.18). The reason they suggested for this phenomenon was the highly oriented structure of trabecular bone, whereby most of the struts and walls are oriented parallel to the axial direction. However, the discrepancy between the tissue yield strain and apparent level yield strain in compression was explained by the combined effect of the asymmetric strength of trabecular tissue and the presence of slightly obliquely oriented trabecular struts, causing tissue-level yielding to occur first in tension even for apparent level compressive yielding. The tissue strength asymmetry was believed to be responsible for reducing the structural strength in compressive loading, resulting in a lowering of the apparent yield strain, in comparison to a case where there was no tissue strength asymmetry.

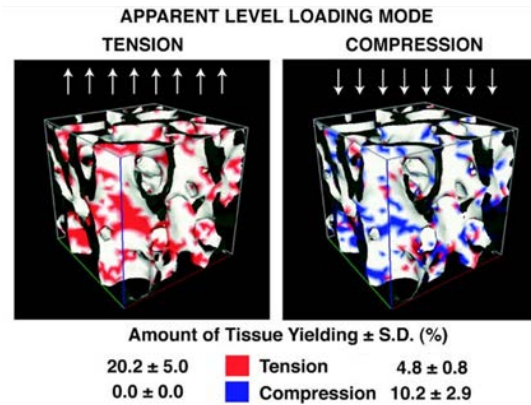


**Figure 1.18** A central portion of the trabecular specimen showing regions of yielded tissue at the apparent level yield points in tension (left) and compression (right). The percentage of tissue yielding in tension and compression are also shown [49]

In order to shed further light on their conclusions, the authors used a simple honeycomb structure with oblique struts, together with cellular solids theory (Figure 1.19).

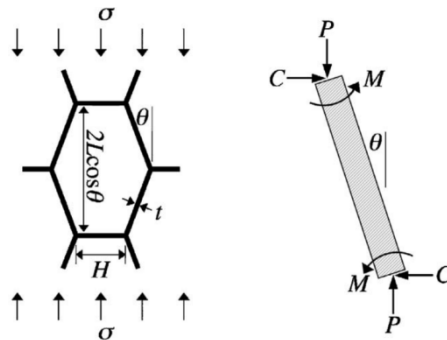


**Figure 1.19** The open-celled rod-based honeycomb structure used by [49] to understand the uniformity of yield strains in tension but not in compression. On the right is a free body diagram of a single oblique strut, modelled as a circular cylinder

They modelled trabecular bone as an open-cell rod-type honeycomb structure with struts oriented obliquely in the loading direction, and, using classical beam theory, derived analytical solutions for the maximum and minimum tissue strains for this apparent level compressive loading.

They then derived the criterion for when tissue yielding will occur first in tension, even though the apparent loading is compressive, and plotted it as in Figure 1.20.

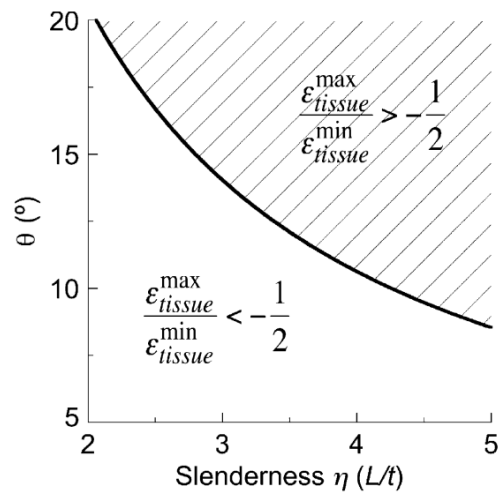


**Figure 1.20** Graph showing regions where tissue-level yielding occurs first, be it in tension or compression, although the apparent level loading is compressive. The shaded region represents tissue-level yielding in tension.  $\eta$  is the slenderness ratio, and  $\theta$  is the angle made between the oblique strut and the axis of compressive loading [49]

The analytical solutions obtained above were then tested using a finite element model with a single trabecular strut oriented at 10 degrees to the vertical axis, and slenderness ratio of 4.9. The results were similar to those obtained for the whole trabecular bone specimens, thereby confirming their hypothesis that the tissue strength asymmetry and the presence of slightly obliquely oriented trabecular struts sufficiently explain the differences in tissue level yield mode distribution and the ratios of apparent to tissue level yield strains in compressive and tensile loading.

On a critical and somewhat digressive note, we opine that one of the authors' assumptions in this work may be crucially limiting. As a secondary objective, they attempted to quantify the amount of elastic bending (i.e., large deformations) in the trabecular struts, and used linear elastic finite element

analysis to investigate this phenomenon. They reported that linear elastic analysis revealed only a small amount of bending of individual trabecular struts. However, we are aware that the use of linear elastic finite element analysis (i.e., the use of purely linear elastic tissue material in an analysis with apparent level loading) is limited to considerations of only elastic bending and/or buckling of the struts. The crucial possibility of inelastic bending and/or buckling (also known as Engesser buckling) is not accounted for in their analysis (and in other recent works, e.g.,[64]). In other words, the authors' discrimination between nonlinearities arising from the material properties (i.e., material nonlinearities) and those arising due to large deformation bending or buckling (i.e., geometric nonlinearities) may itself be spurious. Engesser buckling (discussed in Section 1.3.3.2.2 below) considers the synergistic effect of both types of nonlinearity occurring simultaneously in a given strut. Furthermore, it is important to mention the work by Townsend et al. [65], in which the authors performed experimental tests on single trabecular struts, subjecting them to compression and observing their mechanisms of buckling<sup>1</sup>. They concluded that the buckling of individual trabecular struts must necessarily be inelastic (i.e., according to the Engesser equation). It is our belief that incorporation of the possibility of Engesser buckling in the failure analysis of trabecular bone would furnish us with important information regarding the interrelationships between tissue level material properties and macro-level failure mechanisms (Section 1.3.3.2.2 and also Chapter 6 below).

---

<sup>1</sup> The majority of the 140 or so citations of this work (based on Google Scholar) pertains to the other important result mentioned in this work, namely, the value of the Young's modulus of bone tissue, and is oblivious to the result of interest to us, namely, that pertaining to the inelastic buckling of trabecular struts.

### 1.3 Mechanisms of bone degeneration and failure

#### 1.3.1 Ageing

Ageing is known to play a major role in modifying the geometry and mechanical properties of the skeleton. The frequency of hip fractures is greater in elderly populations than in younger ones [66-68]. This trend may be due to a combination of trabecular bone loss, cortical thinning, and increased outer cortical diameter [69].

Trabecular bone loss occurs when the rate of bone resorption exceeds that of bone deposition. Various factors may speed up the rate of trabecular bone loss, for example, menopause and metabolic diseases like osteoporosis. Cortical thinning is known to occur during ageing, as bone is resorbed at the endosteal surface much faster than it is deposited at the periosteal surface. Lastly, the outer diameter of the cortex expands with age. This phenomenon is thought to be an adaptation mechanism to maintain the section modulus of the bone during ageing, in order to preserve bone integrity during physiological loading.

Several researchers (e.g., [70], [71]) have attempted to quantify more precisely the effect of ageing on individual bone properties, e.g., the percentage decrease of trabecular density per decade, or the rate of expansion of cortical diameter. These studies are often subject to substantial statistical scatter and conclusions drawn therefrom are often not representative of other sample sets obtained from different age-groups or races (Figure 1.21). Nevertheless, they provide important insight into the adaptive strategies recruited by the human skeleton during the inevitable process of ageing and bone degradation.

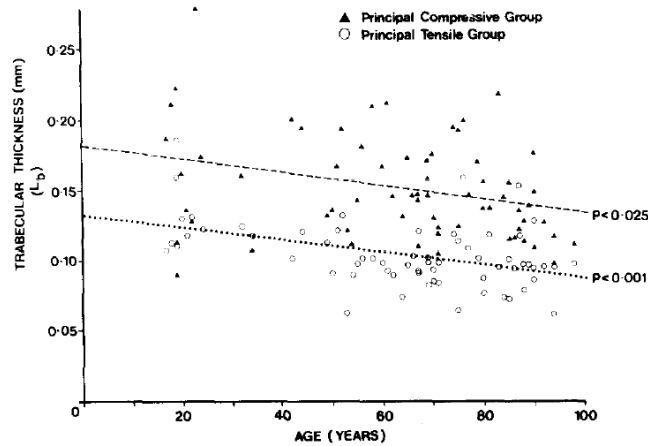


Figure 1.21 Regression of trabecular thickness on age in the femur [70]

### 1.3.2 Osteoporosis and osteopenia

The terms *osteoporosis* and *osteopenia* have been variously used and interpreted over the years, and their current connotations are vague [72]. Both terms generally refer to a condition whereby bone mass (or bone density) is decreased, resulting in an increase in the risk of fracture. Generally, the term *osteopenia* is used to refer particularly to the condition of low bone density, while the term *osteoporosis* is used to place more emphasis on the increased fracture likelihood of low density bone. Osteoporotic fractures are those that occur in subjects that are suffering from osteoporosis – owing to their severely decreased bone density, bones of osteoporotic subjects are often susceptible of catastrophic fracture following even a relatively low-impact stumble or fall (so-called ‘non-traumatic fractures’ [73]).

It has been argued [74] that osteoporosis should not be classified as a disease, but merely as one of the normal manifestations of ageing in humans. In fact, from the engineering point of view, there has been no evidence of any mechanical phenomenon coming into play peculiarly in osteoporosis that is not present in the course of normal ageing. On this basis, researchers



modelling osteoporosis and/or ageing (e.g., [75]), or studying their effects on bone mechanical properties (e.g., [52]), have frequently resorted to decreasing the apparent density of trabecular bone to a chosen degree.

### **1.3.3 Mechanics of micro-scale (trabecular-level) failure**

#### **1.3.3.1 Strut yielding**

By way of terminology, it is to be noted that, in the context of trabeculae level studies in this work, we use the term *trabecular strut* in its most generic sense to denote any of the individual trabecular spicules (or ligaments, or rods and plates, at any orientation), notwithstanding the fact that, in standard texts on mechanics (e.g., [76]) the term *strut* is used in a very special sense to mean columns of very small slenderness ratio.

The majority of numerical investigations undertaken at the micro-scale assign purely linear elastic material properties to the trabecular tissue (e.g., [7, 12, 77, 78]), implying that the possibility of material yield and associated phenomena are *a priori* ruled out. The primary advantage of such linear FE analyses is that they enable the researchers to focus their computational power on aspects of the study that are not influenced by the possibility of tissue yield.

However, of recent, more workers have begun to incorporate some form of tissue-level yield criterion in their choice of material properties [79]. One of the common nonlinear constitutive models used for trabecular tissue assumes elastic perfectly-plastic material with constant yield strength in both tension and compression [21, 52]. A somewhat more complex variant is the bilinear elasto-plastic material, with strain hardening above the initial yield strength,

and tissue strengths being either asymmetric or symmetric in tension and compression [79-81].

At the moment, the mechanisms underlying post-yield behaviour of bone tissue are poorly understood – a recent review article [22] mentions “ductile failure modes [82] involving microcrack damage combined with a plasticity component originating from the collagen fibres [83, 84]”. Therefore, contemporary constitutive models for bone tissue are based primarily on phenomenological considerations and fitting of empirical data; more research has to be done to understand failure and damage mechanisms at the lower (nanometer) level in order to eventually obtain a more reliable basis for constitutive modelling at the tissue level.

### **1.3.3.2 Strut buckling**

Buckling is defined as “the sudden, large, lateral deflection of a column owing to a small increase in an existing compressive load” [76]. It has been suggested sporadically in the literature that buckling of trabecular struts, especially in regions of low volume fraction, may play a significant role in compromising bone integrity [20, 21, 64, 85].

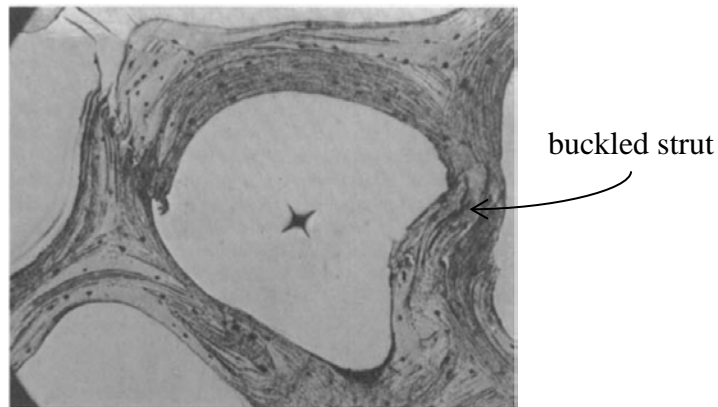


**Figure 1.22 Reflected light photomicrograph of bovine trabecular bone tested in uniaxial strain to 15% compression, showing buckling of one trabecula and shear failure of another (from [85])**

Depending on the nature of the constitutive law assigned to model the tissue material and the slenderness ratios of the trabecular struts, the latter can fail according to two different mechanisms: Euler (elastic) buckling and Engesser (inelastic) buckling.

#### **1.3.3.2.1 Euler (elastic) buckling**

For pin-ended columns, the Euler equation gives the critical load,  $P_{cr}$  as:

$$P_{cr} = \frac{\pi^2 EI}{L^2} \quad .4)$$

where:

$E$ : Young's modulus

$I$ : moment of inertia of the column cross-section

$L$ : length of the column.

By expressing the moment of inertia in terms of the cross-sectional area  $A$  and the radius of gyration  $R$ , the Euler equation can also be written as:

$$P_{cr} = \frac{\pi^2 EA}{\left(\frac{L}{R}\right)^2} \quad .5)$$

The term  $(L/R)$  is called the *slenderness ratio* of the column and is used to classify columns into short, intermediate and long columns, each with its own peculiar failure mechanisms. Long columns are known to fail by Euler buckling at an axial stress below the proportionality limit of the material. Short columns usually fail by yielding (or crushing) when the axial stress exceeds the proportionality limit (or strength) of the material. Intermediate columns are most interesting because they do not fail by direct compression (as in short columns) or by elastic instability (as in long columns), but by a more complex mechanism called *inelastic* (or Engesser) buckling.

#### 1.3.3.2 Engesser (inelastic) buckling

Inelastic buckling occurs in columns of intermediate slenderness ratio whose material is elastoplastic or nonlinearly elastic, when the axial compressive stress exceeds the proportionality limit. For these cases, Engesser proposed the so-called tangent-modulus theory, using which he derived the critical stress to be:

$$P_{cr} = \frac{\pi^2 E_t I}{L^2} \quad .6)$$

where  $E_t$  is now the tangent-modulus, defined as the slope of a tangent to the stress-strain curve:

$$E_t = d\sigma/d\epsilon \quad .7)$$

In other words, Engesser buckling accounts for cases where material nonlinearity (i.e., yielding of short columns) can no longer be considered independently of geometric nonlinearity (i.e., the large-deformation bending or buckling of slender columns). The two phenomena instead interact to further decrease the critical stress that the intermediate column can support.

In the context of bone, Townsend and Rose [65] performed experimental tests by compressing individual trabecular struts and concluded that the *in vivo* buckling of the latter must necessarily be inelastic (see also the brief discussion in [86], pp. 328-229). More recently, McDonald [87] undertook FE analyses to investigate the effects of inelastic buckling in the vertebral trabecular core.

We pursue more detailed studies on the interrelationships between strut yielding and buckling (both elastic and inelastic) in Chapter 6 below, where more details can be found.

#### **1.3.4 Mechanics of macro-scale (femur-level) failure**

At the macro-scale, several criteria have been applied to diagnose failure in different contexts to varying degrees of success. Generally, most failure criteria hitherto employed in bone modelling fall into one of the following two classes: ductile failure with considerable plastic strain, or brittle cracking. The former appear to be more common [88], since they are easier to implement in standard commercially available FE software. The latter, on the other hand, rely on theories developed from fracture mechanics and are typically more challenging to incorporate in FE analyses.

#### 1.3.4.1 Yielding and/or plastic collapse

Keyak and Rossi [89], underscoring our poor understanding of the macro-level failure of bone, reviewed the performance of nine stress and strain-based failure theories against experimentally obtained failure data of the proximal femur and discovered that there was substantial disparity between the theoretical predictions and experimental values. They suggested that two criteria in particular, namely, those based on the distortion energy and on the maximum shear stress, came closest to experimental results and should be further investigated under different loading conditions. They also pointed out the discrepancy between their conclusions (i.e., that stress-based failure criteria better predicted experimental data) and those of [90] which indicate the superiority of strain-based failure criteria.

A further complication arises when one aims to find out whether the macro-scale behaviour of the proximal femur is linearly elastic up to failure or shows clearly recognizable signs of irreversible yielding. There have been studies claiming that either is true to the exclusion of the other; Juszczuk et al. [91] recently surveyed a large number of experimental studies of the human proximal femur and suggested that, under physiological loading conditions (i.e., stance mode), the force-displacement graphs at the structural level are linearly elastic. Further, they dismissed results to the contrary obtained by other researchers [92] as lacking a clearly defined yield point.

At the moment, the choice of macro-scale failure criteria remains an open question and, as such, we shall adopt in our work the one that is most appropriate in the context.

#### **1.3.4.2 Brittle failure following crack propagation**

The possibility of crack growth as a primary failure mechanism in bone (especially in very dense cortical bone) is being explored with increasing interest nowadays [93-95]. It is thought that micro-cracking during cyclic loading may help to dissipate impact loads through the formation of new bone surfaces (due to the increase in surface energy) of the cracked bone and that micro-cracks may play an important role in increasing the fracture toughness of cortical bone [96]. Owing to the fact that researchers have not yet reached a clear consensus on the role of cracks in bone failure and the paucity of numerical studies on crack propagation in the femur, we did not take account of this phenomenon in our own work and instead chose better-established macro-scale failure mechanisms based on metal-like plasticity.

#### **1.3.4.3 Catastrophic buckling**

Lastly, there have been some reports of structural buckling occurring at the femur scale, especially in elderly bones where the cortical bone has thinned substantially and the trabecular density has been severely decreased due to ageing or osteoporosis [66, 97]. If viable, this phenomenon could be treated as a case where the entire proximal femur behaved as one column with eccentric loading that undergoes buckling once a critical load is exceeded. However, experimental evidence of this phenomenon is still tenuous.

### **1.4 Aims and Objectives of Our Study**

The aim of our study was to propose a novel morphological model for trabecular bone and use it to investigate the relationships between the

mechanical behaviour and the deformation mechanisms at different hierarchical levels of the human proximal femur.

More specifically, our objectives were five-fold:

- To propose a unit cell for trabecular bone based on the triply-periodic minimal surface solid called the gyroid;
- To compare the mechanical behaviour and morphometric properties of this gyroid-based unit cell against real bone and other previously proposed models for trabecular bone;
- To employ the gyroid-based unit cell in a non-concurrent dual-scale analysis of the human proximal femur to study the effect of trabecular bone deformation mechanisms on macro-scale (i.e., femur-level) mechanical behaviour;
- To use the gyroid-based unit cell to generate a femoral neck structure with realistic geometry and density distribution, in order to study its macroscopic yield behaviour under different types of loading;
- To improve our understanding of the relationship between micro-scale (i.e., trabecular-level) deformation mechanisms and the macro-scale yield behaviour of the femoral neck structure.

Overall, the thesis may be divided into two parts: Chapters 2 – 4 focus largely on developing micro-scale models representative of bone, while Chapters 5 and 6 demonstrate macro-scale applications of the chosen micro-scale model (the gyroid-based unit cell) in studying the femur.



**Chapter 2. The gyroid-based unit cell as a model for femoral bone**

*“... and He shows you His signs, that haply  
you may have understanding.”*

*(Al-Baqarah, verse 67)*

The biomechanics of trabecular bone has been intensively studied over the last four decades, with current emphasis on characterizing the mechanical properties as functions of variables like volume fraction and age [12]. In the context of bone quality assessment, it has been proposed that trabecular bone micro-architecture plays a significant role in fracture risk prediction [20, 98]. For example, it has been suggested that excessive trabecular thinning and loss of connectivity during ageing predispose trabeculae to large-deformation failure (by buckling) [20, 69]. Of especial clinical importance is knowledge of how ageing, drugs, and diseases like osteoporosis compromise overall bone strength by modifying trabecular bone microstructure.

With recent advances in computational techniques and processing power, numerical methods like finite element analysis (FEA) have become standard tools for the evaluation of bone mechanical behavior, both at the macro-scale and at the micro-scale. In macro-scale continuum-based finite element (FE) models, FE meshes are generated based on computed tomography (CT) images [7]. CT images of bone contain information on the bone shape and density distribution. Based on the density, material properties (e.g., stiffness) can be assigned to the FE model. Macro-scale mapping techniques based on empirically obtained density-modulus relationships suffer a fundamental flaw

in that they do not account for trabecular microstructure, which is not captured in CT images. Absence of microstructural information in the FE model implies that important geometrically nonlinear phenomena like buckling cannot be accounted for in the analysis [7], yet such phenomena may be crucial in assessing bone quality [21].

The above-mentioned limitation of continuum-based FE models can be circumvented by employing so-called micro-FE models [99]. Here, instead of low-resolution CT images, trabecular architecture is accurately captured by the use of high-resolution micro-computed tomography (micro-CT). These micro-CT images can then be converted into micro-FE models using voxel-based conversion techniques [100]. This modelling approach incorporates the full trabecular architecture and obviates the need for stochastic density-modulus relationships. However, micro-CT images are difficult to obtain in clinical settings owing to the extremely high radiation dosage required [7]. Furthermore, extant micro-CT technology only permits scanning of peripheral sites like the ankle and wrist, owing to intrinsic limitations in the machine design and capability [7]. Hence, *in vivo* micro-structural information of other important sites, especially the femur, is currently impossible to obtain, and, as such, micro-FEA remains a laboratory-based research technique [7].

In order to address these shortcomings of continuum-based FEA, researchers have attempted to utilize various morphological models for trabecular bone. Such models could be used to “fill in” microstructural information where only CT images are available. The feasibility of a given model is dependent upon the simplicity of its generation (i.e., the number of independent parameters

required to construct the model *in silico*), and its ability to replicate relevant mechanical properties of real bone. For example, in [54], a 3D Voronoi algorithm was employed to obtain aperiodic random open-cell honeycombs for bone strength investigations. In [44], trabecular bone was modelled as a periodic cellular structure made of open cubic cells. The thicknesses of the parallelepipedic struts employed in creating the unit cell were varied to generate representative volume elements (RVEs) of different volume fractions. To mimic the irregular structure of osteoporotic lumbar vertebra, [101] imposed lattice perturbations on an originally perfect lattice grid. A shortcoming of the above models is that the trabeculae are being modelled as struts of constant cross-sectional area; therefore, the models manifest unusually high stress concentrations at the intersections of two struts. This limitation is overcome in [61], where an analytical cell model comprising doubly tapered struts was used to predict the mechanical properties of vertebral bone. However, the hexagonal columnar structure described is suited primarily to vertebral bone and is thus region-specific. Thus, there is still a need for a simple model that can mimic the mechanical properties of human trabecular bone.

In this chapter, we propose a novel model for trabecular bone based on the minimal surface family of solids. We investigate the feasibility of a minimal surface solid, called the *gyroid*, in modelling trabecular bone. We hypothesize that the gyroid provides an easy-to-construct model that captures relevant mechanical properties of trabecular bone, while avoiding the shortcomings of existing techniques. As such, gyroid-based unit cells can be used to obtain

large-scale nonlinear FE models of whole bone, for clinically viable, accurate fracture prediction.

## 2.1 Generation of gyroid-based unit cell

A minimal surface is one which has mean curvature of zero at every point. In other words, subject to some constraints like total volume, minimal surface solids possess minimized total surface energy [102]. The three well-known cubic minimal surfaces are the primitive or P-surface, the diamond or D-surface, and the gyroid or G-surface [103-105]. In this study, we chose the gyroid to model trabecular bone as it resembles the trabecular structure most closely. The simplest gyroid equation is given below.

For any  $(x, y, z) \in R^3$ ,

$$f(x, y, z) = \sin x \cos y + \sin y \cos z + \cos x \sin z \quad (2.1)$$

Subsequently, the gyroid domain is binarized in order to obtain a unit cell containing either bone (binary 1), or space (binary 0). The binarization equation is described below.

$$g(x, y, z) = \begin{cases} 1 \text{ (bone)}, & \text{if } f(x, y, z) < t \\ 0 \text{ (space)}, & \text{if } f(x, y, z) \geq t \end{cases} \quad (2.2)$$

Human trabecular bone is known to possess a wide range of volume fractions ( $V_f$ ), depending on the anatomical site, age, and other factors. By varying the value of  $t$ , we can modify the amount of bone in the unit cell, i.e., decreasing the value of  $t$  reduces the amount of bone, and therefore the  $V_f$  of the unit cell, and *vice versa* (Figure 2.1). Note that, in this work,  $V_f$  is defined as the ratio of

the bone volume (BV) to the total volume (TV) of the bounding box, i.e.,  $V_f = BV/TV$ . A total of 7 gyroids is generated for a  $V_f$  range between ~10% and ~90%.

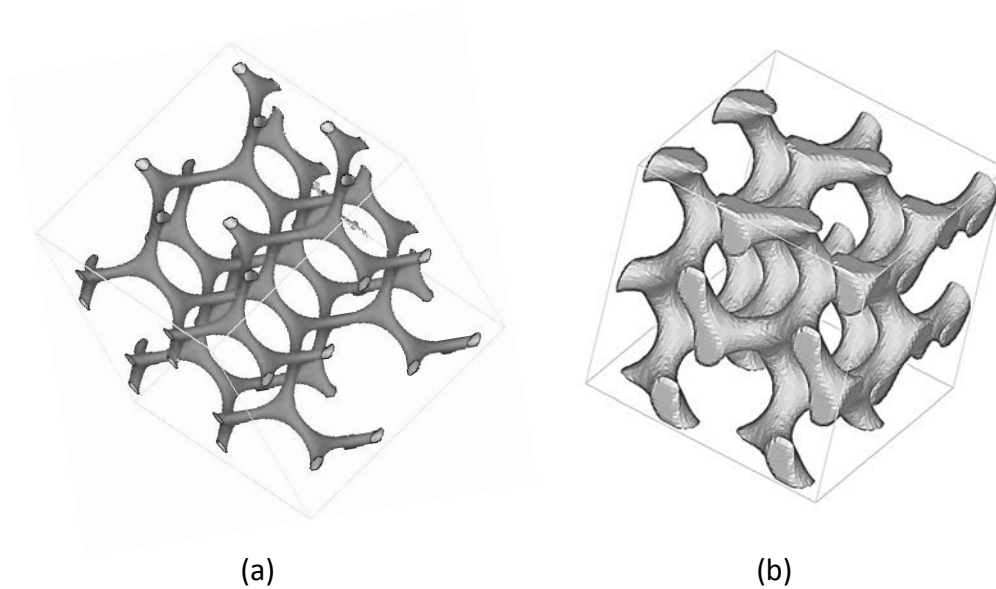


**Figure 2.1 Gyroid-based unit cell, (a) showing the threshold surface corresponding to  $t = -1$ ; (b) after binarization, corresponding to  $t = -0.87$**

The dimensions of the gyroid structures were set to be  $2 \times 2 \times 2 \text{ mm}^3$ . This value was based on a number of considerations, the primary one being its eventual intended application in a dual-scale analysis of bone. The gyroid unit cell would serve as a microstructure from which effective macro-scale material properties could be obtained for importing into a macro-scale analysis. For such multi-scale problems, Hill's condition [106] supplies an estimate of the microstructural size [107]. Hill's condition stipulates that the size of the microstructural RVE must be big enough to manifest a small micro-fluctuation field relative to its size. In our context, the RVE dimensions must be significantly greater than those of the trabecular struts located therein. Since the mean trabecular thickness is approximately  $100 \mu\text{m}$  [108], we believe that

2 mm is sufficiently large for the RVE size. The upper constraint for the RVE size arises from the fact that it must be small relative to the macroscopic structure (i.e., the bone). At certain locations of the femur bone (e.g., the femoral neck), the diameter may be as small as 32mm [109, 110]. Hence, we chose  $2 \times 2 \times 2 \text{ mm}^3$  as a suitable size for our RVE.

## 2.2 Morphometric analysis of gyroid-based unit cell

To quantitatively assess the morphological resemblance of the gyroid structure to trabecular bone, we employed the plug-in BoneJ [111] with the imaging software ImageJ [112] to calculate the following histomorphometric parameters for the gyroid structure: trabecular thickness (*Tb.Th*), trabecular separation (*Tb.Sp*), and Structure Model Index (*SMI*). We compared these values with those in the published literature that were empirically obtained for real bone.

$V_f$ (%)	<i>Tb.Th</i> (mean, $\mu\text{m}$ )	<i>Tb.Sp</i> (mean, $\mu\text{m}$ )	<i>SMI</i>
11.0	216.91	712.98	2.955
24.7	296.03	627.49	2.719
34.6	381.79	539.07	2.363
42.8	459.17	459.16	1.897

**Table 2.1 Morphometric parameters for the gyroid structure ( $V_f$ : volume fraction; *Tb.Th*: trabecular thickness; *Tb.Sp*: trabecular separation; *SMI*: Structure Model Index)**

The morphometric parameters of the gyroid structure (Table 2.1) were seen to fall within the range reported for real trabecular bone. The *Tb.Th* values of the gyroid ranged from 216.91  $\mu\text{m}$  to 459.17  $\mu\text{m}$ , corresponding to  $V_f$  of 11% and 42.8%, respectively, in favourable comparison with [113], whose graphs indicate a range of approximately 80  $\mu\text{m}$  to 520  $\mu\text{m}$  for the femoral head. The *Tb.Sp* of the gyroid ranged from 459.16  $\mu\text{m}$  to 712.98  $\mu\text{m}$ , again

corresponding to  $V_f$  of 11% and 42.8%, respectively, again comparing reasonably well with [114], whose graphs reveal a range of approximately 450  $\mu\text{m}$  to 1000  $\mu\text{m}$  in the femur. The SMI values of the gyroid ranged from approximately 1.8 to 2.9, fitting reasonably well within the range plotted by [113].

### 2.3 Addition of geometric irregularities

The gyroid models created contained perfectly smooth surfaces. Such perfectly periodic structures are expected to overestimate the strength of their natural counterparts. Visual inspection of trabecular bone shows that individual trabecular struts are never perfectly smooth as they contain numerous ‘pits’ and ‘mounds’, known as Howship’s lacunae, along their surfaces. Therefore, it was imperative to introduce geometric irregularities into the gyroid model.

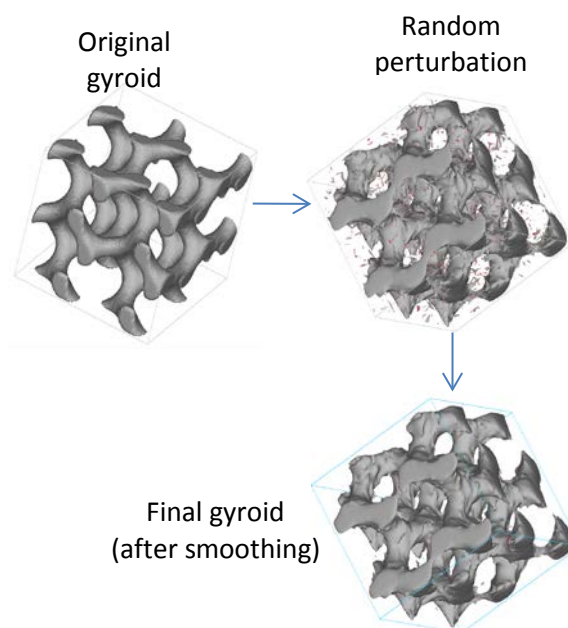


**Figure 2.2** Schematic showing the addition of random geometric perturbations to the original gyroid

Geometric irregularities were computationally imposed on the gyroid model by eroding small volumes of bone material from randomised locations along the surface, and then randomly depositing similar volumes of bone material onto the gyroid surface at different locations (Figure 2.2).

The gyroid models thus produced lost a small degree of their periodicity due to the presence of small ‘pits’ and ‘mounds’ on their surfaces. However, the  $V_f$  of the resultant gyroid is approximately identical with the original model. Gyroids of some typical  $V_f$ s are shown in Figure 2.3, together with their associated  $t$  values.

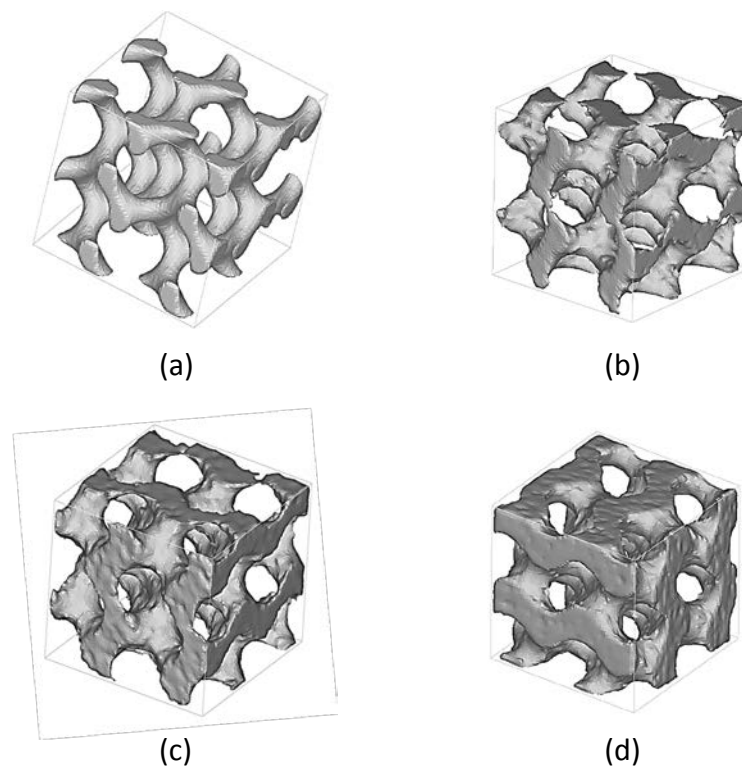


**Figure 2.3** (a)  $V_f = 17\%$  ( $t = -0.87$ ); (b)  $V_f \sim 25\%$  ( $t = -0.62$ ); (c)  $V_f \sim 35\%$  ( $t = -0.31$ ); (d)  $V_f \sim 45\%$  ( $t = 0$ ). Note: (a) is rendered before addition of geometric irregularities, while (b) – (d) are rendered after addition of geometric irregularities. ‘Pits’ and ‘mounds’ can be seen on the surface of the unit cells in (b) to (d).



## 2.4 Determination of mechanical properties using FEA

### 2.4.1 Material properties

In this work, we shall distinguish between tissue properties and apparent properties. In accordance with literature [60], we designate ‘tissue’ properties to mean those obtained at the micro-level, i.e., for the trabecular bone tissue. On the other hand, ‘apparent’ properties refer to the trabecular bone mechanical properties at the macro-level, without any reference to trabecular microarchitecture. Hence, for example, apparent elastic modulus denotes the homogenized stiffness of a sample of trabecular bone with porosities present. Also, note that, assuming that the tissue density is  $1.8 \text{ g/cm}^3$  [5], the relation between apparent density,  $\rho_{app}$ , and  $V_f$  is given by:

$$\rho_{app}(\text{g/cm}^3) = V_f \times 1.8 \quad (2.3)$$

The literature contains a vast range of values for trabecular tissue elastic moduli and Poisson’s ratio. Further complications arise when deciding how to incorporate the plastic regime into the material properties. In this work, we followed the work of [80] in assigning material properties to trabecular bone. A bilinear elastic-plastic material was chosen for our analysis, with tissue elastic modulus  $E_{tissue} = 18 \text{ GPa}$  before yield, and a post-yield modulus of 5% of  $E_{tissue}$ . The 0.2% offset yield strain in compression was taken as 1.04%. For the sake of simplicity, our FE analyses assumed tissue strength symmetry in compression and tension [52, 79].

### 2.4.2 Boundary conditions

The gyroid structure is triply periodic, i.e., it is periodic along each of the three axes. We thus applied compression in one direction only, knowing that the mechanical response is identical along the other two directions. We chose to apply compression instead of tension because we wished to validate the structure against published experimental studies [5, 115-118] which usually employ compressive loading. Based on this rationale, we imposed a compressive strain of 50% by displacing the top surface of the gyroid unit cell, while keeping the bottom surface fixed. Furthermore, to simulate the effect of adjacent unit cells, we applied periodic boundary conditions on opposite faces of the unit cell.

### 2.4.3 Finite element analysis

The gyroid unit cells were meshed with tetrahedral elements (C3D4) using ABAQUS finite element program [119]. Both geometrically linear and nonlinear analyses were performed using ABAQUS software. Geometrically nonlinear simulations account for the possibility of large deformations, i.e., buckling, in the structure. Similar FE analyses are performed for all the 7 gyroid models created above, i.e., for  $V_f$  of ~10% to ~90%. The finite element meshes contained approximately 45000 nodes and 230000 elements (Figure 2.4).

To assess mesh convergence, we generated a finer mesh with approximately 240000 nodes and 840000 elements (i.e., a 4-fold increase in number of elements) and performed identical simulations.

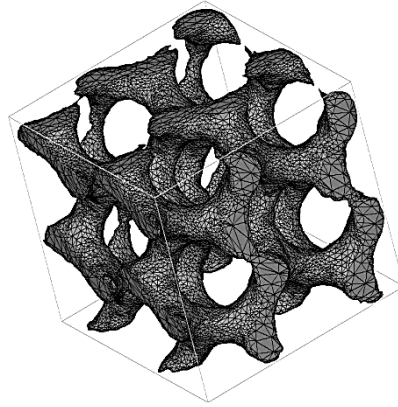


**Figure 2.4 Typical finite element mesh of gyroid-based unit cell**

#### **2.4.4 Homogenization**

Homogenization of trabecular bone involves finding the equivalent mechanical properties of the unit cell. By equivalent mechanical properties, we mean that the tissue properties are ‘smeared’ onto the volume of the bounding box. In other words, a continuum-model of the unit cell would have to possess these equivalent mechanical properties, in order to mimic the effect of the gyroid unit cell.

To obtain the homogenized engineering stress, we calculated the sum of the reaction forces at the top surface of the unit cell and divided it by the cross-sectional area of the undeformed unit cell [77]. Then, dividing the deformed height of the unit cell by the original height provided the homogenized engineering strain at any stage of the compression. The homogenized elastic modulus,  $E$ , defined as the ratio of the engineering stress to the engineering strain, was computed for each of the gyroid models by calculating the ratio of the homogenized stress to strain at infinitesimal strains.

## 2.5 Results

The typical von Mises' stress contours on the gyroid-based unit cell of  $V_f = 25\%$  are shown in Figure 2.5. The corresponding homogenized elastic modulus is calculated from the stress-strain graph (Figure 2.6) for the same gyroid.

In order to validate the gyroid model, we have graphically depicted the homogenized stress-strain graph (Figure 2.7) of a typical gyroid model ( $V_f = 17\%$ ), against a published graph showing sample stress-strain curves for small and large-deformation analyses of a trabecular specimen under compressive loading [20].

The graphs for the gyroid are found to be reasonably close to the published graph. The geometric irregularities introduce points of weakness into the structure and are thus effective in decreasing the strength of the gyroid model. Furthermore, it is seen from the graphs that geometrically nonlinear phenomena do compromise the stiffness of the model, and therefore need to be incorporated in bone quality assessment.

The homogenized elastic moduli were calculated for the gyroids of varying  $V_f$ . A power-law relationship, i.e.,  $E$  (GPa) =  $A \times (\%V_f)^b$  was used to fit the data. To facilitate comparison with the existing literature [5], we converted the  $V_f$  into  $\rho_{app}$  and plotted the graph of  $E$  (GPa) against  $\rho_{app}$  (g/cm<sup>3</sup>) for the gyroid, as well as for other published empirical relations for the femur bone (Figure 2.8). A power-law relationship was similarly used to fit the data for  $E$  vs.  $\rho_{app}$ .

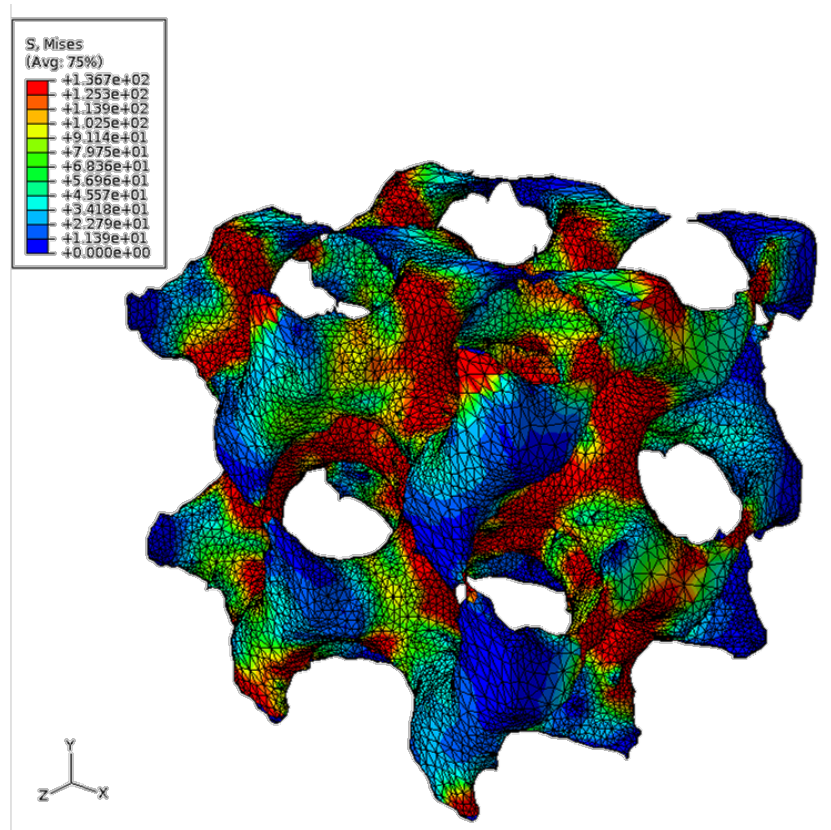


Figure 2.5 Stress contours showing von Mises' stress on the gyroid of  $V_f = 25\%$

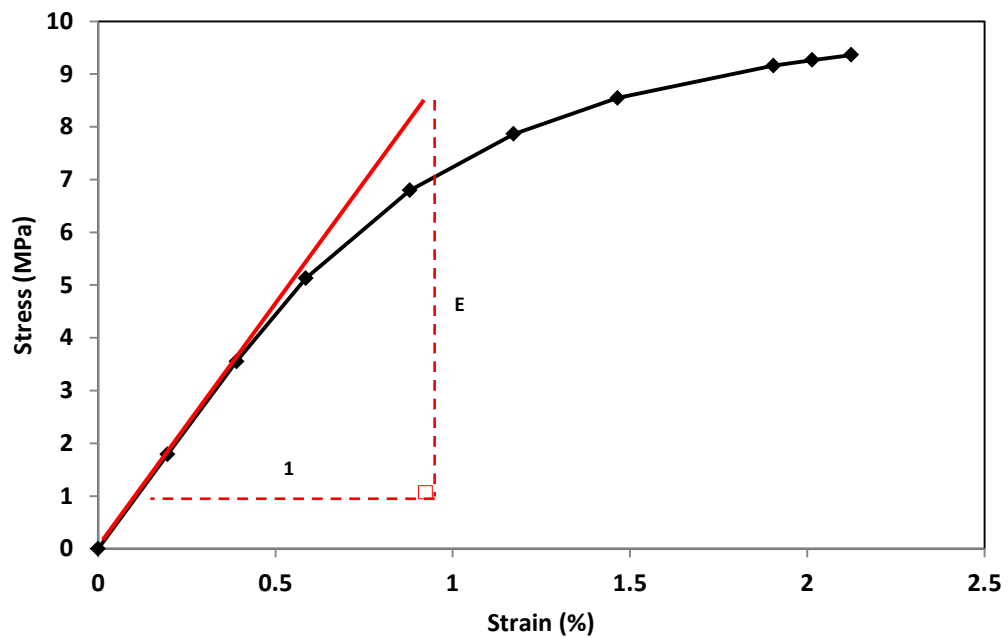


Figure 2.6 Homogenized stress-strain graph for the gyroid-based unit cell of  $V_f = 25\%$ , showing the linear elastic modulus,  $E$ , calculated at small strains

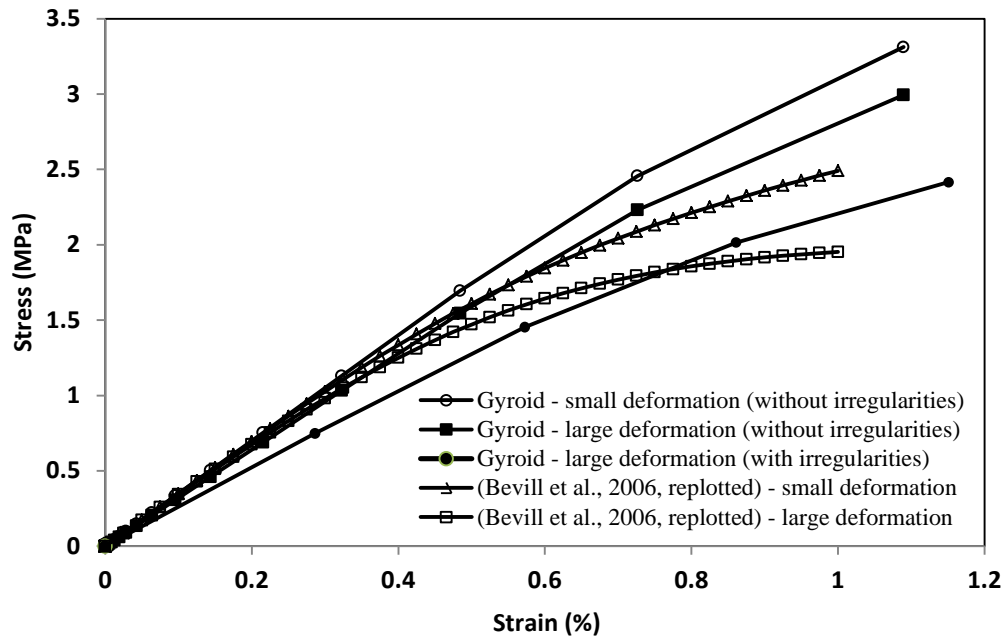


Figure 2.7 Homogenized stress-strain graphs depicting the compressive behavior of the gyroid under small and large deformations. A graph from [20] is re-plotted and superposed for comparison

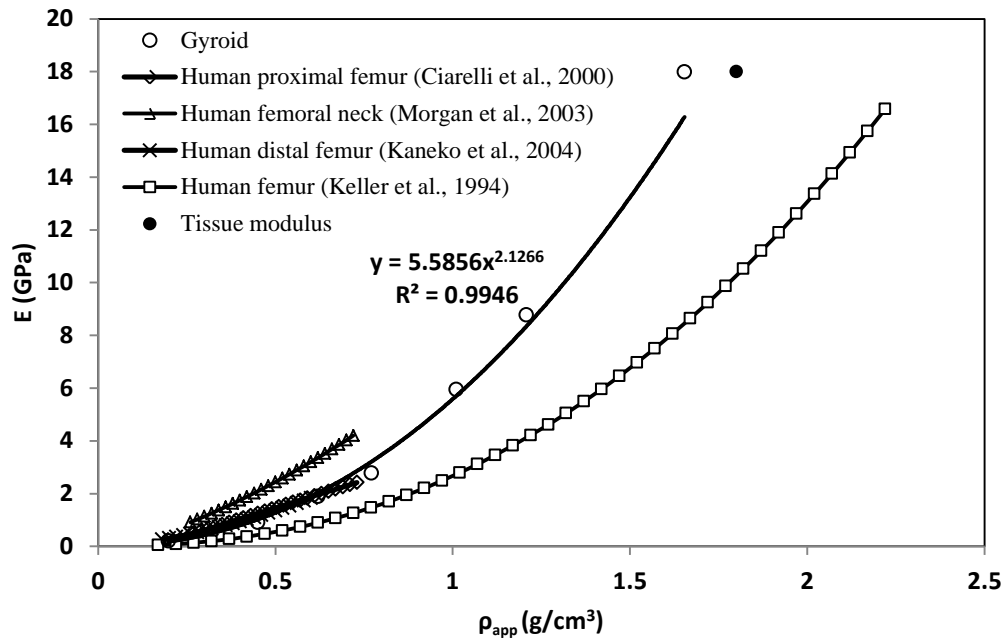


Figure 2.8 Graph showing small-strain elastic moduli of gyroid structure against apparent density. Graphs depicting published data [115-118] on the human femur are re-plotted and superposed for comparison

Increasing the mesh density had no significant effect on the homogenized initial stiffness, though it substantially slowed computations (Table 2.2). Furthermore, while the simulations using the original mesh achieved target homogenized strains of up to 5%, those using the fine mesh aborted at very low strains ( $\sim 0.25\%$ ) due to severe mesh distortions.

Mesh density	Original mesh	Fine mesh
Number of nodes	45889	238684
Number of elements (C3D4)	226480	837748
Homogenized initial stiffness (MPa)	2780.2	2829.0
% error in initial stiffness	-	1.8

Table 2.2 Results of mesh convergence study on the gyroid-based unit cell

## 2.6 Adaptations of the gyroid-based unit cell:

### 2.6.1 For regions of very low $V_f$

One of the shortcomings of the above-described algorithm for generating gyroid-based unit cells is that, at very low values of  $V_f$  (below approximately 5%), it produces structures whose struts are disconnected from each other (Figure 2.9). This occurs whenever the level-set surfaces defined by the chosen threshold  $t$  intersect with each other. Typically, this process occurs at the mid-point between two strut junctions, i.e., at the mid-span of the strut, owing to their tapered geometry. Disconnected struts cause severe meshing difficulties and also lead to spurious reductions in structural strength and stiffness.

Since the  $V_f$  of human trabecular bone may decrease to values below 5%, especially in cases of severe osteoporosis, it is imperative to modify the gyroid equation in order to be able to generate models of  $V_f$  in the range  $< 5\%$ .

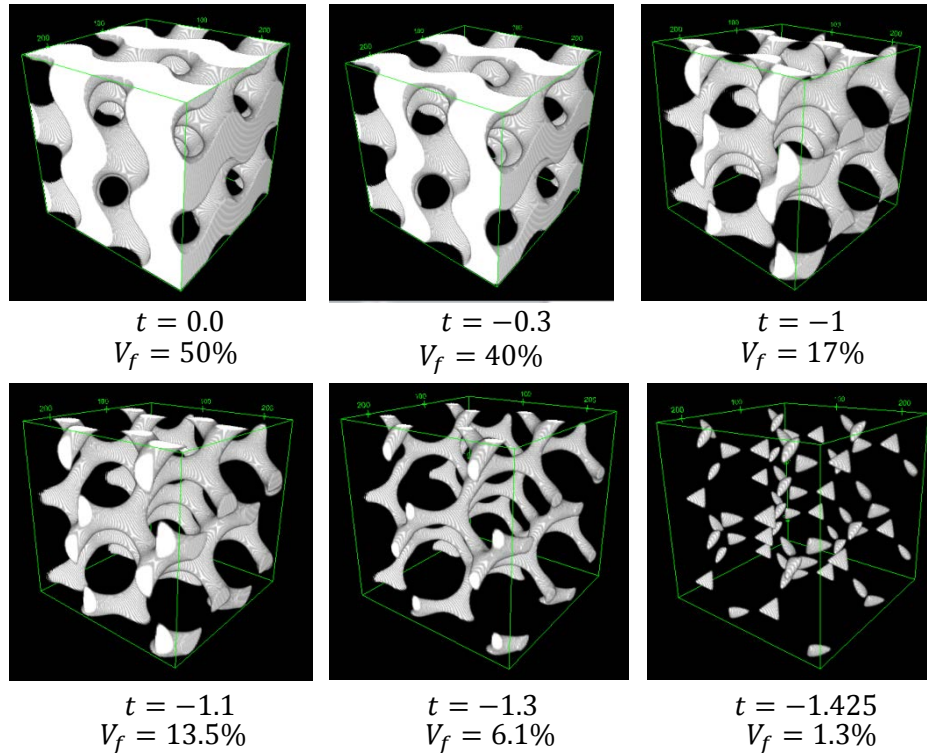


**Figure 2.9** Gyroid-based unit cells for decreasing values of  $t$ , showing the disconnected struts at very low  $V_f$

The method we propose is to isolate the skeleton graph of the gyroid equation and then use it as the basic equation for rendering unit cells. The skeleton graph of the gyroid equation is given by the following equation [120]:

For any  $(x, y, z) \in R^3$ ,

$$s(x, y, z) = 10.0(\cos x \sin y + \cos y \sin z + \cos z \sin x) - 0.5(\cos 2x \cos 2y + \cos 2y \cos 2z + \cos 2z \cos 2x) - 14.0 \quad (2.4)$$



Subsequently, as before, the skeletal gyroid domain is binarized in order to obtain a unit cell containing either bone (binary 1), or space (binary 0). The binarization equation is described below.

$$l(x, y, z) = \begin{cases} 1 \text{ (bone)}, & \text{if } s(x, y, z) > t \\ 0 \text{ (space)}, & \text{if } s(x, y, z) \leq t \end{cases} \quad (2.5)$$

Rasterization of the three-dimensional array  $l$  thus generated reveals gyroid skeleton-based unit cells whose structures remain connected at  $V_f$ s as low as 1% (Figure 2.10). Therefore, the gyroid skeleton-based unit cell can be used to replace the original gyroid-based unit cell when a user needs to generate models of bone of very low  $V_f$ s, for example, when studying the mechanical behaviour and deformation mechanisms of osteoporotic bone.

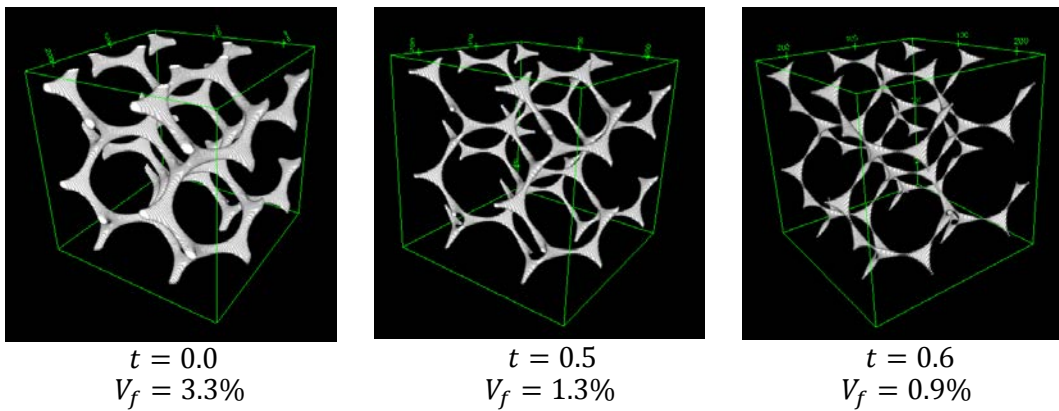


**Figure 2.10** Unit cells based on the skeleton of the gyroid equation, showing struts still connected at  $V_f$  as low as 0.9%

### 2.6.2 For modelling vertebral trabecular bone resembling cubic lattice-like structures

The human vertebral trabecular bone is known to resemble cubic grid-like structures, with vertical struts bearing loads primarily in compression and the horizontal ones providing reinforcement to the vertical ones. In the literature,

researchers have resorted to computer-aided design software to draw simple cubic-grid structures [29] (Figure 2.11).

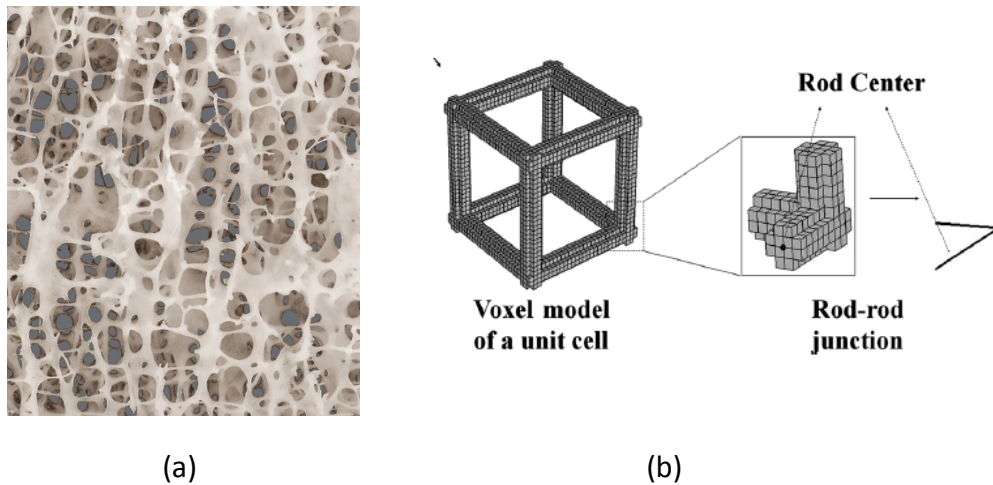


**Figure 2.11 (a) Human vertebral trabecular bone, showing cubic grid-like structure [39] (free for non-commercial use), and (b) unit cell used by Wang et al[40] to model vertebral trabecular bone**

One shortcoming of this cubic grid-like structure is that its struts meet at right angles to each other, manifesting unnaturally high stress concentrations at these junctions. Real human bone is known to remodel itself in such a manner as to minimize sharp junctions which could result in high stress concentrations. On this account, the CAD-based cubic grid-like models are rather poor models for human vertebral trabecular bone.

Although vertebral trabecular bone is not the focus of our work, we mention it to demonstrate the versatility of the minimal surface solid models in representing cellular periodic structures. The gyroid-based unit cell described above cannot directly be used to create cubic grid-like structures. In its place, we here propose to use the skeletal graph of another member of the minimal surface family, called the “primitive” surface [121], to generate structures that best resemble vertebral trabecular bone.

For any  $(x, y, z) \in R^3$ , we have [120]

$$p(x, y, z) = 10.0(\cos x + \cos y + \cos z) - 5.1(\cos x \cos y + \cos y \cos z + \cos z \cos x) - 14.6 \quad (2.6)$$

Subsequently, as before, the skeletal primitive domain is binarized in order to obtain a unit cell containing either bone (binary 1), or space (binary 0). The binarization equation is described below.

$$v(x, y, z) = \begin{cases} 1 \text{ (bone)}, & \text{if } p(x, y, z) \geq t \\ 0 \text{ (space)}, & \text{if } p(x, y, z) < t \end{cases} \quad (2.7)$$

Rasterization of the three-dimensional array  $v$  thus generated reveals primitive skeleton-based unit cells whose structures resemble cubic grid-like structures (Figure 2.12). Therefore, the primitive skeleton-based unit cell can be used when a user needs to generate models of human vertebral trabecular bone. The shortcoming of the CAD-based models involving high stress concentrations at the strut junctions is overcome by our method, which generates tapered struts that are thicker at the junctions and thinner at the mid-points between junctions.

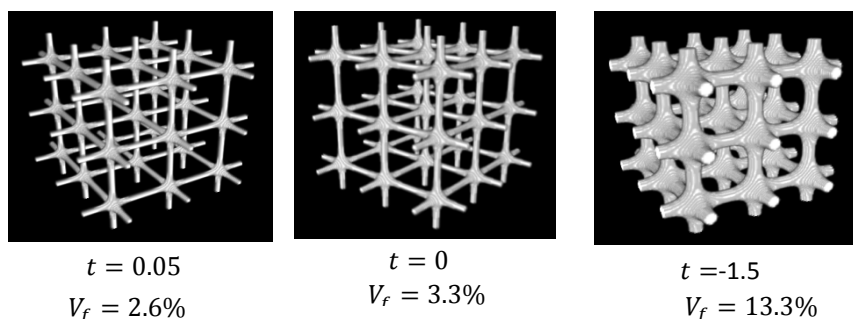


**Figure 2.12** Unit cells based on the skeletal primitive minimal surface which can be used to model vertebral trabecular bone

## 2.7 Discussion

Since its discovery by Alan Schoen in 1970 [104] (as an extension of the earlier work on minimal surface solids by Hermann Schwarz in the 1880s), the gyroid structure has been studied with increasing interest because of its seemingly ubiquitous occurrence in natural materials [102]. To cite just a few examples: Michielsen and Stavenga [103] observed gyroid-like structures in butterfly wing scales; Hyde [122] discusses the gyroid-like structure that underlies many supramolecular materials like lipids and polymeric melts; and Yoo [123-125] has been working on methods to fabricate bone grafts based on triply periodic minimal surfaces for tissue repair.

In this chapter, our goal was to propose and validate the gyroid-based unit cell as a model for trabecular bone. We generated gyroid models for a range of volume fractions, and studied their histomorphometry and mechanical properties. We observed that the gyroid equation could generate structures with a very wide range of volume fractions, but that at very low values (below  $V_f \sim 5\%$ ), there is a possibility of obtaining disconnected struts, while at very high values (above  $V_f \sim 60-70\%$ ), the cell walls fuse together forming closed cells. Notwithstanding these shortcomings, the gyroid is suitable for modeling trabecular bone for most anatomic sites, where the  $V_f$  is known to reside within the range allowable for the gyroid model [113].

The gyroid equations, based on sine and cosine functions, produce smoothly curved surfaces. The individual trabecular struts are doubly-tapered, such that they are of narrowest cross-section at the centre of the strut, and widest at the connections with other struts. This prevents the manifestation of stress-

concentration effects at struts connections, a phenomenon noticed in some of the other models for trabecular bone [44, 54, 60].

The morphometric parameters of the gyroid structure were seen to fall within the range reported for real trabecular bone. Human bone, owing to its capacity for structural adaptation with changing loads, possesses a vast range of morphometric values [126]. Hence, the comparison above between the morphometry of the gyroid structure and real trabecular bone was solely intended for the purpose of investigating their morphological resemblance; further investigation was needed to corroborate their resemblance in mechanical behaviour.

To that effect, we evaluated its mechanical properties by performing uniaxial compressive testing in ABAQUS software. We found that the homogenized stress-strain graphs of the gyroid models closely matched a published graph [20] showing the typical mechanical behavior of a trabecular specimen under compressive loading. This match provided further preliminary validation of the gyroid model as a potential model for human trabecular bone.

We then used the stress-strain data to obtain the apparent level elastic modulus for each of the gyroid models. The plot of elastic moduli,  $E$ , against apparent density,  $\rho_{app}$ , further corroborated the validation of the gyroid model. A familiar power-law relationship was obtained for the gyroid, as is found in the literature on trabecular bone [5]. Figure 2.8 shows a reasonably close match between the gyroid data and four representative empirical relationships obtained from the literature on human femora [5, 115-118]. Therefore, it is

seen that the gyroid equation described above can serve as an easy-to-construct model for trabecular bone of widely differing volume fractions.

One of the advantages of the gyroid model over previously proposed models for trabecular bone is that it is easier to construct computationally, since it is based on a simple mathematical equation. By varying a single variable,  $t$ , the volume fractions of the resulting gyroid models can be smoothly varied. This flexibility of the model is of paramount importance as it is known that trabecular bone volume fractions varies widely in the human body, depending on the anatomic site, age, state of health, etc. More rigorous comparisons between the gyroid model and other previously published unit cells for human bone are undertaken in Chapter 3.

Several studies in the past have used idealized unit cells to generate macroscopic structures to study various phenomena like the effect of uniform thinning of trabecular struts on overall strength [54] and the relationship between trabecular strut erosion and overall stiffness [52]. They typically assemble  $n \times n \times n$  *identical* unit cells to arrive at the macroscopic structure, which is thereby of homogeneous density. However, the distribution of trabecular bone in any human bone is not uniform, with some locations having a significantly greater density than others. This heterogeneity of density within the bone is likely to have a crucial role in determining the macroscopic mechanical properties and should thus be accounted for. The gyroid unit cell furnishes us with a simple method (to be described in Chapter 6) for assembling large structures of heterogeneous bone density, with the density distribution being derived from a CT image. These structures, bearing

remarkable fidelity to the underlying CT image, can then be used to study the effects of microscopic phenomena (like buckling of trabecular struts, biased erosion of tenuous struts during osteoporosis) on the mechanical properties and integrity of the macroscopic structure.

In conclusion, we have described in this chapter a novel model for human trabecular bone based on a minimal surface solid called the gyroid. We have shown that the gyroid model, though based on a simple mathematical function and therefore easy to implement in code, captures the salient mechanical properties of trabecular bone.

### Chapter 3. Investigation of other existing models of trabecular bone

In this chapter, we analyse some typical examples of morphological models of human trabecular bone that have been previously described in the literature. To this end, we chose to study the well-known Gibson-Ashby cellular solid and two variants of the Kelvin cell (sometimes known as the tetrakaidecahedral structure), one containing rods at the cell edges, and the other plates at the square cell faces. Our primary aim is to investigate the feasibility of their construction and their capacity to replicate the mechanical behaviour and morphometric properties of trabecular bone. Subsequently, we compare these models against our gyroid-based unit cell, proposed in Chapter 2, and discuss their respective merits and demerits.

#### 3.1 The Gibson-Ashby model

##### 3.1.1 Construction of the model

The Gibson-Ashby unit cell was constructed using the computer-aided design (CAD) software SolidWorks®. The basic input parameters for the cell are the thickness,  $t$ , and the length,  $l$ , of the cell struts (Figure 3.1). Here, we assume an aspect ratio of unity (i.e., a square) for the strut cross-sections, and constant length for all the struts. Varying the values of  $t$  and  $l$  results in changes in the volume fraction,  $V_f$ , of the cell. In order to mimic the open-celled nature of trabecular bone, the input parameters are constrained in such a way that the cell faces remain open, i.e.,  $t < l/2$ .

The unit cells, being triply periodic, can be assembled to obtain larger structures.



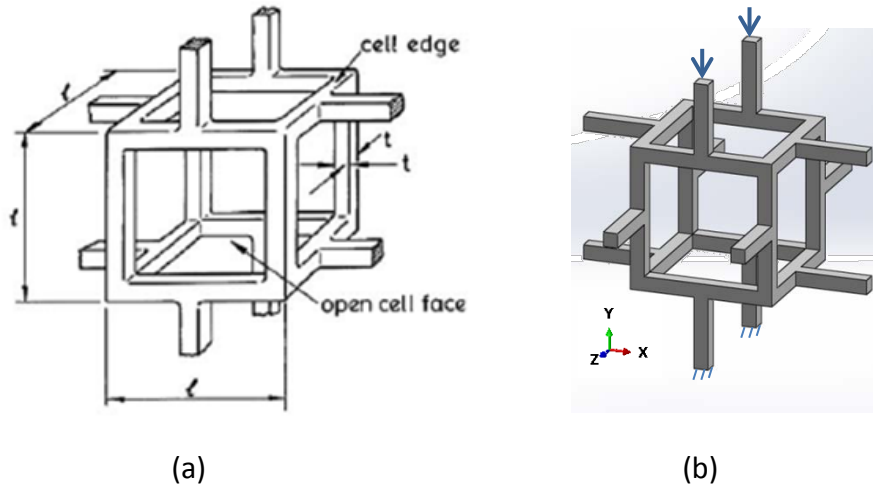


Figure 3.1 (a) Schematic of the Gibson-Ashby unit cell (from [47]), (b) CAD model of the Gibson-Ashby unit cell, for  $t/l = 0.1$ , and  $V_f = 2.1\%$

For example, Figure 3.2 below shows a structure resulting from the assembly of 3 unit cells in each of the three directions. It is to be noted that the  $V_f$  of the resulting structure is identical to that of the unit cell, and furthermore, the homogenized  $V_f$  is constant throughout the structure, i.e., the resulting structure has homogeneous apparent density.

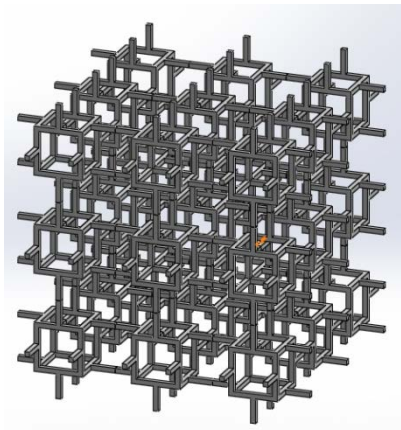


Figure 3.2 CAD model showing assembly of 3 by 3 by 3 Gibson-Ashby unit cells of constant volume fraction

### 3.1.2 Mechanical properties of the model

The CAD model of the Gibson-Ashby cell was imported into ABAQUS for finite element analysis (FEA) and meshed using 10-node tetrahedral elements.

Typically, depending on the  $V_f$  of the unit cell, between 20000 and 70000 elements were required to ensure smooth output fields. Periodic boundary conditions were applied on opposite faces to minimize the cell size effect at the boundaries. Based on [80], a bilinear elastoplastic material was used to model the material in the cell struts, with Young's modulus,  $E = 18 \text{ GPa}$ , post-yield modulus of 5% of  $E$ , and a 0.2% offset yield strain of 1.04%. While keeping the bottom face (i.e., the negative y face) fully constrained, the top face (i.e., the positive y-face) was subjected to a uniform displacement so that the unit cell was compressed to a strain of about 50%.

The results revealed that the unit cell exhibited the relevant deformation mechanisms as described by Gibson and Ashby [127]. At low strains, the cell struts deformed purely by bending and the structure was able to retain its effective stiffness and integrity (Figure 3.3). This deformation mechanism corresponds to the linear elastic region of the stress-strain graph (Figure 3.4). As the applied strains exceeded the effective strength of the cell, the vertical struts began to buckle, thereby causing a drastic reduction in the stiffness. Simultaneously, the stress in the struts exceeded the elastic limit and yielding was also initiated. This corresponds to the plateau region in the stress-strain graph. Typical experimental results of porous materials, e.g., foam, reveal a third regime of deformation, namely the densification/compaction region, where cell struts come into contact with each other and thus exponentially increase the stiffness of the material; however, due to computational difficulties associated with mesh distortions and contact algorithms, our simulations did not reach this region.

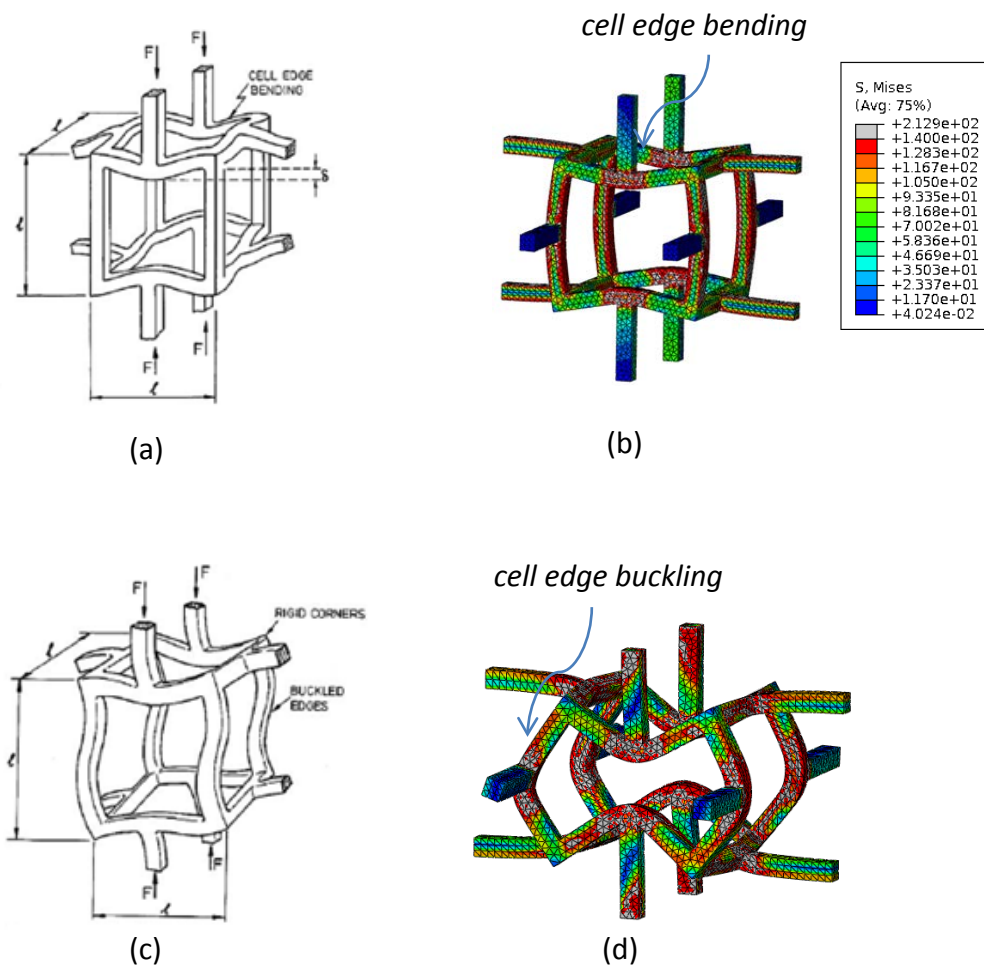
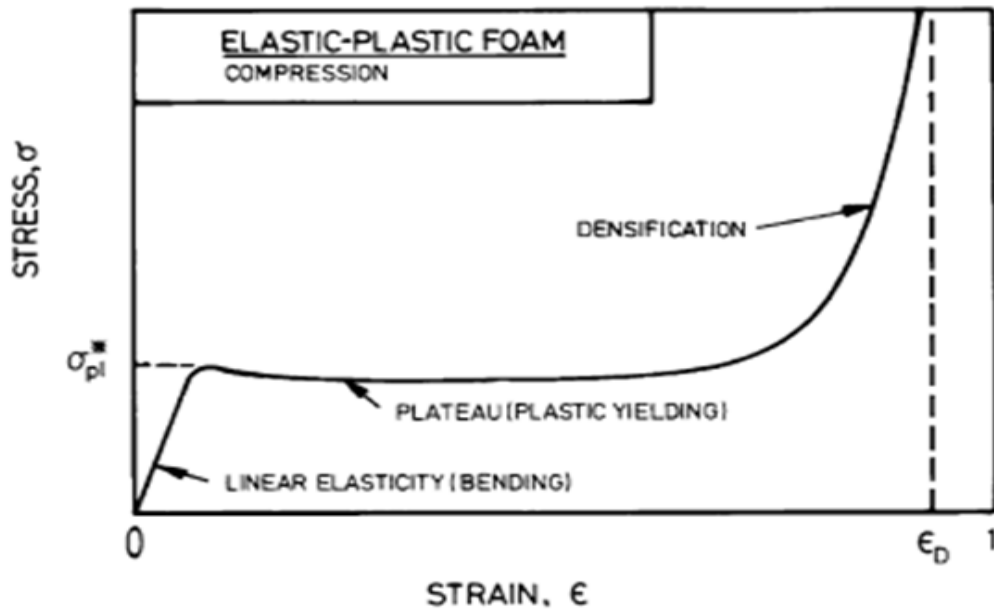
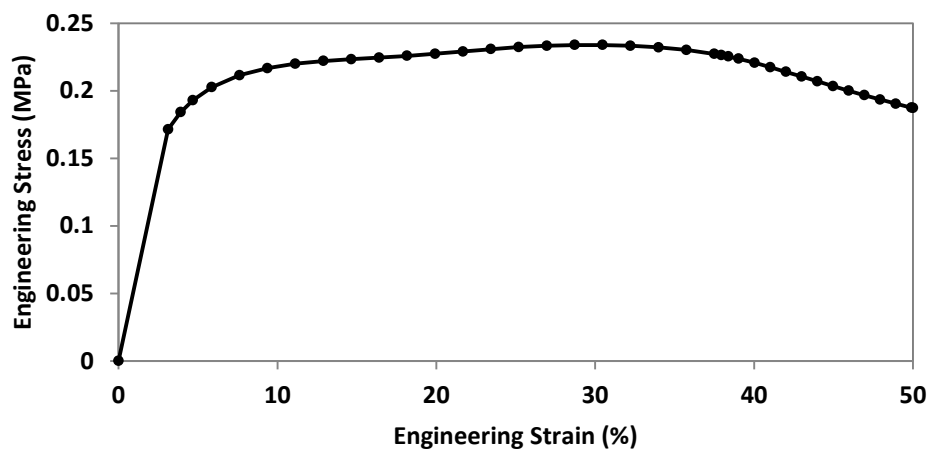


**Figure 3.3** (a) Schematic showing cell struts bending, (b) Our FE simulation showing cell struts bending, occurring at  $\epsilon_y = 7.6\%$ , (c) Schematic showing cell struts buckling, (d) Our FE simulations showing cell struts buckling, occurring at  $\epsilon_y = 29\%$ . The contour plots in (b) and (d) represent von Mises' stresses in MPa. Images (a) and (c) are from [127].



(a)



(b)

Figure 3.4 (a) Schematic of stress vs. strain showing the primary deformation regimes for an elastoplastic foam in compression [47, 127], and (b) Our FE simulation results for the Gibson-Ashby cell of  $V_f = 2.1\%$ , showing a similar deformation path

At higher values of  $V_f$ , i.e., as the struts became thicker, they began to yield directly without suffering buckling (Figure 3.5). For each of the unit cells, the effective stiffness was computed as the ratio of the engineering stress to the engineering strain at the first successfully converged load increment of the FE simulation. Figure 3.6 shows a graph of the effective stiffness thus calculated against the corresponding  $V_f$  of the unit cell using a power-law fit.

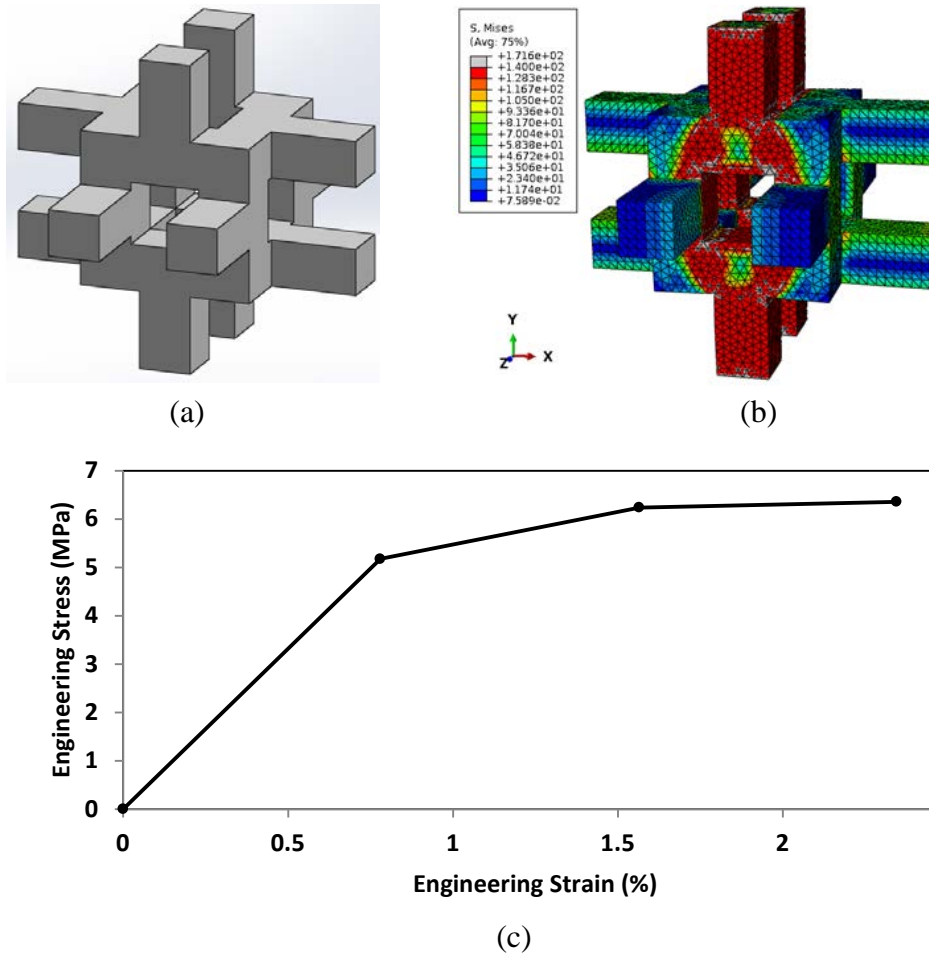


Figure 3.5 (a) CAD model showing Gibson-Ashby unit cell of  $V_f = 14.9\%$ , (b) Stress contour plots showing lack of strut buckling, (c) Graph of engineering stress vs. engineering strain for the same cell

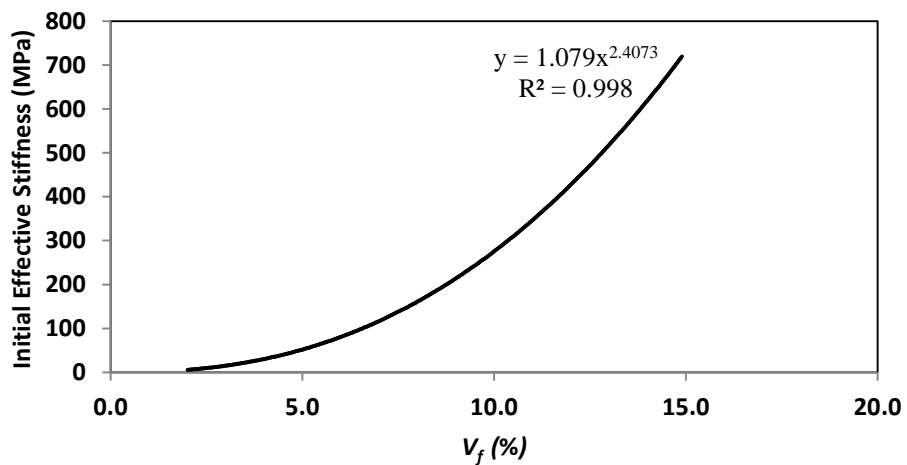


Figure 3.6 Graph of effective stiffness values vs.  $V_f$  for the Gibson-Ashby model, fitted using a power-law equation

### 3.1.3 Morphological properties of the model

#### 3.1.3.1 Structure Model Index (SMI)

The Structure Model Index (SMI) provides a measure of the aspect ratio of the trabecular struts, i.e., whether they are predominantly rod-like (SMI = 3), or plate-like (SMI = 0). Based on [57], the SMI is calculated as:

$$SMI = \frac{6 \left( BV \cdot \left( \frac{dS}{dr} \right) \right)}{BS^2} \quad (3.1)$$

where  $BV$  denotes the volume of bone material in the structure,  $BS$  is the total surface area of bone, and  $dS/dr$  is the change of surface area  $S$  with the half-thickness,  $r$ .

In order to calculate the SMI of the Gibson-Ashby model, a single strut was considered, with the dimensions shown below:

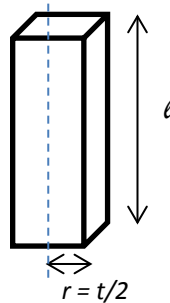


**Figure 3.7** Schematic showing a single strut of the Gibson-Ashby cell

The surface area of the strut is calculated as:

$$S = (2r \times l) \times 4 \quad (3.2)$$

implying that the change in surface area with half-thickness is

$$\frac{dS}{dr} = 8l \quad (3.3)$$

Therefore, the SMI can be calculated for any values of  $r$  and  $l$  as:

$$SMI = \frac{6 \left( BV \cdot \left( \frac{dS}{dr} \right) \right)}{BS^2} = 6 \times \frac{[(2r)^2 \times l] \times 8l}{[(2r \times l) \times 4]^2} = 3.$$

Hence, the SMI for a Gibson-Ashby unit cell of any given  $V_f$  is constant and equal to 3 (i.e., the strut is perfectly rod-like).

### 3.1.3.2 Trabecular thickness ( $Tb.Th$ ):

For a perfectly rod-like cell, the trabecular thickness can be estimated by [128]:

$$Tb.Th = \frac{4}{\left( \frac{BS}{BV} \right)} \quad (3.4)$$

The CAD software SolidWorks was used to quantify the values of  $BS$  and  $BV$  for each unit cell and the results for the  $Tb.Th$  tabulated.

Volume Fraction ( $V_f$ ) (%)	$Tb.Th$ ( $\mu\text{m}$ )
2	98.6
7.4	204.8
14.9	314.8

**Table 3.1**  $Tb.Th$  values for Gibson-Ashby model of different volume fractions

### 3.1.3.3 Trabecular Separation/Spacing ( $Tb.Sp$ ):

The trabecular separation/spacing can be estimated for rod-like models by the equation [128]:

$$Tb.Sp = Tb.Dm \times \left( \sqrt{\frac{\pi}{4} \times \frac{TV}{BV}} - 1 \right) \quad (3.5)$$

where the trabecular diameter,  $Tb.Dm$ , can be approximated by  $Tb.Th$ . The values of  $Tb.Sp$  were calculated for the unit cells corresponding to each  $V_f$  and the results tabulated.

Volume Fraction ( $V_f$ ) (%)	$Tb.Sp$ ( $\mu\text{m}$ )
2	519.28
7.4	462.40
14.9	407.94

Table 3.2  $Tb.Sp$  values for Gibson-Ashby model of different volume fractions

## 3.2 The Kelvin cell (rod-type) model

### 3.2.1 Construction of the model

The input parameters used in the construction of the rod-type Kelvin cell are the thickness  $t$  and the length  $l$  of each strut. Varying the values of these parameters results in unit cells of differing  $V_f$ , based on the equation [52]:

$$V_f = \frac{33\pi}{80\sqrt{2}} \left(\frac{t}{l}\right)^2 \quad (3.6)$$

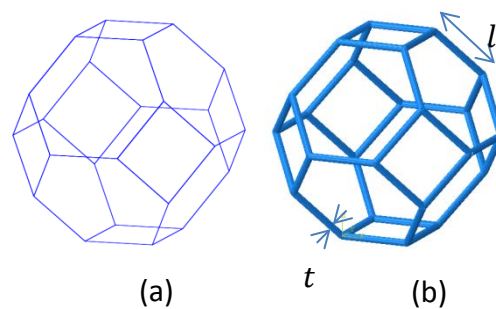


Figure 3.8 (a) Schematic of the rod-type Kelvin cell showing the eight hexagons and six quadrilaterals that constitute the tetrakaidecahedral structure (b) The rod-type Kelvin cell corresponding to  $t/l = 0.1$  after meshing the cell struts with beam elements



The CAD component of ABAQUS was used to plot the positions of the 24 nodes, which were then connected appropriately using “wires” to form the cell struts (Figure 3.8).

### 3.2.2 Mechanical properties of the model

The struts were then meshed in ABAQUS using quadratic beam elements of circular cross-section. Based on [80], a bilinear elasto-plastic material was used to model the material in the cell struts, with Young’s modulus,  $E = 18 \text{ GPa}$ , post-yield modulus of 5% of  $E$ , and a 0.2% offset yield strain of 1.04%. While holding all the degrees of freedom of the bottom face fully constrained, a downward (i.e., compressive) displacement was applied to the four nodes on the top face to simulate uniaxial stress. Similar analyses were performed for unit cells corresponding to different ratios of  $t/l$ .

Subsequent to the simulation, the graphs of homogenized engineering stress were plotted against the homogenized strains for each of the cells. The plot below (Figure 3.9) (corresponding to  $t/l = 0.1$ ) shows a linear elastic region caused by cell strut bending, followed by softening behaviour at about 10% strain, due to strut buckling.

For each of the unit cells, the effective stiffness was then computed as the ratio of the engineering stress to the engineering strain at the first successfully converged load increment of the FE simulation. Figure 3.10 shows a graph of the effective stiffness thus calculated against the corresponding  $t/l$  ratio of the unit cell using a power-law fit.

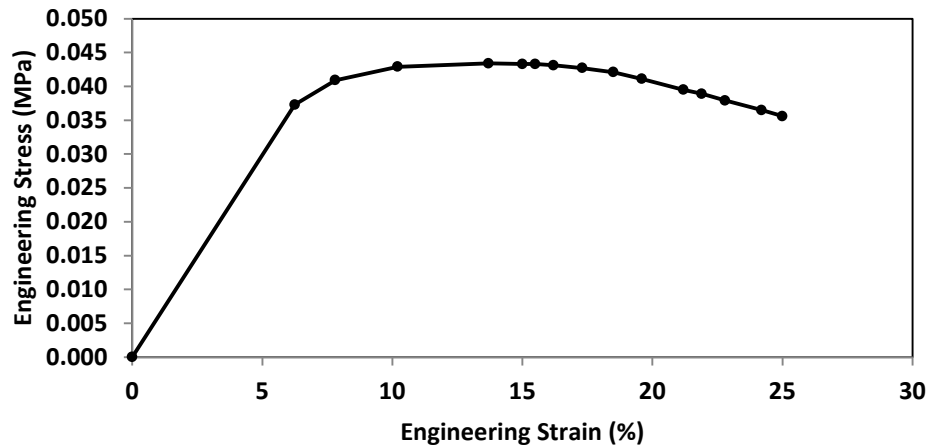


Figure 3.9 Graph of engineering stress vs. engineering strain for the Kelvin (rod-type) cell corresponding to  $t/l = 0.1$ .

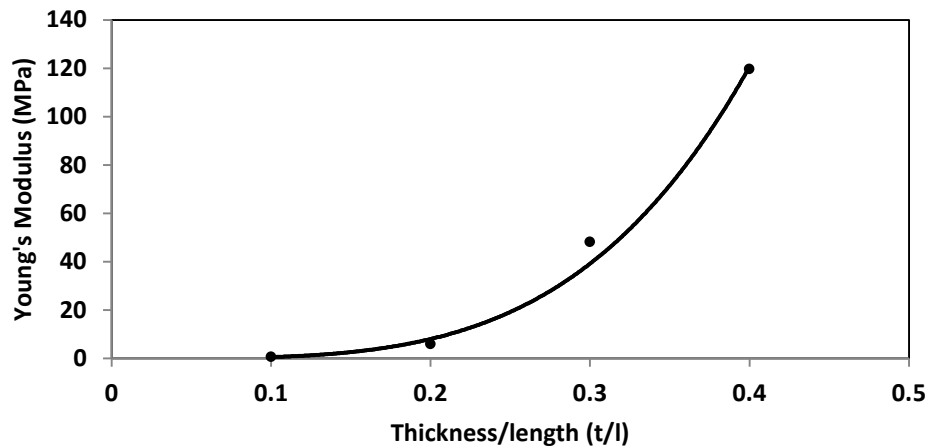


Figure 3.10 Graph of effective Young's modulus vs. thickness-to-length ratio for the Kelvin (rod-type) cell with a power-law fit

### 3.2.3 Morphological properties of the model

#### 3.2.3.1 Structure Model Index (SMI)

Based on [57], the SMI is given by equation (3.1):

$$SMI = \frac{6 \left( BV \cdot \left( \frac{dS}{dr} \right) \right)}{BS^2} \quad (3.1)$$

where  $BV$  denotes the volume of bone material in the unit cell,  $BS$  is the total surface area of bone, and  $dS/dr$  is the change of surface area  $S$  with the half-thickness,  $r$ .

In order to calculate the SMI of the rod-type Kelvin cell, a single strut was considered, with the dimensions shown below:

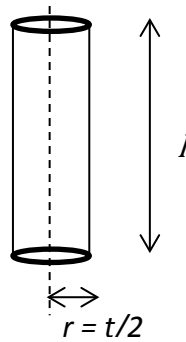


**Figure 3.11 Schematic showing a single strut of the Kelvin (rod-type) cell**

The surface area of the strut is calculated as:

$$S = (2\pi r) \times l \quad (3.7)$$

implying that the change in surface area with half-thickness is:

$$\frac{dS}{dr} = 2\pi l \quad (3.8)$$

Therefore, the SMI can be calculated for any values of  $r$  and  $l$  as:

$$SMI = \frac{6 \left( BV \cdot \left( \frac{dS}{dr} \right) \right)}{BS^2} = 6 \times \frac{[(\pi r^2 \times l) \times 2\pi l]}{[2\pi r \times l]^2} = 3.$$

Hence, the SMI for a rod-like Kelvin cell of any given  $V_f$  is constant and equal to 3 (i.e., the strut is perfectly rod-like).

### 3.2.3.2 Trabecular thickness (*Tb.Th*):

For a perfectly rod-like cell, the trabecular thickness can be estimated by equation (3.4):

$$Tb.Th = \frac{4}{\left(\frac{BS}{BV}\right)} \quad (3.4)$$

The values of *Tb.Th* for unit cells of different  $V_f$  are tabulated below.

Volume Fraction ( $V_f$ ) (%)	<i>Tb.Th</i> ( $\mu\text{m}$ )
0.92	100
3.66	200
8.24	300
14.65	400

**Table 3.3 *Tb.Th* values for Kelvin (rod-type) model of different volume fractions**

### 3.2.3.3 Trabecular Separation/Spacing (*Tb.Sp*):

The trabecular separation/spacing can be estimated for rod-like models by equation (3.5):

$$Tb.Sp = Tb.Dm \times \left( \sqrt{\frac{\pi}{4} \times \frac{TV}{BV} - 1} \right) \quad (3.5)$$

where the trabecular diameter, *Tb.Dm*, can be approximated by *Tb.Th*. The values of *Tb.Sp* were calculated for the unit cells corresponding to each  $V_f$  and the results tabulated.

Volume Fraction ( $V_f$ ) (%)	$Tb.Sp$ ( $\mu\text{m}$ )
0.92	823.96
3.66	726.47
8.24	626.20
14.65	526.16

**Table 3.4**  $Tb.Sp$  values for Kelvin (rod-type) model of different volume fractions

### 3.3 The Kelvin cell (plate-type model)

#### 3.3.1 Construction of the model

The input parameters required in the construction of the plate-type Kelvin cell are the thickness,  $t$ , of each cell wall and the length,  $l$ , of each cell edge. Varying the values of these parameters results in unit cells of different differing  $V_f$ , based on the equation [52]:

$$V_f = \frac{3}{4} \sqrt{\frac{3}{2}} \left(\frac{t}{l}\right) \quad (3.9)$$

The cell edges produced by plotting the nodes given in Appendix 1 are connected to each other using shell elements in Abaqus CAE. In order to preserve the open-celled nature of trabecular bone, the quadrilateral cell faces are left open (Figure 3.12).

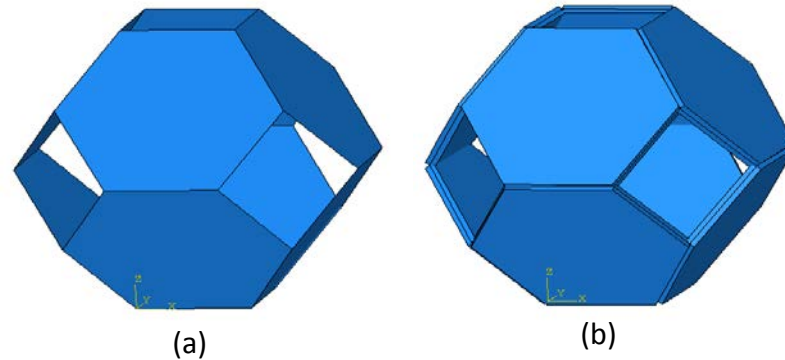


**Figure 3.12** (a) Schematic of the plate-type Kelvin cell showing the eight hexagons and six quadrilaterals that constitute the tetrakaidecahedral structure. Note the absence of cell walls on the quadrilateral faces. (b) The plate-type Kelvin cell corresponding to  $t/l = 0.1$  after replacing the cell walls with quadratic shell elements of thickness  $t$

### 3.3.2 Mechanical properties of the model

The cell walls were meshed in ABAQUS using quadratic shell. Based on [80], a bilinear elastoplastic material was used to model the material in the cell walls, with Young's modulus,  $E = 18 \text{ GPa}$ , post-yield modulus of 5% of  $E$ , and a 0.2% offset yield strain of 1.04%. While holding all the degrees of freedom of the bottom face fully constrained, a downward (i.e., compressive) displacement was applied to the four nodes on the top face. Similar analyses were performed for unit cells corresponding to different ratios of  $t/l$ .

Subsequent to the simulation, the graphs of homogenized engineering stress were plotted against the homogenized strains for each of the cells. The plot below (Figure 3.13) (corresponding to  $t/l = 0.1$ ) shows a linear elastic region caused by cell wall bending, followed by a drastic decrease in tangent stiffness at about 3% strain due to the onset of plastic collapse, leading to softening behaviour at about 10% strain.

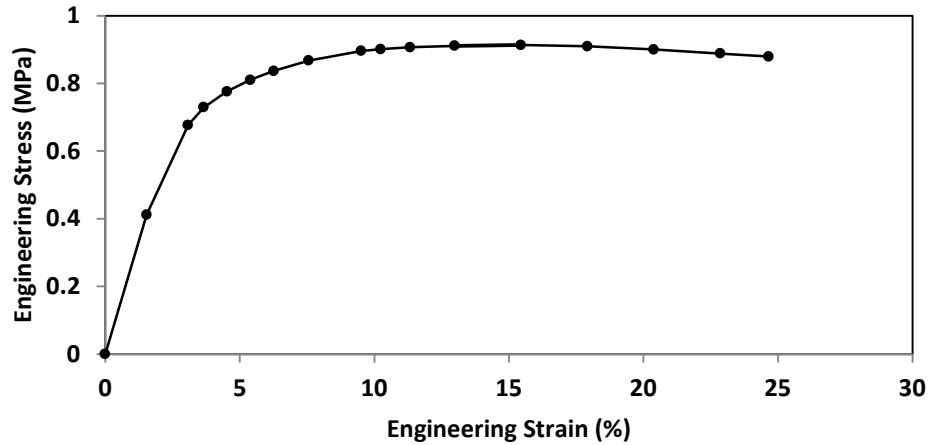


Figure 3.13 Graph of engineering stress vs. engineering strain for the Kelvin (plate-type) cell corresponding to  $t/l = 0.1$

For each of the unit cells, the effective stiffness was then computed as the ratio of the engineering stress to the engineering strain at the first successfully converged load increment of the FE simulation. Figure 3.14 shows a graph of the effective stiffness thus calculated against the corresponding  $t/l$  ratio of the unit cell using a power-law fit.

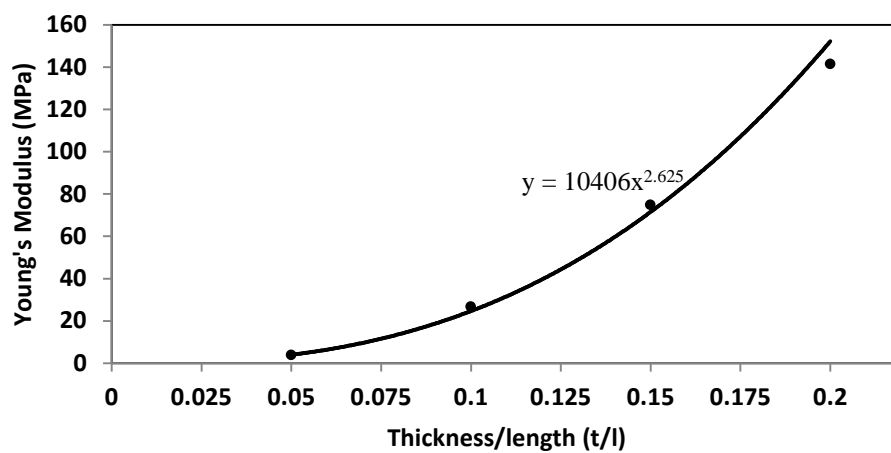


Figure 3.14 Graph of effective Young's modulus vs. thickness-to-length ratio for the Kelvin (plate-type) cell with a power law fit

### 3.3.3 Morphological properties of the model

#### 3.3.3.1 Structure Model Index (SMI)

Based on [57], the SMI is calculated by equation (3.1):

$$SMI = \frac{6 \left( BV \cdot \left( \frac{dS}{dr} \right) \right)}{BS^2} \quad (3.1)$$

where  $BV$  denotes the volume of bone material in the unit cell,  $BS$  is the total surface area of bone, and  $dS/dr$  is the change of surface area  $S$  with the half-thickness,  $r$ .

In order to calculate the SMI of the plate-type Kelvin cell, a single wall was considered, with the dimensions shown below:

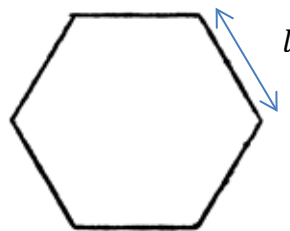


**Figure 3.15** Schematic showing a single face of the Kelvin (plate-type) cell

The surface area of the wall is calculated as:

$$S = \frac{3\sqrt{3}}{2} l^2 \quad (3.10)$$

implying that the change in surface area with half-thickness  $r$  is zero:

$$\frac{dS}{dr} = 0 \quad (3.11)$$

Therefore, the SMI can be calculated for any values of  $r$  and  $l$  as:



$$SMI = \frac{6 \left( BV \cdot \left( \frac{dS}{dr} \right) \right)}{BS^2} = 6 \times \frac{[BV \times 0]}{BS^2} = 0.$$

Hence, the SMI for a plate-like Kelvin cell of any given  $V_f$  is constant and equal to 0 (i.e., the wall is perfectly plate-like).

### 3.3.3.2 Trabecular thickness ( $Tb.Th$ ):

For a perfectly plate-like cell, the trabecular thickness can be estimated by [128]:

$$Tb.Th = \frac{2}{\left( \frac{BS}{BV} \right)} \quad (3.12)$$

The table below shows the relationship between  $Tb.Th$  and  $V_f$ . Note that since the volume fraction depends only on the ratio  $t/l$ , and not on the exact value ascribed to  $t$ , we are free to set  $Tb.Th$  to any value provided  $l$  is modified accordingly. Exact values can be determined for  $Tb.Th$  (and correspondingly for  $Tb.Sp$ ) simply by choosing a value for  $l$ .

Volume Fraction ( $V_f$ ) (%)	$Tb.Th$ ( $\mu\text{m}$ )
4.593	$0.05l$
9.186	$0.10l$
13.779	$0.15l$
18.372	$0.20l$

**Table 3.5  $Tb.Th$  values for Kelvin (plate-type) model of different volume fractions**

### 3.3.3.3 Trabecular Separation/Spacing (Tb.Sp):

The trabecular separation/spacing can be estimated for plate-like models by the equation [128]:

$$Tb.Sp = \frac{1}{Tb.N} - Tb.Th \quad (3.13)$$

where, for plate-like models, the trabecular number,  $Tb.N$  is approximated by:

$$Tb.N = \frac{\frac{BV}{TV}}{Tb.Th} \quad (3.14)$$

The values of  $Tb.Sp$  were calculated for the unit cells corresponding to each  $V_f$  and the results tabulated.

Volume Fraction ( $V_f$ ) (%)	$Tb.Sp$ ( $\mu m$ )
4.593	1.0386l
9.186	0.9886l
13.779	0.9386l
18.372	0.8886l

**Table 3.6  $Tb.Sp$  values for Kelvin (plate-type) model of different volume fractions**

## 3.4 Discussion and Conclusion

Figure 3.16 below shows the effective stiffness vs. the apparent density for all of the models (i.e., the Gibson-Ashby cell, and both the rod-type and the plate-type variants of the Kelvin cell) described above, as well as the gyroid-based model, superposed onto a graph extracted from the published literature [5] on real trabecular bone, for the purpose of comparison. It can be seen that the graphs for all three models lie very close to those obtained by empirical tests on real trabecular bone.

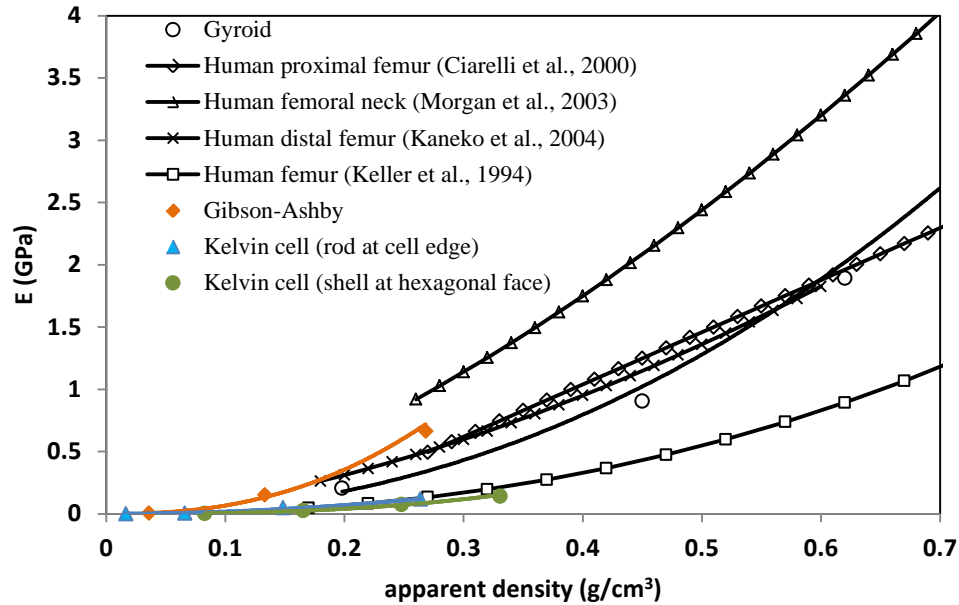


**Figure 3.16** Graph showing effective initial stiffness vs. the apparent density for the three unit cells and the gyroid-based structure, superposed on published empirical data from the human femur [5]

Furthermore, histomorphometric analysis revealed that their morphologies are also reasonably close to those encountered in the literature on human trabecular bone [129]. Hence, with certain important reservations that we shall discuss presently, it is apparent that all three models can act as good morphological models for human trabecular bone.

The limitations of the above-described models are the following:

- (a) Though the mechanical properties (i.e., the effective stiffness) of all models closely approximate those of real trabecular bone for low apparent densities, the models lose their resemblance to trabecular bone at higher apparent densities. In the case of the Gibson-Ashby model, the unit cell becomes closed at volume fractions in excess of about 20% because the cell struts on either end of the face begin to touch each other. Since real trabecular bone is open-celled, it implies that the Gibson-Ashby cell is a poor

representative of high density trabecular bone. In the case of the Kelvin cell, the use of beam and shell elements to render the struts and faces of the model is appropriate only for thin beams and shells, implying that this structure also runs into computational difficulties at higher apparent densities.

The gyroid model, on the other hand, as described in Chapter 2, is capable of rendering unit cells up in excess of even 80% volume fraction before it becomes a closed cell. Since real human trabecular bone possesses a wide range of volume fraction [12], the gyroid is considered to be a better model for trabecular bone than the other models explored above.

(b) From the point of view of morphology, there exists a fundamental advantage of the gyroid unit cell over the others studied above. The SMI values for the gyroid unit cell change automatically with volume fraction, from more rod-like at low volume fraction to more plate-like at high volume fraction (Chapter 2). In contradistinction, the SMI values for the other models investigated do not vary with volume fraction: the SMI values of the Gibson-Ashby model and the rod-like variant of the Kelvin cell remain constant at 3 (perfectly rod-like), whereas, for the plate-like variant of the Kelvin cell, they remain constant at 0 (perfectly plate-like) (Figure 3.17)

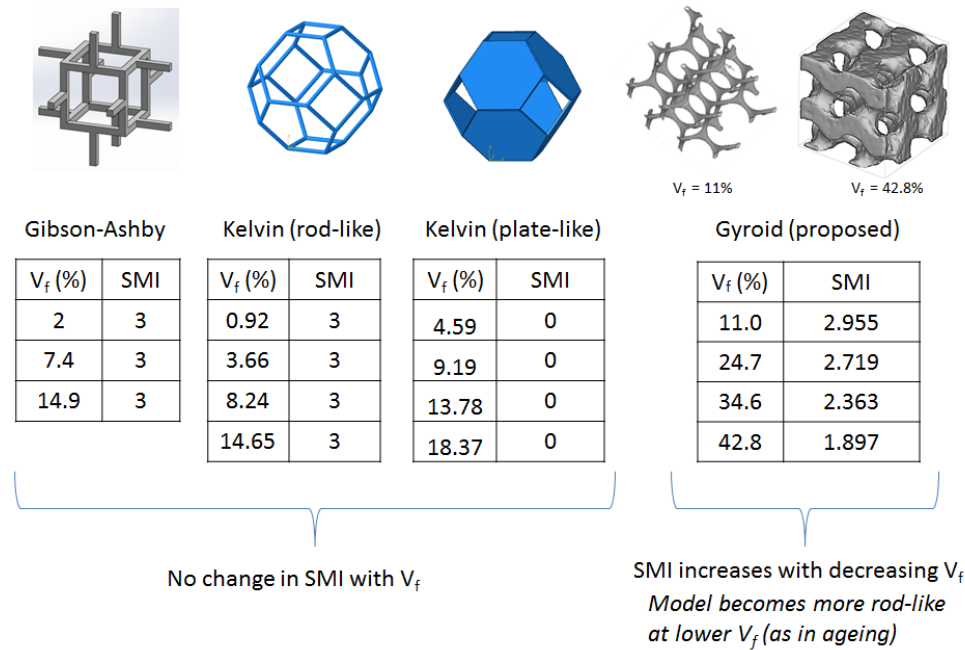


**Figure 3.17** Summary of changes in SMI with changing volume fraction for each of the models

For real trabecular bone, it is well-known that at high volume fractions (e.g., in young healthy subjects), the trabecular spicules are more plate-like, and that, with bone loss through ageing or osteoporosis, they gradually become more rod-like [129, 130]. The gyroid unit cell is thus seen to better capture the changing morphology of trabecular bone struts with change in volume fraction.

(c) Lastly, it is computationally very difficult to assemble the CAD-based unit cells (i.e., those that are constructed using CAD software) like the Gibson-Ashby and the Kelvin cell; to do so, it is necessary to first construct one unit cell, then produce a sufficient number of correctly positioned replicas, and subsequently assemble them to produce one continuous solid structure. This task of assembling unit cells is significantly easier to perform using the equation-based modelling technique employed in generating the gyroid unit cell: if one is interested in modelling a larger domain of, say, 100 x 100 x 100

gyroid unit cells, all one needs to do is to expand the domain boundary in the gyroid equation (i.e., the bounds of  $x$ ,  $y$ , and  $z$ ; see Chapter 2) and re-run the algorithm.

Furthermore, the method for assembling CAD-based unit cells outlined above produces macrostructures of homogeneous apparent density. If it is desired to perform multi-scale modelling of organ-level bone structures, it is necessary to be able to vary the apparent density of the unit cells at adjacent locations based on corresponding variations in the macro-scale bone. This task can be easily performed in equation-based unit cells like the gyroid, as described in detail in Chapter 6 below, by simply modifying the parameter that determines the volume fraction to be a function of the anatomic location.

*In fine*, having compared some representative unit cells previously described in the literature against our proposed unit cell based on the gyroid surface, we conclude that the gyroid-based unit cell provides us with a superior model for human trabecular bone that can be of potential use in applications of current interest including multi-scale modelling of bone and investigating the interactions between mechanical behaviour at different levels of hierarchy

## **Chapter 4. Assessment of two novel methods for modelling bone**

In this chapter, we describe two novel methods for modelling bone. In the first method (Section 4.1), Voronoi tessellation is employed to generate trabecular struts that are then connected to the outer cortical ring to form a structure that resembles the femoral neck cross-section in geometry and bone density distribution. This structure can then be analysed using the Finite Strip Method (FSM), a computationally cheaper alternative to the Finite Element Method (FEM), in order to assess its mechanical behaviour under loading. In the second method (Section 4.2), we investigate a unit cell for trabecular bone based on a so-called ellipsoid-cuboid structure created by deleting the volumes of intersection between a cuboid and nine ellipsoids, eight of the latter of which are located at the vertices of the cuboid and one at its centre.

### **4.1 Voronoi tessellation for modelling the femoral neck**

#### **4.1.1 Introduction**

The finite strip method (FSM) is a computationally cheaper alternative to the FE method. The fundamental assumption underlying the FSM is the homogeneity of material properties along the longitudinal direction [131]. This engenders a trade-off between accuracy and computational speed. The FSM-based models hitherto published considered only the cortical component of the femoral neck [132]. The emphasis of the study described in this subsection was to develop more realistic models which incorporate the contribution of the trabecular core to the overall structural strength of the femoral neck. To that effect, we developed an algorithm based on two-dimensional Voronoi tessellation to generate trabecular networks whose apparent density was

determined from an underlying CT scan of the femoral neck. We believed that such a model would be a better computational representative of naturally occurring bone than those commonly seen in the published literature wherein the density is assumed homogeneous.

#### **4.1.2 Modeling algorithm**

##### **4.1.2.1 Source of specimens and image acquisition procedure**

The femur specimens were from the Institute of Anatomy at the Ludwig Maximilians Universität München, Munich, Germany. The subjects (8 females, 7 males, age range: 50–60 years) were residents of “Upper Bavaria” who had donated their bodies for teaching and research purposes to the Institute during their lifetime per testimonial decree.

A Siemens 16-slice helical CT scanner with a scan-plane pixel size of 0.195 mm and a slice thickness of 0.5 mm was used (Sensation 16; Siemens Medical Solutions, Erlangen, Germany). The specimens were placed in plastic bags filled with 4% formalin–water solution. The plastic bags were sealed after air was removed by a vacuum pump. These bags were positioned in the scanner with mild internal rotation of the femur to simulate in vivo examination of the pelvis and proximal femur. Further scanning parameters were 120 kVp, 100 mA, an image matrix of 512×512 pixels and a field of view of 100 mm. From a high-resolution reconstruction algorithm (kernel U70u) resulted an in-plane spatial resolution of  $0.29 \times 0.29 \text{ mm}^2$ , determined at  $\rho=10\%$  of the modulation transfer function. Voxel size was  $0.19 \times 0.19 \times 0.5 \text{ mm}^3$ . For calibration purposes, a reference phantom with a



bone-like and a water-like phase (Osteo Phantom, Siemens Medical Solutions) was placed in the scanner below the specimens.

#### **4.1.2.2 Image analysis procedure**

Sequential cross-sectional images of the human femoral neck were extracted from three-dimensional CT data sets of the 15 subjects using MIMICS software (Materialise Inc., Ann Arbor, MI, USA). The cross section with the lowest area moment of inertia ( $I$ ) along the femoral neck of each subject was selected using the open source packages of VA-BATTS (a software primarily used to find stresses in bone cross-sections) [133, 134] and CUFSM (a software employed in structural engineering to investigate the buckling loads of various structures using the FSM assumption) [135]. Specifically, VA-BATTS software was used to generate a surface mesh for about 10 slices at a location along the femoral neck where the cross-sectional area is generally smallest. The surface mesh was then imported into CUFSM software. The CUFSM software is capable of analyzing the geometry (e.g., surface area, location of center of area, and area moment of inertia) of a structure. Of the 10 slices analyzed, the slice that possessed the lowest  $I$  about the anterior-posterior axes is chosen as the representative slice for that subject, to be used for subsequent analyses.

#### **4.1.2.3 Cortical shell modelling**

For each specimen, the cortical shell was segmented from the soft tissue using the built-in edge detection algorithm of 'ImageJ' software [112]. The "donut" mesh scheme of VABATTS was used to model the cortical shell (Figure 4.1). The donut mesh is designed to discretize the domains of hollow cross-sections

and is therefore most appropriate for the cortical ring. Based on the suggestions of [132], we chose a mesh density of 72 circumferential elements and 7 radial elements as suitable for our purposes. After the mesh is successfully generated, VABATTS software can be used to output the nodal coordinates and element connectivity data to be used as input parameters in the open-source FSM software, CUFSM [135].

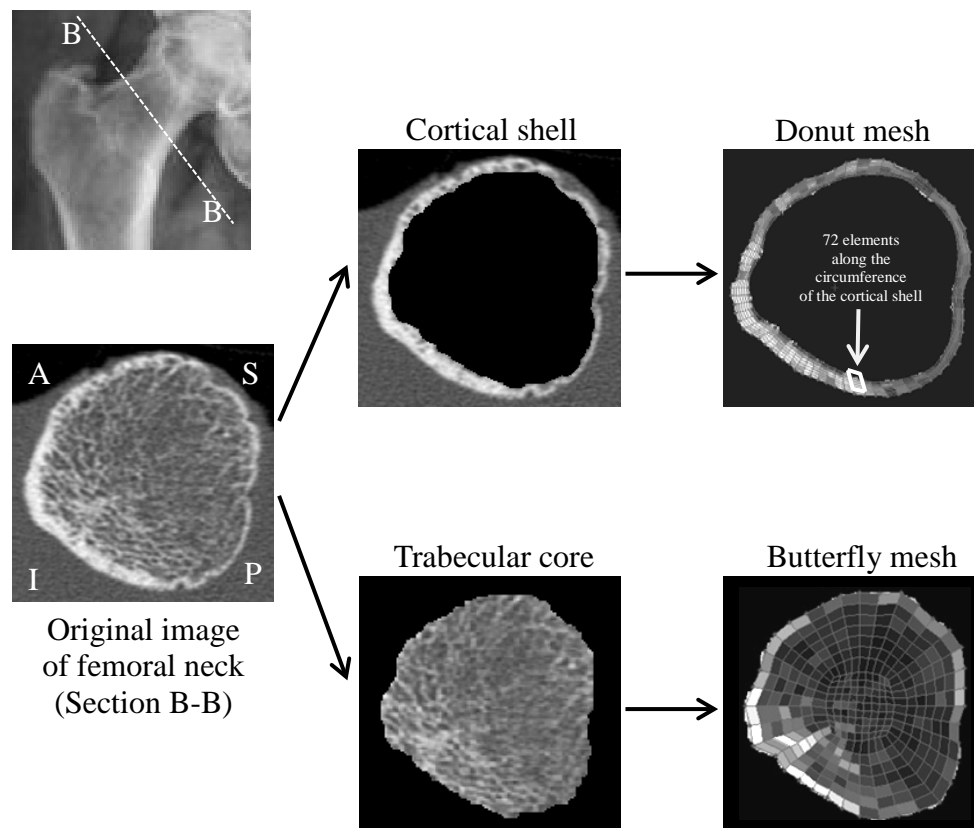


**Figure 4.1 Segmentation of the femoral neck CT image into cortical and trabecular bone using VA-BATTS meshing tool**

#### 4.1.2.4 Trabecular core modelling using Voronoi tessellation

In our model, a trabecular cell denotes a two-dimensional element within the “butterfly” mesh of the VA-BATTS software [133]. This mesh helps to discretize the trabecular core into a set of two dimensional elements for further

processing. VA-BATTS software is capable of reading the pixel densities and computing the average pixel density for the group of pixels that constitute a trabecular cell (Figure 4.1). The average CT number (i.e., the average pixel density) of each trabecular cell, and its corresponding centroidal coordinates and area, were computed using VA-BATTS [133, 134]. Although VA-BATTS can be used to apply boundary conditions and analyze stresses, we utilized it purely for mesh generation and calculation of image-related parameters (e.g., CT-number and centroidal coordinates).

In order to simulate a trabecular network in the computational model, we employed MATLAB (MathWorks Inc., USA) to perform a technique known as Voronoi tessellation (also called Dirichlet tessellation) [136]. Essentially, given a set  $S$  of points  $s$  (called the Voronoi generators or Voronoi sites) on a plane, a Voronoi cell  $V(s)$  for point  $s$  comprises the set of all points closer to generator  $s$  than to any other generator. The edges of each Voronoi cell  $V(s)$  are therefore a set of points that are equidistant to the two nearest generators. A Voronoi node is a point that is equidistant to three or more generators.

During the creation of our model, Voronoi generators (or sites) were locally cast into each trabecular cell according to a proportional relationship, such that trabecular cells with greater CT-numbers contained more Voronoi generators than trabecular cells with lower CT-numbers. The locations of these Voronoi generators were then extracted and used for Voronoi tessellation in MATLAB. MATLAB supports a built-in function for two-dimensional Voronoi tessellation called `VORONOI(x,y)`, where  $(x,y)$  are the planar coordinates of each generator. At the end of the tessellation process, each of the edges of the Voronoi cells depicted an individual trabecular rod. The elemental

connectivity data can subsequently be exported from VA-BATTS into CUFSM software for further structural analysis. This technique enabled us to create a model which had a denser trabecular network in regions where the CT-scan had higher CT-numbers, and vice versa (Figure 4.2).

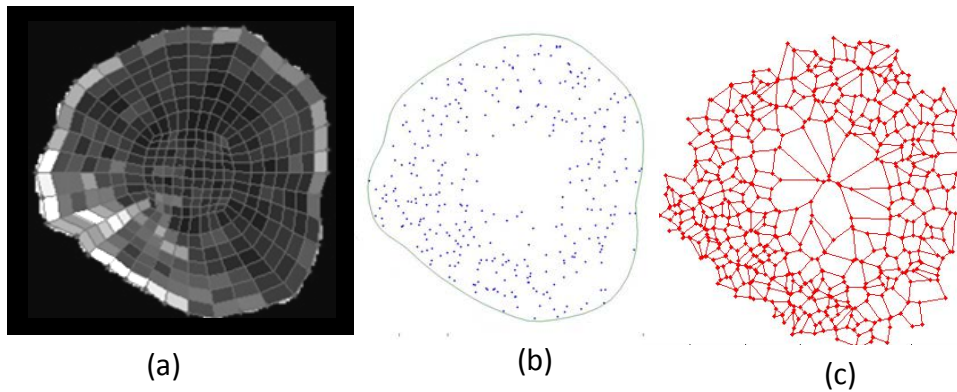


**Figure 4.2 (a) Butterfly mesh of trabecular core (b) Voronoi generators distributed based on the trabecular core apparent density (c) Trabecular core after Voronoi tessellation**

The trabecular thickness ( $Tb.Th$ ), which corresponds to the thicknesses of the edges of the Voronoi cells, was tuned so that the area fraction of the Voronoi cell matched the volume fraction ( $BV/TV$ ) of the same Voronoi cell as calculated from VA-BATTS. The area fraction in this work was defined as the fraction of the total area of the polygon that was occupied by trabecular bone. Hence, an extrusion of a given area fraction by a given length would result in an identical volume fraction, thereby justifying the procedure described above. The nodes on the outermost ring of the trabecular network were connected to the nearest nodes on the cortical shell. These conditions successfully mimicked the primary mechanical function of the trabecular core (to provide lateral support to the cortex).

### 4.1.3 Discussion and Conclusions

The Voronoi tessellation algorithm employed in this subsection was seen to produce trabecular networks that closely resembled the original CT scan in their density distribution (Figure 4.3).

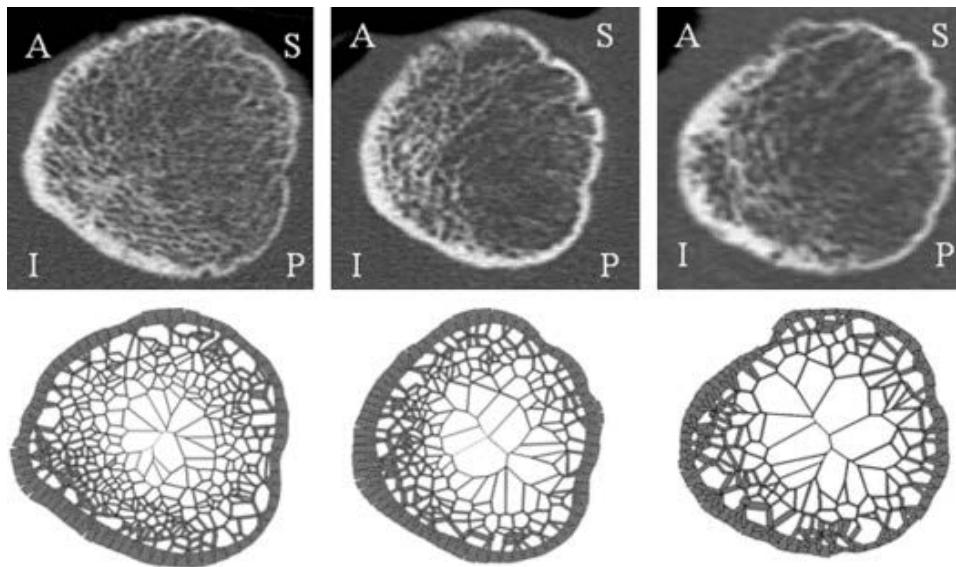


**Figure 4.3** Typical femoral neck cross-sections of three subjects (Top row: original CT image. Bottom row: computational model rendered using proposed method). A: Anterior; I: Inferior; S: Superior; P: Posterior

However, the models generated are two-dimensional structures, implying that their material properties and geometry are assumed to be homogeneous and constant in the longitudinal section. On a related note, the FSM, although computationally very fast, has a critical limitation with respect to the more standard FEM, because it does not account for longitudinal variations in geometry or material properties. In other words, it assumes that the cortical and trabecular geometry and material properties are two-dimensional measures and that they do not vary through the length of the femoral neck, an assumption not valid in real bone (Figure 4.4).

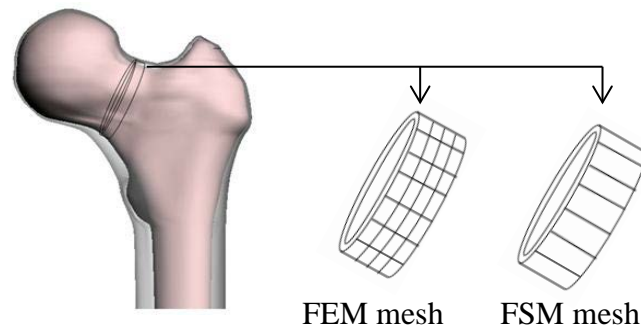


**Figure 4.4 Schematic showing the difference between the FEM mesh and the FSM mesh**

In the light of these observations, it is recommended that the above-described technique for modelling bone, employing two-dimensional Voronoi cells alongside the finite-strip method, be reserved only for investigations where computational speed is to be prioritized at the expense of accuracy.

## **4.2 The ellipsoid-cuboid unit cell as a model for trabecular bone**

### **4.2.1 Introduction**

The work described in this section was performed by Lim [137]. We reproduce her work below, with some emendations, for the purpose of comparing the results with our own modelling algorithms.

The ellipsoid-cuboid structure, originally conceived as a unit cell to study metallic foams, was extended to modelling trabecular bone owing to the fact that both are cellular solids with open cells and a wide range of volume fraction variability. The unit cell characterizes the main structural features of the trabecular architecture, and can be replicated periodically in space to form a matrix that resembles bulk trabecular bone.

## 4.2.2 Generation of the ellipsoid-cuboid unit cell

### 4.2.2.1 Basic structure

The CAD modelling software SolidWorks was used to design the geometry of the ellipsoid-cuboid structure based on several input parameters. An ellipsoid is placed at each corner of a solid cuboid, with the centers of the former coinciding with the vertices of the latter. An additional ellipsoid is placed at the geometric center of the cuboid, following which, the portions of the ellipsoids that intersect with the cuboid are deleted from the latter. This leaves behind a unit cell with a network of struts that resembles the interconnected rods and plates of the trabecular bone structure (Figure 4.5).

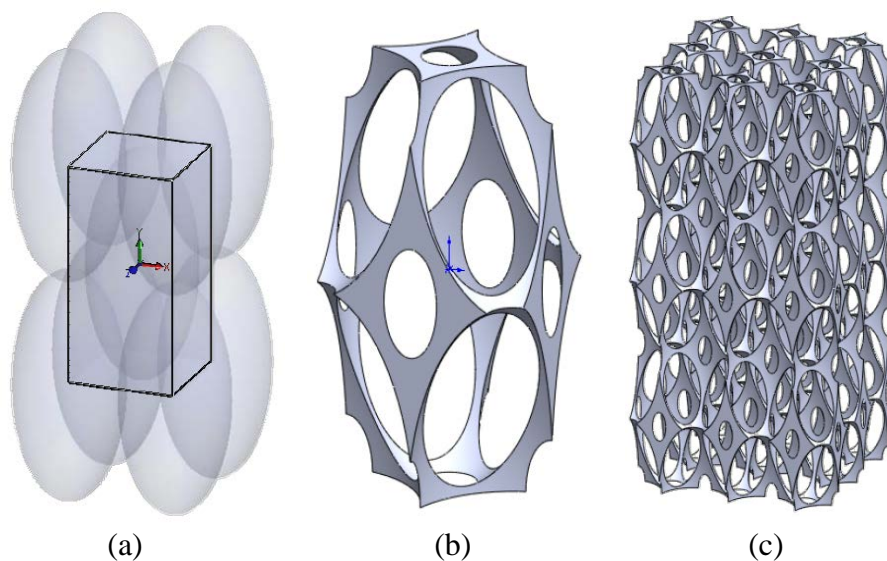


**Figure 4.5 (a) Illustration of the design of the ellipsoid-cuboid unit cell (the cuboid is outlined in black while the nine ellipsoids are in grey), (b) The ellipsoid-cuboid unit cell, (c) An assembly created by stacking 3x3x3 unit cells**

Before establishing the model, there was a need to first determine the physical dimensions of the unit cell to be used throughout the work. The foam model from which the ellipsoid-cuboid bone model is adapted had cross-sectional dimensions of 0.5 mm by 0.5 mm for the cuboid. These dimensions, together

with an aspect ratio of 1, were applied to form a 0.5 x 0.5 x 0.5 mm cube that was used to construct the initial bone model.

The maximum and minimum volume fractions for this initial model were determined, and then a similar model having an averaged volume fraction is created. With this model, the average cell strut thickness, an arithmetic average of the maximum and minimum thicknesses, was obtained (Figure 4.6). Next, the dimensions of the cube are scaled to produce a model in which the average cell strut thickness is similar to the average human trabecular thickness of 100 to 300 microns [1]. The resulting cube has cross-sectional dimensions of 3.5 x 3.5 mm, which are used for all the models throughout this work.

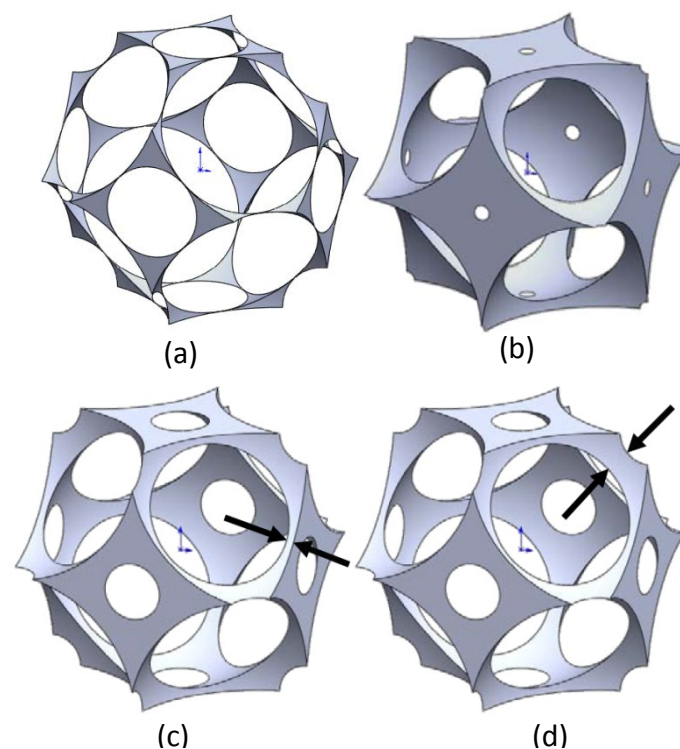


**Figure 4.6 (a) Minimum, and (b) maximum volume fraction of unit cell possible for given cube, (c) minimum, and (d) maximum strut thickness (shown between black arrows) for model with averaged volume fraction for the same cube**



With the basic ellipsoid-cuboid structure thus established, modelling trabecular bone of various apparent densities simply involved modifying the three ellipsoidal parameters, namely the semi-principal axes  $x$ ,  $y$  and  $z$  (Figure 4.7), to obtain models of different volume fractions. For the cuboid, since the transverse cross-section is a square, the aspect ratio,  $AR_c$ , is simply given by  $h/l$  or  $h/b$ . The aspect ratio for the ellipsoid,  $AR_e$ , is defined as  $y/reff$ , where  $reff$  is the radius of the circle that gives the same area as the ellipse on the  $x$ - $z$  plane.

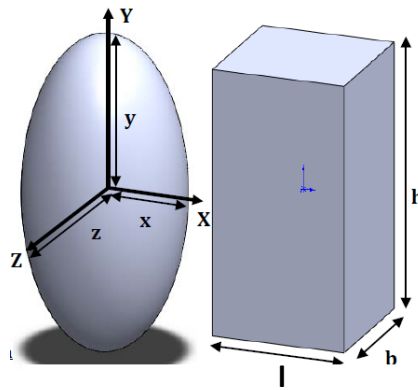


**Figure 4.7** Geometric parameters used to define the ellipsoid and the cuboid

The volume fraction for the resulting model,  $V_f$ , is given by the ratio of the remaining volume after deleting the intersecting material to the volume of the original cuboid. For each bone model, there exists a range of possible volume fractions between the minimum and maximum at which the trabecular-like structure is still distinguishable (Figure 4.8). Going above or below these bounds on the volume fraction will result in models that do not exhibit the overall trabecular structure. In such cases, the spaces in the walls of the unit cell may be missing resulting in closed cells, or the plates and rods of the structure are disconnected and unable to sustain any load. These models are hence unsuitable for simulation in the context of this work.

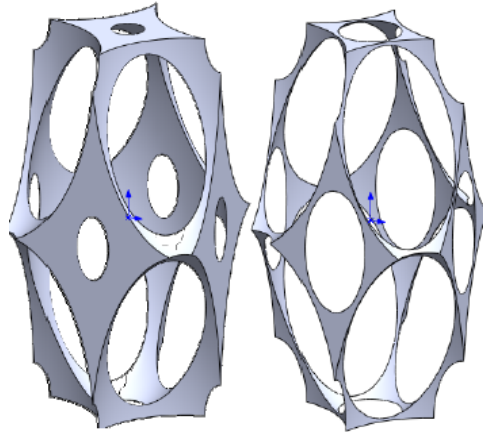


**Figure 4.8** Maximum (left) and minimum (right) volume fractions at which the trabecular-like model is still distinguishable

#### 4.2.2.2 Model 1: Using identical spheroids

Model 1 was created with all 9 ellipsoids having 2 of the 3 semi-principal axes identical, i.e.  $x = z$ . Ellipsoids possessing such a property are also known as spheroids. This model meant that the parameters of all the spheroids have to be varied in an identical manner at the same time. Since the model has to retain the overall trabecular bone geometry with the openings in the walls of the cuboid (Figure 4.9), the resulting values of  $V_f$  obtained were unrealistically small and were not useful for meaningful comparisons.

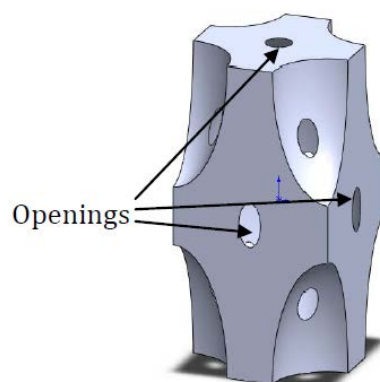


**Figure 4.9** The unit cell should include an opening in each of the walls to better resemble highly porous trabecular bone

#### **4.2.2.3 Model 2: Dissimilar spheroids at the cuboid vertices and center**

In order to obtain models with higher volume fraction while also retaining the desired trabecular bone geometry, dissimilar spheroids at the cuboid center and the cuboid vertices were used. This meant that the ellipsoidal parameters could be varied separately for those corner spheroids at the vertices and for the spheroid at the geometric center. This method gave rise to models with significantly higher volume fraction than before, which produced simulation results that are more meaningful than previous attempts using Model 1.

#### **4.2.2.4 Model 3: Dissimilar ellipsoids at the cuboid vertices and center**

Lastly, in an attempt to more accurately model trabecular bone, full ellipsoids with 3 distinct semi-principal axes are used. Again, dissimilar ellipsoids are used for the 8 vertices of the cuboid and for its geometric center.

### **4.2.3 Finite element analysis of the unit cells**

The models created were imported into Abaqus CAE, specified with trabecular bone tissue properties and appropriate boundary conditions, and then subjected to compression tests to study their mechanical behaviour. The material properties for the bone models were assumed to be purely linear-elastic and isotropic. The Young's modulus and Poisson's ratio of the bone tissue were assumed to be 18,000 MPa and 0.3 respectively [80]. In all simulations the effects of geometric nonlinearity, which can be particularly important for models with low volume fraction [20], were taken into account.

Periodic boundary conditions were applied so that the unit cell deformed similarly on opposite faces and could be replicated in space to form bulk trabecular bone. This was done by applying tie constraints between all pairs of

nodes located on opposite planar walls of the unit cell (Figure 4.10, (a) and (b)). All but the top and bottom walls were tied in this manner, and these tied walls deformed similarly, as desired, during the FE simulation.

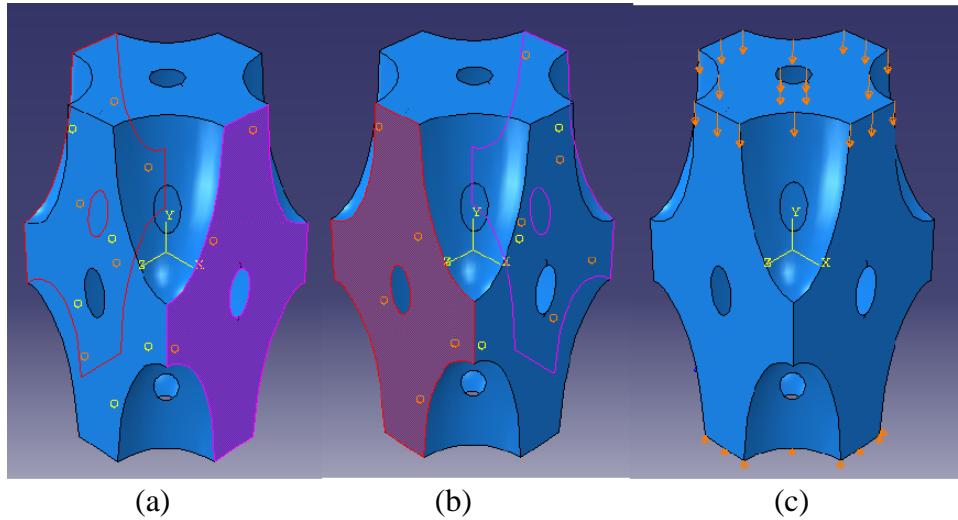


**Figure 4.10** Tie constrains applied between the shaded regions on the (a) left and the right, and (b) front and back, walls of the unit cell, (c) uniaxial compression applied on the top surface of the model while the bottom surface is held fixed

Since the simulations were displacement-controlled, uniaxial compression is applied on the top wall of the model through a displacement boundary condition implemented linearly over the step time (Figure 4.10 (c)). For all the models, a displacement equal to 20% homogenized strain was applied in this manner. The bottom wall of the model was fixed in space so that the model did not undergo bulk movement during the simulation. The models were then automatically meshed using tetrahedral elements, with the approximate global size of each element determined by Abaqus.

The output of the Abaqus simulations included the reaction forces developed on the top surface, which were summed and divided by the cross-sectional area of the bounding box to obtain the homogenized stress acting on the model. Plotting the stress against strain, and then taking the slope of the

resulting stress-strain curve gives the effective stiffness of the unit cell under investigation. The stiffness was calculated at a strain of 0.005 for all but the linear elastic-linear plastic simulations, for which it was calculated at the strain value that is 0.002 below the onset of visible plastic yielding. As the applied strain is rather large, there were a large number of simulations that failed to converge and terminated prematurely. However, the results of such simulations were still useful, since only the initial linear response up to 0.5% strain is of concern for the calculation of the effective stiffness.

#### 4.2.4 Results

##### 4.2.4.1 Simulations on Model 1.

Initially, we aimed to construct 3 models of low, average and high volume fraction for each  $ARc$  and  $ARe$  of 0.5, 1 and 2 using Model 1; this will give a total of 9 models for simulation, which are collectively named Model 1A. The volume fraction and resulting stiffness for each model is presented in Table 7:

<b>ARe</b>	0.5	0.5	0.5	1	1	1	2	2	2
<b>ARc</b>	0.5	0.5	0.5	1	1	1	2	2	2
<b>Vf/%</b>	1.029	3.247	5.980	1.023	3.182	6.007	1.043	2.311	4.175
<b>Effective stiffness/GPa</b>	0.006	0.052	0.185	0.019	0.146	0.372	0.055	0.210	0.439

**Table 7 Simulations results for Model 1A**

It was observed that the simulation results do not quite approximate any experimental data (see Figure 4.12). In fact, the apparent densities obtained using Model 1A are much lower than real bone specimens of all anatomic sites considered, and are hence unrealistic. As such, there was a need to improve on

the model by modifying the parameter  $AR_e$  while keeping  $AR_c$  constant, (as opposed to changing both parameters identically).

With this modification, it was possible to increase the resulting volume fraction of the model while decreasing the radius of the ellipsoid and keeping its height constant (Table 8).

<b>x or z/mm</b>	1.755	1.65	1.55	1.45	1.35
<b>AR<sub>e</sub></b>	2.023	2.152	2.290	2.448	2.630
<b>AR<sub>c</sub></b>	2	2	2	2	2
<b>Vf/%</b>	3.224	11.355	18.576	27.188	36.806
<b>Effective stiffness/GPa</b>	0.410	1.735	3.087	5.251	8.426

**Table 8 Simulation results for Model 1B**

However, when the diameter of the ellipsoid was decreased to less than the length of the cuboid, the overall trabecular geometry, i.e. the openings in the walls of the unit cell, was not preserved (Figure 4.11).

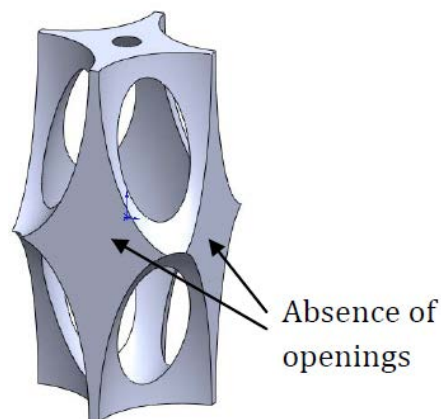


**Figure 4.11 Absence of openings in the side surfaces**

This changes the micro-architecture of the bone model structure, and is undesirable since the resulting model does not resemble the interconnected

plates and rods structure of trabecular bone well. Although the mechanical performance of this model, called Model 1B, has improved considerably compared to the previous model, the effective stiffness at low apparent densities ( $\rho_{app} < 0.5 \text{ g/cm}^3$ ) are significantly higher than real bone specimens. At the same time, the slope of the curve fit for the simulation results does not agree with that of experimental data.

#### 4.2.4.2 Simulations on Model 2

In order to preserve the overall trabecular geometry, either the height,  $2y$ , or diameter,  $2x$  or  $2z$ , of the spheroid must equal the cuboid dimensions (of  $3.5 \times 3.5 \times 7 \text{ mm}$ ), and the parameter  $ARe$  has to be at least as large as  $ARc$ . However, this gives a resulting volume fraction that is at most 4.175% (Table 7), which is too low for practical purposes. A solution to both increase the volume fraction of the models and to keep the overall trabecular structure intact would be to modify the parameters of the corner spheroids separately from those of the spheroid in the center. Only the dimensions of the center spheroid, having aspect ratio  $ARe1$ , have to satisfy the condition listed in the beginning of this paragraph; the other spheroids with aspect ratios  $ARe2$  could be made smaller so as to increase the volume fraction of the resulting models. With this method, new bone models are constructed and simulated by keeping the dimensions for the center spheroid constant (at a minimum required to satisfy the aforementioned condition) while varying those of the corner spheroids. At low apparent densities, with the exception of the model with the lowest volume fraction, Model 2 performed significantly better, and gave stiffness values that agree very closely to the experimental results of [115] (Figure 4.12). For higher values of apparent density, there is no experimental

data from the same study with which to compare. However, the curve fit of these simulation results is close in gradient to the extrapolation of this experimental regression line.

#### 4.2.4.3 Simulations on Model 3

The model can be made more plate-like by ensuring that the  $x$  and  $z$  parameters are dissimilar, such that a transverse cross-section of the ellipsoid gives an ellipse instead of a circle previously (for a spheroid); in other words, all the spheroids are replaced with full ellipsoids. Keeping the parameters of the corner ellipsoids constant (and having the same aspect ratio  $ARe2$  as previous), the  $z$  parameter for the center ellipsoid is varied.

It was observed that the simulation results were close to the previous results using Model 2, with the stiffnesses obtained for Model 3 being slightly lower. Also, the slope of the curve fit for the simulation results seems to agree with the extrapolation of the regression line by [115], even though most of the simulated apparent densities fall beyond those of the experimental data. As such, it can be suggested that the use of ellipsoids instead of spheroids resulted in models that were less stiff, but the differences in effective stiffnesses were insignificant. At the same time, in order to determine if Model 3 can accurately simulate the proximal tibia, models of lower apparent densities ( $\rho_{app} < 0.4 \text{ g/cm}^3$ ) need to be analysed so that direct comparisons with experimental data can be made. This can be done by fixing the  $x$  or  $z$  parameter of the corner ellipsoids at a value higher than 1.1 mm, for example 1.3 mm.



#### **4.2.5 Summary of results and comparison with published experimental data**

In order to assess the validity of the ellipsoid-cuboid structure in simulating human trabecular bone, the graphs of stiffness vs. apparent density obtained from the simulations is compared against the literature. The recently published study by Helgason et al. [5] reviewed twenty-two elasticity-density relationships, pre-selected based on an explicit set of criteria and normalized for density and strain rate. Only the relationships derived from direct mechanical testing are included, which serve as valid comparisons with the simulation results of compression testing on the ellipsoid-cuboid model.

The validity of the ellipsoid-cuboid model is assessed by superimposing the graphical results of the simulations onto the combined plot of all regression lines from the experimental studies reviewed by [5]. It can be observed that the simulation results approximate the experimental results of [115] for the proximal tibia best. As such, the experimental studies on the tibia are isolated in a separate diagram and the simulation results for the ellipsoid-cuboid model are then compared against this plot (Figure 4.12).

For those models of Model 2 with apparent densities between  $0.264 \text{ g/cm}^3$  and  $0.4512 \text{ g/cm}^3$ , the elastic moduli agree very closely to those predicted by the power law regression of [115]. Beyond this range, there is no available experimental data for comparison. As such, the validity of both Model 1 and Model 3 for the purpose of simulating the proximal tibia cannot be established, even though the results are in close agreement with the extrapolation of the regression line.

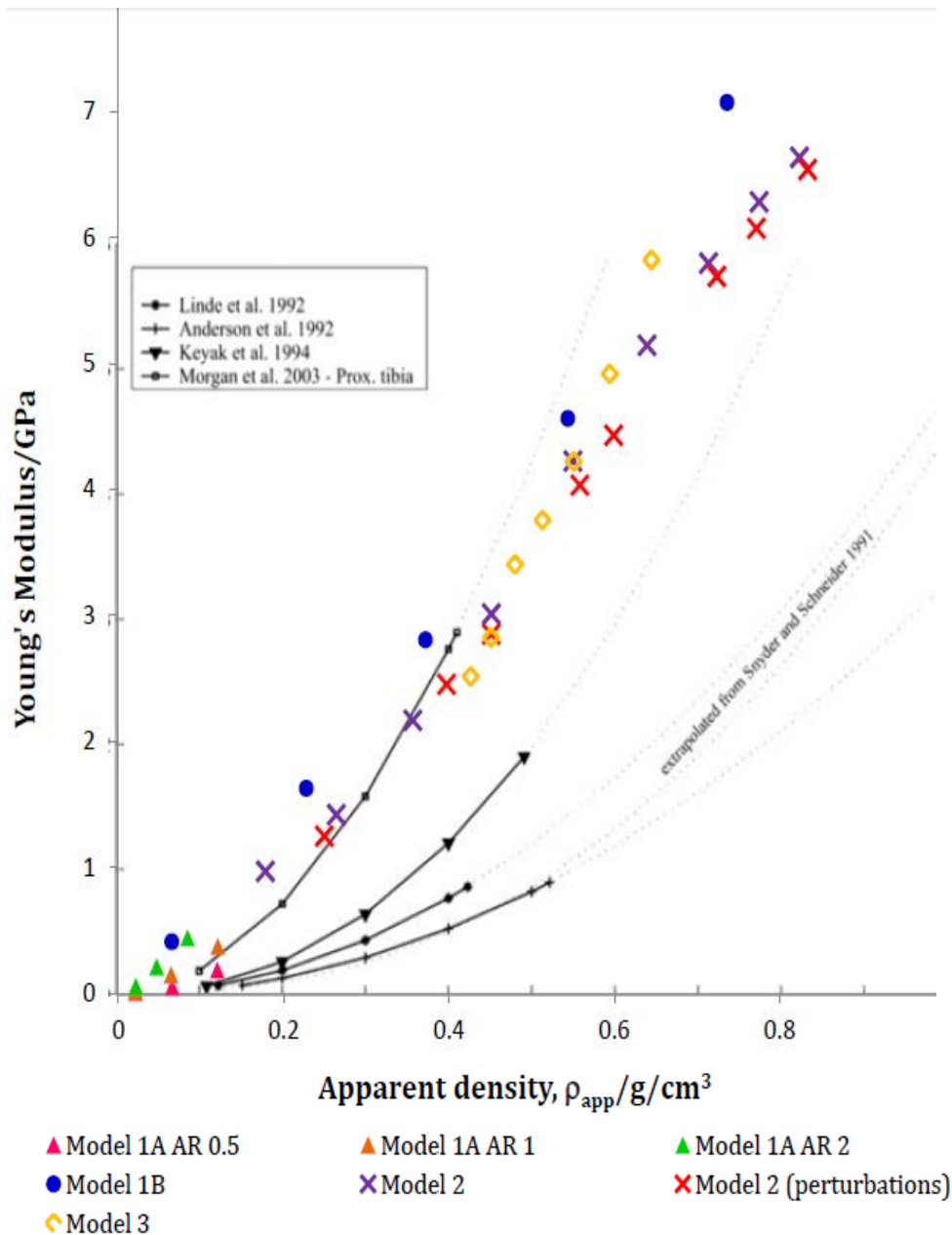


Figure 4.12 Graphs of simulation results superposed onto those obtained by experimental studies on the proximal tibia (from [5])

Taken on a whole, these results suggest that Model 2 is a valid model for the accurate simulation of real proximal tibia bone specimens having a volume fraction of between 13.177% and 22.568%. The suggestion that the ellipsoid-cuboid model may be more suited for the simulation of the proximal tibia in particular can be confirmed by investigating its SMI. Calculation of the SMI is done by the software ImageJ using the BoneJ plugin. Since it was suggested

that Model 2 was suitable for the simulation of the proximal tibia with volume fraction between 13.177% and 22.568%, the model with the average volume fraction of 17.804% was selected for the investigation of its SMI. The SMI value for this unit cell was calculated to be 1.015. For the purpose of comparison, the literature data of [138] for 160 proximal tibia specimens with an average SMI of  $0.99 \pm 0.52$  was used. As the calculated SMI falls within one standard deviation of the sample data, it provides further corroboration to the above-mentioned suggestion that Model 2 can be used to accurately simulate the proximal tibia.

#### **4.2.6 Conclusions**

In summary, the work described in this subsection presented a novel model for simulating the trabecular bone using a representative unit cell that characterizes its main structural features with an inter-connected network of rods and plates. For this ellipsoid-cuboid model, it was found that the effective stiffness corresponded well with experimental data of the proximal tibia for a certain range of apparent densities. At the same time, its SMI was found to be very close to that of real tibia specimens, providing strong evidence for the resemblance between the two microstructures. As such, we recommend the use of the ellipsoid-cuboid unit cell as a model particularly suited for human tibial trabecular bone.

## **Chapter 5. Investigation of the effect of trabecular microstructure on the femur scale**

The application of classical numerical methods employing extremely fine meshes to capture microscopic architecture, though theoretically possible, becomes computationally prohibitive in practice when studying large structures. Multi-scale models and methods have thus been used in the past to probe and understand the mechanical response of heterogeneous materials like foams [139], wood [140], and concrete [141]. Such methods typically involve homogenization at certain scales in order to obtain so-called ‘effective’ material properties, which are then incorporated in studying phenomena at adjacent scales. Multi-scale analyses are broadly divided into two: non-concurrent techniques, where the successive scales are studied sequentially (usually from smaller to larger) with no explicit coupling between the scales, and concurrent techniques, which make use of nested simulations to study different scales simultaneously. Recently, several researchers have successfully applied multi-scale techniques in studying materials such as wood [142], polymers [143] and bone [27, 29, 144].

The use of multi-scale models is particularly appealing in the field of bone mechanics, owing to the well-known fact that bone is a hierarchically and structurally complex material [1, 145]. Spatially, bone spans a vast range of length scales, from collagen fibrils at about 0.1 micron, to trabecular bone with spicules about 2 millimetres in diameter [1]. Apart from this inherent spatial heterogeneity, bone also manifests striking dissimilarities between specimens excised from different anatomic locations, donor ages, extant pathologies, etc.

The combined effect of intrinsic spatial scales and idiosyncratic inhomogeneity makes the study of bone mechanics especially challenging and furnishes sufficient motivation for the application of multi-scale methods.

The recent prodigiousness in computing power has already made finite element analysis (FEA) a standard tool for evaluating bone mechanical behaviour. In macro-scale continuum-based FEA, finite element (FE) meshes are generated from computed tomography (CT) images [7], which contain information only on the bone geometry and density distribution. Based on the apparent density, material properties (stiffness, in particular) can be assigned to the FE model [146]. Such mapping techniques based on empirically obtained density-stiffness relationships suffer a fundamental flaw in that they do not account for trabecular microstructure, which is not captured in CT images. Absence of microstructural information in the FE model implies that important geometrically nonlinear phenomena like buckling of trabecular struts cannot be accounted for in the analysis [7, 21, 147]. In so-called ‘micro-FE analysis’, on the other hand, trabecular architecture is captured with fidelity by the use of high-resolution micro-computed tomography (micro-CT), obviating the need for stochastic density-stiffness relationships. However, micro-CT images are difficult to obtain in clinical settings owing to the extremely high radiation dosage required [7]. Furthermore, extant micro-CT technology only permits scanning of peripheral sites like the ankle and wrist [7].

In Chapter 2, we proposed a novel model for trabecular bone based on the minimal surface family of solids. We investigated the feasibility of a minimal

surface solid, called the gyroid, in modeling trabecular bone. We then calculated the homogenized mechanical properties of the gyroid model for varying volume fractions using FEA. In this chapter, these material properties are used as input data for subsequent macro-scale FEA at the level of the whole proximal femur, with two different physiologically faithful sets of boundary conditions (i.e., stance and sideways-fall modes). We also studied the effect of simulated bone loss (through reduction in trabecular bone volume fraction) on the macro-scale behaviour of the femur. In order to authenticate the need for such a dual-scale method in studying bone, we performed identical simulations using the traditional method of attributing femoral material properties through linear-elastic density-stiffness mapping techniques. Finally, we compared the results between our proposed dual-scale technique, and the traditional method.

## **5.1 Non-concurrent dual-scale FE simulations of the femur**

### **5.1.1 Source of femur model**

The finite element meshes of the human femur were obtained from the VAKHUM (Virtual Animation of the Kinematics of the Human) repository (<http://www.ulb.ac.be/project/vakhum/>), a European initiative to provide medical information and datasets free for academic purposes [148]. Of the six degrees of mesh density available for download on this website, we selected the files called “Refinement\_3” (henceforth called ‘coarse mesh’) and “Refinement\_6” (henceforth called ‘fine mesh’). These two files are available for download in several formats for use in different commercial FE softwares – we chose those in ABAQUS format for this work. The coarse mesh

contained 14797 nodes and 12792 linear hexahedral (C3D8) elements, while the fine mesh consisted of 124954 nodes and 113510 linear hexahedral (C3D8) elements.

### 5.1.2 Assignment of material properties

In the original input files, material properties had already been pre-assigned to each element following an empirical density-modulus mapping algorithm. More specifically, a linear elastic constitutive law had been assigned to all elements, such that the stiffness was a function of the apparent density of the element (more details can be found on the website, <http://www.ulb.ac.be/project/vakhum/>). The fine mesh contained 280 different materials, while the coarse mesh had 199 materials.

In order to study the effect of trabecular micro-architecture on femur-level phenomena, it was imperative to simulate bone loss on the original femur. We thus divided our analyses into two categories: the original mesh was labelled “pristine” bone, while a new category, called “simulated bone loss” was created by uniformly decreasing the  $V_f$  of each of the elements by 30% [52, 56].

Subsequently, we further subdivided each of the two above-mentioned categories into two, based on the algorithm employed for assignment of material properties. Hence, we eventually had four cases (called Cases A – D), each differing from the other in the material properties assigned. More details on each of the four cases follow.

### 5.1.2.1 Case A

Case A retains the original density-modulus mapping present in the model, without any simulated bone loss. It acts as a “control” case against which Case B (described below) will be compared, in order to quantify the effect of micro-scale effects on femur properties in a healthy (“pristine”) bone. It should be noted that most of the elements in Case A possess  $V_f$ s between 40% and 100% (the latter limit being equivalent to cortical bone).

### 5.1.2.2 Case B

In Case B, similar to Case A above, the pristine bone mesh is used, i.e., no bone loss is simulated. However, unlike Case A, material properties for each element in Case B are derived from the gyroid unit cell of corresponding  $V_f$ . For easier manipulation of input material parameters, a database of homogenized gyroid-based material properties was created encompassing gyroid unit cells of  $V_f$  approximately 10%, 25%, 35%, 45%, and 55%. Similarly, the elements in the femur mesh were discretized into groups that spanned 10% (i.e., 20 – 29%, 30 – 39%, 40 – 49%, 50 – 59%), except for the first group, which spanned from 0 – 19%. The latter group covered a larger range than the rest owing partly to the paucity of elements of low  $V_f$  in the original mesh and partly to the fact that the gyroid unit cell becomes disconnected for  $V_f$  around 5%.

The final step in material assignment involved replacing the original (linear-elastic) material properties of the element with the corresponding ones from the gyroid-based database. For example, for an element of  $V_f = 23\%$ , the



homogenized (nonlinear) material properties for the gyroid unit cell of  $V_f \sim 25\%$  was used, while an element of  $V_f = 48\%$  was endowed with the nonlinear material properties corresponding to the gyroid of  $V_f \sim 45\%$ . One should note that, following the findings of Bevill et al. [20], who concluded that geometrically nonlinear phenomena are of critical importance only at lower  $V_f$   $V_f$ s, we retained the original linear-elastic properties for all elements possessing  $V_f$  above 60% (Figure 5.1).

### 5.1.2.3 Case C

In Case C, bone loss which may occur with ageing or osteoporosis was simulated by scaling down the  $V_f$  of all elements in the original mesh by 30%. In other respects, Case C is analogous to Case A above in that linear elastic material properties were recalculated for each element based on its new (reduced)  $V_f$  using the same density-modulus mapping scheme (see Section 4.2.2.1 above, and Figure 5.1). Case C thereby provides a “control” case against which Case D (described below) will be compared, in order to study the effect of trabecular micro-architecture on macro-level femur properties in scenarios where severe bone loss has occurred.

### 5.1.2.4 Case D

In Case D, like in Case C above, bone loss effects were incorporated. However, the difference between Case D and Case C arises from the fact that, in Case D, gyroid-based nonlinear material properties were assigned to elements based on their  $V_f$ , in a fashion similar to Case B above (see Figure 5.1). It should be noted that for all elements with  $V_f$  above 60%, linear elastic

material properties were recalculated through the density-modulus mapping scheme used in Case A and Case C, based on the rationale that geometrically nonlinear effects are of decreasing importance above such high  $V_f$ s.

Figure 5.1 shows a flowchart encapsulating the entire process, while Figure 5.2 depicts the distribution of bone (i.e., the elemental  $V_f$ ) in a typical coronal longitudinal section through the proximal femur.

### 5.1.3 Boundary conditions

Once material properties had been appropriately assigned to all the elements for all the four cases, it was necessary to apply boundary conditions that mimicked physiological scenarios as closely as computationally feasible. We investigated two different sets of boundary conditions: the stance mode, where the femur bone is upright and bears a compressive load directed along the femoral shaft, and the sideways-fall mode, which represents a person having fallen sideways onto his/her hip along the coronal plane, with loads being borne by the femoral neck. Though the mesh geometry spans the entire length of the femur, we focused our attention on the proximal region only, based on the rationale that most femoral fractures occur around the neck and trochanteric regions [97, 149].

Point loads cause stress singularities around the node where the load is applied and are thus computationally unfeasible. To circumvent this obstacle, we designed a digital model of a cup-like hemispherical cushion with inner contours resembling the curvature of the femoral head surface.

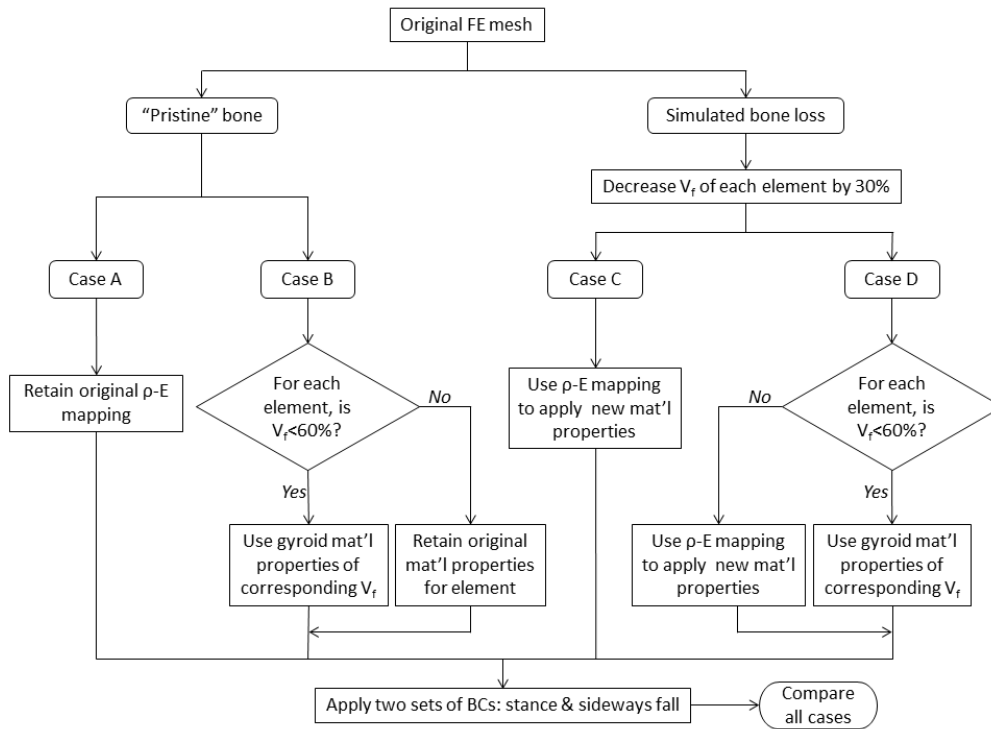
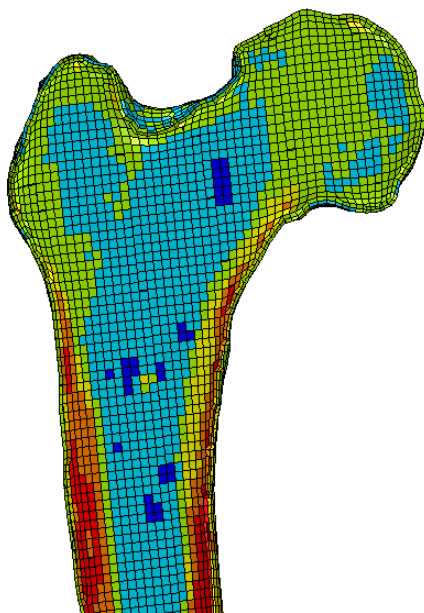


Figure 5.1 Flowchart showing overall methodology adopted in assigning material properties to finite element mesh of femur



(a)

Colour	Cases A and B	Cases C and D
	$V_f$ (%)	$V_f$ (%)
Red	90 – 100	60 – 70
Orange	80 – 90	50 – 60
Yellow	70 – 80	40 – 50
Light Green	60 – 70	30 – 40
Cyan	50 – 60	20 – 30
Blue	40 – 50	10 – 20
White	30 - 40	0 – 10

(b)

Figure 5.2 (a) Material assignment in a coronal longitudinal section of the original femur mesh, after meshing with linear brick elements. (b) Legend describing corresponding  $V_f$  (%) for each element in the mesh for Cases A – D

This cushion material helped to distribute the applied loads over a larger surface of the femoral head, thereby preventing unusually high stress distributions [150]. Furthermore, it also delayed the onset of mesh distortion issues during analysis. The cushion was coupled to the femoral head using ‘tie’ constraints in ABAQUS [119], which transferred loads across the surfaces. For both loading modes, we followed with minor adaptations the protocols established by Keyak and Rossi [89], brief details of which follow.

#### **5.1.3.1 Stance mode**

In the stance mode, the femur models were aligned such that the shaft made an angle of approximately 10 degrees with the vertical plane. Subsequently, we imposed vertical displacements onto the femoral head *via* the cushion that was placed against the femoral head surface. The most distal region of the proximal femur was fully constrained.

#### **5.1.3.2 Sideways-fall mode**

In the sideways-fall mode, the femur models were aligned such that the shaft made an angle of approximately 10 degrees with the horizontal plane. Vertical displacements were again imposed through the cushion onto the femoral head. Again, the most distal region was fully constrained. To mimic the effect of the ground surface upon impact, the outermost surface of the greater trochanter was also constrained.

#### **5.1.4 Finite element analysis and post-processing procedure**

Upon successful imposition of appropriate boundary conditions, FE simulations with finite-deformations activated (i.e., geometrically nonlinear

analyses) were undertaken for all eight femur models described above (i.e., Cases A – D, in both stance and fall modes), using ABAQUS. Subsequent to the completion of the analyses, we calculated the sum of the reaction forces generated on the cushion surface, as well as the displacements of a node chosen on the centre of the femoral head surface. Graphs of reaction force vs. nodal displacement were plotted for each model and then interpreted to obtain parameters of interest (e.g., structural stiffness, maximum force reached, etc). Contour plots depicting maximum principal strains were also obtained to appreciate the effects of microstructural geometrically nonlinear phenomena on the femur.

### **5.1.5 Mesh density dependence**

At the macro-scale (i.e., for the whole femur), it was imperative to study two related aspects of mesh convergence: whether the mesh density is itself sufficient for numerical convergence, and also, more importantly, whether the dual-scale technique proposed in this work is dependent upon the size of elements in the macro-scale model. To this effect, we performed identical simulations on the coarse mesh (described in Section 4.2.1) of the femur, which was originally obtained from the VAKHUM repository, available under the label 'Refinement\_3'. We then compared macro-level results between the two mesh densities.

## 5.2 Results

### 5.2.1 Mechanical behaviour of femur bone at macro-scale

#### 5.2.1.1 Force-displacement behaviour

The graphs depicting the total reaction force against the displacement experienced by the chosen node on the surface of the femoral head are shown in Figure 5.3 and Figure 5.4.

It was noted that the graphs for Cases A and B for both sets of boundary conditions (i.e., stance and side-ways fall) coincided and were linear up to nodal displacements of approximately 6 mm. The graphs for Case C were also linear, but showed significantly reduced structural stiffness. In sharp contradistinction to the other three cases, Case D alone showed a plateauing behaviour for reaction force at nodal displacements in excess of 3 mm. Quantitative details follow.

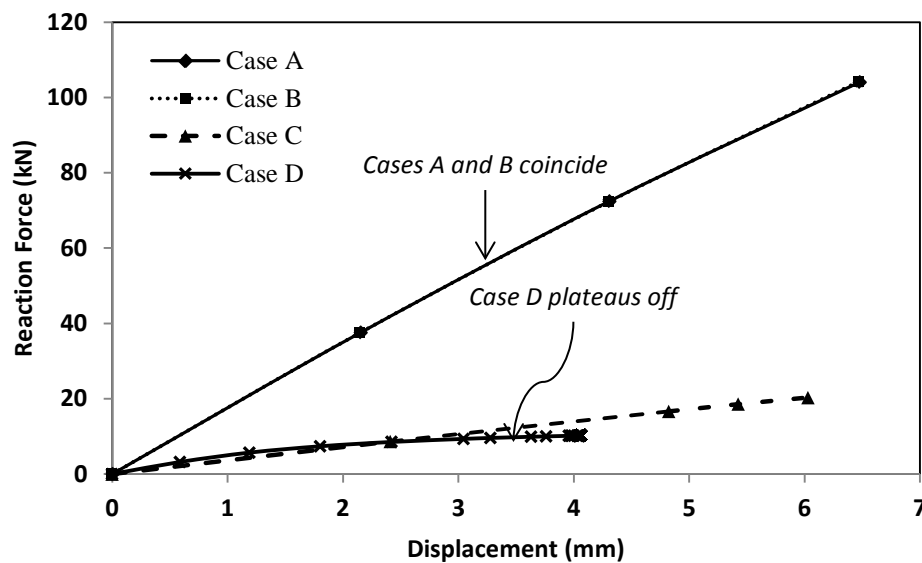
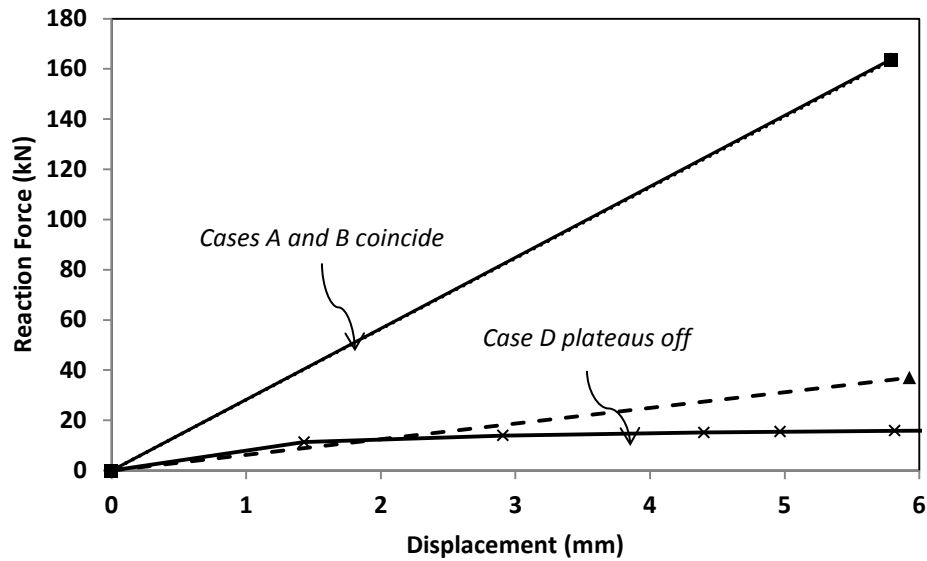


Figure 5.3 Graphs showing reaction force vs. nodal displacement for stance mode for Cases A - D



**Figure 5.4** Graphs showing reaction force vs. nodal displacement for sideways-fall mode for Cases A – D (legend identical to Figure 5.3 above)

#### 5.2.1.1.1 Stance mode

In stance mode, the values for secant stiffness (ratio of reaction force to displacement) at a nodal displacement of 4 mm were: Cases A and B = 16.8 kN/mm; Case C = 3.5 kN/mm; and Case D = 2.6 kN/mm.

While Cases A, B and C revealed that the reaction forces continued to rise almost linearly with increasing nodal displacements, Case D plateaued at a maximum reaction force of 10.2 kN, achieved at a nodal displacement of 3.9 mm.

#### 5.2.1.1.2 Sideways-fall mode

In the sideways-fall mode, the values for secant stiffness at a nodal displacement of 3 mm were: Cases A and B = 28.2 kN/mm; Case C = 6.2 kN/mm; and Case D = 4.6 kN/mm.

Again, similar to the trends for the stance mode described in Section 5.3.1.1.1 above, the reaction forces in Cases A, B, and C continued to increase almost linearly with increasing displacements. Case D plateaued at a maximum reaction force of 14 kN, achieved at a nodal displacement of approximately 3.1 mm.

### **5.2.1.2 Maximum principal strains**

Investigating the distributions of maximum principal strains in the four different cases (Cases A – D) further evinced the effects of gyroid-based micro-architecture on the macro-scale properties of the femur. The maximum principal strains were seen to be substantially dependent upon the nature of micro-scale material properties employed in the macro-scale simulation. Generally, elements with geometric nonlinearity (i.e., with gyroid-based properties) will manifest higher strains and lower stresses than corresponding elements with no material nonlinearity (i.e., the linear elastic case), owing to the fact that the former may undergo yielding when the yield strength is exceeded, while the latter do not. This was seen to be generally true in all the analyses.

#### **5.2.1.2.1 Stance mode**

Figure 5.5 shows the contour plots depicting the maximum principal strains on a coronal longitudinal section for all four cases, at a nodal displacement of 4 mm. We noticed that the maximum principal strains in Cases A and B were very similar. Comparing Cases A and C showed that more elements in the femoral neck area manifested high maximum principal strains in Case C (i.e., the femur with simulated bone loss) than in Case A (i.e., the pristine femur).



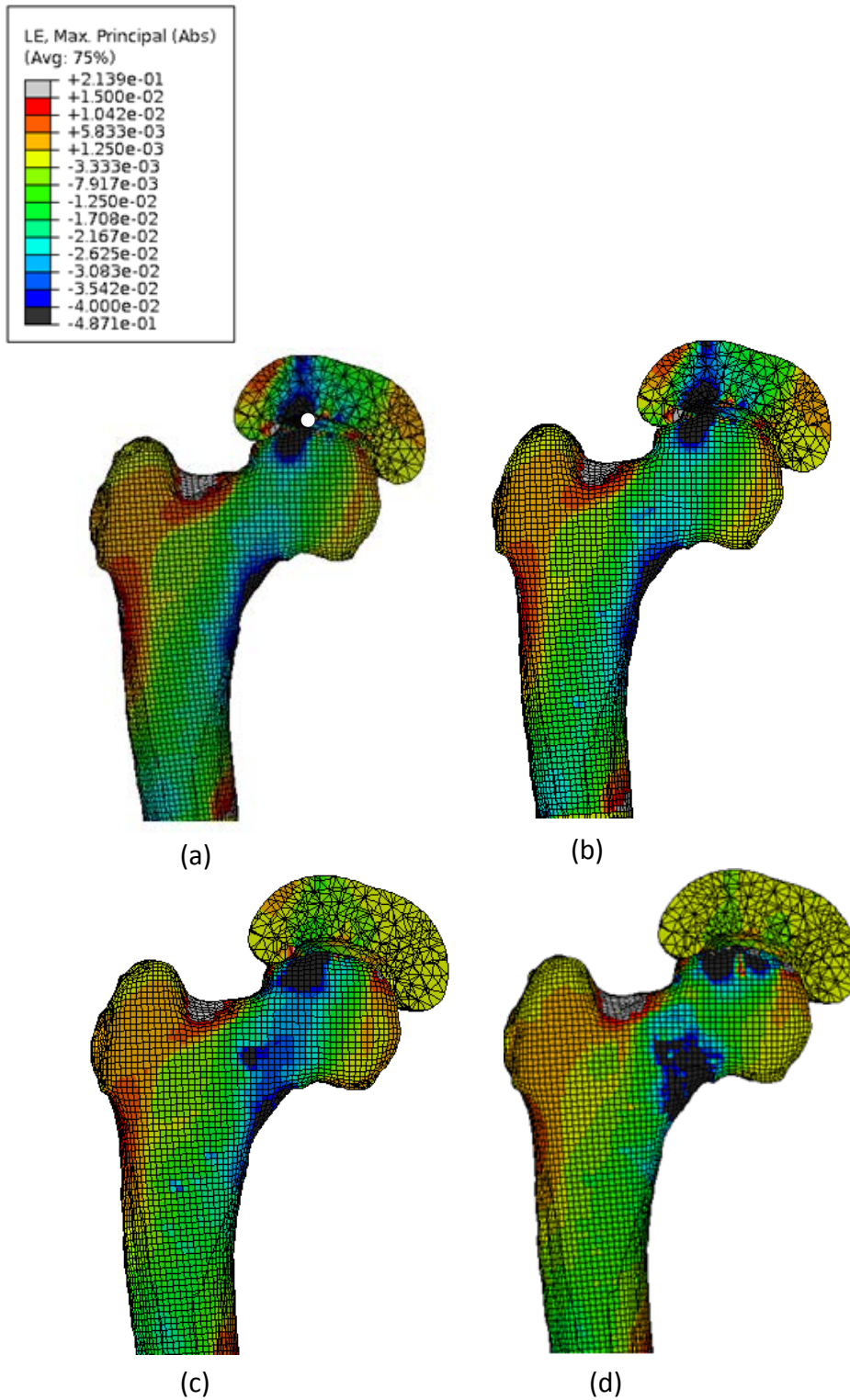


**Figure 5.5** Plot of maximum principal strains in stance mode for (a) Case A, (b) Case B, (c) Case C and (d) Case D. By convention, positive and negative strains denote tension and compression, respectively. White filled circle in (a) schematically shows the location of the node chosen for calculation of nodal displacements. All plots were obtained at identical nodal displacement of approximately 4 mm.

A crucial observation was that Case D (i.e., the femur with simulated bone loss as well as gyroid-based material properties) manifested the highest maximum principal strains (in terms of magnitude of strain, without regard to the sign), mostly distributed over the narrow femoral neck region.

The distribution of bone (i.e.,  $V_f$ ) for both the pristine model as well as that with simulated bone loss was depicted in Figure 5.2. It is seen that, while the majority of the elements in the femoral head are of relatively high  $V_f$  ( $> 60\%$  in Cases A and B;  $> 30\%$  in Cases C and D), there exist several elements of substantially low  $V_f$  ( $\sim 45\%$  in Cases A and B;  $\sim 15\%$  in Cases C and D) located at the centre of the femoral neck region. An observation of crucial importance in this work is that this region of low  $V_f$  coincided with the region of greatest maximum principal strains in Case D. On a similar note, the regions in the femoral head with relatively high  $V_f$  experienced low maximum principal strains in all cases.

It was also seen that, in the stance mode, the inferior region of the femoral neck suffered compressive strains (negative by convention), while the superior region experienced tensile strains (positive by convention), in all four cases [149].

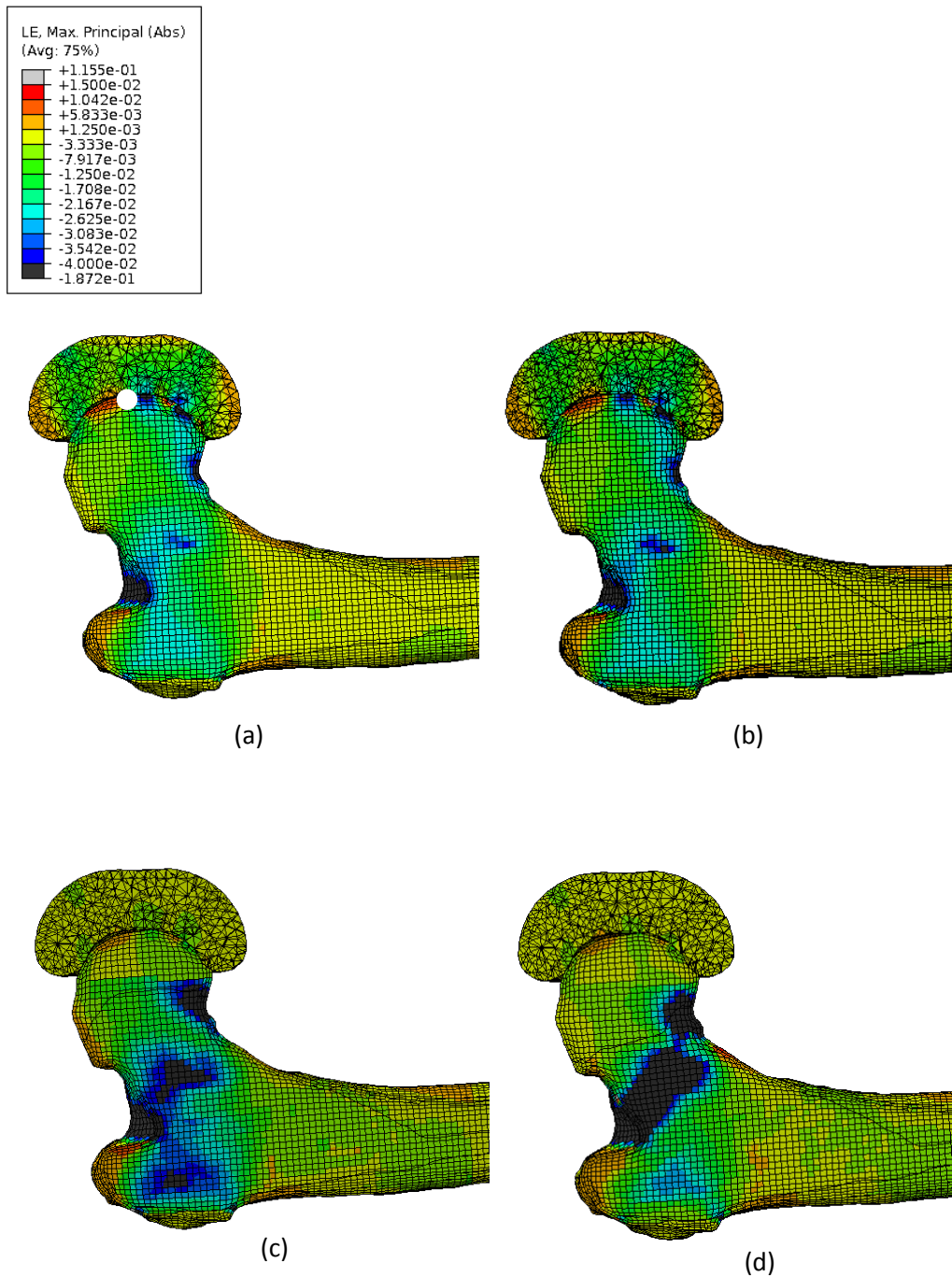
#### 5.2.1.2.2 Sideways-fall mode

Figure 5.6 shows the contour plots depicting the maximum principal strains on a coronal longitudinal section for the four cases, all at a nodal displacement of 3 mm. It was noted that the maximum principal strains in Cases A and B were again very similar, as in the stance mode. Comparison between Cases A and C

revealed that the maximum principal strains in the femur with simulated bone loss (i.e., Case C) were higher, especially in the narrow femoral neck region, than in the pristine femur (i.e., Case A). Of greatest import was the observation that Case D (i.e., the femur with simulated bone loss as well as gyroid-based material properties) showed the highest maximum principal strains, again mostly localized in the femoral neck region.

Similar to the observations made for the stance mode made in Section 5.3.1.2.1 above, we noticed that the area of low  $V_f$  around the centre of the femoral neck region once again coincided with the region of greatest maximum principal strains in Case D. On the other hand, the regions in the femoral head with high  $V_f$  manifested relatively low maximum principal strains in all cases.

Unlike in the stance mode, most of the femoral neck region was under compressive strain, while the outermost elements at the inferior surface of the femoral neck experienced tensile strain [149] in all cases.



**Figure 5.6** Plot of maximum principal strains in sideways-fall mode for (a) Case A, (b) Case B, (c) Case C and (d) Case D. By convention, positive and negative strains denote tension and compression, respectively. White filled circle in (a) schematically shows the location of the node chosen for calculation of nodal displacements. All plots were obtained at identical nodal displacement of approximately 3mm.

### 5.2.2 Mesh density dependence

We noted no variation in the force-displacement behaviour or strain distributions between the coarse and fine meshes of the femur. However, though it was computationally easier to manipulate, the coarse mesh did not capture the geometry of the femur accurately as a result of aliasing errors caused by the low resolution. The fine mesh, on the other hand, was able to capture better the nuances of geometry and density distribution in the original femur.

## 5.3 Discussion

### 5.3.1 On the importance of dual-scale simulations for bone analysis

The importance of accounting for micro-level trabecular architecture when investigating the femur has been a topic of recent debate [7, 22]. For example, Bevill et al. [20] studied the influence of trabecular volume fraction and architecture on large-deformation failure mechanisms and concluded that geometrically nonlinear failure mechanisms can significantly reduce the strength of trabecular bone, especially at low volume fractions. Similarly, Stolken and Kinney [21] simulated trabecular bone failure with and without geometric nonlinearities and asserted that bifurcation-induced failure at the trabecular level may have a more profound effect on structural failure than was previously supposed. Though admirable for their pioneering efforts, both of these studies were limited to small specimens of trabecular bone. Little is still known about how such micro-scale phenomena affect the properties of a larger structure like the proximal femur considered *in toto*.

In Chapter 2, we utilised a new morphological model for trabecular bone, called the gyroid-based unit cell, to derive micro-scale mechanical properties incorporating the effect of geometrically nonlinear phenomena like buckling of trabecular spicules. In this chapter, these micro-scale properties were then used as material input parameters for a macro-scale study of the human femur. The dual-scale technique facilitated a quantitative investigation into the effect of trabecular buckling on femoral strength and stiffness. Furthermore, we applied this technique to study a pristine femur (i.e., one with a high bone density) and one with simulated bone loss. A comparison of these two categories helped to appreciate the different extents to which trabecular architecture contributed to femoral strength and stiffness in the two scenarios. We contrasted the proposed dual-scale technique against classical linear elastic density-modulus mapping algorithms that fail to account for trabecular microstructure.

### **5.3.2 On the effect of incorporating micro-level (gyroid-based) mechanical properties on macro-level behaviour**

#### **5.3.2.1 Case A vs. Case B**

Generally, our results showed that there was negligible difference in the macro-level mechanical behaviour of the femur between Cases A and B. The force vs. displacement graphs for the two cases were nearly identical, even at finite displacements, for both loading modes (stance and sideways-fall). Furthermore, maximum principal strains were also similar in both cases for both loading modes. The implication of this finding is that geometrically nonlinear phenomena at the micro-scale do not have a significant effect on the

structural properties of the femur when the femoral bone is of high apparent density (as is typical in healthy subjects). In other words, in bones of high  $V_f$  the structural stiffness and strength of the femur is not noticeably compromised by trabecular strut buckling. In physiological terms, the dense trabecular network is capable of withstanding microscopic buckling and thus does not have an attenuating effect on the stiffness and strength of the whole femur. In such situations, the classical continuum-based finite element analysis is sufficiently suitable for predicting femoral failure [7, 151].

It is also imperative to interpret the fact that for both Cases A and B, the force-displacement graphs did not reveal a plateauing behaviour for the reaction force. Even at displacements in excess of 5mm, the reaction forces continued to increase, implying that the femoral structure is still capable of withstanding load. Experimental investigations on the proximal femur have shown that typical forces at failure rarely exceed 20 kN [89].

#### **5.3.2.2 Case C vs. Case D**

Our results showed that there are significant differences in the force-displacement behaviour of Cases C and D. For both loading modes, while the reaction force in Case C continued to increase linearly with displacement, that in Case D achieved a peak value beyond which it manifested plateau-like behaviour (i.e., there was no further increase in reaction force). This plateau force was 10.2 kN for the stance mode and 16.8 kN for the sideways-fall mode, which falls favourably within the typical range reported in experimental studies [89].

The fact that only Case D manifests a peak value for reaction force is of importance in the context of our proposed technique. The primary implication of this fact is that the femoral strength has been compromised by trabecular strut buckling occurring at the micro-scale. Only Case D revealed this dual-scale phenomenon owing to the fact that only Case D uses geometrically nonlinear micro-scale material properties as input for macro-scale simulations, in a femur with simulated bone loss.

The contour plots depicting maximum principal strains were also seen to vary considerably between Cases C and D, especially in the femoral neck region. The maximum principal strains were noticeably higher in Case D than in Case C, and were seen to be localized at the femoral neck region. The plot (Figure 5.2) showing the original bone volume fraction is helpful in further understanding the distribution of principal strains. It can be noticed that, in the original structure, there exist some elements of low  $V_f$  at the core of the femoral neck (the Ward's triangle). Physiologically, the trabecular struts in such low density elements are more prone to buckling, and hence the maximum principal strains can be seen to be higher around these locations. Once again, it is noted that only Case D is capable of capturing this phenomenon.

### **5.3.3 Limitations**

The work described in this chapter faces limitations similar to any other multi-scale technique which adopts an idealised unit cell for computing micro-scale properties [152]. Trabecular structure is generally more complex and less periodic than the gyroid. The discretization of the range of apparent densities,



though greatly facilitating computational manipulation of the input parameters, may have an effect on the macro-level strength and stiffness. On a different note altogether, the boundary conditions we modeled capture only static loads. Dynamic gait simulations incorporating muscle effects may be performed using similar multi-scale concepts as proposed here.

#### **5.4 Conclusions**

Bone is hierarchically and structurally very complex. It has been suggested that trabecular micro-architecture could have a profound impact on overall femur behaviour, especially in cases where bone density is attenuated. We used a unit cell structure based on the gyroid family of minimal surfaces (described in Chapter 2) to obtain homogenized mechanical properties for a range of volume fractions. These were then used as input parameters for performing finite element analyses of the proximal femur. We assessed the feasibility of such a dual-scale technique by analysing a publicly available femur mesh under two sets of boundary conditions. We observed that in bones whose trabecular structure is very dense, incorporation of micro-scale buckling-related phenomena does not significantly modify the overall strength or stiffness of the femoral structure; whereas in femur bones with lowered trabecular density, buckling of trabecular struts plays a substantial role in undermining the overall strength of the femur.

## Chapter 6. Deformation mechanisms in the femoral neck region

*“[...]my concern will not be, except perhaps incidentally, that what I say shall seem true to those present, but rather that it shall, as far as possible, seem so to myself.”*  
(Plato, *Phaedo*)

This chapter focuses on studying deformation mechanisms particularly in the femoral neck region. In Section 6.1, we use a CT scan of the femoral neck cross-section as the basis for assembling gyroid-based unit cells of heterogeneous density into a macro-scale structural model of the femoral neck region. The latter is then subjected to finite element simulations in Section 6.2. Section 6.3 compares the gyroid-based macro-scale structure with conventional continuum-based models for assigning material properties. In Section 6.4, we perform more extensive FE simulations on the same structure, with different combinations of loading conditions, in order to develop a structural yield surface of the gyroid-based femoral neck. Lastly, Section 6.5 attempts to link the deformation mechanisms occurring at the micro-scale (i.e., trabecular level) with those associated with yield at the macro-scale (i.e., the femoral neck level).

### 6.1 Generation of femoral neck (FN) structure

#### 6.1.1 Extraction of FN slice from computed tomographic dataset

We downloaded the dataset of computed tomographic (CT) images labelled ‘subj006reg000’ from the online repository ‘*Virtual Animation of the Kinematics of the Human*’ (VAKHUM), a European project that maintains a

complete set of both raw and processed data on the entire human skeleton, including CT images, digital models, FE meshes, gait animation movies, etc, as well as extensive documentation, freely downloadable for academic use [148]. According to the specifications described by the VAKHUM protocol, the dataset we downloaded comprises CT images of the proximal femur of a female subject taken using an Elscint Spiral Twin Flash CT installation, at a power of 120 kV, with slice increment 1.0 mm and slice thickness 2.7 mm. Each of the 250 slices contains 512 by 512 pixels, of pixel size 0.84 mm.

The dataset was imported into the medical image processing software MIMICS (Figure 6.1), which was then used to extract a single FN slice cut transverse to the FN axis at the region of smallest cross-sectional area (i.e., the narrow neck region).

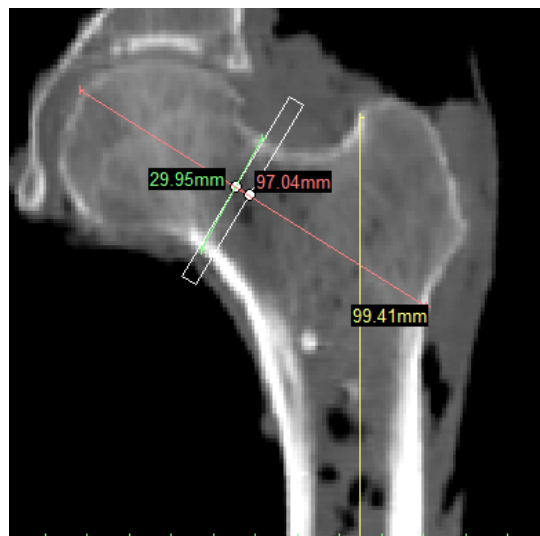


**Figure 6.1** Original CT dataset after importing into MIMICS. The white rectangle shows the process of reslicing perpendicular to the FN axis

The rationale for choosing this location for reslicing lies in the fact that, according to engineering beam theory, the narrow neck region has lowest moments of inertia and is therefore least capable of withstanding bending

moments applied at the femoral head. Furthermore, it is mentioned in the literature [71] that proximal femur fractures frequently occur in the narrow neck region.

Subsequent to reslicing, the CT image of the femoral neck thus generated (Figure 6.2) is processed to remove the soft tissue (muscles surrounding the femoral bone) and digital noise, saved in DICOM format at an optimum resolution of 500 by 500 pixels, and exported to MATLAB for further processing.

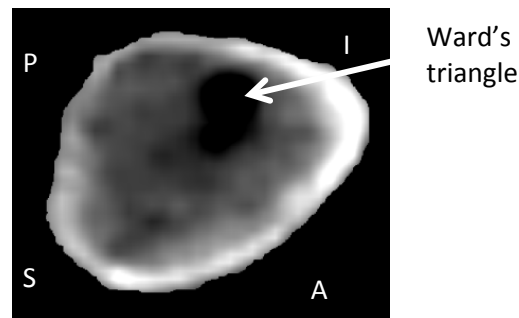


**Figure 6.2** CT image of the femoral neck after reslicing perpendicular to the FN axis. A: Anterior, I: Inferior, P: Posterior, S: Superior. Also shown is the Ward's triangle, a region of very low bone density that occurs due to the nature of the trabecular pattern in the femoral neck

### **6.1.2 Processing of CT slice to obtain geometric and densitometric properties**

Once the CT slice is imported into MATLAB, it is accessible as a two-dimensional square array (matrix) of size 500 by 500, with each constituent number denoting the density of the corresponding pixel in Hounsfield units (HU). The Hounsfield scale provides a quantitative description of the porosity of the bone, with a value of 700 HU being typical for (porous) trabecular bone, and more than 3000 HU for (dense) cortical bone.

Typically, for human bone, empirical studies have shown that there exists a linear relationship between apparent density and Hounsfield units. Possibly due to the intrinsic diversity in the mechanical properties of bone, and the vagaries of experimental measurement, various coefficients have been proposed in the literature for the linear relationship between the Hounsfield scale and the apparent density. In this work, we adopted the following mapping, originally proposed by [153]:

$$\rho_{app}(g/cm^3) = (8.690476e - 4)HU + 0.130952 \quad (6.1)$$

Employing this relationship, we used MATLAB to convert the Hounsfield value of each pixel in the CT image to apparent density, thereby producing another two-dimensional array of the same size as the original, but with the pixel values now denoting the apparent density of the bone at that particular location.

### **6.1.3 Generation of gyroid-based FN structure using geometric and densitometric properties obtained from CT slice**

In order to generate a structure using the gyroid-based unit cell with geometry and density corresponding to those in the original CT slice of the femoral neck region, we employed the following procedure. The apparent density value of each pixel in the two-dimensional array is converted to volume fraction using the linear relationship:

$$V_f = \frac{\rho_{app}}{\rho_{tissue}} \quad (6.2)$$

where the tissue density is given by  $\rho_{tissue} = 1.8 g/cm^3$ .

For the gyroid-based unit cell (Chapter 2), the value of the threshold  $t$  determines the volume fraction ( $V_f$ ) of the unit cell generated, according to the linear relationship:

$$V_f = 0.3354t + 0.5 \quad (6.3)$$

Inverting this relationship, we obtain

$$t = 2.98(V_f) - 1.4898 \quad (6.4)$$

The value of  $t$  derived thus for any pixel is then used in generating gyroid-based unit cells for that particular pixel. Note that owing to the difference in grid size between the FN scale and the trabecular (i.e., gyroid unit cell) scale, we introduce a scaling parameter  $1/\epsilon$  that determines the relative size between the trabecular struts produced by the gyroid equation and the femoral neck itself. The scaling parameter is fine-tuned in order to produce struts of reasonable thickness (as described in Section 2.3), while ensuring ease of finite element mesh generation for subsequent simulations.

Hence, using equations (6.1), (6.2), and (6.4) in succession, the geometric and densitometric information in a CT slice can be used to generate a structure based on the gyroid unit cell, whose apparent density at any given location is identical to that measured from the original CT slice (Figure 6.3).

This algorithm for assembling gyroid unit cells of varying  $\rho_{app}$  corresponding to that of the original CT slice produced structures bearing high fidelity to the femoral neck in terms of geometry and density distribution. The outer envelope of the femoral neck was accurately captured by the algorithm, as

were features like the Ward's triangle (Figure 6.4). Furthermore, the contiguity of the trabecular struts at the boundaries of unit cells corresponding to different  $\rho_{app}$  was seen to be preserved.

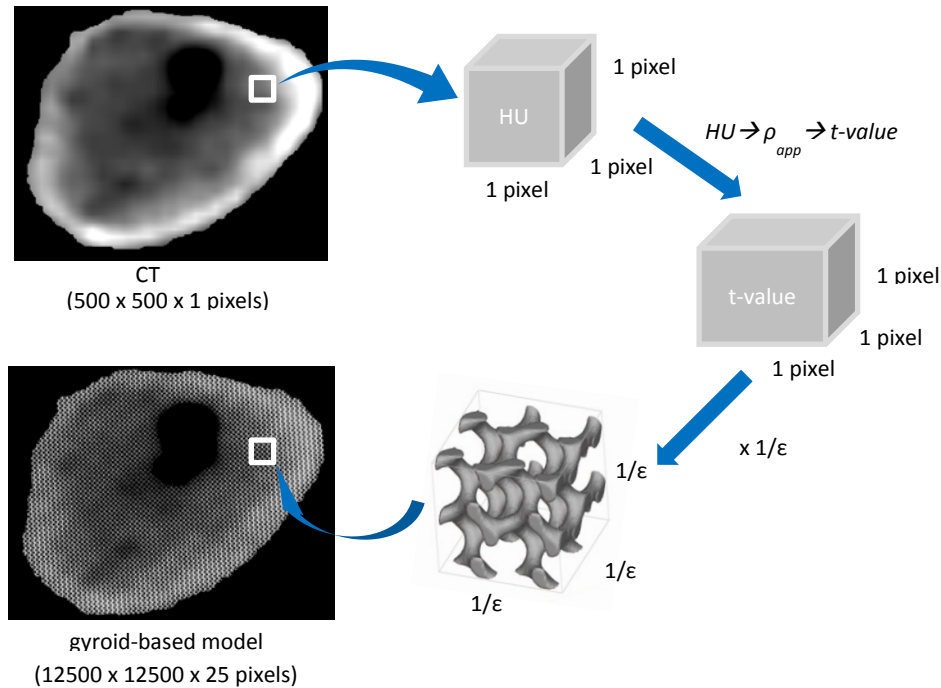


**Figure 6.3 . Schematic showing procedure for assembling gyroid-based unit cells into macroscale structure, based on the density distribution of a CT image obtained perpendicular to the longitudinal axis of the femoral neck**

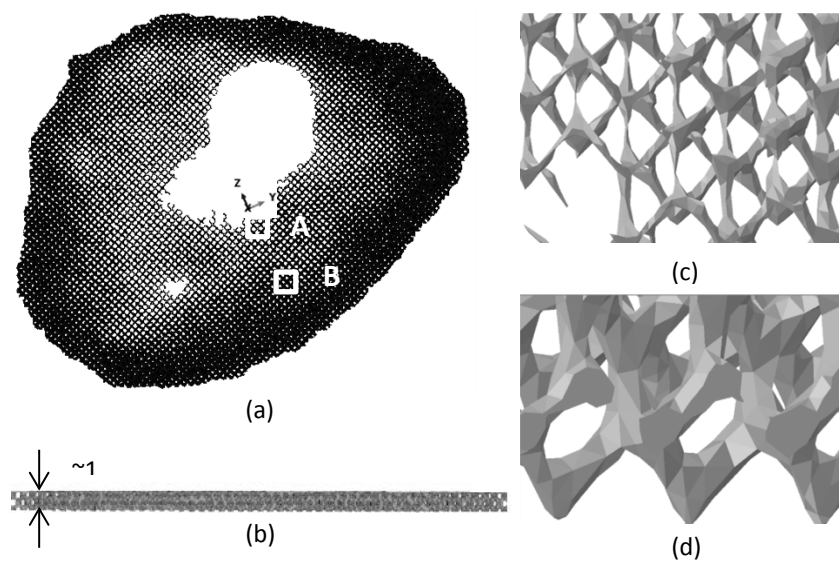


**Figure 6.4 (a) Three-dimensional macroscale structure generated using the assembly procedure, showing the heterogeneous density distribution across the femoral neck, (b) Side view of the macroscale structure, (c) Zoom-in on the low volume fraction region labelled A in (a) showing relatively thin trabecular struts, and (d) Zoom-in on the high volume fraction location labelled B in (a) showing relatively thick trabecular struts**

## 6.2 Finite element (FE) simulation on FN structure

### 6.2.1 Mechanical properties of bone tissue material

The gyroid-based FN structure generated above was imported into ABAQUS software suite for FE analysis. The bone tissue was modelled using a bilinear elastoplastic material, following [80], with the following parameters: Young's modulus,  $E = 18$  GPa, Poisson's ratio,  $\nu = 0.3$ , yield strength of 134.3 MPa and a post-yield modulus of 5% of  $E$ . Furthermore, the tissue strength is assumed to be symmetric in both compression and tension [52, 79, 154].

Furthermore, a second set of simulations were performed using purely linear elastic properties for the tissue material, with Young's modulus,  $E = 18$  GPa and Poisson's ratio,  $\nu = 0.3$ . The motivation for this second set of simulations lies in the fact that it would enable us to discern the influence of tissue-level plastic yielding on the macro-scale (i.e., effective) mechanical behaviour of the FN structure by contrasting it with the previous set of simulations.

### 6.2.2 Loading and boundary conditions

In a physically meaningful loading scenario (whether stance, gait, or fall), the femoral neck region usually bears several types of loading, including compressive stresses and substantial bending stresses. However, at this preliminary stage of our simulations, we intend to investigate the possibility of trabecular strut buckling occurring inside the FN structure, and its effect on macroscopic mechanical properties. To this effect, we ran FE simulations on the FN structure under purely compressive loading, i.e., we constrained all the



nodes on the bottom face of the FN structure and displaced all the nodes on the top face by a uniform value (Figure 6.5).

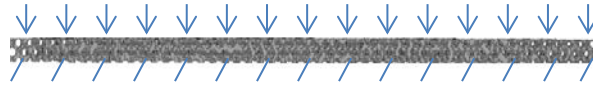


**Figure 6.5** Schematic showing the boundary conditions applied on the gyroid-based femoral neck structure under pure compression

It is to be noted that our rationale for applying only displacements (i.e., Dirichlet boundary conditions), and no forces (i.e., Neumann boundary conditions), in all our simulations, was in order to be able to capture any limit loads and subsequent macroscopic softening that may occur in the structure.

### 6.2.3 Results

Once the simulations were successfully completed, we obtained the effective material properties of the FN structure by summing up the nodal reaction forces on all of the nodes on the top surface of the structure (Figure 6.6). The displacements of the nodes at the top surface were then tabulated against the corresponding reaction force on the nodes and plotted.

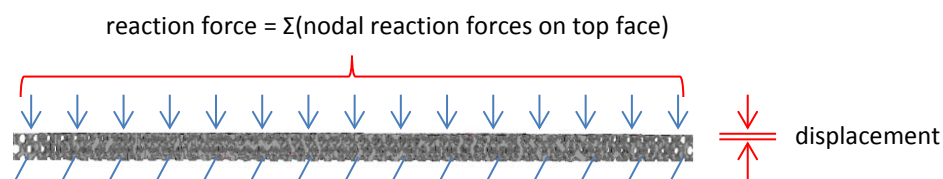


**Figure 6.6** Schematic showing the procedure for obtaining the force vs. displacement graph for the gyroid-based femoral neck structure

The graphs below (Figure 6.7) show that the FN structure with bilinear elastoplastic tissue material exhibited a decrease in its stiffness at a displacement of approximately  $5\mu\text{m}$ . However, there was no limit load (i.e., load maximum) noted in the graphs, i.e., the reaction force continues to

increase with increasing compressive displacement with no explicit evidence of macro-scale softening behaviour.

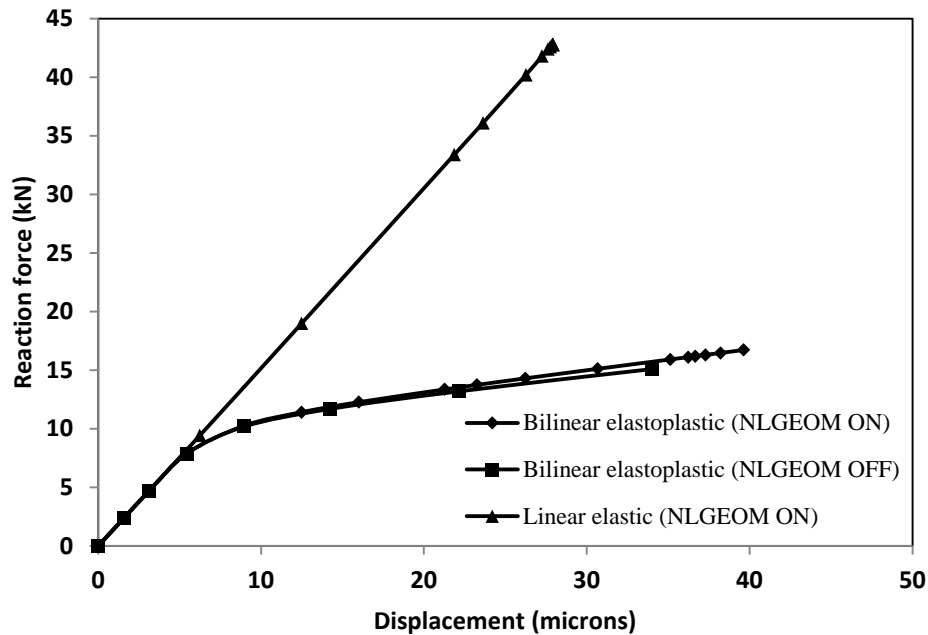


**Figure 6.7** Graphs of reaction force vs. displacement for the gyroid-based femoral neck structure with different tissue materials

Visual inspection of the individual trabecular struts at select locations in the FN structure furnished evidence for large deformation bending occurring in the relatively thinner struts lying in regions of low volume fraction. In contradistinction, thicker trabecular struts occurring in regions of relatively high volume fraction manifested no such large deformation bending phenomena (Figure 6.8).

In order to better understand the relationship between the large deformation bending (i.e., buckling) of individual trabecular struts occurring inside the FN structure and the overall mechanical integrity, we further post-processed the results to obtain the nodal forces for sets of nodes at different locations on the top surface of the FN structure (Figure 6.9).

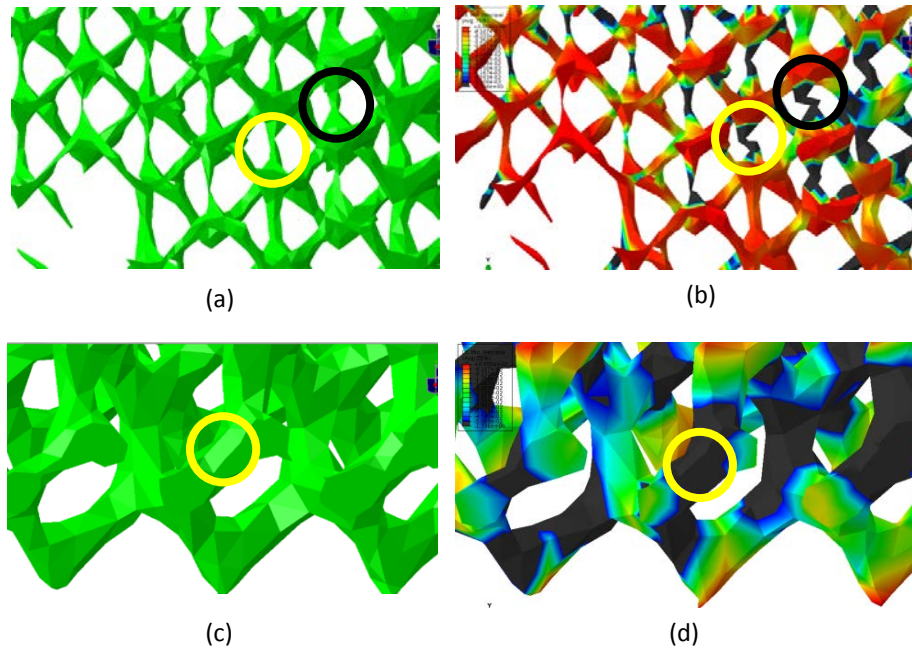


**Figure 6.8** (a) undeformed structure showing the relatively thinner trabecular struts at a region of low volume fraction; (b) deformed structure at the same location as in (a), showing large deformation bending behaviour occurring in the thinner trabecular struts; (c) undeformed structure showing the relatively thicker trabecular struts at a region of high volume fraction; (d) deformed structure at the same location as in (c) showing lack of any large deformation bending behaviour in the thick trabecular struts

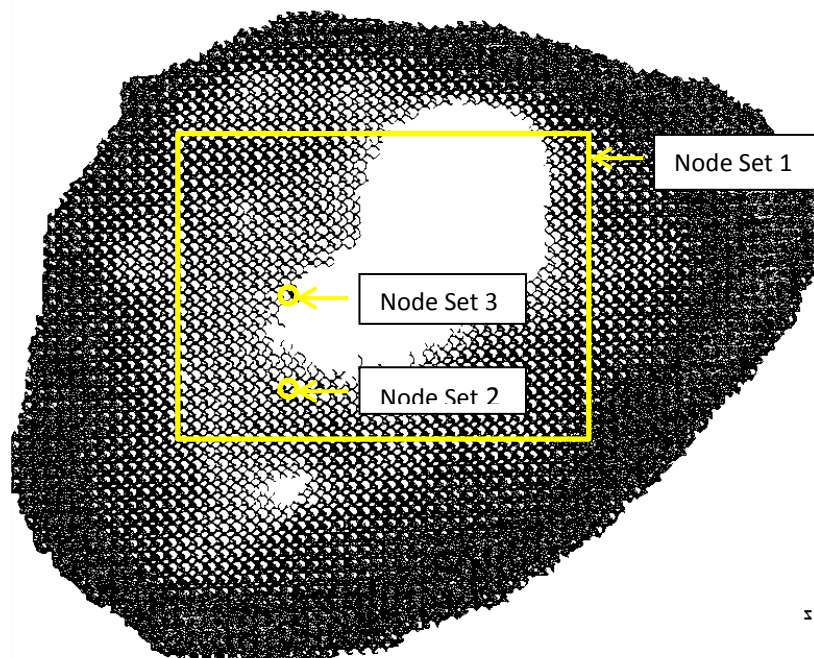


**Figure 6.9** Femoral neck structure showing the locations of the three node sets chosen for further investigation of trabecular buckling phenomena

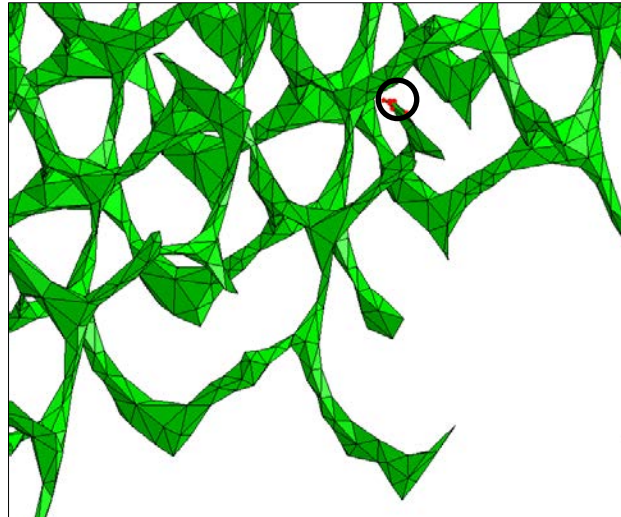


Figure 6.10 Zoom-in on Node Set 3, showing the nodes (circled) on the top surface of a particular trabecular strut at a region of low volume fraction

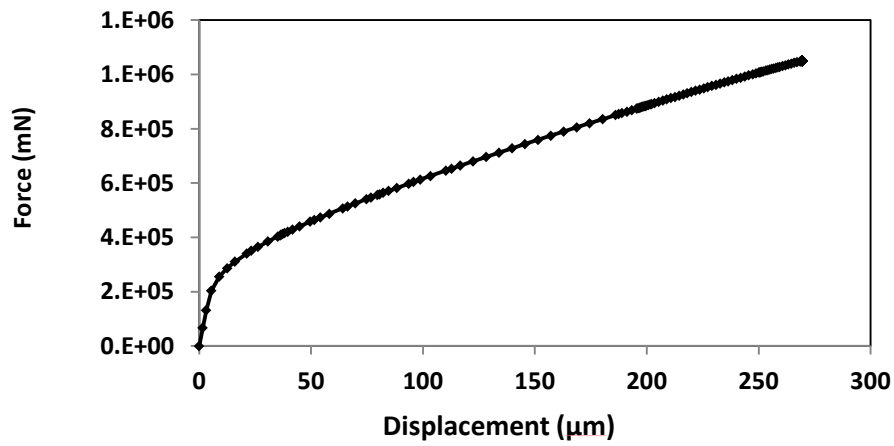


Figure 6.11 Force vs. displacement graph for node set 1

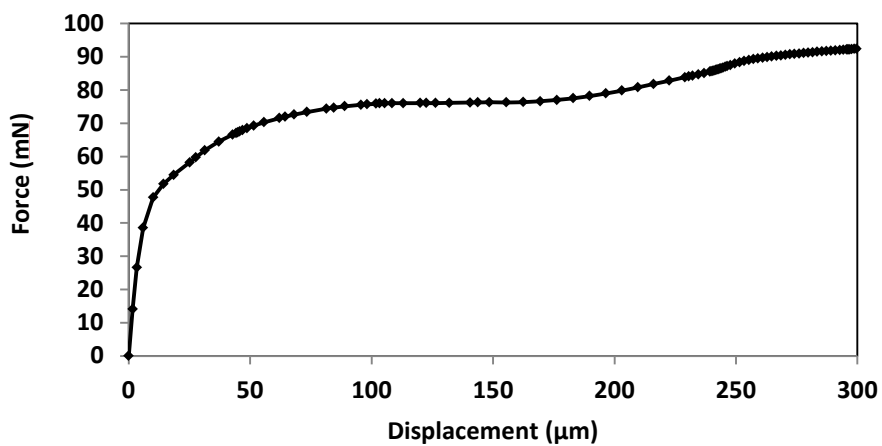
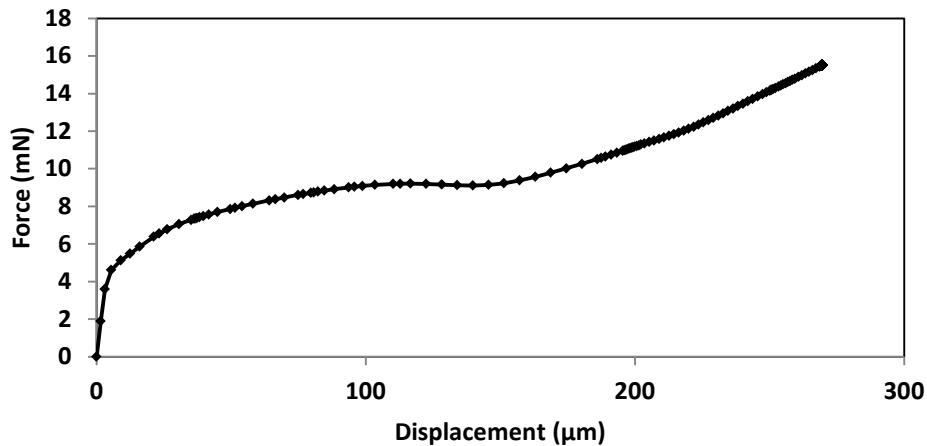


Figure 6.12 Force vs. displacement graph for node set 2



**Figure 6.13 Force vs. displacement graph for node set 3**

Node Set 1 comprises the largest number of nodes located in regions of a diverse range of volume fractions; while Node Sets 2 and 3 contain only the nodes located on two particular struts in regions of relatively low volume fraction, in the immediate vicinity of the Ward's triangle (Figure 6.9 and Figure 6.10).

The graphs of the force vs. displacement were plotted for each of the three abovementioned node sets.

For all three node sets (Figure 6.11, Figure 6.12 and Figure 6.13), the graphs initially show a steady linear increase in the reaction force with increasing compressive displacement of the structure. This linear regime occurs prior to any large deformation bending in the trabecular struts. Subsequently, the graphs show that for Node Set 1 (Figure 6.11), there is no plateau behaviour in the reaction force, i.e., though there is a decrease in the structural stiffness, the reaction force continues to increase steadily with displacement. However, for Node Sets 2 and 3 (Figure 6.12 and Figure 6.13), there exists a pronounced plateau region immediately following the linear regime, during which the

reaction force on these particular node sets does not increase with increasing displacement.

Since Node Set 2 and 3 correspond to trabecular struts lying in regions of comparatively low volume fraction, it can be understood that these particular struts suffer large deformation bending (i.e., buckling). However, since Node Set 1, which occupies a much larger area of the top surface reveals no such plateau-like behaviour, it can be ascertained that the effect of the buckling of individual trabecular struts is most significant in regions of low volume fraction and is diminished in larger regions where the thicker struts lying in adjacent regions of relatively high volume fraction are able to bear the compressive forces adequately, maintaining the stiffness of the structure.

This finding has implications for our understanding of femoral neck fractures occurring in people with severe osteopenia or osteoporosis, whose bone density is drastically attenuated, leading to large regions of bone with very low volume fraction. We interpret our results to understand that such low density bones as are typical in osteoporotic subjects are likely to fail due to the unmitigated buckling of large numbers of trabecular struts located across the entire femoral neck region, leading eventually to catastrophic failure of the entire bone. Our findings further suggest that clinical intervention should place emphasis on checking the cascading nature of trabecular strut buckling occurring in regions of low volume fraction, possibly by application of drugs that boost the volume fraction of bone at critical locations where there are large numbers of trabecular struts all of low volume fraction.

### 6.3 Continuum-based simulations – A comparison

#### 6.3.1 Using classical density-modulus mapping algorithms

In order to compare the effect of adding microstructural detail to the macro-scale structure, we performed similar analysis using the same FN structure, but with material properties based on the classical algorithm to convert apparent density to elastic modulus.

The same CT image of the FN structure that was used in Section 6.1 above was imported into MIMICS image processing suite and a density-based thresholding algorithm used to separate bone tissue from the surrounding pixels. The resulting three-dimensional solid structure was then meshed with tetrahedral elements (C3D4) in the mesh generation software 3-matic. The volume mesh (containing 3187 nodes and 9436 elements) was then exported back to MIMICS software for assignment of material properties. In brief, each of the tetrahedral elements is mapped to its corresponding location in the original CT slice, and the apparent density associated with that location used as the material properties of that particular element. Subsequently, the apparent density is mapped using a cubic relationship [153] in order to obtain the corresponding Young's modulus of that element:

$$E(MPa) = 4249\rho_{app}^3 \quad (6.5)$$

where  $\rho_{app}$  is in  $\text{g/cm}^3$ .

Theoretically, this procedure would generate as many different material definitions as there are elements in the volume mesh, leading to massive input files that require enormous amounts of computational power to manipulate and

solve. Practically, this problem has been addressed by other researchers by clumping a range of apparent densities into one material, such that all elements with apparent density lying within that range possess uniform material properties. To that effect, we chose to discretize the range of apparent densities into seven different element groups. The figure below shows the above-described procedure schematically (Figure 6.14).

Boundary conditions identical to those described in Section 6.2.2 above were applied on the FN structure, and FE simulations performed in ABAQUS software. Subsequently, the output files were post-processed in a manner similar to that described in Section 6.2.3 to obtain the graph of reaction force at the nodes on the top surface versus the displacement enforced at the same nodes.

Figure 6.15 shows the graph generated using this classical density-modulus mapping algorithm superposed on that obtained in Section 6.2 above with gyroid-based microstructure.

The results showed that, for the structure generated using the classical density-modulus mapping algorithm, the reaction force continued to increase linearly with increasing compressive displacement, in contrast to that with the gyroid-generated microstructure, where there was a decrease in the tangent structural stiffness occurring when the reaction force was approximately 10kN.

It is to be noted that, while the structure generated using the classical density-modulus mapping algorithm contains only purely linear-elastic materials, the structure generated using the gyroid-based unit cell contains bilinear elasto-plastic elements.



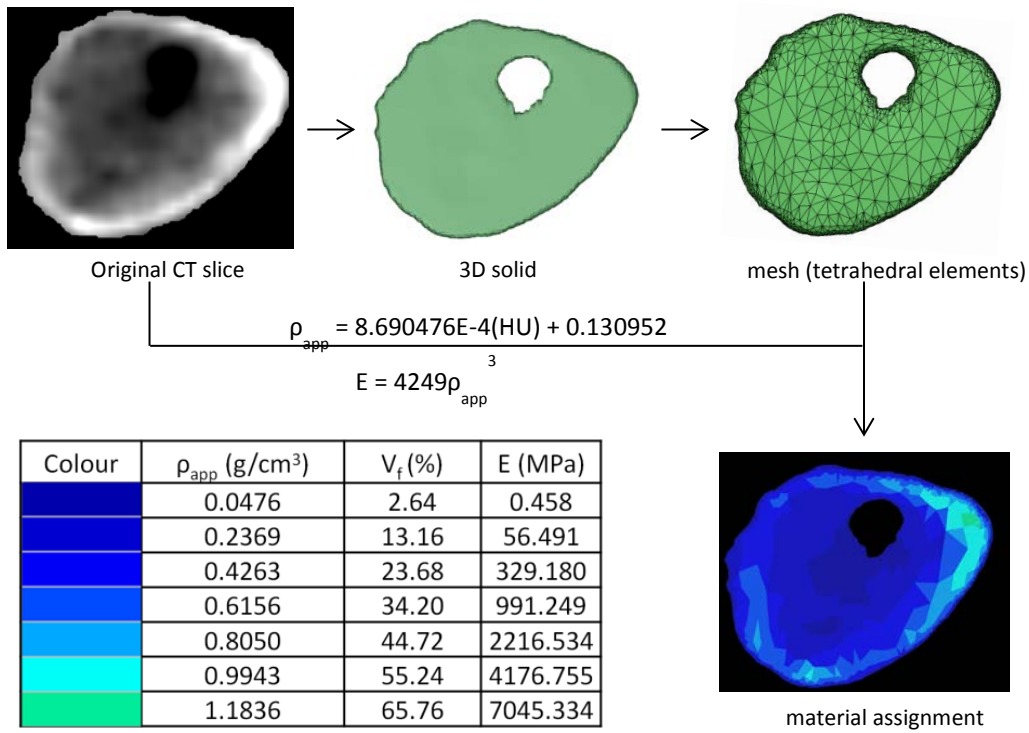


Figure 6.14 Schematic showing procedure followed to assign material properties to original CT slice

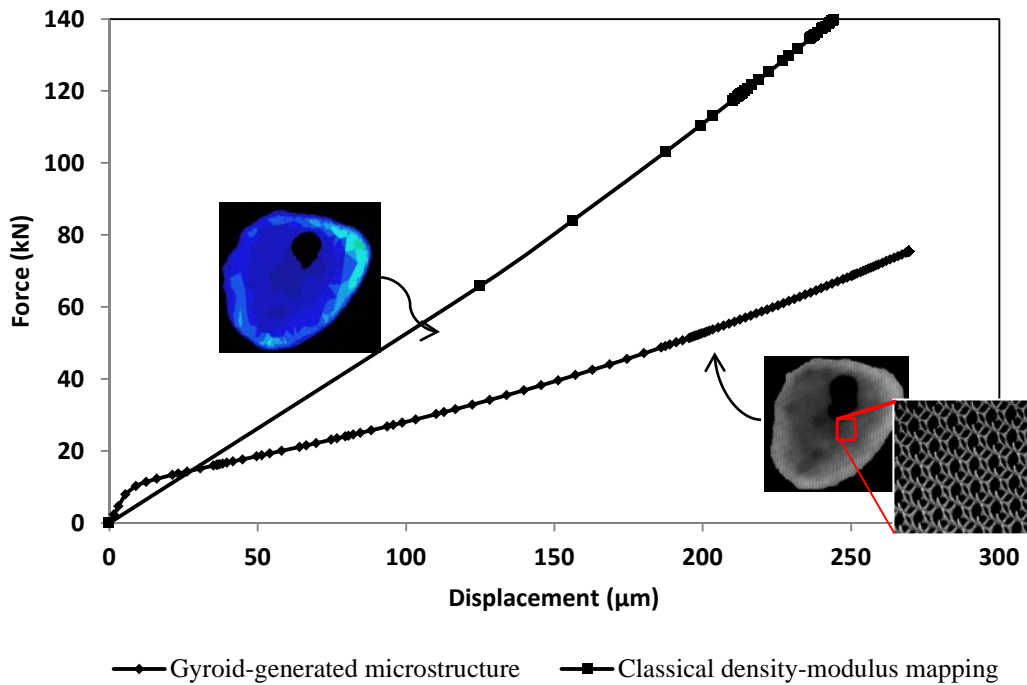


Figure 6.15 Graphs of force vs. displacement for the femoral neck structure with materials defined by classical density-modulus mapping compared with gyroid-generated microstructure (bilinear elasto-plastic material properties)

Hence, the decrease in the structural stiffness of the latter structure could be a result of either, or both, of the two phenomena: buckling and material yielding of trabecular struts, neither for which is present in the structure generated using the classical density-modulus mapping. This enables us to discern a fundamental shortcoming inherent in studies that employ the classical density-modulus mapping algorithms to generate FE models from CT images – such models, owing to their lack of microstructural detail, cannot capture important microscale phenomena like buckling (i.e., large deformation bending) of trabecular struts, which could lead to a drastic decrease in structural stiffness.

### **6.3.2 Using classical density-modulus mapping with phenomenological plasticity**

The material element definitions employed in Section 6.3.1 above were modified to incorporate plasticity, with the hardening modulus (i.e., the tangent modulus in the plastic regime) for each of the seven materials arbitrarily defined to be 5% of the corresponding Young's modulus, and a uniform yield true strain equal to the tissue yield strain of 0.7417%. Figure 6.16 shows the graph of force vs. displacement generated for this structure.

The graph corresponding to the structure with materials defined through the classical density-modulus algorithm incorporating phenomenological plasticity showed a structural stiffness lower than that corresponding to the structure with purely linear elastic materials, and much closer to that of the structure comprising gyroid-based unit cells. It is understood that, in FE studies which define material properties using the classical density-modulus mapping algorithm, it is imperative to incorporate plastic yielding in the models.

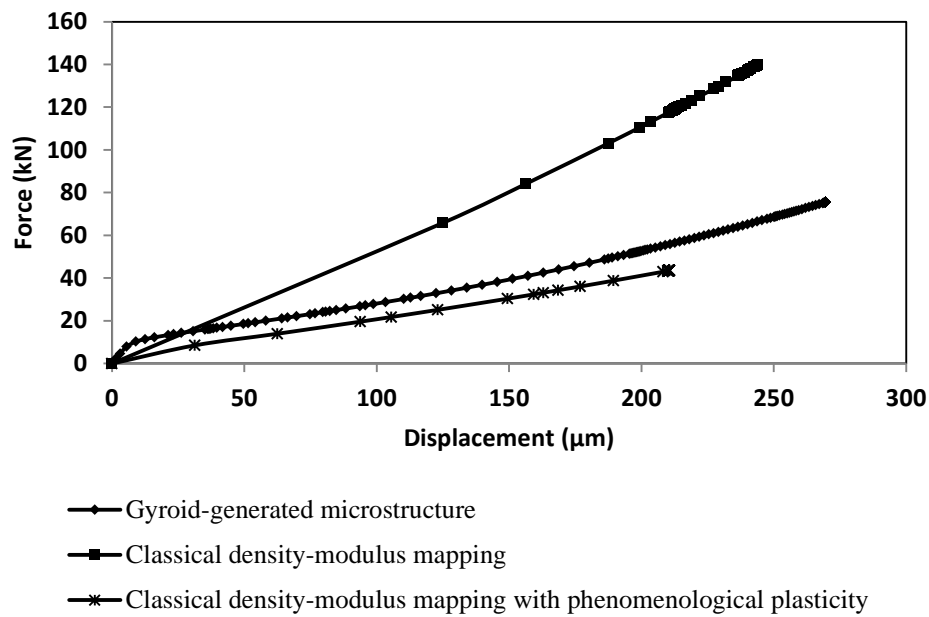


**Figure 6.16** Graphs of force vs. displacement for the femoral neck structure with materials defined by classical density-modulus mapping with phenomenological plasticity included superimposed onto Figure 6.15

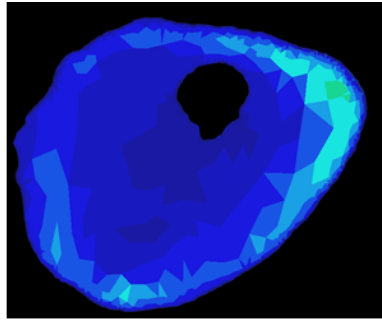
However, the difficulty lies in the choice of the manner of including phenomenological plasticity in the material definitions, especially the parameter relating the hardening modulus to the Young's modulus – extensive large-deformation experimental calibration studies on trabecular bone samples of a wide range of volume fractions are warranted.

### 6.3.3 Using material properties derived by homogenized gyroid-based unit cells

On the one hand, the structure generated using gyroid-based microstructure in Section 6.2 above successfully accounts for microstructural phenomena like trabecular strut buckling; however, it contains a very large number of degrees of freedom, making simulations very computationally intensive. On the other hand, the structures generated using the classical density-modulus mapping algorithms (in Sections 6.3.1 and 6.3.2 above), owing to their substantially fewer degrees of freedom, are computationally much easier to analyse;

however, they fail to capture trabecular-level phenomena that could be critical in failure analysis. We attempt in this section to combine the accuracy of the former method with the computational simplicity of the latter method, by undertaking a sequential dual-scale analysis whereby the homogenized material properties of the gyroid-based unit cells are used as input parameters for the macroscale (i.e., FN scale) analysis. For each of the materials in the FN volume mesh with a volume fraction below 50%, the data of the true stress vs. true strain for a gyroid-based unit cell of identical volume fraction was obtained as described in Chapter 2 and supplied as input material properties. The cutoff value of 50% volume fraction was chosen based on the finding [20] that at very large volume fractions, micro-scale phenomena like trabecular strut buckling become less important as the struts become thicker and are thus better able to avoid large deformation bending. Thus, for all the materials in the FN volume mesh with volume fraction above 50%, the classical density-modulus mapping algorithm with phenomenological plasticity was preserved (Figure 6.17).

For the material corresponding to the lowest volume fraction, i.e., 2.64%, it was not possible to render a corresponding gyroid-based unit cell owing to the fact that the trabecular struts became disconnected from each other. Hence, for this particular case, we preserved the classical density-modulus algorithm with phenomenological plasticity. Since the number of elements in the volume mesh belonging to this material definition was very few, it is assumed that the fact that the gyroid-based unit cell was not used in generating its material properties would have a negligible effect on the overall properties of the structure.



Colour	$\rho_{app}$ (g/cm <sup>3</sup> )	$V_f$ (%)	Material assignment
Dark Blue	0.0476	2.64	Classical $\rho$ -E mapping (linear elastic) + phenomenological plasticity
Blue	0.2369	13.16	Gyroid ( $V_f = 11\%$ )
Light Blue	0.4263	23.68	Gyroid ( $V_f = 25\%$ )
Medium Blue	0.6156	34.20	Gyroid ( $V_f = 35\%$ )
Cyan	0.8050	44.72	Gyroid ( $V_f = 45\%$ )
Light Green	0.9943	55.24	Classical $\rho$ -E mapping (linear elastic) + phenomenological plasticity
Dark Green	1.1836	65.76	Classical $\rho$ -E mapping (linear elastic) + phenomenological plasticity

Figure 6.17 Material assignment in the femoral neck structure

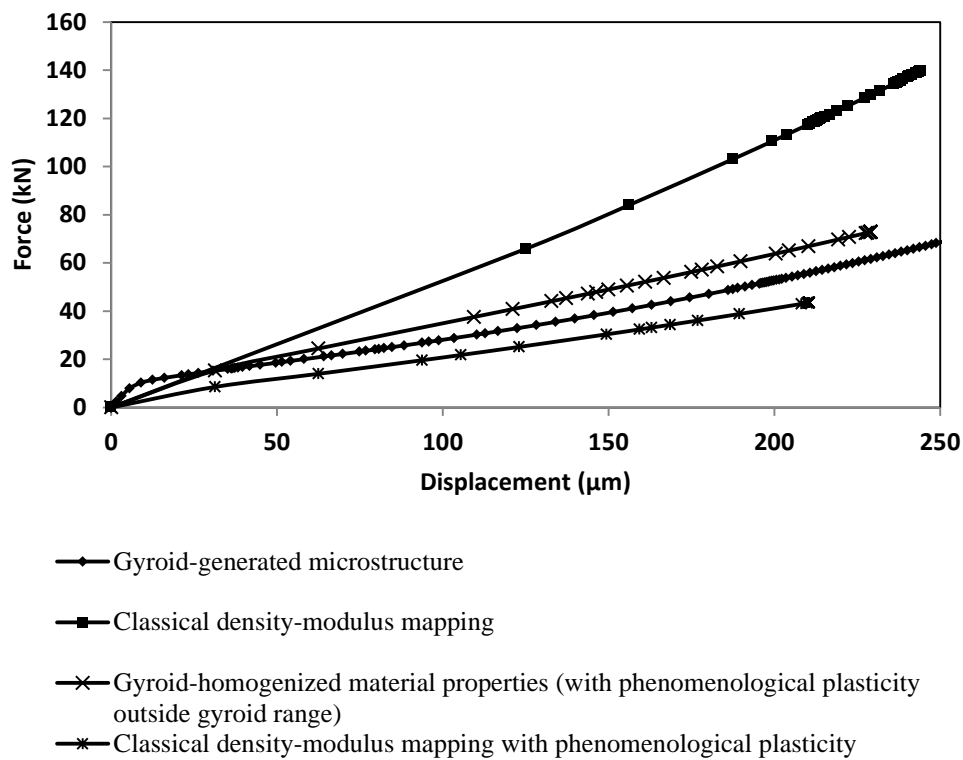


Figure 6.18 Graphs of force vs. displacement for the femoral neck structure with materials defined by various methods

It is seen (Figure 6.18) that the force-displacement graph generated by the structure with material properties obtained by homogenizing the gyroid-based unit cells showed a closer fit to the graph generated by structure comprising gyroid-based microstructure than that corresponding to the structure with linear elastic materials obtained through the classical density-modulus mapping algorithm. This implies that the material properties obtained by homogenizing the gyroid-based unit cells furnish a more suitable input to the macro-scale model than purely linear elastic elements, because the homogenization process captures the decrease in structural stiffness ensuing from micro-scale phenomena like large deformation bending of trabecular struts. Thus, when the homogenized material properties are used as input parameters for the macro-scale simulations, the mechanical consequences of the occurrence of micro-scale buckling are still accounted for in the macro-scale simulations, in spite of the fact that the trabecular struts are no longer physically present in the structure.

## **6.4 Yield surface of FN structure**

### **6.4.1 Boundary conditions and FE analysis**

We studied the yield envelope of the FN structure generated through the procedure described in Section 6.1 in order to understand the mechanisms linking the loads applied to the initiation of yield. Specifically, we imposed two kinds of displacement-controlled loading, namely, a purely compressive displacement in the longitudinal direction, and an angular displacement about the anterior-posterior axis. The former produces compressive longitudinal stresses in the FN structure, while the latter causes a bending moment to be

applied about the anterior-posterior axis. In ABAQUS, it is considerably difficult to apply an angular displacement directly onto a set of nodes. To circumvent this problem, we followed the procedure detailed below.

After importing the original CT slice into the image processing software ImageJ, the coordinates of the centroid  $C$  of the bone area were located using the measurement algorithms available in the software (Figure 6.19). Subsequently, we also obtained the directions of the principal moments of inertia of the bone area in terms of the angle subtended by the principal axes of inertia of the bone area to the positive horizontal axis. We defined one of the principal axes to represent the anterior-posterior axis of the FN structure, about which moments corresponding to either stance or fall modes were to be applied.

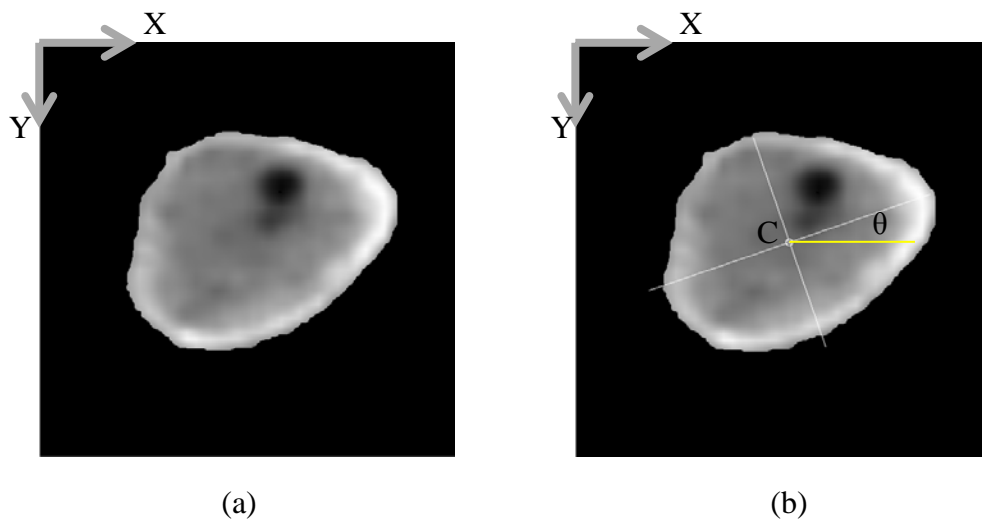


**Figure 6.19** (a) Original CT image of the narrow-neck region. Axes in grey indicate the default ImageJ coordinate system (b) Location of the area centroid  $C$  (256.7 pixels, 240.6 pixels) and angle  $\theta$  (19 degrees) subtended by one of the principal axes of the moment of inertia to the positive x-axis.

After importing into ABAQUS the FN structure as generated in Section 6.3 above, the coordinates of the centroid  $C$  were used to create a reference point (RP) at that location, on one of the surfaces of the FN structure. A right-handed coordinate system was defined so that the positive x-axis points in the longitudinal direction, the positive y-axis towards the inferior region of the FN structure, and the positive z-axis towards the anterior region (Figure 6.20).

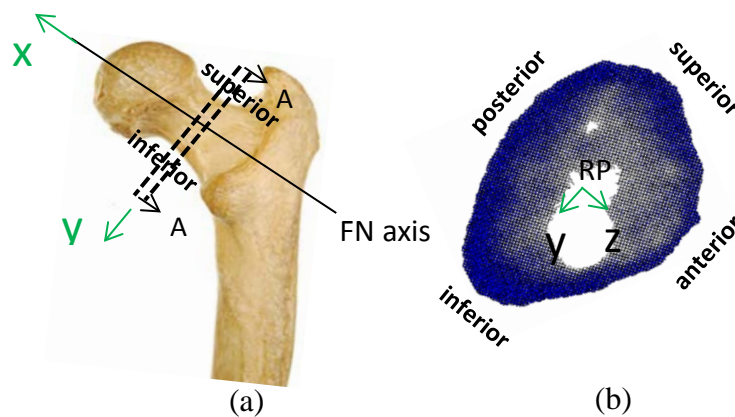


**Figure 6.20** (a) Macroscopic view of the proximal femur, showing the narrow neck region (in black dashed lines), and the right-hand coordinate system; (b) FN structure based on Section A-A, showing the location of the reference point (RP) and the orientation of the right-hand coordinate system as used in ABAQUS

In the next step, we employed kinematical coupling to constrain the RP node to all of the nodes on the top surface of the FN structure [119]. Kinematical coupling constraints are used to limit the motion of a group of nodes to the rigid body motion defined on a reference node. In particular, constraining all the six degrees of freedom (three corresponding to translation and three to rotation) of the RP node ('master') is equivalent to having a rigid beam between the RP node and each of the surface nodes ('slaves'). In other words, once the RP node has been kinematically coupled in the above-described manner to the nodes on the top surface of the FN structure, applying a longitudinal compressive displacement on the RP node alone has the effect of



applying the the same displacement to all of the surface nodes, while applying an angular displacement on the RP node about, say, the z-axis, leads to a couple about the z-axis being applied on the entire surface of the FN structure (Figure 6.21).

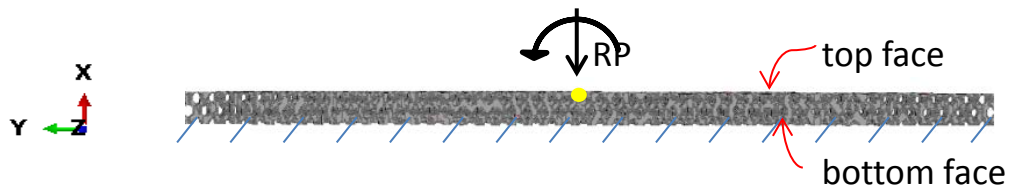


**Figure 6.21** Schematic showing the boundary conditions applied on the FN structure. Arrows in black denote the longitudinal compressive displacement and the angular displacement about the z-axis being applied at the RP node

Keeping the bottom face fully constrained, we applied varying combinations of compressive and angular displacements on the RP node. Specifically, the application of a compressive displacement on the RP node leads to a compressive force in the longitudinal direction of the FN structure, while the application of an angular displacement about the positive z-direction (according to the right-hand rule, whereby the right-hand thumb points along the positive z-axis and the fingers curl in the direction of the ensuing couple) causes a couple about the z-axis in such a manner that the inferior region experiences compression while the superior region experiences tension, thereby replicating stance mode. Conversely, a combination of a compressive force in the longitudinal direction of the FN structure with an angular displacement about the negative z-direction mimics fall mode, during which the inferior region is in tension and the superior region in compression.

Once the boundary conditions have been applied correctly on the FN structure, a geometrically nonlinear FE simulation was performed. Post-processing of the simulation involved extracting the data corresponding to the reaction force

(-RF1) versus the displacement (-U1) of the RP node and the reaction moment (RM3) versus the angle rotated (UR3) by the RP node. The results of a typical simulation are shown below (Figure 6.22 and Figure 6.23), corresponding to the following input parameters:

$U1 = -25$  (displacements are in  $\mu\text{m}$ )

$U2 = U3 = UR1 = UR2 = 0$

$UR3 = +0.05$  radians

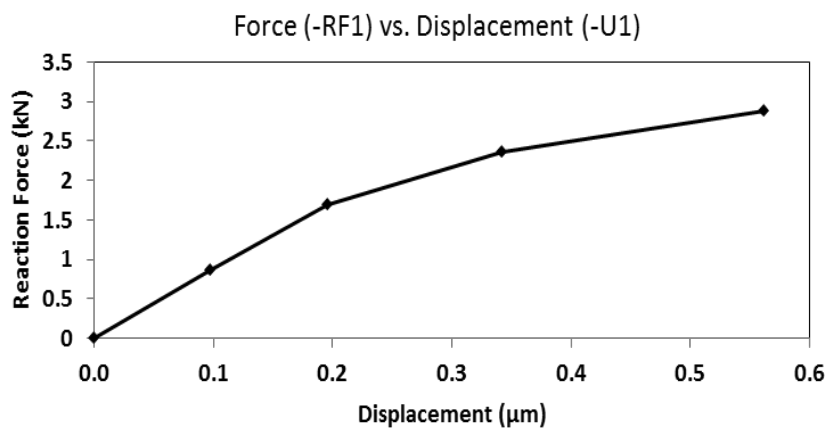


Figure 6.22 Graph of reaction force (-RF1) vs. displacement (-U1)

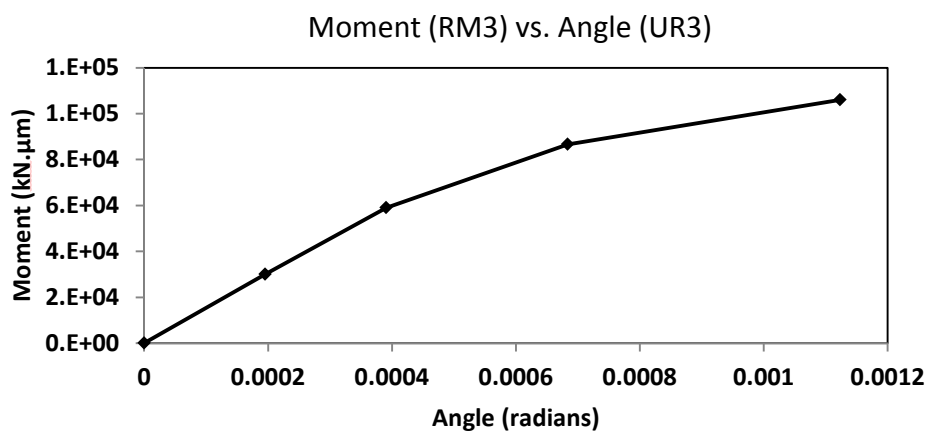


Figure 6.23 Graph of reaction moment (RM3) vs. angular displacement (UR3)

### 6.4.2 Plotting and fitting of yield points

The graphs of force versus displacement and moment versus rotation angle were then processed to establish the point of first yield at the macroscale (i.e., the FN scale). Details of the procedure are illustrated using the force versus displacement plot shown below (Figure 6.24) – the same steps apply, *mutatis mutandis*, to the plot of moment versus rotation angle.

The initial structural stiffness,  $S_{init}$ , is calculated as the slope of the force vs. displacement graph at the first successfully converged load increment of the FE simulation. Then, the tangent structural stiffness,  $S_i$ , is calculated for each successive load increment  $i$  as the slope of the graph at the location corresponding to the load increment  $i$ .

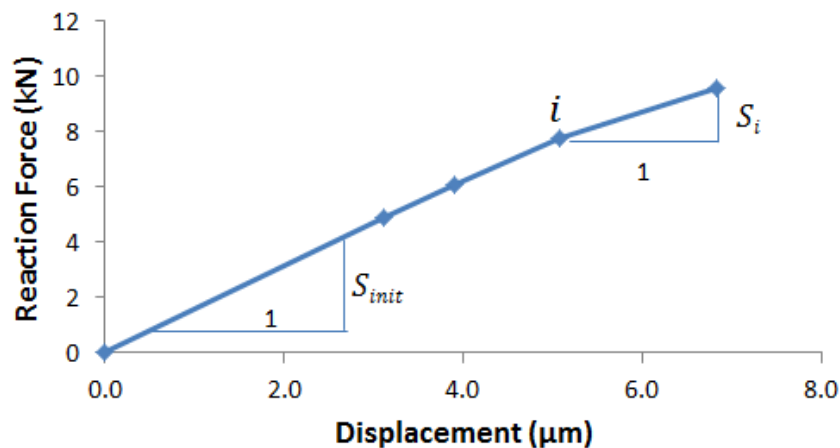


Figure 6.24 Procedure showing the determination of the point of first yield at the macroscale

Subsequently, the ratio of the tangent structural stiffness  $S_i$  to the initial structural stiffness  $S_{init}$  is calculated and tabulated (Table 6.1).

Displacement ( $\mu\text{m}$ )	Reaction Force (kN)	Tangent Stiffness, $S_i$ (kN/ $\mu\text{m}$ )	Ratio of Tangent Stiffness to Initial Stiffness, $S_i/S_{init}$ (%)
0	0	-	-
3.12500	4.87721	$S_{init} = 1.56070720$	100.0
3.90625	6.08559	1.546726400	99.1
5.07812	7.77811	1.444289896	92.5
6.83594	9.61016	1.042228442	66.8

**Table 6.1** Table showing the tangent stiffness values along the force vs. displacement graph

The point of first yield is chosen to be the first point at which the ratio of tangent structural stiffness to the initial structural stiffness decreases to a value less than 90%, i.e., the point of first yield corresponds to the smallest value of  $i$  for which

$$\frac{S_i}{S_{init}} \leq 90\% \quad (6.6)$$

In the case described above, the point of first yield occurs at the displacement of 5.07812  $\mu\text{m}$  and a reaction force of 7.77811 kN. It is to be noted that the value of 90% chosen above to act as the criterion for onset of yield is an arbitrary one – variation in this value would eventually result in a yield envelope that is merely either more, or less, conservative, than the one we obtain. A similar process is carried out for the graph of reaction moment vs. rotation angle, and the point of first yield calculated. The points of first yield corresponding to the two graphs, i.e., reaction force vs. displacement, and reaction moment vs. rotation angle, are compared to ascertain which point was reached first in the course of the simulation, i.e., whether the first occurrence of macroscopic yield in the FN structure was caused by the reaction force or by the reaction moment. Subsequently, the values of reaction force and

reaction moment at this point of first (macroscopic) yield are taken to represent the state of loading on the FN structure.

Application of the same procedure to each of the other simulations corresponding to different permutations of applied longitudinal displacement and rotation angle furnishes us with a set of yield points that can then be plotted on a graph of moment vs. (compressive) force (Figure 6.25). Note that, as described above (Section 6.4.1), a positive moment corresponds to the stance mode and a negative moment to the fall mode, while a positive reaction force denotes longitudinal compression of the FN structure.

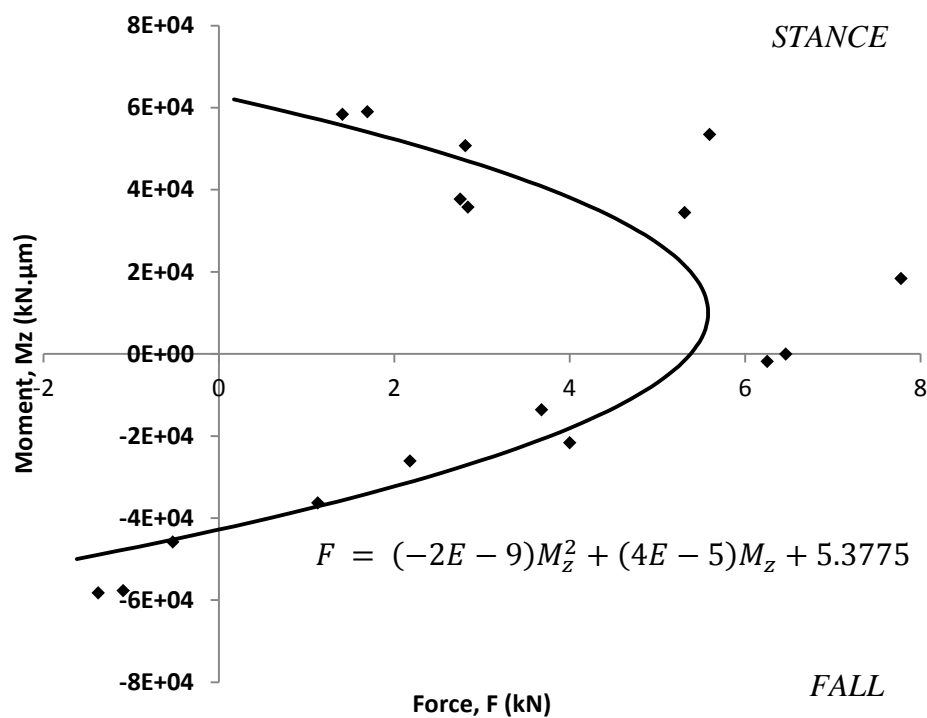


Figure 6.25 Yield surface of femoral neck structure

The yield points are fitted using MS Excel by the parabolic equation

$$F = (-2E - 9)M_z^2 + (4E - 5)M_z + 5.3775 \quad (6.7)$$

We assume in our work that the FN structure, under typical scenarios, experiences only compressive longitudinal forces, whether in stance or fall mode, and never tensile longitudinal forces, implying that, in the yield envelope plotted above, only the first and fourth quadrants are of significance.

### 6.4.3 Translation between organ (i.e., femur) scale and FN scale

The yield envelope as plotted above is based on the longitudinal forces and the moments experienced by the FN structure. Next, we relate these two FN-scale load parameters to the femur-scale loading conditions, in order to understand the link between the skeleton-scale loading (i.e., the loads applied on the proximal femur) and the yielding behaviour of the FN structure. The derivation that follows is based partially on the theory described in [1].

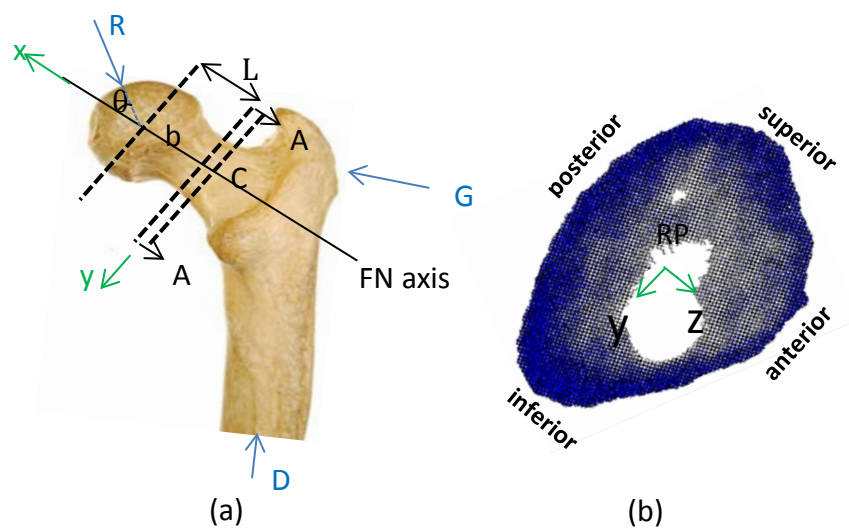


**Figure 6.26** (a) Macroscopic view of the proximal femur, showing the forces acting on the proximal femur (R: hip joint reaction force; G: ground reaction force present during fall; D: force exerted by distal femur) (b) FN structure based on Section A-A.

Considerations of force and moment equilibrium (Figure 6.26) at the point C give:

$$M_z \text{ (at C)} = (R\sin\theta)L \quad (6.8)$$

and

$$F = R\cos\theta \text{ (compressive)} \quad (6.9)$$

where

$$\theta = \begin{cases} +ve \text{ corresponds to stance mode} \\ -ve \text{ corresponds to fall mode} \end{cases} \quad (6.10)$$

Thus, by substituting equations (6.8) and (6.9) in (6.7), the equation of the yield envelope obtained above can be recast in terms of the femur-level parameters  $R$  and  $\theta$ :

$$(2E - 9)L^2R^2 \sin^2 \theta - (4E - 5)LR\sin\theta + R\cos\theta - 5.3775 = 0 \quad (6.11)$$

Assuming  $L$  to be a constant value of 25mm, equation (6.11) above can be plotted on a polar graph of  $R$  vs.  $\theta$  (Figure 6.27).

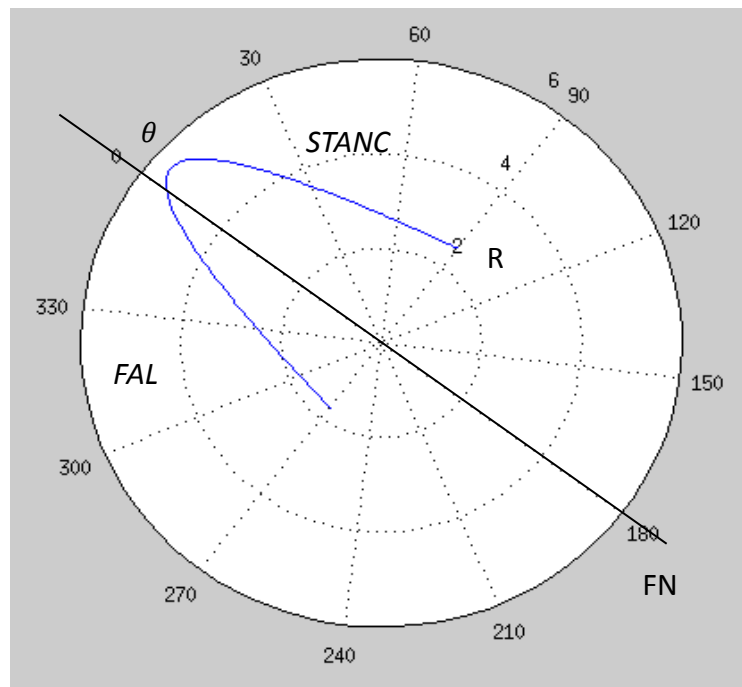


**Figure 6.27** Polar plot of  $R$  vs.  $\theta$  showing the yield surface of the femoral neck structure

#### 6.4.4 Discussion

Here, we illustrate by means of sample calculations how to use the graph shown in Figure 6.25 to determine whether or not the FN structure will suffer macroscopic yield for a given set of physiological loading conditions.

Based on the example described in [1], we assume the following parameters:

$$L = 25\text{mm} = 25000\mu\text{m}$$

$$R = 4 \times \text{body weight} = 2800\text{N} = 2.8\text{kN}$$

$$\theta = \begin{cases} +30^\circ & (\text{stance}) \\ -30^\circ & (\text{fall}) \end{cases}$$

Then, in stance mode, by the use of equation (6.8)

$$M_z = (R\sin\theta)L = 2.8 \sin 30^\circ \times 25000 = 3.5 \times 10^4 \text{kN} \cdot \mu\text{m}$$

and, by the use of equation (6.9)

$$F = R\cos\theta = 2.8\cos 30^\circ = 2.42\text{kN}$$

Conversely, in fall mode,

$$M_z = (R\sin\theta)L = 2.8 \sin(-30^\circ) \times 25000 = -3.5 \times 10^4 \text{kN} \cdot \mu\text{m}$$

and

$$F = R\cos\theta = 2.8\cos(-30^\circ) = 2.42\text{kN}$$

These two points corresponding to stance and fall modes are plotted on the graph shown in (Figure 6.28).



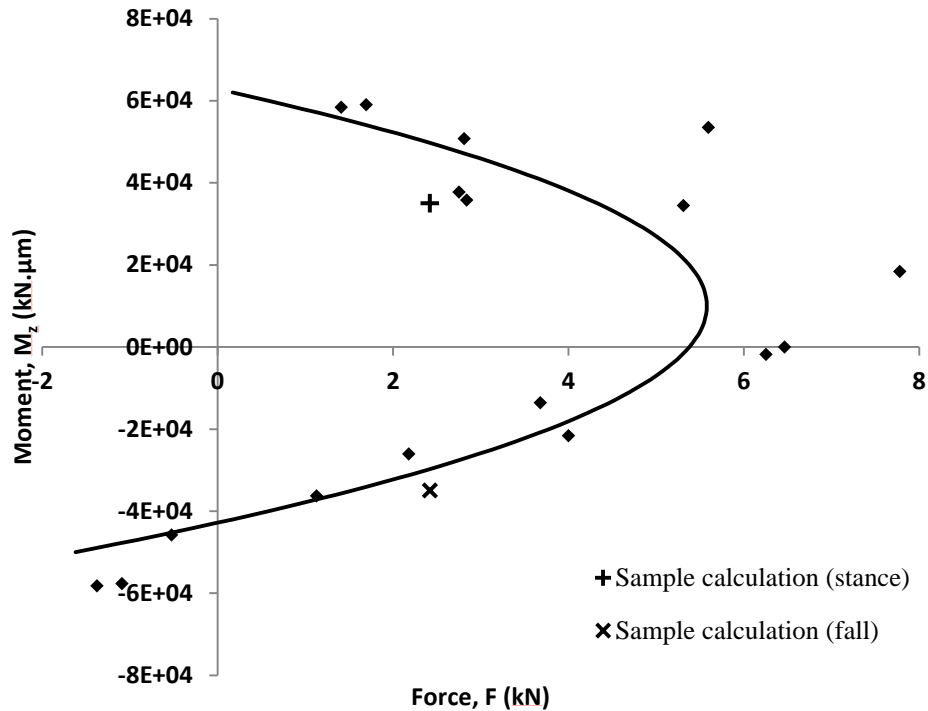


**Figure 6.28** Graph showing sample calculations to assess possibility of macro-scale yield for two cases

It is seen that the point corresponding to the stance mode lies within the yield envelope while that corresponding to the fall mode falls outside the yield envelope. This implies that, for the given set of loading conditions, the FN structure is safe in the stance mode, but likely to suffer failure during a fall to the side (provided that the loads during stance and fall are as assumed in the sample calculations above). This example brings to light one noteworthy feature of the yield envelope: the latter does not exhibit mirror symmetry about the horizontal (i.e., force) axis, but is instead shifted in such a manner that, for zero longitudinal force, the FN structure is capable of withstanding a larger moment in stance mode than in fall mode. A similar observation can be made in Figure 6.27 where the peak force  $R_{max}$  that the femur can withstand is approximately 5.5 kN, oriented at an angle of approximately  $+5^\circ$  (i.e., in stance

mode). This result is noteworthy because it sheds more light on the clinical observation that the human femur appears to be evolved in such a manner as to better withstand stance loads than fall loads, and the related phenomenon whereby a bone specimen that is reasonably healthy and not susceptible of failure under normal stance loading suffers catastrophic failure during a fall to the side of even relatively low severity [155].

Our findings can be better understood by comparing them with [1] and [156], who modelled the narrow neck cross-section by assuming two non-concentric circles, the inner core corresponding to trabecular bone, and the outer shell to cortical bone, as shown in Figure 6.29. The trabecular core was displaced superiorly by an eccentricity  $e$ , to mimic the bone density distribution observed in real human bone (Figure 6.29(a)), whereby the cortical shell at the inferior region is significantly thicker than that at the superior region.

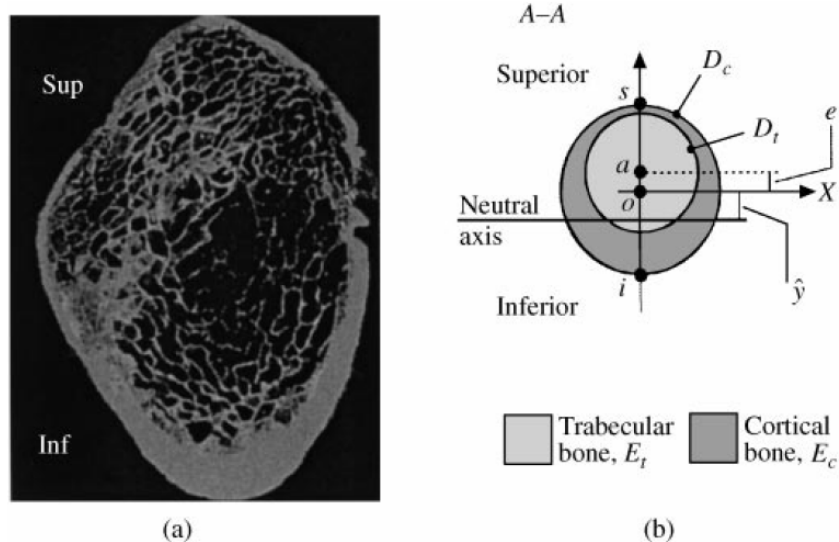


**Figure 6.29 (a) CT image showing cross-section of human femoral neck (b) Analytical model used by [1, 156]**

Their analytical study aimed at investigating the effect of this trabecular core eccentricity on the distribution of axial and bending stresses across the cross-section of the femoral neck, with particular emphasis on the possibility of failure being initiated at the superior or inferior regions of the narrow neck. Their results showed that the eccentricity of the trabecular core played a major role in redistributing stresses during normal gait loading and was thus an important bone adaption mechanism. More specifically, they discovered that:

- i. in stance mode, the trabecular core eccentricity helps to minimize bending stresses in the neck, while, in contradistinction, it causes an increase in the bending stresses in fall mode;
- ii. the superiorly eccentric trabecular bone causes the neutral axis of bending to shift towards the inferior of the neck, i.e., towards the inferior periosteal surface, and away from the superior side.

Their study showed that the eccentric distribution of the low-density trabecular core within the cortical shell is of remarkable biomechanical significance as it minimizes the susceptibility of failure during physiological loading while greatly compromising the femoral neck strength during a fall to the side. Without disparaging their important analytical model and insights, it is imperative to take note of the limitations of the work of Fox and Keaveny [156] described above. They assumed a simple circular cross-section for both the cortical shell and the trabecular core, an assumption that, though greatly simplifying calculation, is not valid for real bone. Secondly, they modelled both the cortical and the trabecular bone by linear elastic materials, ignoring the effect of plasticity and strain-hardening or softening. Thirdly, the apparent

density of trabecular bone is taken to be constant throughout the core, whereas the distribution of trabecular apparent density in real bone is not homogeneous. The last of their limiting assumptions, and possibly the most important in our context, is that the actual microstructure of trabecular bone, i.e., the existence of individual spicules (rods and plates), is ignored and instead a homogenized continuum of equivalent elastic properties is assumed in their model. Replacing the trabecular microstructure with homogenized continuum materials leaves out a fundamental mode of failure, namely, buckling (i.e., large deformation bending) of trabecular rods that may occur when the axial load acting on a single trabecular rod exceeds a critical value.

In the light of these limitations of the work by Fox and Keaveny [156], it behoves us now to extend our own analysis of the macro-scale yield envelope of the femoral neck as described above, by investigating the relationships between tissue-level failure mechanisms (like tissue yielding and strut buckling, and their synergistic effect) and the macro-level failure, both in stance and fall modes, of our own femoral neck structure (whose geometry and apparent density distribution are based on the CT image of a *real* femoral neck).

## **6.5 Deformation mechanisms active at the trabecular scale**

### **6.5.1 Theoretical considerations**

As already foreshadowed in Chapter 1 Section 1.3.3 above, the trabecular spicules are susceptible of failure by several complex mechanisms including yielding (crushing), buckling, or a synergistic combination of these two. Strut yielding occurs in short, thick, trabecular columns when the axial stress

exceeds the material yield strength, while buckling is initiated in more slender columns at axial compressive stresses well beneath the yield strength [76]. The exact mechanism of buckling varies depending on whether the column is modelled as being purely linearly elastic or elasto-plastic. Pin-ended columns that are assumed to be purely linear elastic undergo buckling at a critical stress defined by the Euler equation:

$$P_{cr} = \frac{\pi^2 EI}{L^2} \quad (6.12)$$

where

$E$ : Young's modulus

$I$ : moment of inertia of the column cross-section

$L$ : length of the column.

Conversely, columns whose material is modelled as being elasto-plastic undergo buckling at a critical load lower than that predicted by the Euler equation above – instead, as some localized region in the column begins to experience plastic deformation, the overall stiffness of the column is compromised and the structure manifests the so-called Engesser (or inelastic) buckling, according to the equation:

$$P_{cr} = \frac{\pi^2 E_t I}{L^2} \quad (6.13)$$

where

$E_t$  : tangent stiffness of the column material.

It is to be noted that both Euler (elastic) and Engesser (inelastic) buckling occur in slender columns at compressive axial stresses less than the uniaxial yield strength of the material. Hence, it is imperative to understand and account for the phenomenon of trabecular buckling when trying to gain insight into the macro-scale failure mechanisms of the bone structure.

### **6.5.2 FE simulations on a simple cylindrical geometry**

In the context of trabecular bone, the phenomenon of buckling, and inelastic buckling in particular, is poorly understood, probably partly because of the difficulties inherent in setting up experiments to study structures as minuscule as individual trabecular spicules [65]. Wherefore, we performed FE simulations using a simplified geometry of a trabecular strut based on that developed in [87]. Our primary objectives in this subsection were firstly to ascertain whether struts of dimensions typical of trabecular bone were susceptible of buckling, and secondly to establish the exact limits of slenderness ratio within which columns underwent inelastic buckling (as opposed to yielding and elastic buckling).

In [87], parametric studies using FEA were undertaken to develop and validate a single-strut model with geometry typical of trabecular bone that could manifest buckling. It was concluded therein that a cylindrical column of length 1.1 mm, variable radius (to be chosen based on the required slenderness ratio), a midpoint lateral displacement of 0.01mm, and meshed with two quadratic beam elements, could act as a reasonably accurate computational model for a single trabecular strut (Figure 6.30).

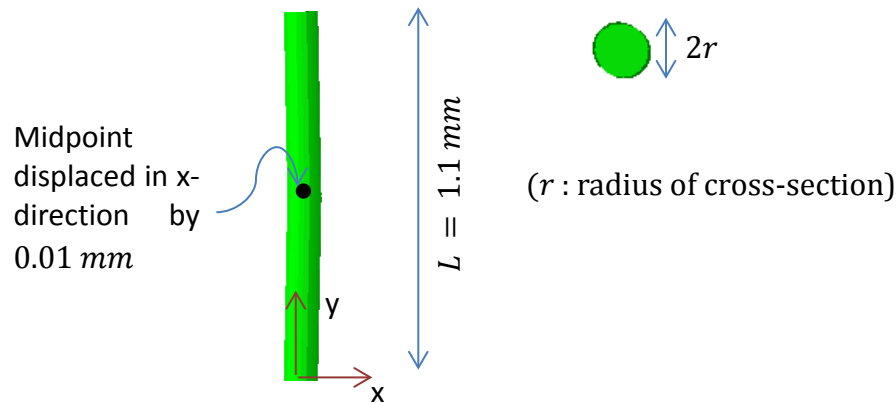


Figure 6.30 Cylindrical column representative of a single trabecular strut (based on [87])

Based on that study, we generated analogous structures for a range of slenderness ratios by varying the radius,  $r$ , of the cross-section while keeping the strut length,  $L$ , constant. The slenderness ratio is defined as:

$$\text{Slenderness ratio} = \frac{L}{R} \quad (6.14)$$

where  $R$  is the radius of gyration given by:

$$R = \sqrt{\frac{I}{A}} = \sqrt{\frac{\left(\frac{\pi r^4}{4}\right)}{\pi r^2}} = \frac{r}{2} \quad (6.15)$$

where  $I$  is the moment of inertia and  $A$  the cross-sectional area. Substituting (6.4) into (6.3) gives:

$$\text{Slenderness ratio} = \frac{2L}{r} \quad (6.16)$$

Two types of material properties are used to model the trabecular struts: purely linear-elastic material with Young's modulus  $E = 18000\text{MPa}$  and  $\nu = 0.3$ ;

and a bilinear elasto-plastic model based on [80], with Young's modulus  $E = 18000MPa$  before yield, a post-yield modulus of 5% of  $E$ , and a 0.2% offset yield strain in compression of 1.04%. For the sake of simplicity, our FE analyses assumed tissue strength symmetry in compression and tension [52, 79, 101].

Subsequently, while holding both ends of the column pinned, a compressive axial displacement  $\delta$  is applied to one end and the axial reaction force  $F$  thereby generated recorded. The graphs of  $F$  vs.  $\delta$  generated for the columns of a range of slenderness ratios, for both types of material properties, are obtained and plotted (Figure 6.31). It is seen that that the graph obtained in the case with linear elastic material properties asymptotically approaches the analytical Euler buckling load, while that obtained in the case with elasto-plastic material properties shows a clear maximum in the force followed by marked softening.

To obtain the critical load for the case with linear elastic material properties, a line of gradient equal to the initial slope of the force vs. displacement graph is drawn at a displacement offset of 0.0022mm (corresponding to 0.2% offset overall strain) and its point of intersection with the force vs. displacement graph obtained with the linear-elastic material is taken to be the critical failure load for that column. For the case with elasto-plastic material properties, on the other hand, the peak force reached is taken to be the critical failure load for that column. Dividing the critical failure load by the cross-sectional area of that particular column gives the critical stress that the column can support without buckling.



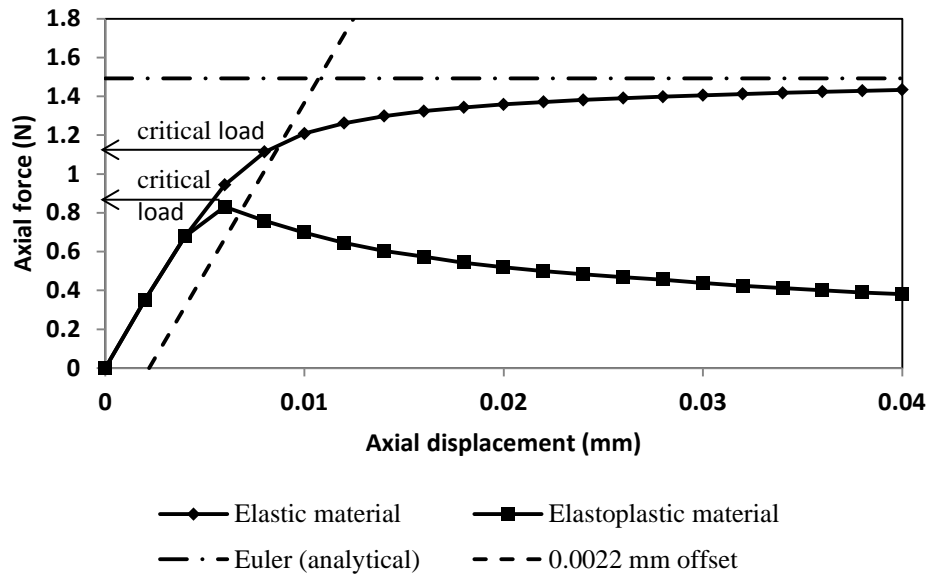


Figure 6.31 Typical graph of force vs. displacement for a trabecular strut showing the critical load that causes buckling in each of the two cases (linear elastic material, and elasto-plastic material)

Similar simulations are performed for columns of a range of slenderness ratios from 0 to 110 and the graph of critical stress vs. slenderness ratio plotted (Figure 6.32).

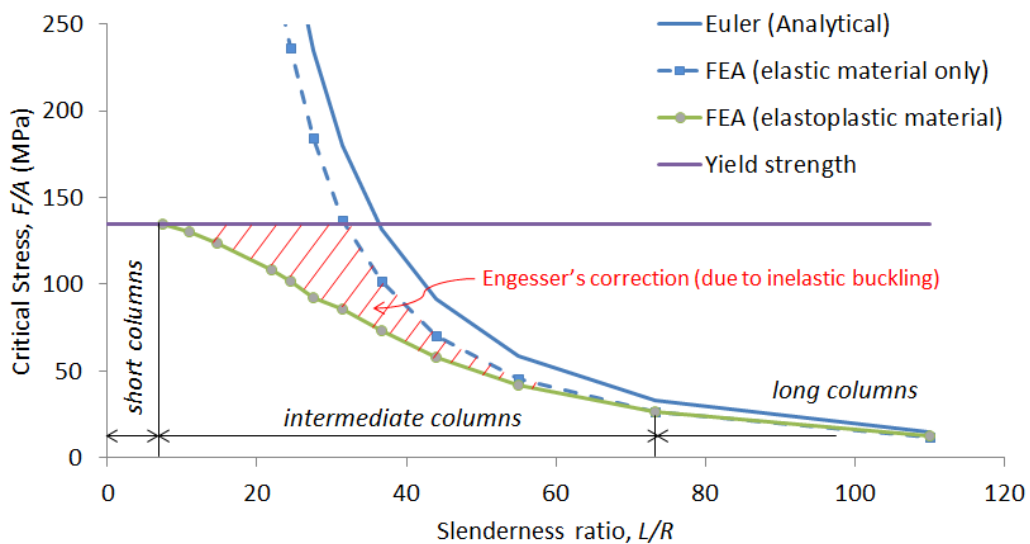


Figure 6.32 Graph of critical stress vs. slenderness ratio showing the effect of inelastic buckling in decreasing the critical stress in columns of intermediate slenderness ratio (i.e., intermediate columns)

### 6.5.3 Discussion

Our results showed that:

- (a) for short columns, the critical stress is determined entirely by the yield strength of the constituent material, implying that the column failed by compressive yielding;
- (b) for long columns, the critical stresses for columns with both constituent material properties (i.e., the linear elastic and the elasto-plastic columns) are identical. This implies that, though the column may have failed after the onset of localized yield, the Euler equation and the Engesser equation both predict the same critical stress.
- (c) for intermediate columns, the critical stress for the columns with elasto-plastic material is less than that for the columns with linear-elastic material, implying that the predominant failure mechanism here is Engesser (inelastic) buckling (i.e., buckling following localized yielding).

The graph above (Figure 6.32) enables us to tabulate the range of slenderness ratios for each of these modes of failure (Table 6.2):

Column type	Slenderness ratio	Predominant failure mechanism
Short	$<7.3$	Material yielding
Intermediate	$7.3 - 73.3$	Engesser buckling (buckling + localized yielding)
Long	$>73.3$	Engesser buckling = Euler buckling

**Table 6.2 Classification of cylindrical columns and their predominant failure mechanisms under axial compression**

In [87], the author had compared her results against typical dimensions of real osteoporotic trabecular struts in the vertebral column, as reported in the

literature, and concluded that their slenderness ratios lie well within the range corresponding to intermediate columns, implying that Engesser buckling would be the predominant strut-level failure mechanism, especially in regions of low volume fraction. We undertook a similar literature search for the femoral neck region and derived the following values by averaging the data furnished in [129], obtained from 56 femoral necks belonging to a cohort of middle-aged to elderly subjects:

$$L \text{ (average)} = 0.95 \text{ mm}$$

$$r \text{ (average)} = 0.08 \text{ mm}$$

$$R = \frac{r}{2} = \frac{0.08}{2} = 0.04 \text{ mm}$$

Assuming pin-ended boundaries [87], we obtain

$$\frac{L}{R} = \left( \frac{0.95}{0.04} \right) = \sim 24$$

Assuming clamped-end conditions [87], we obtain

$$\frac{L}{R} = \frac{0.95/2}{0.04} = \sim 12$$

The values of slenderness ratio obtained for both idealized boundary conditions fall within the range corresponding to the intermediate columns, underscoring the predominance of Engesser buckling in femoral neck trabecular bone. It is to be noted that, as discussed by [87], physiologically realistic boundary conditions for trabecular struts are expected to be somewhere between the pinned and clamped end cases.

Having established the importance of Engesser buckling in microscale (i.e., strut-level) failure, it is imperative to visually examine the buckled struts so as to be better able to diagnose the occurrence of Engesser buckling of individual trabecular struts when inspecting the whole FN structure.

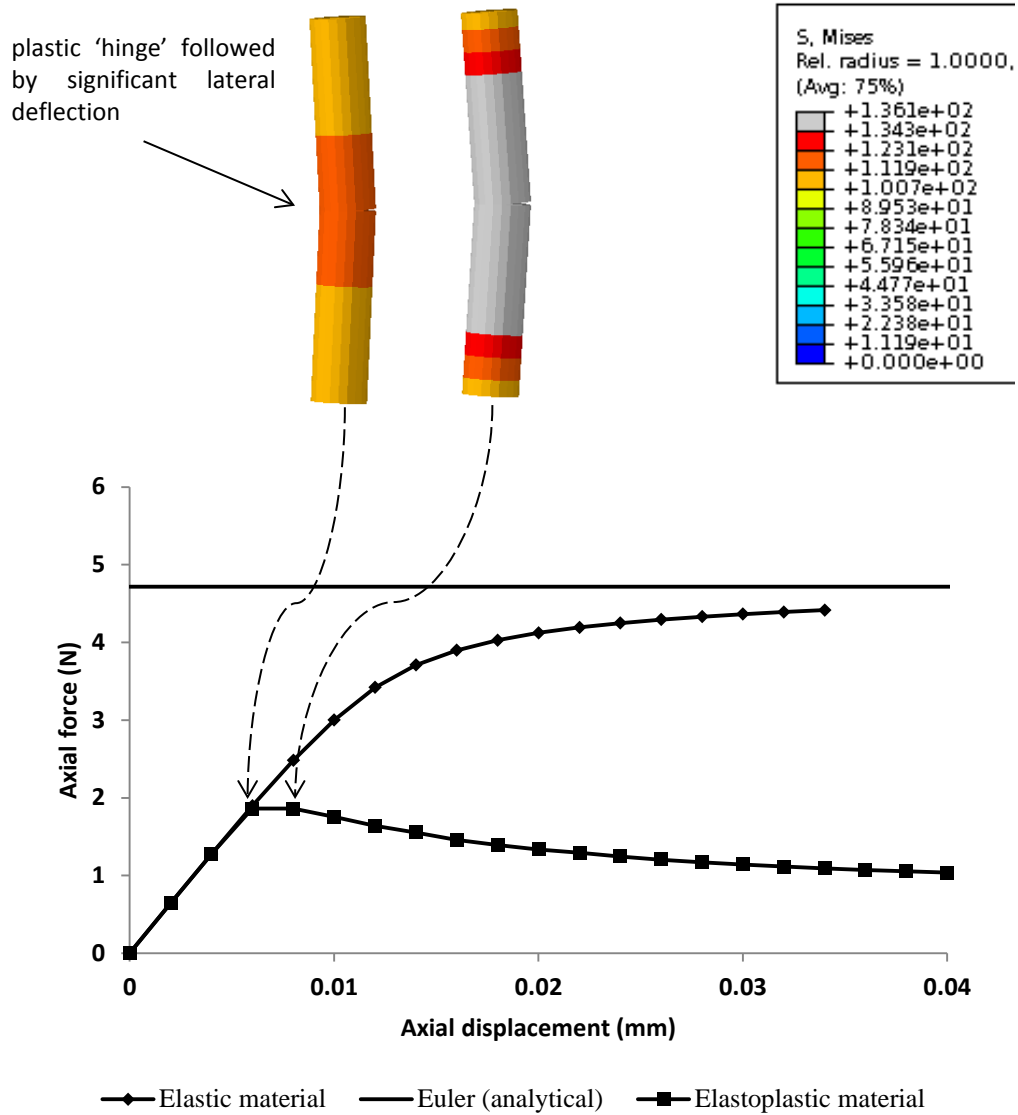


Figure 6.33 Graph of force vs. displacement for a column of intermediate slenderness ratio, showing the Mises stress contours at the critical load. Note the formation of plastic 'hinges' at the mid-span of the column at the point of buckling, followed by substantial lateral deflection thereafter.

Figure 6.33 shows the graph of force vs. displacement for a column of intermediate slenderness ratio, together with the Mises stress plots at the peak force and at a point immediately thereafter.

We note the formation of a plastic ‘hinge’ [86] roughly at the mid-span of the column (where the original lateral imperfection was created prior to simulation) caused by localized yielding, followed by significant lateral deflection of the column with increasing axial compressive force. This phenomenon is colloquially known as ‘kneeling’ [157]. Therefore, we regard the formation of a plastic hinge followed by a large degree of lateral deflection as diagnostic of the occurrence of Engesser buckling in a slender strut. We hereafter employ the abovementioned criteria for identifying struts that have suffered Engesser buckling when relating the trabecular-scale failure mechanisms to the macro-scale yield envelope obtained in Section 6.4 above.

## **6.6 Discussion of the relationships between trabecular-scale and macro-scale failure**

In this subsection, our emphasis is on understanding the micro-structural (i.e., trabecular-level) basis of the yield surface (Figure 6.25) of the macro-scale (i.e., femoral neck-level) structure. To this end, we focus our attention on three cases:

- i. Case 1, corresponding to fall mode, where a bending moment of *negative* sign and very large magnitude acts on the structure simultaneously with a small compressive axial force;

- ii. Case 2, corresponding to stance mode, where a bending moment of *positive* sign and very large magnitude acts on the structure simultaneously with a small compressive axial force;
- iii. Case 3, corresponding to pure compression, where the femoral neck structure is under a large purely compressive axial force with no bending moment.

These three cases are illustrated in Figure 6.34.

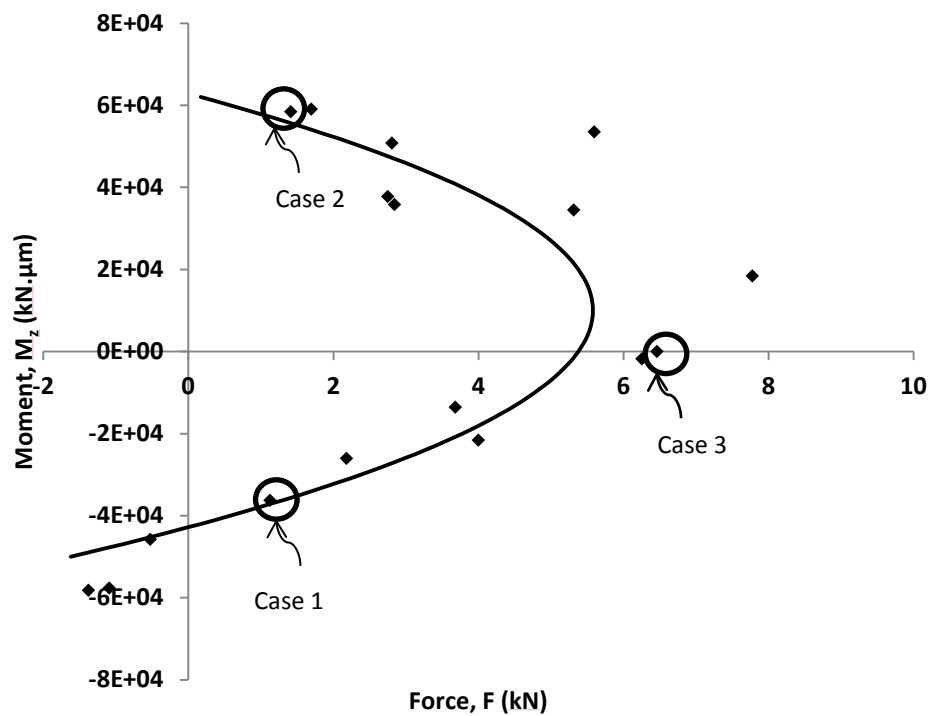


Figure 6.34 Yield surface of femoral neck structure illustrating the three cases to be investigated

### 6.6.1 Case 1:

In Case 1, the femoral neck structure is in fall mode, implying that there exists a negative (about the z-axis, see Figure 6.26) bending moment acting on it. This results in compressive bending stresses in the superior region of the femoral neck and tensile bending stresses in the inferior region.

To discern the occurrence of tissue-level yield, we used the Mises criterion and plotted the regions of active yield (Figure 6.35). Overall, it is seen that there is some tissue yielding occurring at the superior-most region, while there is none at the inferior-most region.

Subsequently, an investigation of regions of low volume fractions in the superior region revealed the presence of plastic hinge formation localized to the superior-most region (Figure 6.36). A plot of the lateral displacement (i.e., in the plane of the femoral neck) shows that the struts which manifest plastic hinges also suffer significantly large lateral displacements (Figure 6.37).

We therefore infer the following with respect to Case 1:

- Most struts in the low volume fraction regions of the superior-half femoral neck structure manifest Engesser buckling (indicated by the formation of plastic hinges combined with significant lateral deflection). This phenomenon is particularly pronounced in the superior-most region.
- There occurs some strut yielding at superior-most region (under compression) while there is no strut yielding in inferior half (under tension).

The mode of macroscopic yield in Case 1 is therefore diagnosed as a combination of Engesser buckling of struts of low volume fraction and compressive yielding of thicker struts, both occurring in the superior-most region of the femoral neck structure.

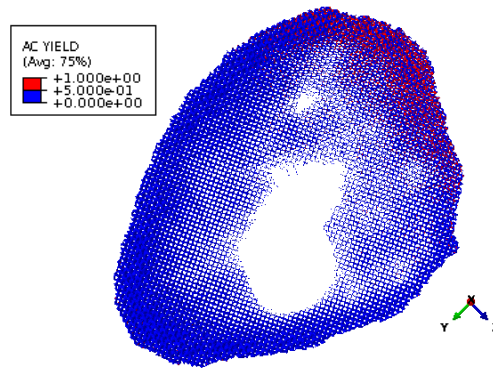


Figure 6.35 Active yield regions (in red) corresponding to Case 1

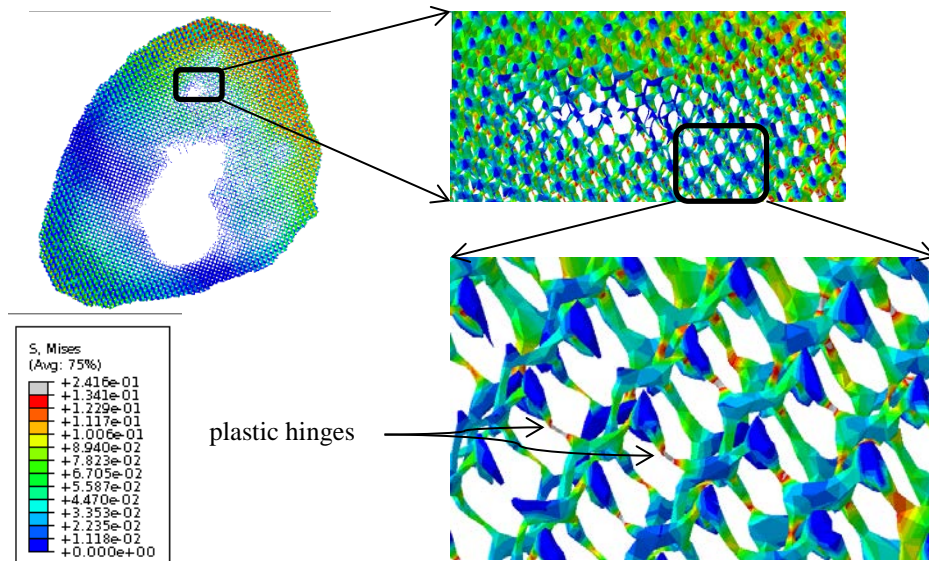


Figure 6.36 Mises stress contours showing formation of plastic hinges in the superior-most region

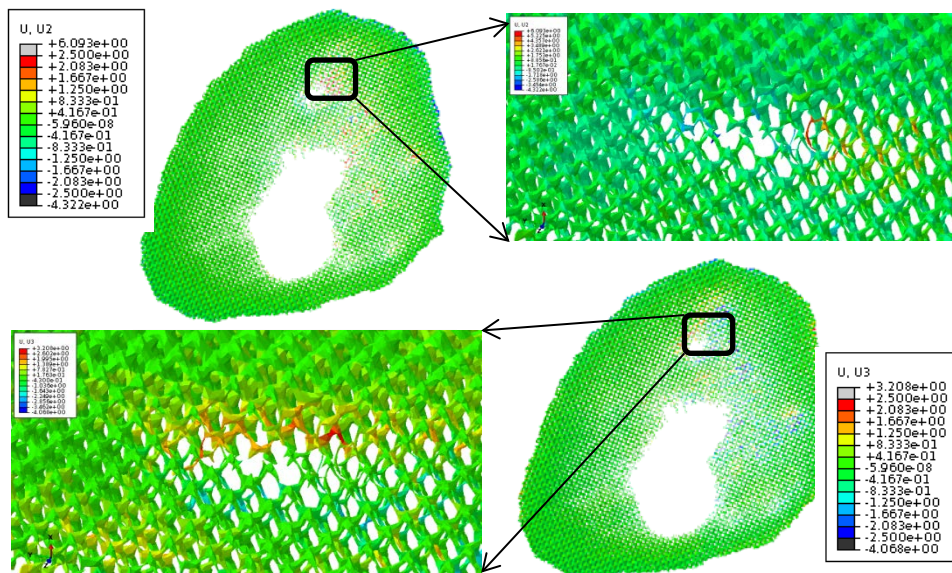


Figure 6.37 Contours showing significant lateral displacements in the same locations as in Figure 6.36



### 6.6.2 Case 2:

In Case 2, the femoral neck structure is in stance mode, implying that there exists a positive (about the z-axis, see Figure 6.26) bending moment acting on it. This results in compressive bending stresses in the inferior region of the femoral neck and tensile bending stresses in the superior region.

To discern the occurrence of tissue-level yield, we used the Mises criterion and plotted the regions of active yield (Figure 6.38). Overall, it is seen that there is substantial tissue yielding at both the inferior and superior regions of the femoral neck structure. It was also noted that there was no Engesser buckling occurring across the cross-section.

We therefore infer the following with respect to Case 2:

- There occurs substantial yielding of struts at both the superior region (under tension) and the inferior region (under compression),
- Engesser buckling, which is expected to occur in struts of low volume fraction regions, is absent. Recalling that the phenomenon of buckling occurs only in compression and not in tension, we believe that the inferior region of the femoral neck structure, which comes under compression in stance mode, is of a relatively high volume fraction and therefore the struts located therein are not susceptible of Engesser buckling.

The mode of macroscopic yield in Case 2 is therefore diagnosed as caused purely by strut yielding, in compression at the inferior region and in tension at the superior region.

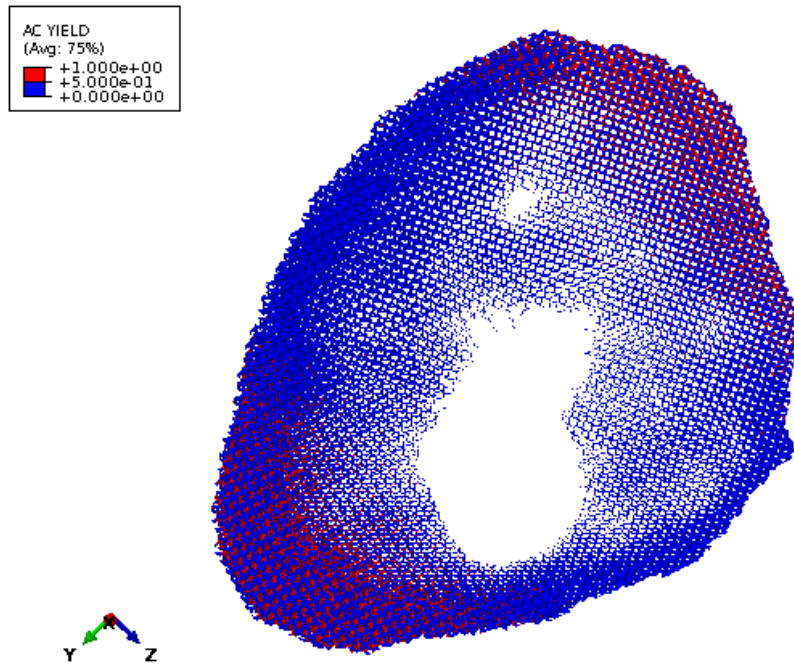


Figure 6.38 Active yield regions (in red) corresponding to Case 2

### 6.6.3 Case 3:

In Case 3, the femoral neck structure is in pure compression – there exists no bending moment acting on it.

To discern the occurrence of tissue-level yield, we used the Mises criterion and plotted the regions of active yield (Figure 6.39). Overall, it is seen that there is some tissue yielding occurring at the entire superior-half of the cross-section as well as in several low volume fraction regions of the inferior-half.

Subsequently, an investigation of regions of low volume fractions in the superior region revealed the presence of plastic hinge formation localized to the superior-most region Figure 6.40. A plot of the lateral displacement (i.e., in the plane of the femoral neck) shows that the struts which manifest plastic hinges also suffer significantly large lateral displacements (Figure 6.41).

We therefore infer the following with respect to Case 3:

- Most struts in the low volume fraction areas of the entire cross-section of femoral neck structure manifest Engesser buckling (indicated by the formation of plastic hinges combined with significant lateral deflection).
- There occurs significant strut yielding in compression across the entire cross-section, particularly noticeable in the cortical ring, except at the inferior cortex.

The mode of macroscopic yield in Case 3 is therefore diagnosed as a combination of Engesser buckling of struts in low volume fraction areas across

the entire cross-section and compressive yielding of thicker struts along the entire cortical ring, except at the inferior cortex.

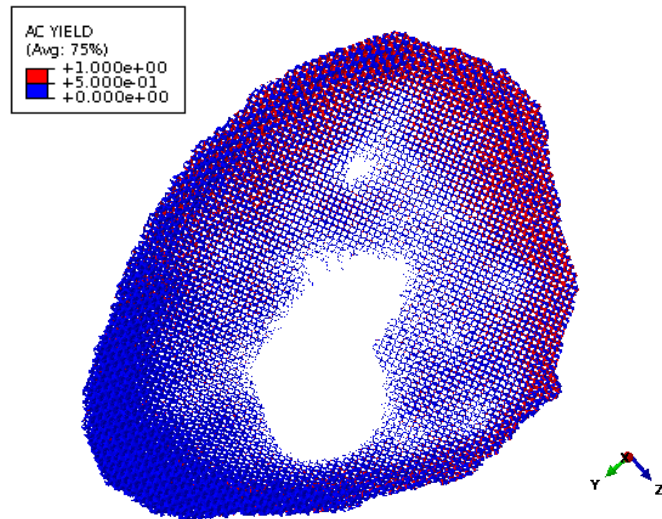


Figure 6.39 Active yield regions (in red) corresponding to Case 3

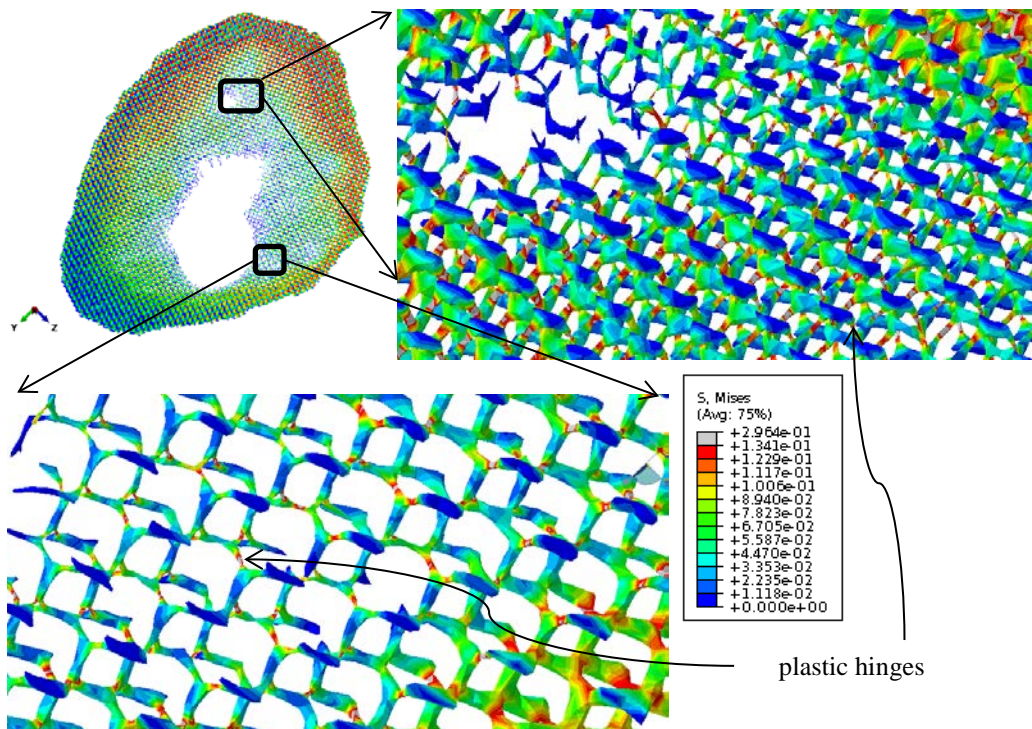
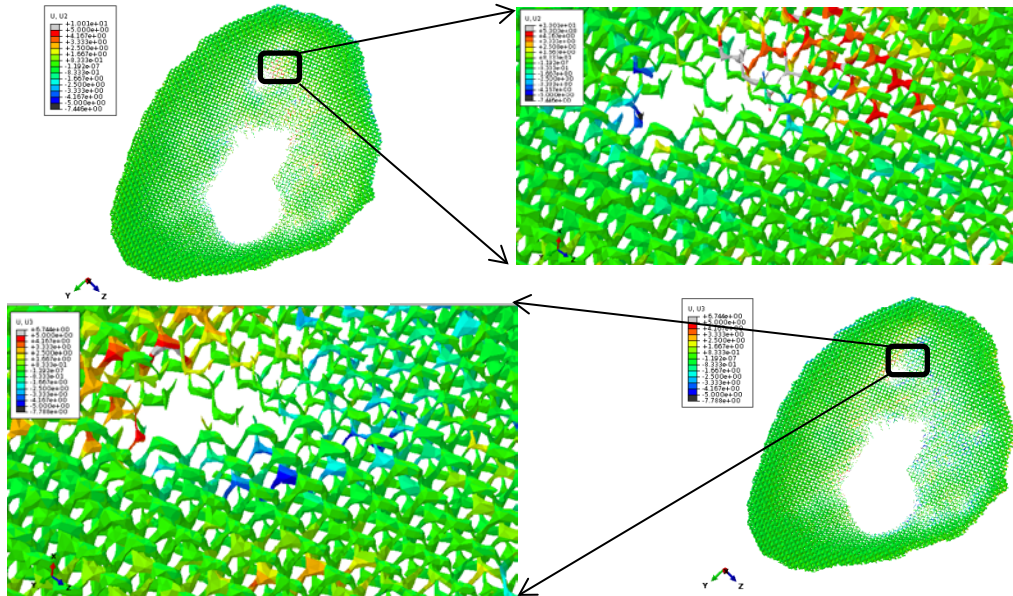


Figure 6.40 Mises stress contours showing formation of plastic hinges in low volume fraction areas of both the superior and inferior regions



**Figure 6.41** Contours showing significant lateral displacements in one of the locations as in Figure 6.40.

## 6.7 Conclusion:

In this section of our work, we have arrived at a better understanding of the micro-scale mechanisms (inelastic buckling of slender struts or yielding of thicker struts) that underlie the macro-scale yield of the femoral neck structure. Specifically, our analysis has shown that the poorly-understood phenomenon of inelastic buckling is a mechanism that is not active in physiological loading conditions (i.e., typical stance) but is activated in fall mode, contributing significantly to macro-scale (i.e., femoral neck) failure.

We summarize the findings of this section in Table 6.3.

	Fall (Case 1)	Stance (Case 2)	Pure compression (Case 3)
Bending moment ( $M_z$ )	Negative	Positive	Zero
Axial Force	Compressive	Compressive	Compressive
Bending stress	Compressive at superior, tensile at inferior	Tensile at superior; compressive at inferior	Zero
Axial stress	Compressive	Compressive	Compressive
Engesser buckling	Present (localized to superior-most region)	None	Present (across entire cross-section)
Yielding	Localized to superior-most region	Localized to inferior-most and superior-most regions	Present (at cortical ring, except at inferior)

**Table 6.3 Summary of micro-scale mechanisms for the three cases (fall, stance, and pure compression)**

**Chapter 7. Conclusions and Scope for Future Work**

*“[...] what is sought with difficulty is  
discovered with more pleasure.”  
(St. Augustine, On Christian Doctrine)*

It is well-known that human bone is a hierarchically very complex material with a diverse range of shapes, densities, and mechanical properties. It has also been sufficiently emphasized, especially in recent years, that variations in bone geometry and density, especially during natural ageing or with the onset of pathological conditions like osteoporosis, may have a significant role to play in undermining the strength and mechanical integrity of the skeletal system. What is lamentable at present is our poor appreciation of, and insight into, the intrinsically *multi-scale* nature of the problem: how the mechanical behaviour and, more particularly, the deformation mechanisms at one scale of the bone may have a cascading effect on adjacent scales, leading eventually to catastrophic failure of the entire organ. We deem this work herein presented as the coming to fruition of nothing more than a modest attempt on our part to perfect our understanding of the natural marvel that is bone.

Inspired by the works of the nineteenth-century German mathematician Hermann Schwarz on minimal surfaces, and sensitive to the fact that natural materials are often based on simple underlying geometric patterns, we investigated the ability of the triply-periodic minimal surface cellular solid called the gyroid to act as a morphological model of trabecular bone. We discovered that, based on both its mechanical behaviour and morphometric properties, the gyroid-based unit cell is a good representative of real trabecular



bone, a finding further corroborated by comparison with other previously proposed models of bone.

Subsequently, we employed the gyroid-based unit cell as a micro-scale model for deriving mechanical properties for a range of apparent densities, which were then used as input parameters for a macro-scale numerical study of the proximal femur under two different loading conditions. By performing analyses on the same structure after simulating trabecular bone density attenuation, we were also able to assess the impact of ageing or osteoporosis (both of which are associated with severe bone loss) on the femoral strength. Significantly, we discovered that femur bones that have suffered severe bone loss exhibit a drastic reduction in their structural stiffness and also a peculiar plateau-like behaviour in their load-displacement curves, indicative of a complete loss in their ability to withstand any further increase in external loads.

In order to make more explicit the link between deformation and failure mechanisms at two adjacent scales of bone, namely, the level of individual trabecular spicule and that of the whole femoral neck region, we used the gyroid model, together with a CT-image of a real femoral neck cross-section, to render a structure that resembled the femoral neck in geometry as well as density distribution. Performing numerical simulations on this structure using various boundary conditions (both stance and fall) furnished us with a macro-scale yield envelope that could enable one to diagnose whether a given set of loading conditions is likely, or not, to result in structural yield of the femoral neck. Finally, we explored the somewhat poorly understood phenomenon of the buckling (especially by the so-called Engesser theory of inelastic buckling)

of trabecular struts by using simplified cylindrical geometries and discovered that, based on typical statistical data for the slenderness ratios of femoral trabecular bone in the middle-aged and elderly, inelastic buckling is a very real possibility in trabecular bone. Further inspection of our computational model of the femoral neck structure after macro-scale yield revealed that trabecular struts in low volume fraction areas of the superior-most region of the femoral neck did manifest inelastic buckling in the fall mode, an occurrence absent in the stance mode. This finding could be of significance in improving our understanding of the aetiology of fall-mode fractures.

It is now incumbent upon us to enumerate the limitations of this work, with the belief that a full disclosure will enhance, and not diminish, the readers' understanding and appraisal thereof.

- The gyroid-based unit cell is periodic and isotropic. Real trabecular bone, however, is more chaotic and may frequently exhibit a degree of anisotropy. The anisotropy of trabecular bone is more pronounced in certain anatomic locations like the vertebral column where the loads are typically oriented in one direction, than in regions like the femoral head where the loads and moments may be applied in various directions during gait.
- Since our goal in this thesis was to perform multi-scale analyses on bone with particular emphasis on studying hierarchical deformation and failure mechanisms, we chose simplified boundary conditions to represent stance and fall modes. Furthermore, for the same reason, the constitutive laws we used to model tissue-level and apparent-level

behaviour do not account for complex phenomena like tissue-strength asymmetry, damage and crack growth, etc.

- Only static simulations are undertaken. Dynamic (impact) tests are not considered. No muscle tissues are explicitly incorporated in the macro-scale models, though these may dissipate impact forces during falls in real-life.
- The structure studied in the penultimate chapter (Chapter 6) is based on a single CT slice extracted from the femoral neck region of a proximal femur. Use of a stack of slices may produce more realistic results; however, the computational resources required to mesh and simulate the larger structures thereby produced are prohibitive.

Our posterity may not be bound by the same constraints as we were. They could then study the following in greater detail:

- The effect of impact loading on the hierarchical deformation mechanisms of bone.
- The influence of the presence of soft tissue encasing the femur during falls.
- Aspects of crack growth and trabecular-level damage.
- Interactions between deformation mechanisms at even lower scales (e.g., fibril failure) and the trabecular strut level behaviour.
- More complex constitutive laws incorporating visco-elasticity and poroelastic phenomena.

## References

1. Bartel, D.L., D.T. Davy, and T.M. Keaveny, *Orthopaedic biomechanics: mechanics and design in musculoskeletal systems*. 2006: Prentice Hall.
2. Skedros, J.G. and S.L. Baucom, *Mathematical analysis of trabecular 'trajectories' in apparent trajectorial structures: the unfortunate historical emphasis on the human proximal femur*. Journal of theoretical biology, 2007. **244**(1): p. 15-45.
3. Gibson, L.J., *The mechanical behaviour of cancellous bone*. Journal of biomechanics, 1985. **18**(5): p. 317-328.
4. Carter, D.R. and W.C. Hayes, *The compressive behavior of bone as a two-phase porous structure*. The Journal of bone and joint surgery. American volume, 1977. **59**(7): p. 954-962.
5. Helgason, B., E. Perilli, E. Schileo, F. Taddei, S. Brynjolfsson, and M. Viceconti, *Mathematical relationships between bone density and mechanical properties: a literature review*. Clin Biomech (Bristol, Avon), 2008. **23**(2): p. 135-46.
6. Herman, G.T., *Fundamentals of computerized tomography: image reconstruction from projections*. 2009: Springer.
7. Verhulp, E., B. van Rietbergen, and R. Huiskes, *Comparison of micro-level and continuum-level voxel models of the proximal femur*. J Biomech, 2006. **39**(16): p. 2951-7.
8. Siffert, R.S. and J.J. Kaufman, *Ultrasonic bone assessment: "The time has come"*. Bone, 2007. **40**(1): p. 5.
9. Rho, J.Y., R.B. Ashman, and C.H. Turner, *Young's modulus of trabecular and cortical bone material: ultrasonic and microtensile measurements*. J Biomech, 1993. **26**(2): p. 111-9.
10. Linde, F., I. Hvid, and F. Madsen, *The effect of specimen geometry on the mechanical behaviour of trabecular bone specimens*. Journal of biomechanics, 1992. **25**(4): p. 359-368.
11. Eberle, S., M. Göttliger, and P. Augat, *An investigation to determine if a single validated density–elasticity relationship can be used for subject specific finite element analyses of human long bones*. Medical engineering & physics, 2013. **35**(7): p. 875-883.
12. Keaveny, T.M., E.F. Morgan, G.L. Niebur, and O.C. Yeh, *Biomechanics of trabecular bone*. Annu Rev Biomed Eng, 2001. **3**: p. 307-33.
13. Lenaerts, L. and G.H. Van Lenthe, *Multi-level patient-specific modelling of the proximal femur. A promising tool to quantify the effect of osteoporosis treatment*. Philosophical Transactions of the Royal Society A: Mathematical, Physical and Engineering Sciences, 2009. **367**(1895): p. 2079-2093.
14. Taddei, F., S. Martelli, B. Reggiani, L. Cristofolini, and M. Viceconti, *Finite-element modeling of bones from CT data: sensitivity to geometry and material uncertainties*. IEEE Trans Biomed Eng, 2006. **53**(11): p. 2194-200.

15. Khanoki, S.A. and D. Pasini, *Fatigue design of a mechanically biocompatible lattice for a proof-of-concept femoral stem*. journal of the mechanical behavior of biomedical materials, 2013. **22**: p. 65-83.
16. Keyak, J.H. and S.A. Rossi, *Reply to letter*. Journal of Biomechanics, 2001. **34**(4): p. 561.
17. Peng, L., J. Bai, X. Zeng, and Y. Zhou, *Comparison of isotropic and orthotropic material property assignments on femoral finite element models under two loading conditions*. Medical engineering & physics, 2006. **28**(3): p. 227-233.
18. Baca, V., Z. Horak, P. Mikulenka, and V. Dzupa, *Comparison of an inhomogeneous orthotropic and isotropic material models used for FE analyses*. Medical engineering & physics, 2008. **30**(7): p. 924-930.
19. Turner, C.H., J. Rho, Y. Takano, T.Y. Tsui, and G.M. Pharr, *The elastic properties of trabecular and cortical bone tissues are similar: results from two microscopic measurement techniques*. Journal of biomechanics, 1999. **32**(4): p. 437-441.
20. Bevill, G., S.K. Eswaran, A. Gupta, P. Papadopoulos, and T.M. Keaveny, *Influence of bone volume fraction and architecture on computed large-deformation failure mechanisms in human trabecular bone*. Bone, 2006. **39**(6): p. 1218-25.
21. Stolken, J.S. and J.H. Kinney, *On the importance of geometric nonlinearity in finite-element simulations of trabecular bone failure*. Bone, 2003. **33**(4): p. 494-504.
22. Christen, D., D.J. Webster, and R. Müller, *Multiscale modelling and nonlinear finite element analysis as clinical tools for the assessment of fracture risk*. Philosophical Transactions of the Royal Society A: Mathematical, Physical and Engineering Sciences, 2010. **368**(1920): p. 2653-2668.
23. Hazrati Marangalou, J., K. Ito, and B. van Rietbergen, *A new approach to determine the accuracy of morphology-elasticity relationships in continuum FE analyses of human proximal femur*. J Biomech, 2012. **45**(16): p. 2884-92.
24. Miehe, C., J. Schröder, and M. Becker, *Computational homogenization analysis in finite elasticity: material and structural instabilities on the micro-and macro-scales of periodic composites and their interaction*. Computer Methods in Applied Mechanics and Engineering, 2002. **191**(44): p. 4971-5005.
25. Nezamabadi, S., J. Yvonnet, H. Zahrouni, and M. Potier-Ferry, *A multilevel computational strategy for handling microscopic and macroscopic instabilities*. Computer Methods in Applied Mechanics and Engineering, 2009. **198**(27): p. 2099-2110.
26. Ghanbari, J. and R. Naghdabadi, *Nonlinear hierarchical multiscale modeling of cortical bone considering its nanoscale microstructure*. J Biomech, 2009. **42**(10): p. 1560-5.
27. Vaughan, T.J., C.T. McCarthy, and L.M. McNamara, *A three-scale finite element investigation into the effects of tissue mineralisation and lamellar organisation in human cortical and trabecular bone*. J Mech Behav Biomed Mater, 2012. **12**: p. 50-62.
28. Turner, C.H., J. Rho, Y. Takano, T.Y. Tsui, and G.M. Pharr, *The elastic properties of trabecular and cortical bone tissues are similar:*

- results from two microscopic measurement techniques.* J Biomech, 1999. **32**(4): p. 437-41.
29. Ilic, S., K. Hackl, and R. Gilbert, *Application of the multiscale FEM to the modeling of cancellous bone.* Biomechanics and modeling in mechanobiology, 2010. **9**(1): p. 87-102.
  30. Porter, D., *Pragmatic multiscale modelling of bone as a natural hybrid nanocomposite.* Materials Science and Engineering: A, 2004. **365**(1): p. 38-45.
  31. Ji, B. and H. Gao, *Elastic properties of nanocomposite structure of bone.* Composites science and technology, 2006. **66**(9): p. 1212-1218.
  32. Hamed, E., Y. Lee, and I. Jasiuk, *Multiscale modeling of elastic properties of cortical bone.* Acta mechanica, 2010. **213**(1-2): p. 131-154.
  33. Martínez-Reina, J., J. Domínguez, and J. García-Aznar, *Effect of porosity and mineral content on the elastic constants of cortical bone: a multiscale approach.* Biomechanics and modeling in mechanobiology, 2011. **10**(3): p. 309-322.
  34. Predoi-Racila, M. and J.M. Crolet, *Human cortical bone: the SiNuProS model: Part I—description and elastic macroscopic results.* Computer Methods in Biomechanics and Biomedical Engineering, 2008. **11**(2): p. 169-187.
  35. Predoi-Racila, M. and J.M. Crolet, *SINUPROS: human cortical bone multiscale model with a fluid–structure interaction.* Computer Methods in Biomechanics and Biomedical Engineering, 2007. **10**(sup1): p. 179-180.
  36. Gonçalves Coelho, P., P. Rui Fernandes, and H. Carriço Rodrigues, *Multiscale modeling of bone tissue with surface and permeability control.* Journal of biomechanics, 2011. **44**(2): p. 321-329.
  37. Hellmich, C., F.-J. Ulm, and L. Dormieux, *Can the diverse elastic properties of trabecular and cortical bone be attributed to only a few tissue-independent phase properties and their interactions?* Biomechanics and modeling in mechanobiology, 2004. **2**(4): p. 219-238.
  38. Fritsch, A. and C. Hellmich, *‘Universal’ microstructural patterns in cortical and trabecular, extracellular and extravascular bone materials: Micromechanics-based prediction of anisotropic elasticity.* Journal of Theoretical Biology, 2007. **244**(4): p. 597-620.
  39. Podshivalov, L., A. Fischer, and P. Bar-Yoseph, *3D hierarchical geometric modeling and multiscale FE analysis as a base for individualized medical diagnosis of bone structure.* Bone, 2011. **48**(4): p. 693-703.
  40. Podshivalov, L., A. Fischer, and P. Bar-Yoseph, *Multiscale FE method for analysis of bone micro-structures.* Journal of the mechanical behavior of biomedical materials, 2011. **4**(6): p. 888-899.
  41. Eringen, A.C., *Microcontinuum field theories.* 1999, New York: Springer.
  42. Eringen, A.C., *Nonlocal continuum field theories.* 2002, New York: Springer. xvi, 376 p.

43. Fatemi, J., F. Van Keulen, and P. Onck, *Generalized Continuum Theories: Application to Stress Analysis in Bone\**. Meccanica, 2002. **37**(4-5): p. 385-396.
44. Yoo, A. and I. Jasiuk, *Couple-stress moduli of a trabecular bone idealized as a 3D periodic cellular network*. Journal of biomechanics, 2006. **39**(12): p. 2241-2252.
45. Gibson, L.J. and M. Ashby, *The mechanics of three-dimensional cellular materials*. Proceedings of the Royal Society of London. A. Mathematical and Physical Sciences, 1982. **382**(1782): p. 43-59.
46. Roberts, A. and E.J. Garboczi, *Elastic properties of model random three-dimensional open-cell solids*. Journal of the Mechanics and Physics of Solids, 2002. **50**(1): p. 33-55.
47. Gibson, L.J. and M.F. Ashby, *Cellular Solids: Structure and Properties*. 1997, 2009, Cambridge University Press, Cambridge.
48. Gibson, L.J., *Biomechanics of cellular solids*. Journal of Biomechanics, 2005. **38**(3): p. 377-399.
49. Bayraktar, H.H. and T.M. Keaveny, *Mechanisms of uniformity of yield strains for trabecular bone*. J Biomech, 2004. **37**(11): p. 1671-8.
50. Weaire, D. and R. Phelan, *A counter-example to Kelvin's conjecture on minimal surfaces*. Philosophical Magazine Letters, 1994. **69**(2): p. 107-110.
51. Zysset, P., M. Ominsky, and S. Goldstein, *A novel 3D microstructural model for trabecular bone: I. The relationship between fabric and elasticity*. COMPUTER METHODS IN BIOMECHANICS AND BIO MEDICAL ENGINEERING, 1998. **1**(4): p. 321-331.
52. Guo, X. and C. Kim, *Mechanical consequence of trabecular bone loss and its treatment: a three-dimensional model simulation*. Bone, 2002. **30**(2): p. 404-411.
53. Okabe, A., B. Boots, K. Sugihara, and S.N. Chiu, *Spatial tessellations: concepts and applications of Voronoi diagrams*. Vol. 501. 2009: John Wiley & Sons.
54. Vajjhala, S., A. Kraynik, and L. Gibson, *A cellular solid model for modulus reduction due to resorption of trabeculae in bone*. Journal of biomechanical engineering, 2000. **122**(5): p. 511-515.
55. Silva, M.J., W.C. Hayes, and L.J. Gibson, *The effects of non-periodic microstructure on the elastic properties of two-dimensional cellular solids*. International Journal of Mechanical Sciences, 1995. **37**(11): p. 1161-1177.
56. Silva, M. and L. Gibson, *Modeling the mechanical behavior of vertebral trabecular bone: effects of age-related changes in microstructure*. Bone, 1997. **21**(2): p. 191-199.
57. Hildebrand, T. and P. RÜEGSEGG, *Quantification of bone microarchitecture with the structure model index*. Computer Methods in Biomechanics and Bio Medical Engineering, 1997. **1**(1): p. 15-23.
58. Kim, T., W. Hwang, A. Zhang, and M. Ramanathan. *Computational Framework for Microstructural Bone Dynamics Model and Its Evaluation*. in *BIBE*. 2010.
59. Kim, T., M. Ramanathan, and A. Zhang. *A graph-based approach for computational model of bone microstructure*. in *Proceedings of the*

- First ACM International Conference on Bioinformatics and Computational Biology*. 2010. ACM.
60. McDonald, K., J. Little, M. Percy, and C. Adam, *Development of a multi-scale finite element model of the osteoporotic lumbar vertebral body for the investigation of apparent level vertebra mechanics and micro-level trabecular mechanics*. *Medical engineering & physics*, 2010. **32**(6): p. 653-661.
  61. Kim, H. and S. Al-Hassani, *A morphological model of vertebral trabecular bone*. *Journal of Biomechanics*, 2002. **35**(8): p. 1101-1114.
  62. Weaver, J.K. and J. Chalmers, *Cancellous Bone: Its Strength and Changes with Aging and an Evaluation of Some Methods for Measuring Its Mineral Content I. AGE CHANGES IN CANCELLOUS BONE*. *The Journal of Bone & Joint Surgery*, 1966. **48**(2): p. 289-299.
  63. Morgan, E.F. and T.M. Keaveny, *Dependence of yield strain of human trabecular bone on anatomic site*. *J Biomech*, 2001. **34**(5): p. 569-77.
  64. Nagaraja, S., T.L. Couse, and R.E. Guldberg, *Trabecular bone microdamage and microstructural stresses under uniaxial compression*. *Journal of biomechanics*, 2005. **38**(4): p. 707-716.
  65. Townsend, P.R., R.M. Rose, and E.L. Radin, *Buckling studies of single human trabeculae*. *Journal of Biomechanics*, 1975. **8**(3): p. 199-201.
  66. Mayhew, P.M., C.D. Thomas, J.G. Clement, N. Loveridge, T.J. Beck, W. Bonfield, C.J. Burgoyne, and J. Reeve, *Relation between age, femoral neck cortical stability, and hip fracture risk*. *Lancet*, 2005. **366**(9480): p. 129-35.
  67. Orwoll, E.S., L.M. Marshall, C.M. Nielson, S.R. Cummings, J. Lapidus, J.A. Cauley, K. Ensrud, N. Lane, P.R. Hoffmann, D.L. Kopperdahl, and T.M. Keaveny, *Finite element analysis of the proximal femur and hip fracture risk in older men*. *J Bone Miner Res*, 2009. **24**(3): p. 475-83.
  68. Bell, K., N. Loveridge, J. Power, N. Garrahan, M. Stanton, M. Lunt, B. Meggitt, and J. Reeve, *Structure of the femoral neck in hip fracture: cortical bone loss in the inferoanterior to superoposterior axis*. *Journal of Bone and Mineral Research*, 1999. **14**(1): p. 111-119.
  69. Lee, T., A.V. Rammohan, A. Chan, V.B. Tan, S. Das De, T.M. Link, F. Eckstein, and B.W. Schafer, *The susceptibility of the femoral neck to fracture: an assessment incorporating the effects of age-remodeling and stress reduction*. *J Biomech*, 2012. **45**(6): p. 931-7.
  70. Fazzalari, N., J. Darracott, and B. Vernon-Roberts, *A quantitative description of selected stress regions of cancellous bone in the head of the femur using automatic image analysis*. *Metabolic Bone Disease and Related Research*, 1984. **5**(3): p. 119-125.
  71. Beck, T.J., A.C. Looker, C.B. Ruff, H. Sievanen, and H.W. Wahner, *Structural trends in the aging femoral neck and proximal shaft: analysis of the Third National Health and Nutrition Examination Survey dual-energy X-ray absorptiometry data*. *J Bone Miner Res*, 2000. **15**(12): p. 2297-304.
  72. Kanis, J.A., *Osteoporosis and osteopenia*. *Journal of bone and mineral research*, 1990. **5**(3): p. 209-211.



73. Morin, S., L. Lix, M. Azimae, C. Metge, P. Caetano, and W. Leslie, *Mortality rates after incident non-traumatic fractures in older men and women*. Osteoporosis international, 2011. **22**(9): p. 2439-2448.
74. Keaveny, T.M. and O.C. Yeh, *Architecture and trabecular bone - toward an improved understanding of the biomechanical effects of age, sex and osteoporosis*. J Musculoskelet Neuronal Interact, 2002. **2**(3): p. 205-8.
75. Lee, J.D., Y. Chen, X. Zeng, A. Eskandarian, and M. Oskard, *Modeling and simulation of osteoporosis and fracture of trabecular bone by meshless method*. International journal of engineering science, 2007. **45**(2): p. 329-338.
76. Ugural, A.C., *Mechanics of Materials*. 1991, Singapore: McGraw-Hill.
77. Kadir, M.R., A. Syahrom, and A. Ochsner, *Finite element analysis of idealised unit cell cancellous structure based on morphological indices of cancellous bone*. Med Biol Eng Comput, 2010. **48**(5): p. 497-505.
78. Van Rietbergen, B., R. Huiskes, F. Eckstein, and P. Ruegsegger, *Trabecular bone tissue strains in the healthy and osteoporotic human femur*. J Bone Miner Res, 2003. **18**(10): p. 1781-8.
79. Carretta, R., S. Lorenzetti, and R. Müller, *Towards patient-specific material modeling of trabecular bone post-yield behavior*. International journal for numerical methods in biomedical engineering, 2012.
80. Bayraktar, H.H., E.F. Morgan, G.L. Niebur, G.E. Morris, E.K. Wong, and T.M. Keaveny, *Comparison of the elastic and yield properties of human femoral trabecular and cortical bone tissue*. J Biomech, 2004. **37**(1): p. 27-35.
81. Niebur, G.L., M.J. Feldstein, J.C. Yuen, T.J. Chen, and T.M. Keaveny, *High-resolution finite element models with tissue strength asymmetry accurately predict failure of trabecular bone*. J Biomech, 2000. **33**(12): p. 1575-83.
82. Nalla, R.K., J.H. Kinney, and R.O. Ritchie, *Mechanistic fracture criteria for the failure of human cortical bone*. Nature materials, 2003. **2**(3): p. 164-168.
83. Fratzl, P., H. Gupta, E. Paschalis, and P. Roschger, *Structure and mechanical quality of the collagen–mineral nano-composite in bone*. Journal of Materials Chemistry, 2004. **14**(14): p. 2115-2123.
84. Thurner, P.J., P. Wyss, R. Voide, M. Stauber, M. Stämpf, U. Sennhauser, and R. Müller, *Time-lapsed investigation of three-dimensional failure and damage accumulation in trabecular bone using synchrotron light*. Bone, 2006. **39**(2): p. 289-299.
85. Hayes, W. and D. Carter, *Postyield behavior of subchondral trabecular bone*. Journal of biomedical materials research, 1976. **10**(4): p. 537-544.
86. Gibson, L.J. and M. Ashby, *Cellular solids: structure & properties*. 1988.
87. McDonald, K.A., *An Experimental and Finite Element Investigation of the Biomechanics of Vertebral Compression Fractures*, 2009, Queensland University of Technology.
88. Gupta, A., H.H. Bayraktar, J.C. Fox, T.M. Keaveny, and P. Papadopoulos, *Constitutive modeling and algorithmic implementation*

- of a plasticity-like model for trabecular bone structures*. Computational Mechanics, 2007. **40**(1): p. 61-72.
89. Keyak, J.H. and S.A. Rossi, *Prediction of femoral fracture load using finite element models: an examination of stress-and strain-based failure theories*. Journal of biomechanics, 2000. **33**(2): p. 209-214.
  90. Ford, C.M. and T.M. Keaveny, *The dependence of shear failure properties of trabecular bone on apparent density and trabecular orientation*. Journal of biomechanics, 1996. **29**(10): p. 1309-1317.
  91. Juszczak, M.M., L. Cristofolini, and M. Viceconti, *The human proximal femur behaves linearly elastic up to failure under physiological loading conditions*. J Biomech, 2011. **44**(12): p. 2259-66.
  92. Bessho, M., I. Ohnishi, J. Matsuyama, T. Matsumoto, K. Imai, and K. Nakamura, *Prediction of strength and strain of the proximal femur by a CT-based finite element method*. Journal of biomechanics, 2007. **40**(8): p. 1745-1753.
  93. !!! INVALID CITATION !!!
  94. Vashishth, D., K. Tanner, and W. Bonfield, *Contribution, development and morphology of microcracking in cortical bone during crack propagation*. Journal of Biomechanics, 2000. **33**(9): p. 1169-1174.
  95. Nalla, R.K., J.J. Kruzic, J.H. Kinney, and R.O. Ritchie, *Effect of aging on the toughness of human cortical bone: evaluation by R-curves*. Bone, 2004. **35**(6): p. 1240-1246.
  96. Vashishth, D., J. Behiri, and W. Bonfield, *Crack growth resistance in cortical bone: concept of microcrack toughening*. Journal of Biomechanics, 1997. **30**(8): p. 763-769.
  97. Thomas, C.D., P.M. Mayhew, J. Power, K.E. Poole, N. Loveridge, J.G. Clement, C.J. Burgoyne, and J. Reeve, *Femoral neck trabecular bone: loss with aging and role in preventing fracture*. J Bone Miner Res, 2009. **24**(11): p. 1808-18.
  98. Snyder, B., S. Piazza, W. Edwards, and W. Hayes, *Role of trabecular morphology in the etiology of age-related vertebral fractures*. Calcified tissue international, 1993. **53**(1): p. S14-S22.
  99. Verhulp, E., B. Van Rietbergen, R. Muller, and R. Huiskes, *Micro-finite element simulation of trabecular-bone post-yield behaviour--effects of material model, element size and type*. Comput Methods Biomech Biomed Engin, 2008. **11**(4): p. 389-95.
  100. Van Rietbergen, B., H. Weinans, R. Huiskes, and A. Odgaard, *A new method to determine trabecular bone elastic properties and loading using micromechanical finite-element models*. Journal of biomechanics, 1995. **28**(1): p. 69-81.
  101. McDonald, K.A., *An experimental and finite element investigation of the biomechanics of vertebral compression fractures*, 2009.
  102. Hyde, S.T., M. O'Keeffe, and D.M. Proserpio, *A short history of an elusive yet ubiquitous structure in chemistry, materials, and mathematics*. Angewandte Chemie International Edition, 2008. **47**(42): p. 7996-8000.
  103. Michielsen, K. and D. Stavenga, *Gyroid cuticular structures in butterfly wing scales: biological photonic crystals*. Journal of The Royal Society Interface, 2008. **5**(18): p. 85-94.

104. Schoen, A.H., *Reflections concerning triply-periodic minimal surfaces*. Interface focus, 2012. **2**(5): p. 658-668.
105. Lord, E.A. and A.L. Mackay, *Periodic minimal surfaces of cubic symmetry*. Current Science, 2003. **85**(3): p. 346-362.
106. Hill, R., *The elastic behaviour of a crystalline aggregate*. Proceedings of the Physical Society. Section A, 1952. **65**(5): p. 349.
107. Zohdi, T.I. and P. Wriggers, *An introduction to computational micromechanics*. Vol. 20. 2008: Springer.
108. Müller, R., H. Van Campenhout, B. Van Damme, G. Van der Perre, J. Dequeker, T. Hildebrand, and P. Rüegeegger, *Morphometric analysis of human bone biopsies: a quantitative structural comparison of histological sections and micro-computed tomography*. Bone, 1998. **23**(1): p. 59-66.
109. Peacock, M., C. Turner, G. Liu, A. Manatunga, L. Timmerman, and C. Johnston Jr, *Better discrimination of hip fracture using bone density, geometry and architecture*. Osteoporosis international, 1995. **5**(3): p. 167-173.
110. Michelotti, J. and J. Clark, *Femoral neck length and hip fracture risk*. Journal of Bone and Mineral Research, 1999. **14**(10): p. 1714-1720.
111. Doube, M., M.M. Kłosowski, I. Arganda-Carreras, F.P. Cordelières, R.P. Dougherty, J.S. Jackson, B. Schmid, J.R. Hutchinson, and S.J. Shefelbine, *BoneJ: Free and extensible bone image analysis in ImageJ*. Bone, 2010. **47**(6): p. 1076-1079.
112. Abràmoff, M.D., P.J. Magalhães, and S.J. Ram, *Image processing with ImageJ*. Biophotonics international, 2004. **11**(7): p. 36-43.
113. Tanck, E., A. Bakker, S. Kregting, B. Cornelissen, J. Klein-Nulend, and B. Van Rietbergen, *Predictive value of femoral head heterogeneity for fracture risk*. Bone, 2009. **44**(4): p. 590-595.
114. Stauber, M. and R. Müller, *Age-related changes in trabecular bone microstructures: global and local morphometry*. Osteoporosis International, 2006. **17**(4): p. 616-626.
115. Morgan, E.F., H.H. Bayraktar, and T.M. Keaveny, *Trabecular bone modulus-density relationships depend on anatomic site*. J Biomech, 2003. **36**(7): p. 897-904.
116. Ciarelli, T., D. Fyhrie, M. Schaffler, and S. Goldstein, *Variations in Three-Dimensional Cancellous Bone Architecture of the Proximal Femur in Female Hip Fractures and in Controls*. Journal of Bone and Mineral Research, 2000. **15**(1): p. 32-40.
117. Kaneko, T.S., J.S. Bell, M.R. Pejicic, J. Tehranzadeh, and J.H. Keyak, *Mechanical properties, density and quantitative CT scan data of trabecular bone with and without metastases*. J Biomech, 2004. **37**(4): p. 523-30.
118. Keller, T.S., *Predicting the compressive mechanical behavior of bone*. Journal of biomechanics, 1994. **27**(9): p. 1159-1168.
119. Manual, A.U.s., *Version 6.5, Hibbitt, Karlsson and Sorensen. Inc.*, Pawtucket, RI, 2004.
120. David Hoffman, J.T.H. *Scientific Graphics Project, Mathematical Sciences Research Institute*. Available from: <http://www.msri.org/publications/sgp/jim/geom/level/skeletal/index.html>.

121. Karcher, H., *The triply periodic minimal surfaces of Alan Schoen and their constant mean curvature companions*. Manuscripta mathematica, 1989. **64**(3): p. 291-357.
122. Hyde, S., Z. Blum, T. Landh, S. Lidin, B. Ninham, S. Andersson, and K. Larsson, *The language of shape: the role of curvature in condensed matter: physics, chemistry and biology*. 1996: Elsevier.
123. Yoo, D.-J., *Computer-aided porous scaffold design for tissue engineering using triply periodic minimal surfaces*. International Journal of Precision Engineering and Manufacturing, 2011. **12**(1): p. 61-71.
124. Yoo, D.J., *Porous scaffold design using the distance field and triply periodic minimal surface models*. Biomaterials, 2011. **32**(31): p. 7741-7754.
125. Yoo, D., *New paradigms in hierarchical porous scaffold design for tissue engineering*. Materials Science and Engineering: C, 2013. **33**(3): p. 1759-1772.
126. Hildebrand, T. and P. Rügsegger, *A new method for the model-independent assessment of thickness in three-dimensional images*. Journal of microscopy, 1997. **185**(1): p. 67-75.
127. Gibson, L.J. and M.F. Ashby, *Cellular solids: structure and properties*. 1999: Cambridge university press.
128. Day, J., M. Ding, A. Odgaard, D. Sumner, I. Hvid, and H. Weinans, *Parallel plate model for trabecular bone exhibits volume fraction-dependent bias*. Bone, 2000. **27**(5): p. 715-720.
129. Chen, H., X. Zhou, S. Shoumura, S. Emura, and Y. Bunai, *Age-and gender-dependent changes in three-dimensional microstructure of cortical and trabecular bone at the human femoral neck*. Osteoporosis international, 2010. **21**(4): p. 627-636.
130. Hildebrand, T., A. Laib, R. Müller, J. Dequeker, and P. Rügsegger, *Direct Three-Dimensional Morphometric Analysis of Human Cancellous Bone: Microstructural Data from Spine, Femur, Iliac Crest, and Calcaneus*. Journal of Bone and Mineral Research, 1999. **14**(7): p. 1167-1174.
131. Cheung, Y.K., *Finite strip method in structural analysis*, 1976.
132. Lee, T., J.B. Choi, B.W. Schafer, W.P. Segars, F. Eckstein, V. Kuhn, and T.J. Beck, *Assessing the susceptibility to local buckling at the femoral neck cortex to age-related bone loss*. Annals of biomedical engineering, 2009. **37**(9): p. 1910-1920.
133. Kourtis, L.C., D.R. Carter, H. Kesari, and G.S. Beaupre, *A new software tool (VA-BATTS) to calculate bending, axial, torsional and transverse shear stresses within bone cross sections having inhomogeneous material properties*. Computer methods in biomechanics and biomedical engineering, 2008. **11**(5): p. 463-476.
134. Kourtis, L., H. Kesari, D. Carter, and G. Beaupré, *Transverse and torsional shear stresses in prismatic bodies having inhomogeneous material properties using a new 2D stress function*. Journal of Mechanics of Materials and Structures, 2009. **4**(4): p. 659-674.
135. Li, Z. and B.W. Schafer. *Buckling analysis of cold-formed steel members with general boundary conditions using CUFSM: conventional and constrained finite strip methods*. in *20th*

- International Specialised Conference on Cold-Formed Steel Structures*. 2010.
136. Du, Q., V. Faber, and M. Gunzburger, *Centroidal Voronoi tessellations: applications and algorithms*. SIAM review, 1999. **41**(4): p. 637-676.
  137. Lim, Y.X., *Modeling of Trabecular Bone*, in *Mechanical Engineering* 2012, National University of Singapore.
  138. Ding, M. and I. Hvid, *Quantification of age-related changes in the structure model type and trabecular thickness of human tibial cancellous bone*. Bone, 2000. **26**(3): p. 291-295.
  139. Sehlhorst, H.-G., R. Jänicke, A. Düster, E. Rank, H. Steeb, and S. Diebels, *Numerical investigations of foam-like materials by nested high-order finite element methods*. Computational Mechanics, 2009. **45**(1): p. 45-59.
  140. Gershon, A.L., H.A. Bruck, S. Xu, M.A. Sutton, and V. Tiwari, *Multiscale mechanical and structural characterizations of Palmetto wood for bio-inspired hierarchically structured polymer composites*. Materials Science and Engineering: C, 2010. **30**(2): p. 235-244.
  141. Nguyen, V.P., M. Stroeve, and L.J. Sluys, *Multiscale failure modeling of concrete: micromechanical modeling, discontinuous homogenization and parallel computations*. Computer Methods in Applied Mechanics and Engineering, 2012. **201**: p. 139-156.
  142. Saavedra Flores, E. and M. Friswell, *Multi-scale finite element model for a new material inspired by the mechanics and structure of wood cell-walls*. Journal of the Mechanics and Physics of Solids, 2012. **60**(7): p. 1296-1309.
  143. Su, Z., V. Tan, and T. Tay, *Concurrent multiscale modeling of amorphous materials in 3D*. International Journal for Numerical Methods in Engineering, 2012. **92**(13): p. 1081-1099.
  144. Hamed, E., I. Jasiuk, A. Yoo, Y. Lee, and T. Litzka, *Multi-scale modelling of elastic moduli of trabecular bone*. Journal of The Royal Society Interface, 2012. **9**(72): p. 1654-1673.
  145. Viceconti, M., *Multiscale Modeling of the Skeletal System*. 2012: Cambridge University Press.
  146. Schileo, E., F. Taddei, A. Malandrino, L. Cristofolini, and M. Viceconti, *Subject-specific finite element models can accurately predict strain levels in long bones*. J Biomech, 2007. **40**(13): p. 2982-9.
  147. Harrigan, T.P., M. Jasty, R.W. Mann, and W.H. Harris, *Limitations of the continuum assumption in cancellous bone*. Journal of Biomechanics, 1988. **21**(4): p. 269-275.
  148. Van Sint Jan\*, S., *The VAKHUM project: virtual animation of the kinematics of the human*. Theoretical Issues in Ergonomics Science, 2005. **6**(3-4): p. 277-279.
  149. de Bakker, P.M., S.L. Manske, V. Ebacher, T.R. Oxland, P.A. Cripton, and P. Guy, *During sideways falls proximal femur fractures initiate in the superolateral cortex: evidence from high-speed video of simulated fractures*. Journal of biomechanics, 2009. **42**(12): p. 1917-1925.
  150. Dall'Ara, E., B. Luisier, R. Schmidt, F. Kainberger, P. Zysset, and D. Pahr, *A nonlinear QCT-based finite element model validation study for*

- the human femur tested in two configurations < i > in vitro </i>. Bone, 2013. **52**(1): p. 27-38.*
151. van Beek, Y., D.J. Hessen, R. Hutteman, E.E. Verhulp, and M. van Leuven, *Age and gender differences in depression across adolescence: real or 'bias'?* J Child Psychol Psychiatry, 2012. **53**(9): p. 973-85.
152. Dagan, D., M. Be'ery, and A. Gefen, *Single-trabecula building block for large-scale finite element models of cancellous bone*. Medical and Biological Engineering and Computing, 2004. **42**(4): p. 549-556.
153. Zannoni, C., R. Mantovani, and M. Viceconti, *Material properties assignment to finite element models of bone structures: a new method*. Medical Engineering & Physics, 1999. **20**(10): p. 735-740.
154. Doblaré, M., J. Garcia, and M. Gómez, *Modelling bone tissue fracture and healing: a review*. Engineering Fracture Mechanics, 2004. **71**(13): p. 1809-1840.
155. Verhulp, E., B. van Rietbergen, and R. Huiskes, *Load distribution in the healthy and osteoporotic human proximal femur during a fall to the side*. Bone, 2008. **42**(1): p. 30-5.
156. Fox, J.C. and T.M. Keaveny, *Trabecular eccentricity and bone adaptation*. J Theor Biol, 2001. **212**(2): p. 211-21.
157. eFunda. [cited 2014 07.02.2014]; Available from: [http://www.efunda.com/formulae/solid\\_mechanics/columns/intro.cfm](http://www.efunda.com/formulae/solid_mechanics/columns/intro.cfm).